Technische Universität München
TUM School of Computation, Information and Technology

Reactive Motion Generation and Control of Elastic-Joint Robots for Reaching and Grasping

Xuming Meng

Vollständiger Abdruck der von der TUM School of Computation, Information and Technology der Technischen Universität München zur Erlangung eines

Doktors der Ingenieurwissenschaften (Dr.-Ing.)

genehmigten Dissertation.

Vorsitz: Prof. Dr.-Ing. Eckehard Steinbach

Prüfende der Dissertation:

1. Prof. Dr. Alin Albu-Schäffer
2. Prof. Dr. Cristina Piazza

Die Dissertation wurde am 5. Februar 2026 bei der Technischen Universität München eingereicht und durch die TUM School of Computation, Information and Technology am 15. Juli 2026 angenommen.

Abstract

In the human motor system, the interplay between musculoskeletal elasticity and neural reflexes enables seamless adjustments during interaction tasks such as object reaching and grasping. This synergy unifies motion planning and control into a single, reactive process that ensures adaptability and fluidity. In contrast, robotic hand-arm systems typically rely on a decoupled approach, where arm and finger motions are planned separately within a "Sense-Plan-Act" paradigm. This leads to sequential, open-loop execution, which limits reactivity and results in less natural movement. The high dimensionality of multi-fingered hands further complicates real-time motion planning, while achieving effective compliant control in robots with elastic joints remains a significant challenge. Consequently, robotic grasping often appears rigid and brittle, struggling to cope with dynamic environments or produce adaptive, human-like behaviors. This thesis addresses these challenges by exploring the integration of reactive, compliant, and dynamic control into robotic reaching and grasping, inspired by the remarkable adaptability of the human motor systems. The work makes three primary contributions to advance the field of elastic-joint robotics.

To emulate the role of reflexive control in the human motor system, the thesis begins by developing specialized control laws for antagonistic actuators, such as bidirectional variable-stiffness designs and unidirectional tendon-coupled systems, commonly used in robotic arms with multi-fingered robotic hands. Building on the original Elastic Structure Preserving impedance (ESPi) framework, the extended control law preserves the intrinsic elasticity of these actuators while enabling user-defined impedance behavior. The closed-loop system ensures global asymptotic stability and output-strict passivity, providing a robust foundation when executing compliant and responsive reaching and grasping motions.

Leveraging the compliant and stable foundation established by the extended ESPi control framework, the thesis introduces Finger Flow (FF), a real-time vector-field-based motion generation framework that utilizes real-time visual and proprioceptive feedback into continuous velocity commands. A computationally efficient geometric abstraction for hands with high degrees of freedom enables real-time finger-avoidant reaching motion. This empowers robots to grasp unpredictably moving cylindrical objects in free space.

After a grasp is established, the thesis proposes a task-space motion and force tracking controller that preserves the robot's intrinsic elastic structure during constrained interactions. Preserving this structure maintains natural compliance and ensures safe, stable interaction. Unlike conventional approaches that enforce full decoupling of motion and force subspaces, the method avoids canceling out the intrinsic dynamic coupling between them. This prevents potential instability in compliant systems due to the modeling errors. Instead, the controller ensures passive closed-loop dynamics and global asymptotic stability, enabling simultaneous tracking of desired motion and force while respecting the robot's physical compliance.

Together, these contributions form a reactive "Sense-Act" paradigm that enables smooth, continuous transitions between reaching, grasping, and manipulation through reactive control. Experiments and simulations on the DLR robot *neoDavid* validate the approach, demonstrating the practical viability of preserving physical dynamics while delivering robust performance in dynamic, human-shared environments, enabling more natural, adaptive, and safe robotic manipulation.

Zusammenfassung

Im menschlichen motorischen System ermöglicht das Zusammenspiel von muskuloskelettaler Elastizität und neuronalen Reflexen nahtlose Anpassungen bei Interaktionsaufgaben wie dem Erreichen und Greifen von Objekten. Diese Synergie vereint Bewegungsplanung und Regelung zu einem einzigen, reaktiven Prozess, der Anpassungsfähigkeit und Flüssigkeit gewährleistet. Im Gegensatz dazu stützen sich robotische Hand-Arm-Systeme typischerweise auf einen entkoppelten Ansatz, bei dem Arm- und Fingerbewegungen separat innerhalb des „Sense-Plan-Act"-Paradigmas geplant werden. Dies führt zu einer sequentiellen, offenen Ausführung, wodurch die Reaktivität eingeschränkt wird und Bewegungen weniger natürlich erscheinen. Die hohe Dimensionalität mehrfingriger Hände erschwert zusätzlich die echtzeitfähige Bewegungsplanung, während die Realisierung einer effektiven nachgiebigen Regelung bei Robotern mit elastischen Gelenken weiterhin eine erhebliche Herausforderung darstellt. Folglich wirkt robotisches Greifen oft starr und abgehackt, hat Schwierigkeiten mit dynamischen Umgebungen und zeigt nur eingeschränkt adaptive, menschenähnliche Verhaltensweisen. Diese Arbeit geht diese Herausforderungen an, indem sie die Integration reaktiver, nachgiebiger und dynamischer Regelung in koordinierten robotischen Greifbewegungen von Arm und Hand untersucht, inspiriert von der bemerkenswerten Anpassungsfähigkeit des menschlichen motorischen Systems. Die Arbeit leistet drei zentrale Beiträge im Bereich der elastisch-gelenkigen Robotik.

Um die Rolle der Reflexregelung im menschlichen motorischen System nachzuahmen, entwickelt die Arbeit zunächst spezialisierte Regelgesetze für antagonistische Antriebe, wie bidirektionale variable-Steifigkeits-Designs und unidirektionale seilzuggekoppelte Systeme, die häufig in Roboterarmen mit mehrfingrigen Händen verwendet werden. Aufbauend auf dem ursprünglichen Elastic-Structure-Preserving Impedance (ESPi)-Framework erhält das erweiterte Regelgesetz die intrinsische Elastizität dieser Antriebe, während es gleichzeitig ein benutzerdefiniertes Impedanzverhalten ermöglicht. Das geschlossene System gewährleistet globale asymptotische Stabilität und strikt passive Ausgangsdynamik und schafft damit eine robuste Grundlage für die Ausführung nachgiebiger und reaktiver Bewegungen beim Greifen.

Aufbauend auf dieser nachgiebigen und stabilen Grundlage führt die Arbeit Finger Flow (FF) - ein vektorfeldbasiertes Framework zur Bewegungsgenerierung in Echtzeit, das visuelles und propriozeptives Feedback in kontinuierliche Geschwindigkeitskommandos umsetzt. Eine recheneffiziente geometrische Abstraktion für Hände mit vielen Freiheitsgraden ermöglicht echtzeitfähige, fingervermeidende Erreichbewegungen. Dadurch können Roboter unvorhersehbar bewegte zylindrische Objekte im freien Raum greifen.

Nach erfolgreichem Greifen schlägt die Arbeit einen Bewegungs- und Kraftregelungsansatz im Aufgabenraum vor, der die intrinsische elastische Struktur des Roboters auch während eingeschränkter Interaktionen bewahrt. Diese Struktur erhält die natürliche Nachgiebigkeit und gewährleistet eine sichere, stabile Interaktion. Im Gegensatz zu konventionellen Ansätzen, die eine vollständige Entkopplung von Bewegungs- und Kraftunterräumen erzwingen, vermeidet die Methode das Aufheben der intrinsischen dynamischen Kopplung zwischen ihnen. Dadurch wird potenzielle Instabilität in nachgiebigen Systemen aufgrund von Modellierungsfehlern verhindert. Stattdessen stellt der Regler passive geschlossene Dynamik und globale asymptotische Stabilität sicher und ermöglicht gleichzeitig das Nachführen der gewünschten Bewegung und Kraft unter Berücksichtigung der physikalischen Nachgiebigkeit des Roboters.

Zusammen bilden diese Beiträge ein reaktives „Sense-Act"-Paradigma, das fließende, kontinuierliche Übergänge zwischen Erreichen, Greifen und Manipulation durch reaktive Regelung ermöglicht. Experimente und Simulationen am DLR-Roboter neoDavid validieren den Ansatz und demonstrieren

die praktische Umsetzbarkeit der Erhaltung der physikalischen Dynamik bei gleichzeitiger robuster Leistung in dynamischen, menschlich geteilten Umgebungen. Dadurch wird eine natürlichere, adaptivere und sichere robotische Manipulation ermöglicht.

Acknowledgement

This dissertation is the result of research carried out between 2020 and 2025 at the Institute of Robotics and Mechatronics of the German Aerospace Center (DLR) in Oberpfaffenhofen, Germany: a period marked by both challenges and growth, during which I had the privilege to learn, explore, and contribute within an inspiring research environment.

First and foremost, I would like to express my deepest gratitude to Prof. Alin Albu-Schäffer. I am profoundly thankful for the opportunity to pursue my PhD under his supervision, and for the trust and freedom he provided me throughout this journey. His vision in robotics and support gave me the chance to explore deeply in the field of elastic robots, to take risks in pursuing new ideas.

I am also very grateful to Prof. Christian Ott for his insightful technical discussions and for generously sharing his expertise. His in-depth insights from new perspectives greatly enriched this work and often helped me to look at my research challenges in a different light.

I sincerely thank Dr. Manuel Keppler, my close mentor, for his continuous support, countless technical discussions, and patient supervision, even during holidays. His encouragement and advice were invaluable in shaping this research and keeping me motivated. Beyond that, Manuel has shown me through his own example what true research should embody: the persistence to pursue questions to their very depth, with rigor and curiosity.

I would like to thank the team members in the neoDavid team: Sebastian Wolf, Ana Elvira Huezo Martin, Henry Maurenbrecher, Viktor Langofer, Anne Reichert, Leonard Klüpfel, Marie Harder, Cynthia Hofmann, Dr. Bastian Deutschmann, Dr. Manuel Stoiber, Dr. Martin Pfanne and also colleagues at DLR: Antonin Raffin, Ria Vijayan, David Wandinger, Clara Raschel, Samuel Bustamante, Florian Schmidt, Robert Burger, Jan Cremer and many others, for their support in mechatronics, software infrastructure, and project management.

Special thanks go to Robert Schuller, Xuwei Wu, Oliver Neumann, and Dr. Jianxiang Feng for our in-depth technical discussions and the moments of reflection about career, life, and the future. I am also thankful to Dr. Annika Schmidt, Dr. Davide Calzolari, Dr. Bastian Deutschmann, Dr. Hao Xing, and Robert once again for their effort in reviewing my papers and this thesis.

I am grateful to Dr. George Pollayil, Dr. Mathew Pollayil, Dr. Grazia Zambella, and Dr. Riccardo Mengacci, as well as the colleagues from the University of Pisa and IIT, for their fruitful collaborations and contributions. To Ria, Antonin, and Ribin, thank you for the technical discussions and our enjoyable "cooking nights," which brought much-needed balance during this journey.

I also wish to acknowledge my university friends at TU Munich: Qiming Yu, Le Li, and Qian Feng, for the countless discussions about future robotics, embodied AI, and beyond. Special thanks to Tao Ge and Jiaying He, for the food, conversations, and support that helped me get through the most difficult phases of my PhD.

Finally, and most importantly, I owe my deepest gratitude to my beloved parents. Their support often came in the form of the recurring question, "Have you finished your PhD yet?" To them I can finally answer: yes - thank you.

Munich, December 2, 2025 *Xuming Meng*

List of Symbols

Symbol	Unit	Description
$\boldsymbol{x}$	m	Position vector in task space (e.g., end-effector or object center of mass)
$\dot{\boldsymbol{x}}, \ddot{\boldsymbol{x}}$	m/s, m/s^2	Velocity and acceleration in task space
$\boldsymbol{q}$	rad	Joint position vector (link-side)
$\boldsymbol{\theta}$	rad	Motor position vector
$\tilde{\boldsymbol{x}}$	m	Task-space tracking error: $\boldsymbol{x} - \boldsymbol{x}_d$
$\tilde{\boldsymbol{q}}$	rad	Joint position error
$\boldsymbol{A}$	—	Positive definite matrix in linear flow dynamics
$\boldsymbol{M}(\boldsymbol{q})$	kg·m^2	Link-side inertia matrix
$\boldsymbol{C}(\boldsymbol{q}, \dot{\boldsymbol{q}})$	—	Coriolis and centrifugal force matrix
$\boldsymbol{g}(\boldsymbol{q})$	N	Gravitational torque vector
$\boldsymbol{B}$	kg·m^2	Reflected motor inertia matrix
$\boldsymbol{\psi}$	N·m	Link-side elastic torque
$\boldsymbol{\tau}$	N·m	Motor-side elastic torque
k_i	N·m/rad	Stiffness of elastic element i
$\boldsymbol{\kappa}$	N·m/rad	Physical stiffness on link side
$\boldsymbol{J}$	—	Jacobian matrix (task to joint space)
$\boldsymbol{K}$	N·m/rad	Stiffness matrices in control laws
$\boldsymbol{D}$	N·m/rad·s	Damping matrices in control laws
$\boldsymbol{\eta}$	rad	Virtual motor coordinate introduced for control design
$\boldsymbol{\lambda}$	N	Constraint force in constrained motion
$\boldsymbol{\lambda}_d$	N	Desired constraint force
$\tilde{\boldsymbol{\lambda}}$	N	Force tracking error: $\boldsymbol{\lambda} - \boldsymbol{\lambda}_d$
Ω_z	—	Domain of the state variable z
$\gamma(\boldsymbol{x})$	—	State-dependent transition function for semi-tangent flow
$\boldsymbol{q}_f$	rad	Finger joint angles
$\boldsymbol{q}_{f,d}$	rad	Desired finger joint configuration
$\boldsymbol{q}_{f,o}$	rad	Open finger configuration
$\Gamma(\boldsymbol{x})$	—	Distance function for ellipse: $(\boldsymbol{x} - \boldsymbol{x}_c)^\top Q(\boldsymbol{x} - \boldsymbol{x}_c)$
$\mathrm{sgn}(\cdot)$	—	Sign function
$\tanh(\cdot)$	—	Hyperbolic tangent function, used in smooth transitions
$\mathbb{R}^n$	—	n-dimensional real vector space
$\mathcal{D}, \mathcal{R}$	—	Sets (e.g., domains, regions) in state space
$\boldsymbol{u}$	N·m	Control input (motor torque)
t	s	Time

List of Acronyms

Acronym	Description
BAVS	Bidirectional Antagonistic Variable Stiffness (actuator)
CoM	Center of Mass
DLR	German Aerospace Center (Deutsches Zentrum für Luft- und Raumfahrt)
DoF	Degree of Freedom
DMP	Dynamic Motion Primitives
DP	Dynamic Plane
ESP	Elastic Structure Preserving Control
ESPi	Elastic Structure Preserving Impedance Control
FAS	Flexible Antagonistic Spring (actuator component)
FC	Force Closure
FF	Finger Flow (proposed framework)
FSJ	Floating Spring Joint
KMP	Kernelized Motion Primitives
neoDavid	Wheeled Humanoid Robot developed at DLR
ODE3, ODE4	Numerical solvers (e.g., Runge-Kutta methods)
ProMPs	Probabilistic Movement Primitives
RMP	Riemannian Motion Policies
RL	Reinforcement Learning
SEDS	Stable Estimator of Dynamical Systems
SP	Static Plane (hand-fixed reference plane)
VSA	Variable Stiffness Actuator

Contents

1 Introduction **1**
- 1.1 Motivation . . . 1
  - 1.1.1 Compliant Robots for Reaching and Grasping . . . 3
- 1.2 Related Work . . . 6
  - 1.2.1 Reactive Finger-Arm Reaching Planning . . . 6
  - 1.2.2 Increase Grasp Success under Uncertainty . . . 8
  - 1.2.3 Motion Control of Robots with Compliant Antagonistic Actuators . . . 8
  - 1.2.4 Force and Motion Control with Constraints . . . 9
- 1.3 Research Gaps and Thesis Goals . . . 9
- 1.4 Thesis Overview and Contributions . . . 11
- 1.5 Publications . . . 14
  - 1.5.1 Main Publications in this Thesis . . . 14
  - 1.5.2 Other Publications . . . 14

2 Fundamentals **15**
- 2.1 Notations . . . 15
- 2.2 Modeling Elastic Torque of Antagonistic Actuators . . . 16
  - 2.2.1 Bidirectional Type: BAVS . . . 16
  - 2.2.2 Unidirectional Type: Tendon-Coupled FAS . . . 18
- 2.3 Modeling Rigid-link Dynamics with Compliant Antagonistic Actuators . . . 21
  - 2.3.1 Dynamics Under Constraints . . . 22
  - 2.3.2 Motor Inertia Shaping . . . 24
- 2.4 Designing Vector Fields as Feedback Motion Planning . . . 25
  - 2.4.1 Vector Fields . . . 25
  - 2.4.2 Integral Curves . . . 26

3 Elastic Structure Preserving Control for Compliant Antagonistic Actuators **31**
- 3.1 Introduction . . . 32
- 3.2 A Single-Joint Example . . . 33
  - 3.2.1 Control Objectives . . . 33
  - 3.2.2 Controller Design . . . 35
  - 3.2.3 Passivity and Stability Analysis . . . 38
- 3.3 Tendon-Coupled Multi-Joint System with FAS Actuation . . . 39
  - 3.3.1 Target Closed-Loop Dynamics . . . 40
  - 3.3.2 Control Design . . . 41
  - 3.3.3 Stability and Passivity Analysis . . . 43
- 3.4 Experiment: Interaction Test on a Single BAVS Joint . . . 46

3.5 Simulations on Elastic Tendon-Driven Fingers . . . 48
3.5.1 Regulatory Behavior . . . 49
3.5.2 Interaction Behavior . . . 52
3.6 Summary . . . 53

4 Finger Flow (FF): Reactive Reach-While-Grasp Motion Generation 55
4.1 Challenges . . . 57
4.2 Methods and Framework Overview . . . 58
4.2.1 Core Ideas . . . 58
4.2.2 Overview . . . 59
4.3 Hand Hull: A Simplified Hand Mesh . . . 60
4.3.1 2D Hand Hull . . . 61
4.3.2 3D Hand Hull . . . 61
4.4 Hand Motion Generation . . . 63
4.4.1 Problem Statement . . . 64
4.4.2 Semi-tangent Flow: An Attractive and Collision-Avoiding Translational Velocity Field for the Object . . . 64
4.4.3 Guiding flow for the hand . . . 71
4.4.4 Convergence and Collision Avoidance . . . 74
4.5 Finger Motion Generation . . . 78
4.5.1 Selection of the Hand-Cage Configuration . . . 80
4.6 Experimental Validation, Simulation Study, and Discussion . . . 80
4.6.1 Experiment 1: Grasping a Stationary Tabletop Object . . . 82
4.6.2 Experiment 2: Grasping an Unpredictably Moving Object . . . 86
4.6.3 Experiment 3: Interactive and Adversarial Human-to-Robot Handover . . . 87
4.6.4 Simulation Study . . . 91
4.6.5 Limitations and Outlook . . . 94
4.7 Summary . . . 96

5 Passivity-based Motion and Force Tracking Control 97
5.1 Introduction . . . 98
5.2 Open-Loop Task-Space Dynamics . . . 99
5.3 Control Objectives and Design . . . 102
5.3.1 Desired Closed-Loop Dynamics . . . 102
5.3.2 Equilibrium Analysis . . . 104
5.3.3 Coordinate Transformation . . . 104
5.3.4 Controller Design . . . 105
5.4 Passivity and Stability Analysis . . . 106
5.4.1 Output Strict Passivity (OSP) . . . 107
5.4.2 Uniform Asymptotic Stability (UAS) . . . 108
5.5 Case Study: A Constrained Dual-Arm System . . . 109
5.5.1 Reference Trajectories and Disturbance . . . 110
5.5.2 Parameter and Simulation Setup . . . 111
5.5.3 Results and Discussion . . . 111
5.5.4 Robustness to Numerical Integration Solver Settings . . . 114
5.6 Summary . . . 114

6 Conclusion and Discussion **117**
6.1 Conclusion . . . 117
6.2 Limitations and Lessons Learned . . . 118
6.2.1 Tendon-Driven Hand Control: Gaps in Real World . . . 118
6.2.2 Hand-Arm Coordination and Human Motor Control Parallels . . . 120
6.2.3 Reactive Control but Non-predictive . . . 120
6.2.4 Assumption on Constraint Modeling in Force Tracking Control . . . 121
6.3 Future Directions . . . 121

A Appendix: Stability Analysis for the Constrained System **125**
A.1 Vidyasagar's Theorem on Hierarchical Systems . . . 125
A.2 Proof of Uniform Asymptotic Stability . . . 125

B Appendix: Finger Flow **129**
B.1 Hand Hull Generation . . . 129
B.1.1 Preliminaries: Rotated and Center-Shifted Ellipses . . . 129
B.1.2 Estimation of Finger Configuration and Length . . . 131
B.1.3 Estimated Finger Kinematics . . . 131
B.1.4 Closed Forms of Region Definitions . . . 132
B.2 Tangent Flow . . . 134
B.2.1 Closed Forms for Tangent Flow . . . 134
B.2.2 Tangent Line and Tangent Point . . . 135
B.2.3 Continuous Tangent Flow Across s_1 via virtual ellipse . . . 136
B.2.4 State-dependent Transition Function . . . 136
B.2.5 Lipschitz Continuity of the Rotation Angle . . . 137
B.3 Invariant Set . . . 138
B.3.1 Proof of an Invariant Set . . . 138
B.4 Implementation Details in Experimental Validations . . . 139
B.4.1 System Parameters . . . 139
B.4.2 Object Pouring and Placing Motion . . . 139

Bibliography **141**

1

Introduction

1.1 Motivation

Humans exhibit remarkably fluid and adaptive grasping by exploiting the intrinsic elasticity of their musculoskeletal system. Tendinous tissues, acting in series with muscles, store and release mechanical energy. This enables reflexive responses to perturbations, quick adjustments that occur without deliberate high-level feedback or planning [1]. Whether catching a falling object or adjusting grip on a slippery cup, humans use passive compliance in combination with neural reflexes to modulate forces, absorb impacts, and seamlessly transition between reaching and grasping. These processes naturally merge motion planning and control into one integrated behavior.

By contrast, most traditional robotic grasping approaches decouple reach and grasp into two sequential stages, as reported as early as 1992 [2] and still in 2022 [3]: first, a planned trajectory positions the manipulator; then, the end-effector closes around the object, often resulting in stiff, mechanically obvious motions that lack adaptability to unmodeled disturbances. This "first reach, then grasp" paradigm is widespread in both industrial applications and research, as illustrated in Figure 1.1 (a)-(b), but it fails to harness the benefits of compliance for both dynamic and reactive grasping.

In this thesis, the terms *dynamic*, *reactive*, and *compliant* describe complementary aspects of reaching and grasping behavior, distinguishing between task-intrinsic dynamics, responses to extrinsic disturbances, and physical interaction properties:

- "**Dynamic**" refers to grasping tasks characterized by *intrinsic* object motion, such as catching or intercepting predictable moving objects [4, 5]. These tasks require online adaptation to known but time-dependent task dynamics.

- "**Reactive**" refers to the ability to adapt motion in response to *extrinsic* and often *unforeseen* changes in the environment or interaction conditions. Examples include avoiding unexpected obstacles [6, 7], enabling natural object handovers [8, 9], or recovering from failed grasps.

- "**Compliant**" describes the physical interaction behavior of the robot, enabled by mechanical and control design choices that allow it to conform to object geometry and surface properties, and ensure safe interaction in shared human environments.

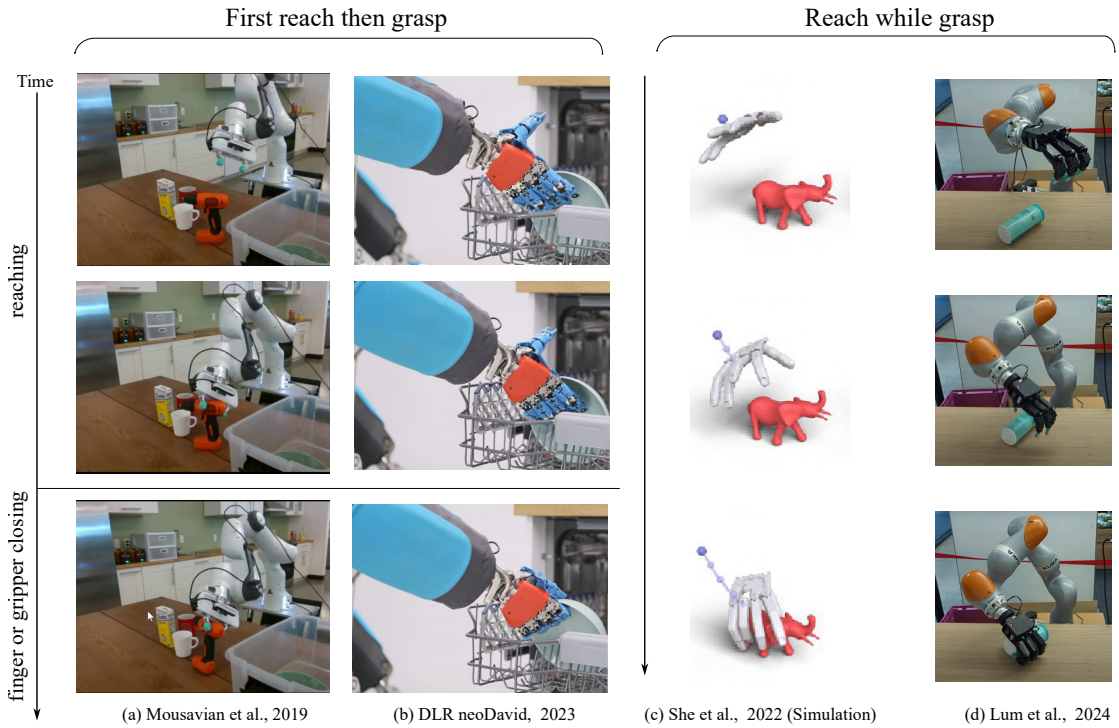


Figure 1.1: Sequential grasp planning and execution. (a) Grasping using a 7-DoF Franka Panda arm with a parallel-jaw gripper [10], and (b) DLR humanoid *neoDavid* unloading the dishwasher. Both demonstrations show the end-effector first approaching the pre-grasp pose and then performing the grasp execution (gripper or hand closing), which is triggered after the approaching motion sequence is fully completed. (c) Researchers in [3] demonstrated the ideal natural seamless reach-and-grasp when planning high-DoF finger configurations and hand pose simultaneously, which is computationally expensive for online planning when the object is perturbed. and (d) Recent work [11] utilized reinforcement learning for online grasp pose and finger configuration generation using a KUKA iiwa arm with an Allegro hand.

From a system's perspective, human-like robotic hand–arm grasping is conventionally realized through two primary paradigms, as illustrated in Figure 1.2: the "sense–plan–act" paradigm, also referred to as the deliberative system [12, 13], and the "sense–act" paradigm, also referred to as the reactive system [14]. Examples of both paradigms for a reaching and grasping task are shown in Figure 1.1. Deliberative systems require constructing comprehensive world models [15], aiming to solve a considerate long-horizon grasp motion plan [16], and initiating execution only after the plan is finalized. Conversely, reactive systems draw inspiration from biological stimulus-response mechanisms [17, 18], enabling rapid responses by embedding the controller within a set of concurrent condition–action rules, operating with minimal internal state [19].

Compared to the deliberate systems, reactive systems trade off the complexity of reasoning for fast reaction time. They are particularly suitable for rapid motion generation in dynamic environments where quick responses to changes are necessary. Several prior works have shown the effectiveness [6, 20–22]. We see this reactivity stemming from two aspects. As depicted in Figure 1.2 (b), the intermediate-level motion generators use feedback (e.g., vision, proprioception, force, joint position, etc.) to continuously adapt motions during execution. The lower level ensures compliance through intrinsic mechanical compliance or closed-loop control, ensuring a safe interaction when an external disturbance is present.

To achieve robotic grasping that integrates reactivity, dynamics, and compliance, efforts span multiple domains: elastic mechanical design (e.g., actuator-based elasticity), compliant control frameworks, and reactive planning algorithms.

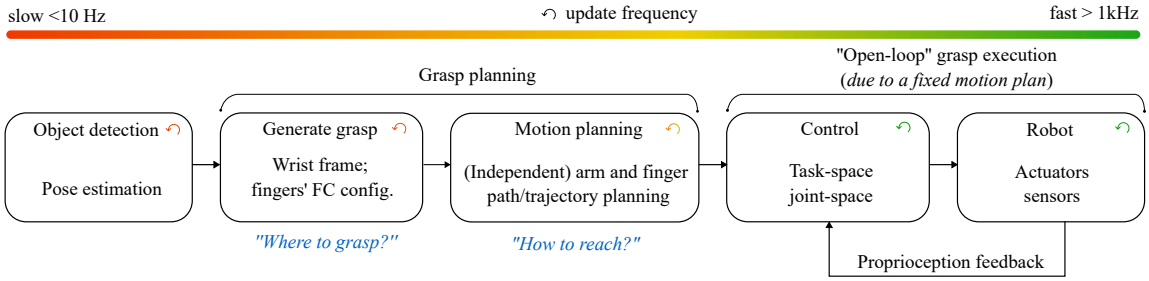
1.1.1 Compliant Robots for Reaching and Grasping

Elastic-joint robots integrate compliant actuation mechanisms that enhance safety and natural interactions in human-robot collaboration scenarios, leveraging their inherent elasticity for improved shock absorption during physical contact [24], making them well-suited for high-speed reach-and-grasp tasks in dynamic environments [24]. Elastic-joint robots usually have rigid bones (skeletons) connected with compliant elastic actuators. Prominent examples are Series Elastic Actuators (SEAs) [25] in the 1990s and Variable-Stiffness Actuators (VSAs) [26] in the 2000s, which embed springs either in series with motor outputs.

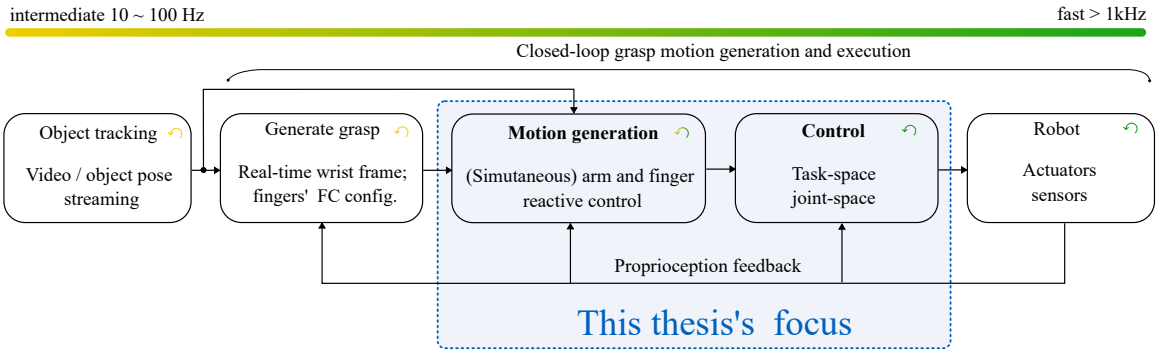
Elastic tendon-driven hands Compliant robotic hands combine elastic actuators and tendons to mimic the adaptability of human musculoskeletal systems [27]. Robotic hands with tendon-driven, antagonistic actuation further emulate human biomechanics by distributing compliance across multiple degrees of freedom. For instance, tendon-driven anthropomorphic fingers equipped with series elasticity not only enhance safety in human–robot interaction but also enable the robot to adapt grasp force continuously in the face of external disturbances [28]. Similarly, grippers with cable-driven compliance have been shown to maintain grasp stability under significant pose uncertainty [29]. Some representatives of these elastic tendon-driven hands are depicted in Figure 1.3.

This elasticity allows tendons to act as natural springs, absorbing shocks and facilitating smooth, continuous motion by bridging the gap of the unnatural, rigid grip.

DLR humanoid Robot neoDavid The elastic humanoid robot DLR *neoDavid* [44] integrates various types of variable stiffness actuators [45], as illustrated in Figure 1.4. In the arm, the first four joints, comprising three shoulder joints and one elbow joint, are realized using Floating Spring Joints

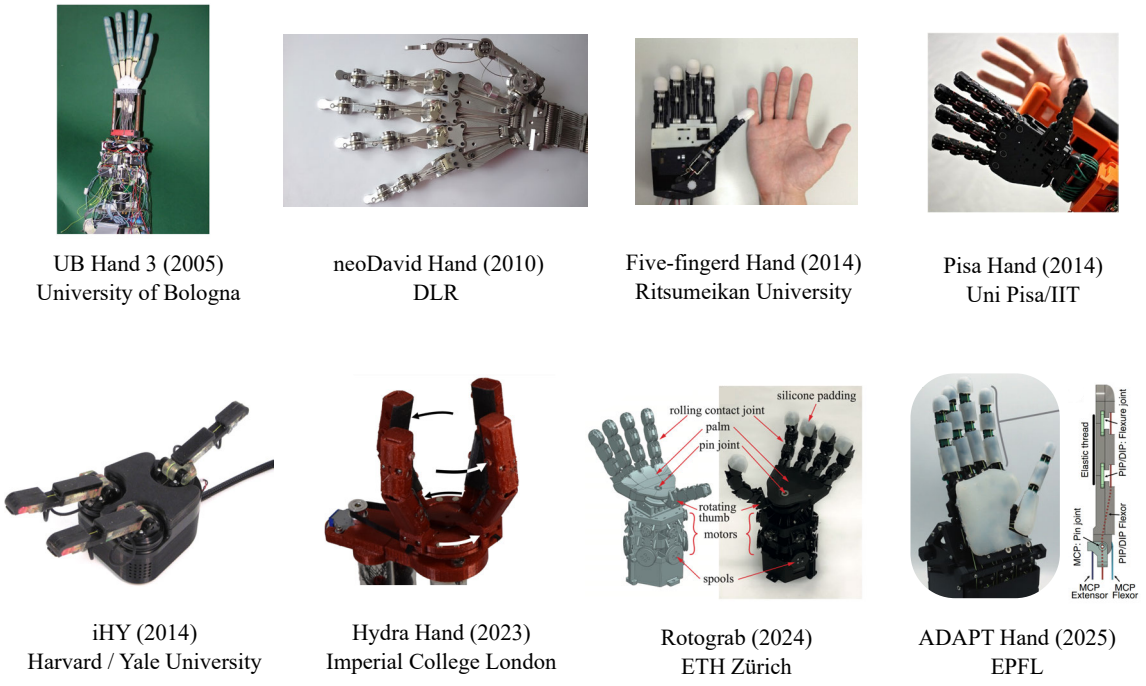


(a) Sense–Plan–Act



(b) Sense–Act ("stimulus–response")

Figure 1.2: Two common paradigms for grasping tasks, categorized in the context of behavior-based robotics [12]. (a) The **Sense-Plan-Act** paradigm is typically used for generating (ideally global) optimized motions in cluttered, complex, and mostly slow-changing environments, where real-time performance is less critical. Computational cost rises significantly with the complexity of grasp generation, which includes determining 6D wrist frame poses and corresponding finger configurations that satisfy force-closure (FC) conditions [23], as well as planning collision-free motions for both arm and fingers toward the target pose. (b) The **Sense-Act** paradigm prioritizes fast reaction times over computational complexity, making it well-suited for dynamic and reactive scenarios. This thesis adopts the **Sense-Act** paradigm, which aligns better with the requirements of reactive and dynamic grasping tasks.



UB Hand 3 (2005)
University of Bologna

neoDavid Hand (2010)
DLR

Five-fingerd Hand (2014)
Ritsumeikan University

Pisa Hand (2014)
Uni Pisa/IIT

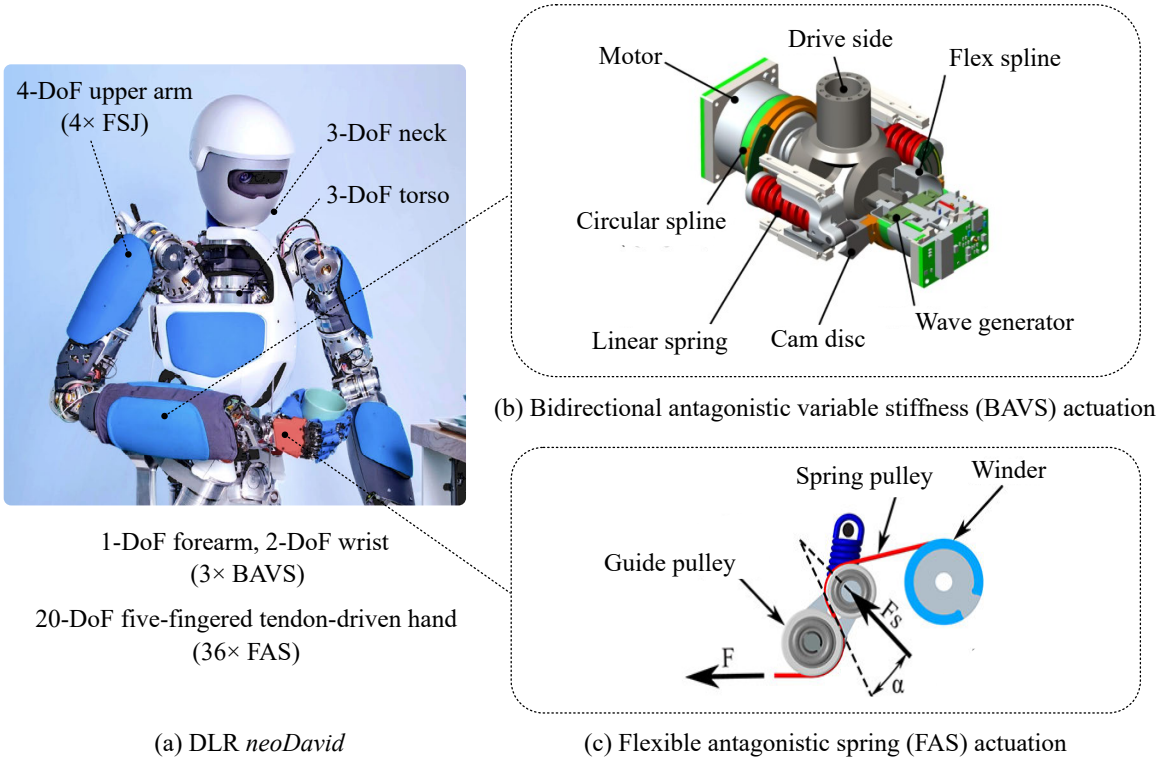
iHY (2014)
Harvard / Yale University

Hydra Hand (2023)
Imperial College London

Rotograb (2024)
ETH Zürich

ADAPT Hand (2025)
EPFL

Figure 1.3: Some notable examples of elastic tendon-driven multi-fingered hands developed in research domain: UB Hand 3 [30], DLR David hand [31], the five-fingered hand by Ozawa et al. [32], and Pisa/IIT SoftHand [33], iHY hand [34], Hydra hand [35], Rotograb [36], ADAPT hand [37].



(a) DLR *neoDavid*

(b) Bidirectional antagonistic variable stiffness (BAVS) actuation

(c) Flexible antagonistic spring (FAS) actuation

Figure 1.4: (a) The upper body of DLR robot *neoDavid* is driven by several types of compliant actuators: Floating Spring Joint (FSJs) [38], (b) Bidirectional Antagonistic Variable Stiffness Actuators (BAVS) [39, 40], and (c) Flexible Antagonistic Spring (FAS) component [41]. The neck is driven by tendon-driven continuum joints [42], and the torso is actuated by adjustable linear spring mechanisms [43] © DLR.

(FSJ)s [38], each driven by two motors: one for adjusting the stiffness preset and the other for generating torque at the joint. For the remaining three arm joints, including two wrist Degree of Freedoms (DoFs) and one for forearm rotation, more compact Bidirectional Antagonistic Variable Stiffness (BAVS) joints [39, 40] are employed. Unlike conventional antagonistic mechanisms that require positive tendon forces to maintain joint actuation [46], BAVS joints allow both motors to either push or pull on the joint, enabling bidirectional force application [39]. The hand, featuring 20 degrees of freedom, is actuated by 36 antagonistic-type Flexible Antagonistic Springs (FAS) [41], which provide intrinsic compliance and fine motor control through passive elasticity.

1.2 Related Work

Two primary fields are surveyed: reactive grasping motion generation and elastic actuator control for robotic arms and hands.

1.2.1 Reactive Finger-Arm Reaching Planning

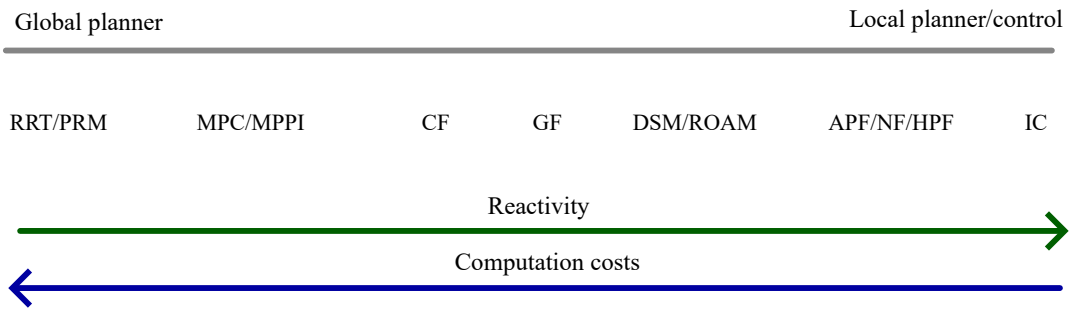


Figure 1.5: Spectrum of state-of-the-art planning- or control-based reactive motion generation with known models of environment. The methods from the left to the right are: Rapidly exploring Random Tree (RRT) [47], Probabilistic Road Map (PRM) [48], Model Predictive Control (MPC) [49], Model Predictive Path Integrator (MPPI) [22], Circular Field (with predictive multi-agents) (CF) [50, 51], Geometric Fabric (GF) [52], Dynamical-system-based Modulation (DSM) [53], Rotational Obstacle Avoidance Method (ROAM) [54], [55] Artificial Potential Field (APF), [56, 57] Navigation Function (NF), Harmonic Potential Field (HPF) [58], Impedance Control (IC) [59].

Motion planning methods in general are designed to identify feasible, collision-free trajectories between two robot states, often with the goal of achieving optimality in terms of path length, energy, or time [60]. In dynamic environments, however, reactivity, measured by the system's ability to rapidly adapt to changes, becomes a critical performance metric. Highly reactive methods typically have to operate with limited environmental information, which reduces computational overhead and enables higher update frequencies.

As illustrated in Figure 1.5, this creates a spectrum of planning approaches: at one end are global planners that generate optimal but slow-to-update trajectories; at the other are low-level, reactive controllers that prioritize fast response over long-term optimality. This thesis focuses on the reactive end of this spectrum, targeting real-time motion generation for dynamic reaching tasks. Accordingly, the following section reviews local, reactive motion generation techniques that support continuous adaptation through real-time sensory feedback.

Reactive object reaching

For multi-fingered hands, generating collision-free reaching motions in real-time is difficult due to high degrees of freedom and geometric complexity. While methods like those by [3] offer offline planning for coordinated arm-hand motion, they struggle in dynamic settings. The authors in [6] use imitation learning for local collision avoidance but lack generalization across finger configurations. Other approaches focus on efficient grasp pose synthesis and filtering [61–64], yet scalability remains an issue with increasing model complexity, which is, for example, stemming from contact evaluation, which is scaled up by an increasing number of vertices or faces in fingers and object meshes.

In contrast, parallel-jaw grippers benefit from learning-based methods enabling faster grasp pose generation [65–67] thanks to simple geometric shapes and usually low DoFs. Generative Grasping Convolutional Neural Network (GG-CNN) [20] achieves up to 50 Hz operation rate by integrating object tracking and grasp prediction. The previously mentioned work has been applied successfully in mobile and human-robot interaction scenarios using position-based visual servoing (PBVS) [68] [8, 69–71]. However, they are limited to simple top-down grasps, and some may require powerful GPUs for real-time inference.

Object catching and reactive finger closing

For dynamic object grasping, work like [5] uses Recurrent Neural Networks (RNNs) trained on object trajectories, while authors in [4] and [72] rely on learned dynamical systems to predict intercept points and generate online trajectories. These often require prior demonstrations and assume predictable object motion (e.g., following a parabolic trajectory governed by gravity), making them unsuitable for unpredictable targets. Object reaching trajectories are generated via dynamical systems toward the predicted intercept point, followed by PD+ or inverse dynamics controllers for tracking [73]. Inspired by the natural human motion, the authors in [73] motivate the necessity for building a coordinated finger-arm controller for seamless and rapid finger motion in coordination with hand posture. In this work, the finger and arm motion were not learned in one Dynamical System (DS) but learned separately. A smooth handover action using a dynamical system was demonstrated in [9].

Most methods use trigger-based strategies to initiate finger closure. Examples include binary open/close decisions based on grasp quality metrics [74], timed triggers near predicted intercept points [4], distance thresholds for grippers [69], or continuous control based on object proximity [20].

Real-time finger-object collision avoidance

Few works explicitly address finger-object collisions when the whole hand is still approaching the object, though many leverage efficient motion generation techniques from robot navigation, such as artificial potential fields [55], navigation functions [56], and dynamical systems [75]. These provide computationally efficient, closed-form solutions ideal for reactive grasping tasks.

Finally, we note that recent data-driven grasping approaches, such as learning from demonstration using Dynamic Motion Primitives (DMP) [76], Probabilistic Movement Primitives (ProMPs) [77], Stable Estimator of Dynamical Systems (SEDS) [78], Riemannian Motion Policies (RMP) [79], and Kernelized Motion Primitives (KMP) [80], are beyond the scope of this thesis. With advances in large models, Diffusion Policies (DP) [81] have been used to generate continuous grasp sequences, including end-effector and finger motions [82], and recent work combines Reinforcement Learning (RL) with geometric fabrics for reactive grasping on real-world platforms like the KUKA arm with Allegro Hand [11]. For an overview of data-driven and learning-based methods, see surveys, e.g., [83, 84].

1.2.2 Increase Grasp Success under Uncertainty

Traditional multi-finger grasp planners rely on contact models, including the locations and wrenches fulfilling the force-closure conditions [23]. However, these approaches can be prone to fail very easily in the real world due to sensing noises and uncertainties from proprioceptive or visual feedback [34, 85].

Grasping via caging

In contrast, robust strategies explicitly reduce dependency on exact geometry. For example, caging (or enveloping) grasps intentionally trap the object in a partially closed loop of fingers rather than requiring all contacts to be perfectly placed [85]. Elastic or compliant finger joints further enhance robustness: flexible cover deform on impact and passively conform to object shape, providing collision tolerance and adaptive alignment [34]. Together, these mechanisms raise the likelihood of a successful grasp despite uncertainty in object pose or hand positioning.

Rodriguez et al. [86] have formalized such enveloping grasps as caging. They have shown that for a two-finger hand, any valid caging configuration guarantees a simple blind grasp: one needs to only close (or open) the fingers to capture the object, without precise sensing or control [86]. Zarubin et al. [85] categorize these as "circle caging" (nearly enclosing a long axis of the object) and "sphere caging" (wrapping the object with a virtual loop). In practice, these wrap-around grasps constrain the object's motion so that rough finger motions inevitably tighten the hold. By surrounding the object, caging strategies effectively transform approach uncertainty into a reliable final capture: the object cannot escape while the hand closes, greatly improving success under imprecise conditions.

Grasping using compliant hands

Elastic and underactuated hand designs further improve grasp robustness. For instance, torsional compliance in flexure joints (as in the i-HY hand) [34] lets fingertips passively conform to an object's surface, automatically compensating for small pose errors. More generally, built-in compliance or passive springs allow fingers to adapt their posture to variations in object geometry or unexpected collisions without active feedback. This passive adaptation both cushions impacts and "wraps" the fingers more snugly around the object, raising grip reliability. As demonstrated in compliant multi-fingered hands, the combination of structural flexibility and adaptive grasp postures simplifies execution: the hand can "find" the object and form a stable hold without precise positioning or sensing.

1.2.3 Motion Control of Robots with Compliant Antagonistic Actuators

Numerous methods were developed for controlling robots with elastic joints in terms of regulation or tracking tasks, e.g., PD-regulator with gravity compensation [87, 88], feedback linearization [89, 90], backstepping [91]. Recently, control methods based on inverse dynamics [92] and linear quadratic regulator [93] have been developed for VSA that allow the active variation of the mechanical stiffness. In [94][95], passivity-based control laws are proposed and show excellent performance for impedance control on robots with relatively stiff joints.

However, the reduction of the joint stiffness by several magnitudes rendered previous state-of-the-art approaches unsatisfactory. Typically, two control loops are employed to achieve the desired joint motion and stiffness: an inner loop for tendon force control and an outer loop for enforcing

the desired link behavior. A method for statically decoupling joint motion and stiffness variation was introduced in [96]. Following the two-loop strategy, the authors in [97] proposed a cascaded approach that carefully considered tendon tension constraints by solving an optimization problem. Similarly, [98] presented a method in which a force control law with an optimized tendon tension distribution algorithm was derived. However, none of these works provides a guarantee of stability. Despite their effectiveness, these approaches focus on canceling or modifying the system's intrinsic properties through control design.

The problem of robustly controlling robots through a passive design and minimal shaping of the dynamic structure was discussed in [99, 100]. In particular, a perfect gravity cancellation in order to allow the control of the robot without accounting for the gravity bias was studied in [100]. Instead, [101] proposed control laws for implementing a desired interaction behavior on the motor or link side, respectively, while preserving the elastic structure. The concept of Elastic Structure Preserving (ESP) control was extended to bidirectional antagonistic actuation in [102]. Even though [101]-[103] address the case of multi-DoF robots, the reduced elastic model employed therein cannot be used to model tendon-driven systems; thus, the ESP control cannot be applied straightforwardly to our case.

1.2.4 Force and Motion Control with Constraints

Controlling both motion and force simultaneously presents a more complex challenge than pure motion control, particularly when the robot operates under constraints. In such cases, robots can be modeled as multi-body systems with a kinematic closed loop, as seen in cooperative manipulation tasks or robotic hands performing grasping. The task is to achieve accurate force control, while the desired motion should also be well-controlled.

In the field of hybrid motion and force control for robots with elastic joints, Spong [104] introduced the concept of integral manifolds and corrective control, applied to both constrained (motion) and unconstrained (force) spaces. However, this approach assumes a singularly perturbed system, which necessitates a fast inner control loop. A similar strategy was adopted by Mills [105], who incorporated a corrective term into the slow control loop to account for joint flexibility. More recently, Aghili [106] proposed a projected inverse-dynamics method for rigid-joint robots, decoupling the system dynamics into two orthogonal subspaces. This formulation was later extended to operational space control by Mistry et al. [107, 108], enabling its application to underactuated systems such as humanoid robots.

Since then, various extensions of these projection-based approaches have been developed. For instance, Ortenzi et al. [109] experimentally demonstrated full decoupling of motion and force control in a lightweight robot using an explicit force control formulation. The general projection framework, where an inverse-dynamics controller operates in the constraint-free space and an optimization-based approach handles the constrained space, has also been successfully applied to multi-arm systems and quadrupedal robots for both manipulation and locomotion tasks [110, 111].

1.3 Research Gaps and Thesis Goals

While system-level performance in reactive grasping is influenced by multiple factors, including vision update rates, sensing latency, and limited bandwidth inherent in compliant actuation, this thesis discusses two necessary technical domains: real-time motion generation and low-level control of

compliant actuators. Even with ideal perception and hardware, failure in either domain precludes fluid, adaptive grasping, making them the primary targets of the methodology developed herein.

Challenges in real-time motion generation Motion generation entails computing collision-free, dynamically feasible trajectories from the current state to a time-varying target, while reacting to object motion.[1] The high dimensionality of systems like a 7-DoF arm + 20-DoF hand introduces combinatorial complexity in collision checking and trajectory generation, especially under perturbations or with unpredictable objects.

Equally limiting is the rigid decoupling of arm and finger motion in traditional "first-reach-then-grasp" pipelines. Triggered by heuristics like distance or time cf. Figure 1.2 (a), these approaches prevent concurrent finger adaptation during approach, undermining robustness and naturalness. As the authors of [73] note, this precludes fluid behaviors like "grasping while reaching," where continuous co-adaptation is essential.

Challenges in controlling compliant actuators Even optimal trajectories fail if the actuators cannot execute them faithfully. Compliant mechanisms, particularly antagonistic (e.g., FAS [41], BAVS [39, 40]) or tendon-driven designs, introduce nonlinearities in elastic torques that complicate the modeling for control design. Low mechanical stiffness reduces system bandwidth, causing sluggish response and oscillations during tracking [101]. In tendon-driven hands, a single motor often influences multiple joints via complex routing, creating underactuation. Moreover, tendons only pull, requiring continuous pretension to avoid slack.

Addressing these challenges in tandem is essential for achieving human-like, adaptive grasping and forms the central contribution of this thesis: an integrated framework that unifies real-time motion generation with compliant actuator control.

Research Gaps

These challenges translate into three unaddressed gaps in the literature:

> **Gap 1: Lack of a structure-preserving control for antagonistic actuators.** While ESP control [101] offers a principled, passivity-based approach to compliant actuation, it has not been extended to antagonistic systems (e.g., BAVS, FAS). Existing methods for such actuators typically cancel compliance rather than exploit it. This work adapts and generalizes ESP control to both bi- and unidirectional antagonistic topologies, enabling impedance modulation while preserving the system's natural elastic dynamics.
>
> **Gap 2: Absence of reactive, computationally efficient motion generation.** Despite advances in grasp synthesis (e.g., [11, 66, 112]), no existing approaches demonstrate dynamic grasping of objects with unpredictable motion in free space using a multi-fingered hand-arm system.
>
> **Gap 3: No passivity-based force-motion control for constrained elastic-joint robots.** Once contact is established, maintaining grasp stability while tracking object motion and internal forces is challenging. Existing methods for constrained elastic-joint robots often compromise passivity with fully decoupled motion and force control, risking instability during interaction.

[1] Several recent works in real-time grasp generation have shown promising results, and interested readers are referred to [11, 66, 112] for further details. Therefore, the synthesis of finger configurations that satisfy force-closure conditions is not within the scope of this thesis.

Goals

This thesis aims to develop reactive robotic hand–arm systems with high-degree-of-freedom elastic joints, enabling fluid, adaptive, and human-like interactions with the world. The goal is to enable grasping that is not only robust for stationary objects but also responsive to those that move unpredictably, without the need for repeated discrete re-planning, even under highly dynamic conditions. Guided by this overarching vision, the thesis is structured around the following specific goals:

G1 Develop structure-preserving passivity-based motion control for robots with compliant antagonistic actuators, enabling safe and natural human-robot interaction.

G2 Generate fluid and natural hand-arm motion that integrates grasping during the reaching phase, eliminating the need for discrete planning stages.

G3 Enable intuitive, closed-form reaction plans for fast and effective responses to reaching target changes.

G4 Ensure computational efficiency in motion generation to support real-world deployment on low-power hardware.

G5 Retaining grasping force tracking control under constraints (e.g., assuming fixed in-hand contacts when a stable grasp is established) while maintaining passivity in the closed-loop system.

These goals are pursued from two perspectives: motion generation and control design, within a "sense-act"-type system pipeline, see Figure 1.2(b).

1.4 Thesis Overview and Contributions

The thesis is structured according to the natural sequence of a one-shot grasping motion, as illustrated in Figure 1.6 (a) to (c). Following the introduction in Chapter 1, Chapter 2 reviews the modeling and control foundations for antagonistic elastic actuators (e.g., BAVS, FAS) and for constrained robot dynamics. These elements are essential for the following control design. A brief introduction to vector field design is presented, which is utilized for feedback motion planning that supports the reactive motion generation approach discussed in the later chapter.

Chapter 3 addresses **Gap 1** by extending the Elastic Structure Preserving (ESP) control framework [101, 113] to both single-DoF bidirectional and multi-DoF tendon-coupled antagonistic actuators. The resulting controller ensures link-side impedance behavior while preserving the system's intrinsic compliance, thereby providing stable joint-level references for motion execution.

Chapter 4 tackles **Gap 2** through the introduction of Finger Flow (FF), a reactive motion generation framework that enables fluid, simultaneous arm-hand coordination during the approach phase. By integrating real-time visual feedback with dynamical systems, FF achieves natural "grasping-while-reaching" behavior with high computational efficiency, eliminating reliance on discrete, re-planning motion stages.

In Chapter 5, the **Gap 3** is closed by proposing a passivity-based motion and force tracking control method, applied after a stable grasp has been established. Using a dynamically consistent projection method, the controller is specifically tailored for constrained dynamics under compliant actuation.

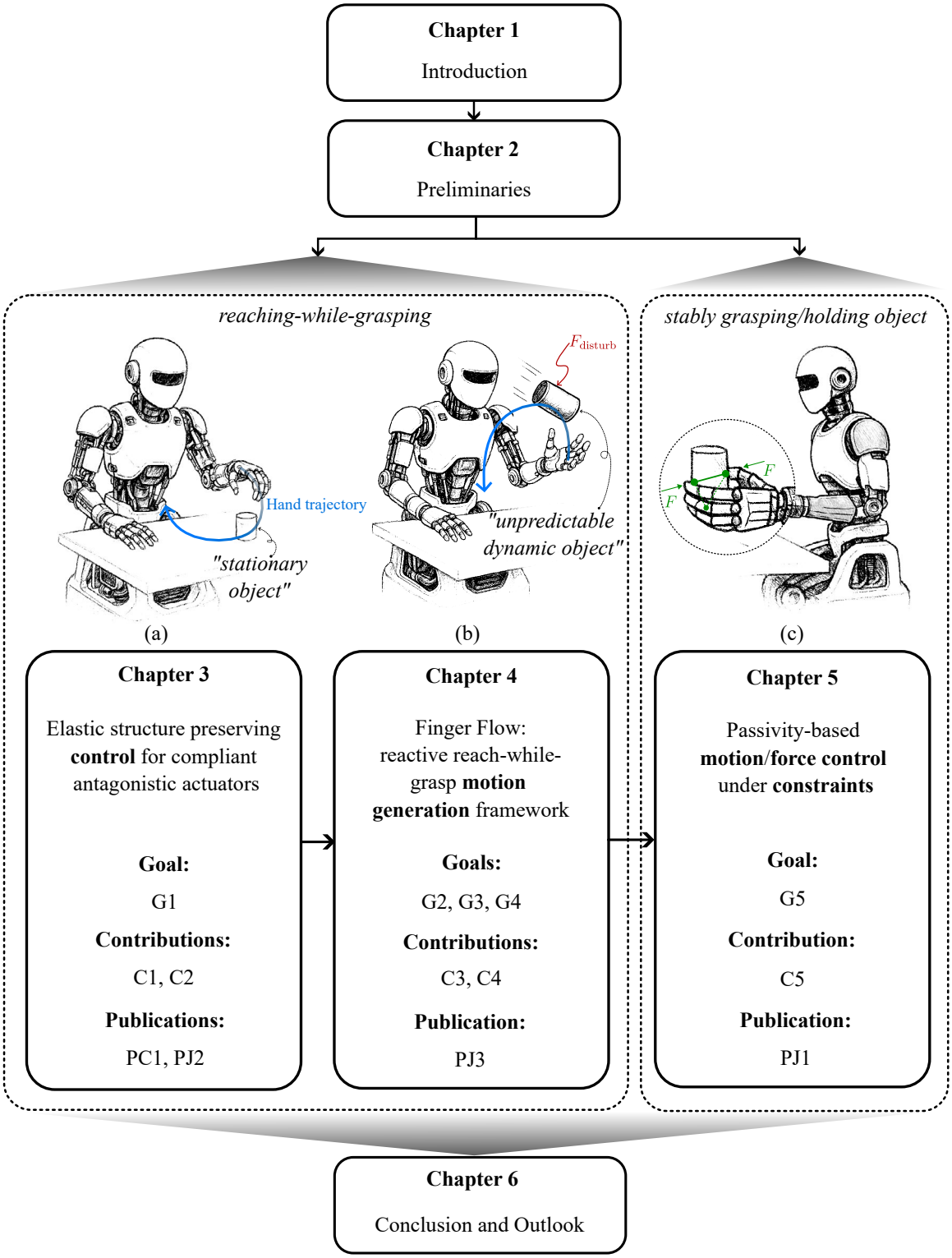


Figure 1.6: Thesis Outline. To achieve fluidity and responsiveness in reaching and grasping, the thesis focuses on two phases: (a)-(b) "grasping-while-reaching" and (c) stably holding an object for motion and force-based manipulation. Images (a)-(c) are generated by GPT-4o-mini, OpenAI.

This enables the robot to maintain a stable grasp, such as when manipulating fragile objects, while adaptively regulating internal forces without altering contact points.

Finally, Chapter 6 summarizes the contributions of this thesis. The lessons learned and key insights gained are discussed, along with suggestions for future research directions.

Contributions

The major contributions are summarized as follows.

C1 **ESPi control for bidirectional antagonistic actuators**. Generalization of ESPi controller [101] to a bidirectional antagonistic-type actuator (BAVS). Compared to [102], the presented solution allows for greater freedom in shaping the interaction behavior of a BAVS actuator by allowing the implementation of a desired impedance behavior directly on the link side. 👉 **Publication** [PC1].

C2 **ESPi control for multi-tendon-coupled unilateral antagonistic actuators**. Extension of the ESPi framework to multi-DoF mechanical coupled tendon-driven systems with unilateral antagonism; The desired closed-loop dynamics is achieved with an added impedance behavior on the link side while minimally modifying the dynamics and the elastic coupling due to tendon routing. 👉 **Publication** [PJ2].

C3 **Finger Flow (FF) for dynamic and reactive multi-fingered grasping**. A motion generator that generates reactive grasp-while-approach motions for both the hand and fingers by utilizing the feedback of the object's pose and finger joint positions. The underlying hand motion generator continuously adjusts the hand's pose to prevent collisions between a multi-fingered hand and the object during approach. For stationary spherical objects, formal guarantees of both convergence and collision avoidance are provided. The FF is based on a finger's position-dependent hand hull, a computationally efficient mesh representation, particularly well-suited for multi-fingered hands with high degrees of freedom and complex geometries. The proposed framework achieves an execution frequency of more than 3 kHz on low-power mobile CPUs. 👉 **Publication** [PJ3].

C4 **Extensive real-world experiments of FF**. The FF framework is validated through vast experiments on the DLR robot, neoDavid, which performs over 130 successful grasps of stationary tabletop objects. The framework's adaptability in dynamic scenarios is further demonstrated, including its ability to grasp moving objects, facilitate smooth human-to-robot handovers, and operate reliably under both cooperative and adversarial conditions throughout the entire reaching and grasping phases. 👉 **Publication** [PJ3].

C5 **Passivity-based motion and force tracking for constrained elastic-joint robots**. A control framework is proposed for constrained elastic-joint robots to ensure passivity during interactions. By employing a dynamically consistent projection method, the system's natural inertial and elastic properties are preserved. An integral force controller addresses steady-state errors that arise from constant disturbances. This method guarantees output strict passivity (OSP) during interactions and ensures uniform asymptotic stability during unconstrained motion. 👉 **Publication** [PJ1].

1.5 Publications

1.5.1 Main Publications in this Thesis

The main publications on which this thesis is based are listed as follows:

Journals

[PJ1] **X. Meng**, M. Keppler and C. Ott, "Passivity-Based Motion and Force Tracking Control for Constrained Elastic Joint Robots," in *IEEE Control Systems Letters*, vol. 7, pp. 217-222, 2023.

[PJ2] **X. Meng***, G. J. Pollayil*, M. Keppler, M. Pfanne, A. Bicchi and C. Ott, "Elastic Structure Preserving Impedance Control for Nonlinearly Coupled Tendon-Driven Systems," in *IEEE Control Systems Letters*, vol. 6, pp. 1982-1987, 2022. (*: equal contribution)

[PJ3] **X. Meng**, H. Maurenbrecher, A. Albu-Schäffer, and M. Keppler, "Finger flow: Reactive Reach-while-Grasp Generation for Robotic Arms with Multi-Fingered Hands", in *Robotics and Autonomous Systems*, 2025.

Conferences

[PC1] **X. Meng**, M. Keppler and C. Ott, "Elastic Structure Preserving Impedance Control of Bidirectional Antagonistic Variable Stiffness Actuation," 2021 European Control Conference (ECC), 2021, pp. 263-269.

1.5.2 Other Publications

Furthermore, the following journal publications have been co-authored, which are related to the thesis's topic but not integrated into this thesis:

- [44] S. Wolf, Thomas Bahls, B. Deutschmann, A. Dietrich, M. Harder, H. Höppner, C. Hofmann, A. H. Martin, M. Keppler, L. Klüpfel, H. Maurenbrecher, **X. Meng**, A. E. Reichert, M. Bihler, M. Chalon, O. Eiberger, W. Friedl, M. Grebenstein, M. Iskandar,V. Langofer, M. Pfanne, A. Raffin, J. Reinecke, T. Wüsthoff and A. Albu-Schäffer, "neoDavid - A humanoid robot with variable stiffness actuation and dexterous manipulation skills", in *IEEE Robotics and Automation Magazine*, 2025.
- [114] M. C. Harder, M. Keppler, **X. Meng**, C. Ott, H. Hoeppner and A. Dietrich, "Simultaneous Motion Tracking and Joint Stiffness Control of Bidirectional Antagonistic Variable-Stiffness Actuators," in IEEE Robotics and Automation Letters. (**Honorable Mention**)[2]
- [115] **X. Meng** and R. Weitschat, "Dynamic Projection of Human Motion for Safe and Efficient Human-Robot Collaboration," 2021 IEEE International Conference on Robotics and Automation (ICRA), 2021, pp. 3765-3771.

[2]Honorable Mention of the IEEE Robotics and Automation Letters, May 2022.

2

Fundamentals

This chapter provides an overview of the modeling basics and the tools used in this thesis. The torque characteristics of two common types of antagonistic actuation are modeled: (1) the bidirectional BAVS joint and (2) the unidirectional Flexible Antagonistic Spring (FAS) actuation. The resulting elastic torque models are essential for formulating the reduced robot dynamics, including the link-side dynamics, motor dynamics, and their coupling, often referred to as the Spong model [116], which is widely used for elastic-joint robots. This dynamics serves as the basis for the control law design presented in Chapter 3. As an extension, this model is adapted to incorporate kinematic constraints, laying the basis for the constrained motion and force control strategies explored in Chapter 5. Finally, a brief introduction to vector field design is provided. A vector field is a commonly used approach in feedback motion planning. This concept is central to the dynamical system formulation underlying the reactive motion generation framework developed in Chapter 4.

Publication Note

The following contents in Section 2.2 are partially adapted based on Section II of [103] and Section II of [117].

- [103]: **X. Meng**, M. Keppler, and C. Ott. "Elastic Structure Preserving Impedance Control of Bidirectional Antagonistic Variable Stiffness Actuation". In: *2021 European Control Conference (ECC 2021)*. 2021, pp. 263–269.
- [117]: **X. Meng***, G. Jose Pollayil*, M. Keppler, M. Pfanne, A. Bicchi, C. Ott (2021). Elastic Structure Preserving Impedance Control for Nonlinearly Coupled Tendon-Driven Systems. *IEEE Control Systems Letters*, 6, 1982-1987. (*: equal contribution).

2.1 Notations

Throughout this thesis, the following notation conventions are used: Scalars are represented by standard italic letters (e.g., t, m, n). Vectors are denoted by bold lowercase letters (e.g., $\boldsymbol{x}$), matrices by bold uppercase letters (e.g., $\boldsymbol{M}$), and sets by calligraphic uppercase letters (e.g., $\mathcal{S}$). A left superscript, such as ${}^{\mathcal{H}}(\cdot)$, indicates the reference frame in which a quantity is expressed. This applies to

vectors, rotation matrices in the Lie group $SO(3)$, and rigid-body poses in $SE(3)$. The transpose of a matrix is denoted by a superscript $^\top$ (e.g., $\boldsymbol{M}^\top$), the inverse by a superscript $^{-1}$ (e.g., $\boldsymbol{M}^{-1}$), and the Moore-Penrose pseudo-inverse by a superscript $^+$ (e.g., $\boldsymbol{M}^+$). $\|\cdot\|$ denotes the Euclidean norm (vector magnitude).

The cross product of two 3D vectors $\boldsymbol{a}, \boldsymbol{b} \in \mathbb{R}^3$ is denoted by $\boldsymbol{a} \times \boldsymbol{b}$. The wedge operator, $[(\cdot)]_\times : \mathbb{R}^3 \to \mathbb{R}^{3\times 3}$, maps a vector to its corresponding skew-symmetric matrix, such that for $\boldsymbol{a} \in \mathbb{R}^3$,

$$[\boldsymbol{a}]_\times = \begin{bmatrix} 0 & -a_3 & a_2 \\ a_3 & 0 & -a_1 \\ -a_2 & a_1 & 0 \end{bmatrix}$$

and satisfies $\boldsymbol{a} \times \boldsymbol{b} = \boldsymbol{a}^\wedge \boldsymbol{b}$. The vee operator, $(\cdot)^\vee : \mathbb{R}^{3\times 3} \to \mathbb{R}^3$, is the inverse of the wedge operator, mapping a skew-symmetric matrix back to a vector.

The configuration of a robot with n degrees of freedom is denoted as $\boldsymbol{q} \in \mathbb{Q} \subset \mathbb{R}^n$, where $\mathbb{Q}$ is the configuration space. The time-dependent configuration is given by $\boldsymbol{q}(t)$, and its time derivatives are denoted as $\dot{\boldsymbol{q}}(t)$, $\ddot{\boldsymbol{q}}(t)$, and higher-order derivatives such as jerk $\boldsymbol{q}^{(3)}(t)$ and snap $\boldsymbol{q}^{(4)}(t)$. A task-space variable is denoted by $\boldsymbol{x} \in \mathbb{R}^m$, where typically $m < n$. The relationship between configuration and task space is defined by a smooth Jacobian matrix $\boldsymbol{J}(\boldsymbol{q}) \in \mathbb{R}^{m\times n}$, which satisfies $\dot{\boldsymbol{x}} = \boldsymbol{J}(\boldsymbol{q})\dot{\boldsymbol{q}}$. Finally, partial derivatives are expressed using standard notation, e.g., $\frac{\partial f}{\partial x}$, and appear throughout when describing gradients, Jacobians, or Hessians of scalar and vector-valued functions. The variables $\boldsymbol{\tau}$ and $\boldsymbol{\psi}$ denote the motor-side and link-side elastic torques, respectively.

2.2 Modeling Elastic Torque of Antagonistic Actuators

Compared to constant stiffness, which is commonly found in Series Elastic Actuators (SEAs), antagonistic type actuators typically exhibit nonlinear elastic torque characteristics. This behavior enables them to better mimic the variable stiffness observed in human joints due to muscle contraction [118]. In this thesis, two types of variable stiffness antagonistic actuators are mainly focused on as representative examples, which are implemented in the humanoid robot DLR *neoDavid*.

The discussion begins with a bidirectional actuator. Its push-and-pull capability [39] allows it to operate independently, in a manner similar to SEAs. In contrast, the *unidirectional-type* actuator, such as FAS, relies on unilateral pulling force and is typically integrated with tendon-driven systems [46]. By routing tendons across multiple joints, each joint can achieve motion in both directions, despite the unidirectional nature of the actuator itself.

2.2.1 Bidirectional Type: BAVS

Figure 2.1 presents a schematic diagram of the BAVS joint implemented at the forearm rotation joint. The system comprises two identical motors, each with a rotor's reflected inertia denoted by B, and a single link with inertia M. The motor positions are described by generalized coordinates θ_i for $i = 1, 2$, while the link position is represented by q.

Each motor is connected to the link through a nonlinear elastic element. This nonlinearity is realized via a cam disc with a specifically designed profile (see [40] for further details), which transforms the rotational motion of the motor into a nonlinear spring displacement. By co-contracting these

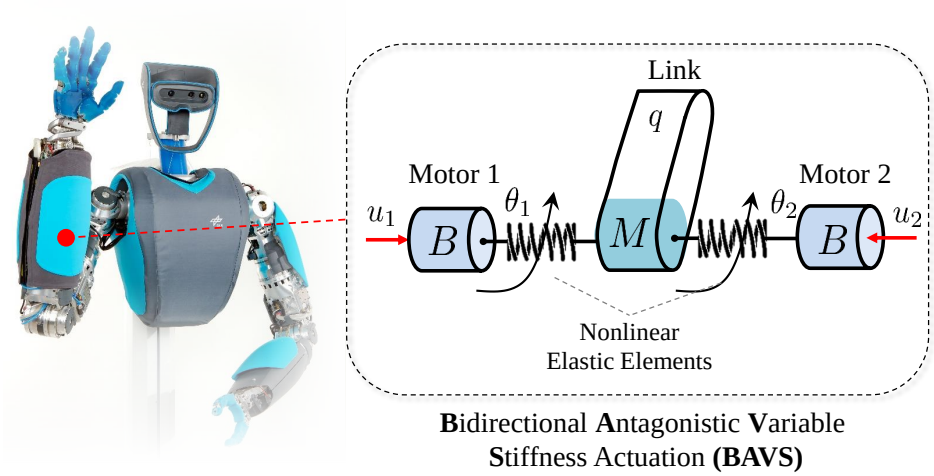


Figure 2.1: The anthropomorphic robot David [119]. The forearm rotation joint and wrist joint are implemented with Bidirectional Antagonistic Variable Stiffness (BAVS) joints. A schematic diagram of the BAVS joint is depicted on the right. © 2021 IEEE.

springs, the stiffness of the system can be actively modulated, and asynchronous motor movements generate torque on the link [39].

The general form of the elastic torques and stiffness in the BAVS actuation mechanism originates from a positive definite potential function $U_i(\theta_i - q) : \mathbb{R} \to \mathbb{R}^+$, assumed to be at least three times differentiable. The corresponding elastic torque, $\tau_i : \mathbb{R} \to \mathbb{R}$, is defined as the gradient of this potential and is strictly monotonic increasing:

$$\tau_i(\theta_i - q) := \frac{\partial U_i(\theta_i - q)}{\partial(\theta_i - q)} \,. \tag{2.1}$$

A right-hand-side (RHS) link-side elastic torque is defined by $\psi : \mathbb{R}^2 \to \mathbb{R}$, which is derived from the potentials U_i as follows:

$$\psi(\theta_1 - q, \theta_2 - q) := -\sum_{i=1}^{2} \frac{\partial U_i(\theta_i - q)}{\partial q} = \sum_{i=1}^{2} \frac{\partial U_i(\theta_i - q)}{\partial(\theta_i - q)} \,, \tag{2.2}$$

which simplifies to the superposition of the individual elastic torques (2.1):

$$\psi(\theta_1 - q, \theta_2 - q) = \tau_1(\theta_1 - q) + \tau_2(\theta_2 - q). \tag{2.3}$$

The stiffness of each elastic element, $k_i : \mathbb{R} \to \mathbb{R}^+$, is given by the derivative of the respective elastic torque:

$$k_i(\theta_i - q) := \frac{\partial \tau_i(\theta_i - q)}{\partial(\theta_i - q)} > 0 \,. \tag{2.4}$$

Similarly, the RHS physical stiffness on the link side, denoted $\kappa : \mathbb{R}^2 \to \mathbb{R}$, is obtained as the gradient of the link-side torque ψ:

$$\kappa(\theta_1 - q, \theta_2 - q) := -\frac{\partial \psi}{\partial q} = k_1(\theta_1 - q) + k_2(\theta_2 - q) \,. \tag{2.5}$$

Figure 2.2 illustrates the link-side torque and stiffness characteristics of the BAVS joint in *neoDavid*'s forearm. The pretension of the joint is determined by the relative motor positions, expressed as $\sigma = \theta_1 - \theta_2$, with a detailed explanation provided in [39]. The colored lines in the top and bottom

plots of Figure 2.2 indicate the feasible range of link-side torque ψ and stiffness κ for three distinct pretension levels. As σ increases, the mechanically achievable range of both ψ and κ decreases. These properties will play a key role in the analysis presented in Section 3.2.2.

2.2.2 Unidirectional Type: Tendon-Coupled FAS

After analyzing BAVS joints, the next step is to examine unidirectional antagonistic actuators that operate using tendon-driven mechanisms. In contrast to BAVS joints that employ dual motors for direct stiffness modulation through co-contraction, tendon-coupled architectures generally utilize either single-motor-driven configurations or pre-tensioned passive tendons to transfer forces and regulate stiffness throughout all joints via strategic tendon routing design [120].

The elastic torques exhibit nonlinear coupling between the link-side dynamics (3.33a) and motor-side dynamics (3.33b), characterized by $\boldsymbol{\psi}(\boldsymbol{\theta}, \boldsymbol{q})$ and $\boldsymbol{\tau}(\boldsymbol{\theta}, \boldsymbol{q})$, representing the elastic torques on the link side and motor side, respectively. These torques are functions of the tendon forces $\boldsymbol{f}_{te}$ according to

$$\boldsymbol{\psi}(\boldsymbol{\theta}, \boldsymbol{q}) = \boldsymbol{L}^\top \boldsymbol{f}_{te}(\boldsymbol{\theta}, \boldsymbol{q}), \tag{2.6}$$

$$\boldsymbol{\tau}(\boldsymbol{\theta}, \boldsymbol{q}) = \boldsymbol{E}\boldsymbol{f}_{te}(\boldsymbol{\theta}, \boldsymbol{q}). \tag{2.7}$$

Here, $\boldsymbol{L} \in \mathbb{R}^{n_\theta \times n}$ denotes the *coupling matrix*, while $\boldsymbol{E} \in \mathbb{R}^{n_\theta \times n_\theta}$ represents a constant diagonal matrix encoding motor radius values, ensuring invertibility. The tendon force $\boldsymbol{f}_{te}$ demonstrates highly nonlinear characteristics as functions of elongations $\Delta\boldsymbol{l}$, which are dependent on $\boldsymbol{\theta}, \boldsymbol{q}$. Due to the various mapping functions of $\boldsymbol{\theta}$ and $\boldsymbol{q}$ influenced by tendon routing, the following assumption is considered in this thesis.

Assumption 1. *The tendon elongation follows the relationship:*

$$\Delta\boldsymbol{l} = \boldsymbol{E}\boldsymbol{\theta} - \boldsymbol{L}\boldsymbol{q}. \tag{2.8}$$

Additionally, for every tendon indexed by $j = 1, \cdots, n_\theta$, the tendon force function $f_{t,j}(\Delta l_j)$ possesses C^3 continuity and exhibits strict monotonic increase with respect to Δl_j. Consequently, the elastic potential function $U_{e,j}(\Delta l_j)$ demonstrates convexity and radial unboundedness.

Furthermore, the tendon-driven architecture requires keeping tension, specifically

$$\boldsymbol{f}_{te} > \boldsymbol{0}. \tag{2.9}$$

For each tendon, the elastic potential function is written as $U_{e,j}(\Delta l_j) : \mathbb{R} \to \mathbb{R}^+$. The associated tendon force is expressed as

$$f_{te,j}(\Delta l_j) := \frac{\partial U_{e,j}(\Delta l_j)}{\partial \Delta l_j}. \tag{2.10}$$

Through application of the virtual work principle, the motor-side and link-side elastic torques are

$$\delta U_e(\Delta\boldsymbol{l}) = \delta U_e(\boldsymbol{\theta}, \boldsymbol{q}) = \delta\boldsymbol{\theta}^\top \underbrace{(\boldsymbol{E}\boldsymbol{f}_{te})}_{\boldsymbol{\tau}} + \delta\boldsymbol{q}^\top \underbrace{(-\boldsymbol{L}^\top \boldsymbol{f}_{te})}_{-\boldsymbol{\psi}}. \tag{2.11}$$

Our analysis incorporates the following assumption regarding the coupling matrix

Assumption 2. *The coupling matrix $\boldsymbol{L}$ maintains constant values, with dimensionality satisfying $n_\theta > n$ and having full rank, i.e., rank$(\boldsymbol{L}) = n_q$.*

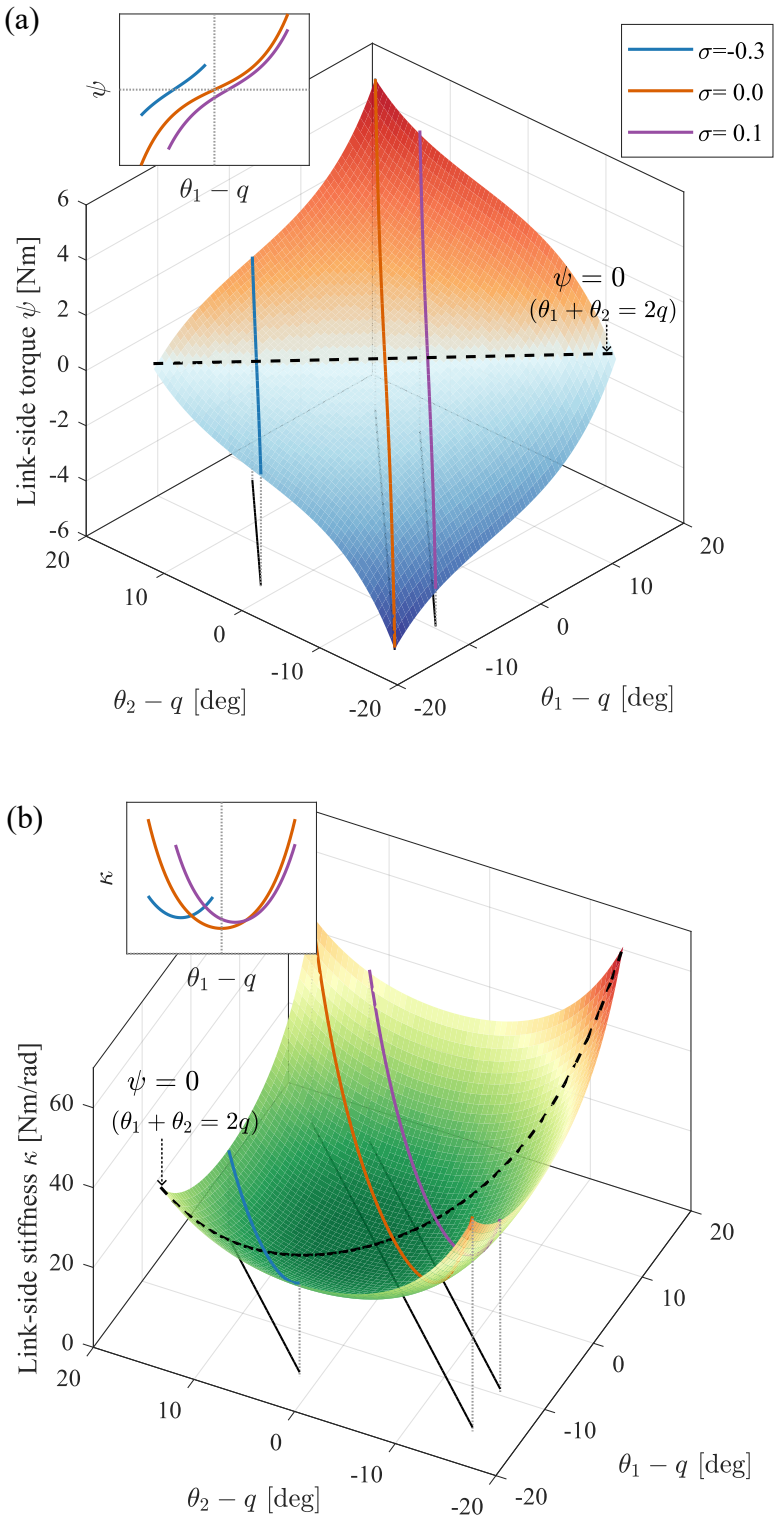
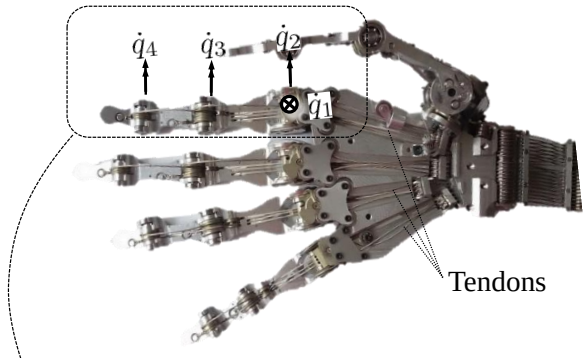
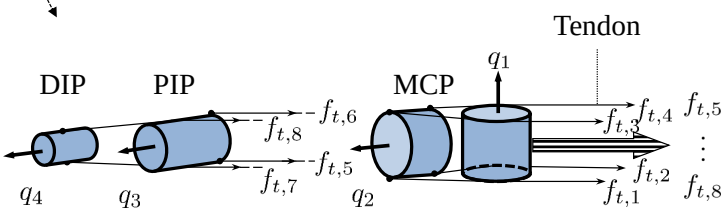


Figure 2.2: (a) The elastic torque ψ and (b) the local stiffness κ are shown in the deflection coordinates $\theta_i - q$. The maximum deflection is $|\theta_i - q|_{\max} = 15.5°$. The colored lines indicate the feasible region for ψ and κ when the motor coordinate difference $\sigma = \theta_1 - \theta_2$ [rad] is held constant. The two inset plots display ψ and κ as functions of $\theta_1 - q$ for different values of σ. The blue curve, corresponding to the largest absolute value of σ, exhibits the narrowest feasible range for both torque and stiffness. This figure is partially adapted from [103, Fig. 2].



(a) DLR neoDavid hand



(b) Tendon routing

Figure 2.3: Illustration of a tendon-driven system: (a) The DLR *neoDavid* hand, displaying the joint coordinates $\boldsymbol{q} \in \mathbb{R}^4$ of the index finger. (b) The index finger routing with coupled tendons. Tendon forces $\boldsymbol{f}_{te} \in \mathbb{R}^8$ in tension are depicted. Figure adapted from [117].

Remark on assumptions

The tendon elongation expression [120, Sec. 6.4.2] and the requirement for 3x continuous differentiability stated in Assumption 1 are widely applicable across numerous tendon-driven architectures, as demonstrated in systems like [121] and [31]. The monotonic increasing property of $\boldsymbol{f}_{te}$ with respect to $\Delta \boldsymbol{l}$ represents a fundamental characteristic of such systems.

Regarding Assumption 2, the constant nature of $\boldsymbol{L}$ can be achieved through the implementation of additional pulley turns. Well-designed tendon networks inherently possess a *coupling matrix* with full rank properties [120]. The dimensional constraint on $\boldsymbol{L}$ relates directly to Caratheodory's theorem [120], establishing that a minimum of $n+1$ tendons is required for tendon-driven robot actuation. Practical implementation is exemplified in the DLR *neoDavid* Hand, where $n_\theta = 2n$ tendons serve the thumb, index, and middle fingers, while $n_\theta < 2n$ tendons are employed for the ring and little fingers. The tendon routing of the index finger is illustrated in Figure 2.3 (b).

Summary

The elastic torques $\boldsymbol{\tau}(\boldsymbol{\theta}, \boldsymbol{q})$ on the motor side or $\boldsymbol{\psi}(\boldsymbol{\theta}, \boldsymbol{q})$ on the link side depend on the types of compliant actuators

Table 2.1: Elastic torque of the actuators in the robot *neoDavid*.

Actuation type	Motor-side $\boldsymbol{\tau}$ for i-th motor	Link-side $\boldsymbol{\psi}$
Forearm BAVS	$\tau_i(q, \theta_i)$	$\boldsymbol{\tau}_1(\boldsymbol{\theta}, \boldsymbol{q}_1) + \boldsymbol{\tau}_2(\boldsymbol{\theta}, \boldsymbol{q}_2)$
Finger FAS	$r_m f_{t,i}$, (or: $\boldsymbol{E}\boldsymbol{f}_{te}$, where $\boldsymbol{E} = r_m \boldsymbol{I}$)	$\boldsymbol{L}^\top \boldsymbol{f}_{te}(\boldsymbol{q}, \boldsymbol{\theta})$

2.3 Modeling Rigid-link Dynamics with Compliant Antagonistic Actuators

It is well established that systems governed by Euler-Lagrange equations exhibit inherent passivity properties, which arise naturally from energy conservation principles and power flow analysis [122]. For elastic-joint robotic systems, these equations can be systematically derived using the Lagrangian formalism.

Let $\bar{\boldsymbol{q}}$ denote the generalized coordinates of a system. The Lagrangian function $\mathcal{L}(\bar{\boldsymbol{q}}, \dot{\bar{\boldsymbol{q}}}) = \mathcal{T}(\bar{\boldsymbol{q}}, \dot{\bar{\boldsymbol{q}}}) - \mathcal{V}(\bar{\boldsymbol{q}})$ combines kinetic energy $\mathcal{T}$ and potential energy $\mathcal{V}$ [123]. The resulting dynamics are expressed as

$$\frac{\mathrm{d}}{\mathrm{d}t}\left(\frac{\partial \mathcal{L}(\bar{\boldsymbol{q}}, \dot{\bar{\boldsymbol{q}}})}{\partial \dot{\bar{\boldsymbol{q}}}}\right)^\top - \left(\frac{\partial \mathcal{L}(\bar{\boldsymbol{q}}, \dot{\bar{\boldsymbol{q}}})}{\partial \bar{\boldsymbol{q}}}\right)^\top = \boldsymbol{\psi}_{nc} = \boldsymbol{u} + \boldsymbol{\psi}_{ext}, \tag{2.12}$$

where $\boldsymbol{\psi}_{nc}$ represents non-conservative forces, including motor torques $\boldsymbol{u}$ and external disturbances $\boldsymbol{\psi}_{ext}$ [122].

For articulated elastic-joint robots, this framework yields an underactuated Euler-Lagrange system, where $\bar{\boldsymbol{q}} = \mathrm{col}[\boldsymbol{\theta}, \boldsymbol{q}]$ partitions generalized coordinates into actuated motor positions $\boldsymbol{\theta}$ and unactuated link positions $\boldsymbol{q}$ [124]. In such systems, elastic forces often dominate inertial effects, as Spong noted in classical simplifications for elastic joint robots [116]. Two key assumptions justify this approximation:

(A1) Rotor kinetic energy depends solely on its rotational motion relative to an inertial frame.

(A2) Rotor/gear inertia symmetry ensures gravitational potential and center-of-mass velocity remain independent of rotor position.

These assumptions are particularly valid for antagonistic actuators in systems like DLR *neoDavid*, where high gear ratios minimize dynamic coupling between motor and link motions [45].

Single-DoF dynamics

The process of deriving system dynamics for a single-DoF BAVS joint is illustrated, as shown in Figure 2.1. The system states are represented by $\bar{\boldsymbol{q}}$.

$$\bar{\boldsymbol{q}} := \mathrm{col}\begin{bmatrix} q & \theta_1 & \theta_2 \end{bmatrix} \in \mathbb{R}^3 , \tag{2.13}$$

Assuming that the rotors have constant inertia, the potential energy due to gravity is independent of the motor positions θ_i, $i = 1, 2$. Further, let B be a constant denoting the reflected rotor inertia to the link side. Under (A1) and (A2), the kinetic energy is written as

$$\mathcal{T}(\theta_1, \theta_2, q) = \frac{1}{2} M \dot{q}^2 + \frac{1}{2} B \dot{\theta}_1^2 + \frac{1}{2} B \dot{\theta}_2^2 , \tag{2.14}$$

The potential energy consists of the gravitational potential U_g and the elastic-torque potential U_e introduced in Section 2.2.1, given by

$$\mathcal{V}(\theta_1, \theta_2, q) = U_g(q) + \sum_{i=1}^{2} U_{e,i}(\theta_i, q). \tag{2.15}$$

Substituting (2.14)-(2.15) into (2.12) and assuming no external force $\psi_{ext} = 0$ leading to the overall dynamics (2.12) is rewritten as

$$\begin{bmatrix} M & 0 & 0 \\ 0 & B & 0 \\ 0 & 0 & B \end{bmatrix} \begin{bmatrix} \ddot{q} \\ \ddot{\theta}_1 \\ \ddot{\theta}_2 \end{bmatrix} + \begin{bmatrix} \psi(\theta_1, \theta_2, q) \\ \tau_1(\theta_1, q) \\ \tau_2(\theta_2, q) \end{bmatrix} + \begin{bmatrix} g(q) \\ 0 \\ 0 \end{bmatrix} = \begin{bmatrix} 0 \\ u_1 \\ u_2 \end{bmatrix} . \tag{2.16}$$

where ψ is given in (2.3) and τ_i with $i = 1, 2$ is given in (2.1), $g(q) = \frac{\partial U_g(q)}{\partial q}$ and control input denoted as u_i.

Multi-DoF dynamics with coupling of elasticity

A key distinction from the single-degree-of-freedom (DoF) case is that tendon-driven systems exhibit complex coupling dynamics and interdependent elastic torques arising from the tendon routing [120]. This results in a coupling matrix ($\boldsymbol{L}$ in (2.6)) that is typically neither square nor sparse, allowing a single tendon force to influence the dynamics of every generalized coordinate $\boldsymbol{q}$ individually. By applying the Lagrangian equation (2.12) to a multi-DoF system, the multi-DoF dynamics [116] is written as

$$\boldsymbol{M}(\boldsymbol{q})\ddot{\boldsymbol{q}} + \boldsymbol{C}(\boldsymbol{q}, \dot{\boldsymbol{q}})\dot{\boldsymbol{q}} + \boldsymbol{g}(\boldsymbol{q}) = \boldsymbol{\psi}(\boldsymbol{\theta}, \boldsymbol{q}) + \boldsymbol{\psi}_{ext} \tag{2.17a}$$

$$\boldsymbol{B}\ddot{\boldsymbol{\theta}} + \boldsymbol{\tau}(\boldsymbol{\theta}, \boldsymbol{q}) = \boldsymbol{u}\,, \tag{2.17b}$$

where $\boldsymbol{M}(\boldsymbol{q})$ denotes the generalized inertia matrix of the links, $\boldsymbol{C}(\boldsymbol{q}, \dot{\boldsymbol{q}})$ contains the Coriolis and centrifugal terms, and $\boldsymbol{g}(\boldsymbol{q})$ represents the gravitational torques. The constant matrix $\boldsymbol{B}$ accounts for the reflected motor inertia. It is well known that the matrix $\dot{\boldsymbol{M}}(\boldsymbol{q}) - 2\boldsymbol{C}(\boldsymbol{q}, \dot{\boldsymbol{q}})$ is skew-symmetric when $\boldsymbol{C}$ is constructed using the Christoffel symbols [120]. The vectors $\boldsymbol{\tau}$ and $\boldsymbol{\psi}$ denote the elastic torques at the actuator and joint sides, respectively, and are defined according to the type of actuation used, as summarized in Table 2.1.

In a tendon-driven system, each tendon is typically actuated by a dedicated motor, a configuration commonly used in various tendon-driven mechanisms (e.g., [31, 121, 125–127]). As an example, for systems employing FAS, the resulting elastic torques $\boldsymbol{\tau}$ and $\boldsymbol{\psi}$ are defined in (2.6) and (2.7), respectively.

2.3.1 Dynamics Under Constraints

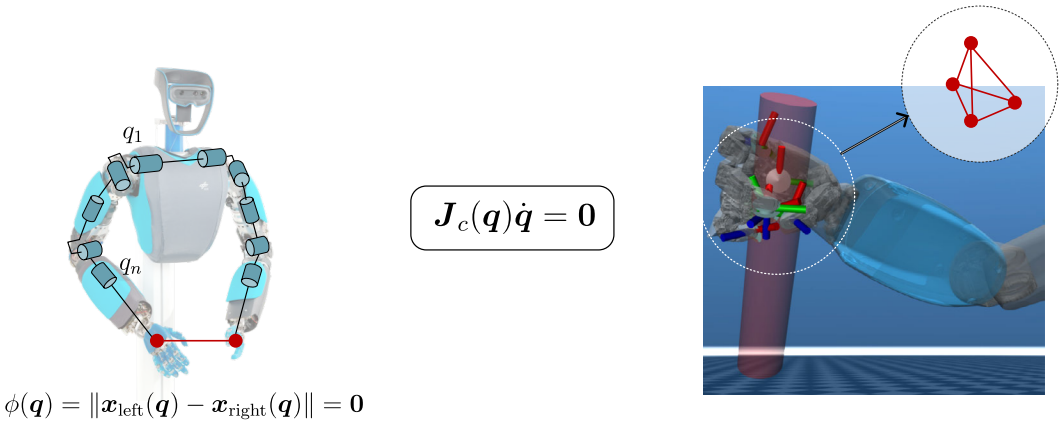
The equations of motion for an open-chain manipulator are typically derived using Lagrangian mechanics, as outlined in (2.12). This approach requires identifying a set of generalized coordinates that offer a complete and minimal description of the system's configuration space. The resulting dynamics are then expressed in terms of these coordinates and the corresponding generalized forces.

In the case of a multifingered robotic hand or interconnected open-chain manipulators, the overall system configuration is influenced not only by the joint angles of the fingers but also by the position

and orientation of the grasped object (see Figure 2.4). However, these variables are not independent; their velocities are coupled through the constraints imposed by the grasp [120]. As a result, the direct application of Lagrange's equations becomes problematic. Determining a suitable set of generalized coordinates for such constrained systems is often non-trivial and, in some cases, may not be feasible at all [120].

Pfaffian constraints

A constraint is said to be *holonomic* if it restricts the system's motion to a smooth hypersurface within the (unconstrained) configuration space $\mathbb{Q}$, where $\mathbb{Q}$ is an open subset of $\mathbb{R}^n$ and the configuration is parameterized by coordinates $\boldsymbol{q} = \text{col}\begin{bmatrix} q_1 & \cdots & q_n \end{bmatrix}$; see also the definition in [120, Section 1.1 of Chapter 6]. In this scenario, the vector $\boldsymbol{q}$ belongs to the set of rational numbers $\mathbb{Q}$, which is a subset of the real numbers $\mathbb{R}^n$. For a system with configuration space $\mathbb{Q}$, consider velocity constraints of the form $\boldsymbol{J}_c(\boldsymbol{q})\dot{\boldsymbol{q}} = \boldsymbol{0}$, where $\boldsymbol{J}_c(\boldsymbol{q})$ denotes a matrix whose rows represent the coefficients of the linear velocity constraints. Such constraints are referred to as *Pfaffian constraints* [120]. All constraints are assumed linearly independent, which implies that the matrix $\boldsymbol{J}_c(\boldsymbol{q})$ has full row rank for all $\boldsymbol{q} \in \mathbb{Q}$.



(a) A constrained dual-arm system

(b) A constrained object in a power grasp

Figure 2.4: Two example systems under Pfaffian constraints. (a): a constrained dual-arm system and (b) an object constrained by a power grasp.

Constrained dynamics with compliant actuators

Consider $n - m$ linearly independent holonomic kinematic constraints, which are integrable Pfaffian constraints, expressed by a set of algebraic equations [128], $\boldsymbol{\phi}(\boldsymbol{q}) : \boldsymbol{Q} \mapsto \mathbb{R}^{n-m}$, written as:

$$\boldsymbol{\phi}(\boldsymbol{q}) = \boldsymbol{0}. \tag{2.18}$$

Hence, the constraint Jacobian matrix for this set of algebraic equations (2.18) in terms of $\boldsymbol{q}$ is written as

$$\boldsymbol{J}_c(\boldsymbol{q}) := \frac{\partial \boldsymbol{\phi}(\boldsymbol{q})}{\partial \boldsymbol{q}} \in \mathbb{R}^{(n-m)\times n}. \tag{2.19}$$

Due to kinematic constraints, $\boldsymbol{q}$ is not a minimal coordinate anymore. The minimal generalized coordinates have dimension m. The actual range of set $\dot{\boldsymbol{q}}$ is intrinsically guaranteed (constrained)

within $\mathcal{N}(\boldsymbol{J}_c) = \{\dot{\boldsymbol{q}} \in \mathbb{R}^n : \boldsymbol{J}_c(\boldsymbol{q})\dot{\boldsymbol{q}} = \boldsymbol{0}\}$. Therefore, the reduced robot dynamics models given in (2.17a) and (2.17b) including the constraints now become

$$\boldsymbol{M}(\boldsymbol{q})\ddot{\boldsymbol{q}} + \boldsymbol{C}(\boldsymbol{q}, \dot{\boldsymbol{q}})\dot{\boldsymbol{q}} + \boldsymbol{g}(\boldsymbol{q}) = \boldsymbol{\psi} + \boldsymbol{J}_c(\boldsymbol{q})^\top \boldsymbol{\lambda} + \boldsymbol{\tau}_{ext}, \tag{2.20a}$$

$$\boldsymbol{B}\ddot{\boldsymbol{\theta}} + \boldsymbol{\tau} = \boldsymbol{u}, \tag{2.20b}$$

$$\boldsymbol{J}_c(\boldsymbol{q})\dot{\boldsymbol{q}} = \boldsymbol{0}, \tag{2.20c}$$

where $\boldsymbol{\lambda}$ is a Lagrange multiplier that denotes the constraint force. Note that a reduced range of general velocity $\dot{\boldsymbol{q}}$ fulfills

$$\dot{\boldsymbol{q}} = \boldsymbol{P}(\boldsymbol{q})\dot{\boldsymbol{q}}, \quad \forall \dot{\boldsymbol{q}} \in \mathcal{N}(\boldsymbol{J}_c(\boldsymbol{q})), \tag{2.21}$$

where the projection matrix $\boldsymbol{P}(\boldsymbol{q}) \in \mathbb{R}^{n\times n}$ fulfills $\boldsymbol{J}_c(\boldsymbol{q})\boldsymbol{P}(\boldsymbol{q}) = \boldsymbol{0}$ and $\boldsymbol{P}(\boldsymbol{q}) = \boldsymbol{P}(\boldsymbol{q})^2$. The choice of $\boldsymbol{P}(\boldsymbol{q})$ is not unique. The typical projectors are listed in Table 2.2.

Table 2.2: Different choices for the projector $\boldsymbol{P}(\boldsymbol{q})$.

Projector Type	Expression	Feature
Orthogonal projection [106, 108]	$\boldsymbol{P}(\boldsymbol{q}) = \boldsymbol{I} - \boldsymbol{J}_c^+(\boldsymbol{q})\boldsymbol{J}_c(\boldsymbol{q})$	$\boldsymbol{P}(\boldsymbol{q}) = \boldsymbol{P}^\top(\boldsymbol{q})$
Dynamically consistent projection [129]	$\boldsymbol{P}(\boldsymbol{q}) = \boldsymbol{I} - \boldsymbol{J}_c^{M+}(\boldsymbol{q})\boldsymbol{J}_c(\boldsymbol{q})$	preserving the inertial properties

The Moore-Penrose inverse of matrix $\boldsymbol{J}_c(\boldsymbol{q})$ is computed by $\boldsymbol{J}_c^+(\boldsymbol{q}) = \boldsymbol{J}_c^\top(\boldsymbol{q})(\boldsymbol{J}_c(\boldsymbol{q})\boldsymbol{J}_c^\top(\boldsymbol{q}))^{-1}$.
The inertia-weighted inverse of matrix is $\boldsymbol{J}_c^{M+}(\boldsymbol{q}) = \boldsymbol{M}^{-1}(\boldsymbol{q})\boldsymbol{J}_c^\top(\boldsymbol{q})(\boldsymbol{J}_c(\boldsymbol{q})\boldsymbol{M}^{-1}(\boldsymbol{q})\boldsymbol{J}_c^\top(\boldsymbol{q}))^{-1}$.

2.3.2 Motor Inertia Shaping

While physical springs provide beneficial compliance, the relatively large motor inertia often limits bandwidth and introduces oscillatory behavior during trajectory tracking [101]. Motor inertia shaping refers to the intentional scaling of the effective motor inertia in the closed-loop dynamics through utilizing joint torque in the feedback loop [130]. Consider the original motor dynamics

$$\boldsymbol{B}\ddot{\boldsymbol{\theta}} + \boldsymbol{\tau}(\boldsymbol{\theta}, \boldsymbol{q}) = \boldsymbol{u}, \tag{2.22}$$

with the control input

$$\boldsymbol{u} = \boldsymbol{B}\boldsymbol{B}^{\star-1}\overline{\boldsymbol{u}} + (\boldsymbol{I} - \boldsymbol{B}\boldsymbol{B}^{\star-1})\boldsymbol{\tau}, \tag{2.23}$$

where $\overline{\boldsymbol{u}}$ is the new control input. The physical motor inertia $\boldsymbol{B}$ is scaled to $\boldsymbol{B}^\star = \beta\boldsymbol{B}$, where $\beta \in (0, 1]$ is a design parameter that effectively reduces the inertia contribution in the closed-loop system. The resulting closed-loop dynamics become

$$\boldsymbol{B}^\star\ddot{\boldsymbol{\theta}} + \boldsymbol{\tau} = \bar{\boldsymbol{u}}. \tag{2.24}$$

Inertia shaping does not imply physical mass reduction but rather a feedback-based reconfiguration of the actuator dynamics.

2.4 Designing Vector Fields as Feedback Motion Planning

Traditional motion planning methods typically disregard both feedback mechanisms and system dynamics. In such approaches, the solution is an open-loop path, implying that there is no feedback during execution to correct deviations from the planned trajectory [131]. However, in real-world applications, feedback is often essential. The actions within a plan should adapt based on information gathered during execution, especially due to the unpredictability of future states. One implicit strategy to manage model uncertainty is to design a feedback plan that determines the appropriate action to take if the system encounters an unexpected state during execution [131].

In the context of this thesis, such uncertainties may arise from complex object dynamics, variable contact points between multifingered hands and objects during grasping, unforeseen interactions with the environment or humans, and unreliable visual feedback when objects are occluded. Therefore, this work adopts feedback motion planning, anticipating that feedback-based solutions will generally offer greater reliability compared to open-loop paths derived from traditional motion planning algorithms.

Vector field design in motion planning involves defining a continuous vector field over the workspace or configuration space to guide a robot or dynamical system toward a goal while avoiding obstacles. The subsequent section revisits mathematical fundamental concepts of vector and velocity fields. This discussion primarily focuses on $\mathbb{R}^2$ and $\mathbb{R}^3$. For readers interested in constructing vector fields on smooth manifolds, further details can be found in Section 8.3.2 of LaValle's work [131].

2.4.1 Vector Fields

Vector fields provide a powerful framework for representing feedback strategies over continuous state spaces. To model motion planning influenced by feedback in these contexts, the process begins by defining a vector field and explaining how it generates trajectories through integration from an initial state.

Intuitively, a vector field can be visualized as a spatial distribution of directed arrows across $\mathbb{R}^n$, as shown in Figure 2.5. Each arrow at a point $\boldsymbol{x} \in \mathbb{R}^n$ encodes a direction and magnitude, which, in the context of robotic planning, prescribes how a system should adjust its velocity when located at that state [131].

To clarify this concept, each point $\boldsymbol{x} \in \mathbb{R}^n$ is associated with an n-dimensional vector space known as the *tangent space* at $\boldsymbol{x}$, denoted as $T_{\boldsymbol{x}}(\mathbb{R}^n)$. Utilizing this structure, a vector field is defined as follows:

Definition 1 (Vector field [132])**.** *A vector field $\boldsymbol{V}$ on $\mathbb{R}^n$ is a mapping that assigns to each point $\boldsymbol{x} \in \mathbb{R}^n$ a vector $\boldsymbol{v} \in T_{\boldsymbol{x}}(\mathbb{R}^n)$, i.e.,*

$$\boldsymbol{V} : \mathbb{R}^n \to \bigcup_{\boldsymbol{x} \in \mathbb{R}^n} T_{\boldsymbol{x}}(\mathbb{R}^n), \tag{2.25}$$

such that $\boldsymbol{V}(\boldsymbol{x}) \in T_{\boldsymbol{x}}(\mathbb{R}^n)$ for all $\boldsymbol{x} \in \mathbb{R}^n$.

In practice, such a field can be expressed using n scalar-valued functions $f_i(x_1, \ldots, x_n)$, where $i = 1, \ldots, n$. The vector field $\boldsymbol{f}(\boldsymbol{x})$ then takes the form:

$$\boldsymbol{f}(\boldsymbol{x}) = \text{col}\begin{bmatrix} f_1(x_1, ..., x_n) & f_2(x_1, ..., x_n) & \ldots & f_n(x_1, ..., x_n) \end{bmatrix}. \tag{2.26}$$

A particularly important class of vector fields consists of those that are smooth:

Definition 2 (A smooth vector field [132]). *A function $f_i : \Omega \subseteq \mathbb{R}^n \to \mathbb{R}$ is said to be smooth if it is infinitely differentiable on its domain U, i.e., all partial derivatives of any order exist at every point in Ω. A vector field is called smooth if each of its component functions $f_1, \ldots, f_n$ is smooth.*

In various practical situations, particularly in hybrid or piecewise-defined control systems, vector fields are often smooth only within specific regions or patches. Across the boundaries between these patches, typically $(n-1)$-dimensional spaces in $\mathbb{R}^n$, the vector field may become discontinuous. Specifically, along a switching boundary $S \subset \mathbb{R}^n$, the vector field may exhibit abrupt changes or jumps [131].

Vector fields as velocity fields

A specific vector field, known as a velocity field [131], is illustrated here. This field is naturally expressed using (2.26), which defines a system of first-order differential equations.

$$\begin{aligned} \dot{x}_1 &= f_1(x_1, ..., x_n) \\ &\vdots \\ \dot{x}_n &= f_n(x_1, ..., x_n), \end{aligned} \tag{2.27}$$

which represents the time derivative of each coordinate as a function of the state. At each point $\boldsymbol{x} \in \mathbb{R}^n$, this construction yields a velocity vector given by

$$\dot{\boldsymbol{x}} = \text{col}\begin{bmatrix} \dot{x}_1 & \cdots & \dot{x}_n \end{bmatrix}. \tag{2.28}$$

Letting $\boldsymbol{f} = (f_1, \ldots, f_n)$ denote the collection of component functions, the dynamics can be compactly written as

$$\dot{\boldsymbol{x}} = \boldsymbol{f}(\boldsymbol{x}). \tag{2.29}$$

This formulation allows us to interpret the vector field $\boldsymbol{f}$ as a velocity field, where at each point in space, the vector $\boldsymbol{f}(\boldsymbol{x})$ represents the instantaneous velocity that a particle (or robot) should follow when located at $\boldsymbol{x}$.

2.4.2 Integral Curves

Given a vector field $\boldsymbol{f}$, a velocity vector is assigned to each point in $\mathbb{R}^n$ via (2.29). Consider a particle starting at an initial position $\boldsymbol{\xi}_0 \in \mathbb{R}^n$ at time $t = 0$, and moving such that its velocity at any instant aligns with the vector field at its current location. The path traced by this particle over time can be described by a function $\boldsymbol{\xi} : [0, \infty) \to \mathbb{R}^n$, where $\boldsymbol{\xi}(t)$ denotes the system's state at time t.

Such a function ξ is called an *integral curve* (or *solution trajectory*) of the vector field $\boldsymbol{f}$ if it satisfies the differential equation

$$\dot{\boldsymbol{\xi}}(t) = \boldsymbol{f}(\boldsymbol{\xi}(t)), \tag{2.30}$$

for all $t \in (0, \infty)$, with the initial condition $\boldsymbol{\xi}(0) = \boldsymbol{\xi}_0$. Equivalently, the trajectory can be expressed in integral form as

$$\boldsymbol{\xi}(t) = \boldsymbol{\xi}_0 + \int_0^t \boldsymbol{f}(\boldsymbol{\xi}(\sigma))\, d\sigma, \tag{2.31}$$

which explicitly shows how the motion evolves from the initial state by accumulating changes dictated by the vector field along the path. Intuitively, an integral curve follows the direction of the vector field at every point, smoothly evolving from the starting point $\boldsymbol{\xi}_0$ in accordance with the local flow defined by $\boldsymbol{f}$.

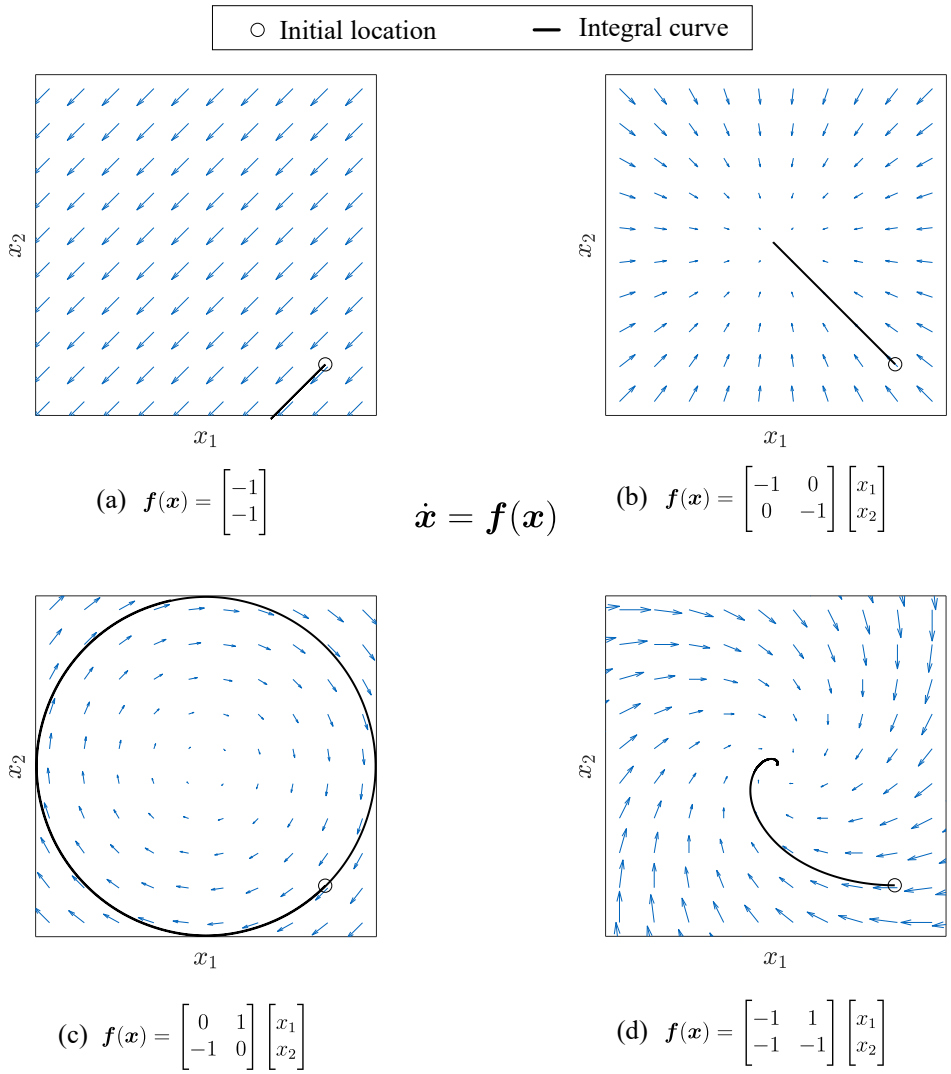


Figure 2.5: Examples of 2D vector fields $\boldsymbol{f}(\boldsymbol{x}) : \mathbb{R}^2 \to \mathbb{R}^2$ with distinct topological properties. (a) Constant, (b) Curl-free (irrotational), (c) Circular (rotational), (d) Convergent (attracting).

Existence and uniqueness of integral curves

A key result in the theory of ordinary differential equations ensures that the system described by (2.29) admits a unique integral curve through any given initial state, provided that the vector field f is smooth [131]. This guarantees both the existence and uniqueness of solutions under suitable regularity conditions on f. An alternative but equivalent requirement for ensuring this property is that the vector field satisfies a *Lipschitz condition*. Specifically, there must exist a finite positive constant c such that for all points x_1, x_2 in the state space $\mathcal{X}$ (assumed to be continuous and smooth), the inequality

$$\|f(x_1) - f(x_2)\| \leq c\|x_1 - x_2\| \tag{2.32}$$

holds. The value c is known as the Lipschitz constant and bounds the rate at which the vector field can change with respect to its input.

It's worth noting that Lipschitz continuity implies continuity of f. Furthermore, if all partial derivatives of f are uniformly bounded over $\mathcal{X}$, then f automatically satisfies the Lipschitz condition on that domain. However, the formulation in (2.32) is more general, as it does not require differentiability everywhere and applies to a wider class of vector fields, including those that may exhibit limited smoothness or even discontinuities in certain regions.

Existence of a unique integral curve of a piecewise-smooth vector field

Let a switching boundary S be defined as

$$S = \{\boldsymbol{x} \in \mathbb{R}^n | s(\boldsymbol{x}) = 0\}, \tag{2.33}$$

where $s(\boldsymbol{x}) : \mathbb{R}^n \to \mathbb{R}$ is a function. When s is non-singular, S becomes an $(n-1)$-dimensional sub-manifold of $\mathbb{R}^n$. The open regions are defined by

$$S^+ = \{\boldsymbol{x} \in \mathbb{R}^n | s(\boldsymbol{x}) > 0\}, \quad \text{and} \quad S^- = \{\boldsymbol{x} \in \mathbb{R}^n | s(\boldsymbol{x}) < 0\}. \tag{2.34}$$

Suppose that the vector field $\boldsymbol{f}(\boldsymbol{x})$ is smooth within each of the regions S^+ and S^-, respectively, but experiences a discontinuity across S. Such piecewise-smooth dynamical systems are commonly used to model hybrid systems in control theory [133, 134].

Under a special condition known as Filipov's sense of solution, referenced in [131, eq. (8.21)], it is possible to determine the unique integral with a piecewise-smooth vector field. The details are omitted in the main text of this thesis. For readers who are interested, please refer to [131, pp. 388-389]. As LaValle intuitively introduced in [131], several vector fields can yield solutions in the *sense of Filipov* [135, 136], see Figure 2.6 for different examples of vector flows in the neighborhood of a switching boundary fulfilling the permitted conditions.

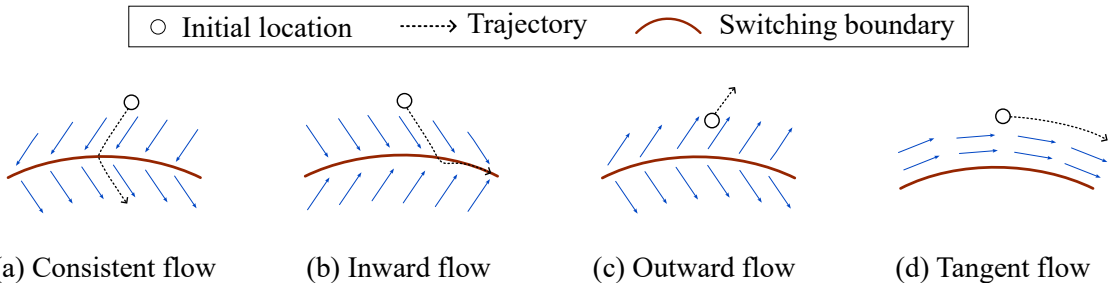


Figure 2.6: Various flow patterns near a switching boundary, illustrated with example trajectories originating from different initial locations (marked by circles). Image adapted from [131, pp. 388-389].

3

Elastic Structure Preserving Control for Compliant Antagonistic Actuators

In classical nonlinear control approaches for elastic robotic systems, the dominant strategy has been to achieve a desired closed-loop behavior by significantly altering the intrinsic mechanical properties of the system. However, this often involves compensating for the oscillatory dynamics introduced by highly elastic components, such as those found in elastic-joint robots or tendon-driven systems, which can lead to complex and fragile control designs. In contrast to traditional approaches that aim to suppress compliance, this chapter follows the modern philosophy of exploiting mechanical elasticity rather than counteracting it.

This chapter builds upon and extends previous research, particularly the ESP control framework introduced in [102, 137], achieving the goal **G1** in Section 1.3. The contributions corresponding to **C1** and **C2** mentioned in Section 1.4 are summarized as follows:

- The ESPi controller is generalized to BAVS actuators, enabling the direct imposition of a desired impedance profile on the link side.
- The ESP framework is further extended to multi-degree-of-freedom tendon-driven systems, capable of handling nonlinear mechanical couplings introduced by tendon routing.
- It is shown that for such systems, a desired closed-loop behavior, including link-side impedance, can be achieved while minimally modifying the inherent inertial and elastic coupling dynamics.
- The proposed control law is experimentally validated on the forearm joint of the *neoDavid* humanoid robot, confirming its ability to realize desired link-side compliance.
- Simulation results further demonstrate the controller's effectiveness in achieving accurate link position regulation and desired impedance during environmental interactions, using a 4-DoF finger actuated by 8 tendons.

The chapter is organized as follows. Section 3.2 formulates the control problem for a single-degree-of-freedom system actuated by a BAVS joint. The ESPi control law is derived, and passivity and global asymptotic stability of the resulting closed-loop system are rigorously established for the free-motion case. Building on this foundation, Section 3.3 generalizes the approach to multi-DoF unidirectional antagonistic tendon-driven mechanisms, preserving the same structural principles while

accommodating nonlinear kinematic and elastic couplings. Experimental validation of the BAVS implementation on the neoDavid forearm is presented in Section 3.4, with emphasis on the realization of commanded link-side stiffness under human interaction. Section 3.5 reports simulation results on a multi-tendon finger, evaluating both regulation performance and impedance fidelity during dynamic interaction. Finally, Section 3.6 provides a concluding summary of the chapter's findings and implications.

Publication Note

- [103]: **X. Meng**, M. Keppler, and C. Ott. "Elastic Structure Preserving Impedance Control of Bidirectional Antagonistic Variable Stiffness Actuation". In: *2021 European Control Conference (ECC 2021)*. 2021, pp. 263–269.
- [117]: **X. Meng***, G. Jose Pollayil*, M. Keppler, M. Pfanne, A. Bicchi, C. Ott (2021). Elastic structure preserving impedance control for nonlinearly coupled tendon-driven systems. *IEEE Control Systems Letters*, 6, 1982-1987. (*: equal contribution)[a].

[a] George Jose Pollayil and I jointly developed the study design and research questions. I was primarily responsible for the dynamics modeling, simulation implementation, debugging, and baseline comparison, while George focused on symbolic coordinate transformations; we collaborated closely on controller implementation and the collection of simulation results. Both of us analyzed the interaction and regulation tests, with my additional contribution to the baseline comparison and data visualization. In writing, I drafted the simulation and results sections, while George prepared the introduction, preliminaries, proofs, and conclusion; we jointly refined the control design description. We also shared responsibility for revisions and rebuttals during the review process. Our supervisor, Christian Ott, and mentor, Manuel Keppler, guided the overall direction of the research but were not involved in daily execution.

3.1 Introduction

The integration of mechanical compliance in robotic systems has emerged as a paradigm shift, enabling natural dynamics [138], energy-efficient locomotion [139, 140], and safer human-robot interaction [141–143]. Many designs combine rigid skeletons with elastic joints, leveraging SEAs [144] or VSAs [38, 145] to achieve high impact tolerance, low reflected inertia, and energy storage for dynamic motions. Control strategies for such systems have evolved from classical methods like PD regulation with gravity compensation [87, 88] and feedback linearization [89, 90] to advanced approaches including inverse dynamics [92], linear quadratic regulation [93], and passivity-based frameworks [94, 95]. However, these methods often struggle when joint stiffness is significantly reduced, as they typically aim to cancel or reshape intrinsic compliance rather than exploit it.

Tendon-driven systems, inspired by biological musculoskeletal structures, further exemplify the benefits of compliance. Designs like the UB Hand III [121], DLR *David* Hand (or *neoDavid*) [31, 44], and Pisa/IIT SoftHand [33] utilize lightweight, compact tendon couplings to enable robust grasping [146] and adapt to environmental interactions. Despite their advantages, nonlinear elastic couplings and complex tendon routing pose significant control challenges. Traditional two-loop architectures, combining inner tendon-force control with outer link-behavior loops, often rely on static decoupling [96], optimization-based tension distribution [97, 98], or decentralized H_∞ control [147]. While effective, these approaches frequently modify the system's natural dynamics, deviating from the goal of preserving mechanical compliance. Exceptions include Lyapunov-stable designs for single-degree-of-freedom systems with adjustable springs [148] and integrator backstepping techniques for antago-

nistic joints [149], which prioritize stability while respecting physical constraints.

Recent efforts emphasize minimizing dynamic shaping to retain intrinsic compliance. Our prior work introduced passivity-based control laws that preserve the elastic structure while achieving regulation and tracking by injecting damping directly on the link side [101]. This was extended to Elastic Structure Preserving Impedance Control for Floating Spring Joints [38], enabling desired interaction behavior without altering the plant's mechanical properties [137]. Further extensions to BAVS actuation [102, 103] addressed output regulation with adjustable passive stiffness. However, these formulations rely on simplified elastic models unsuitable for tendon-driven systems with nonlinear couplings, highlighting the need for a generalized framework that bridges compliant actuation and complex mechanical transmissions.

We first focus on the control design for a single-DoF BAVS actuator, a canonical example of elastic robotic systems with embedded compliance. This analysis serves as the foundation for extending the framework to more complex tendon-driven systems with nonlinear couplings, which are discussed later in the subsection.

3.2 A Single-Joint Example

A model of a one-degree-of-freedom (1-DoF) robotic system incorporating a single BAVS joint is considered. The configuration of the system is described by two motor coordinates, denoted θ_1 and θ_2, and a single link coordinate q. The actuators consist of two motors, each possessing identical inertia B, which are coupled to the link, characterized by inertia M, through nonlinear elastic elements that generate torques τ_1 and τ_2. Gravitational effects acting on the link are represented by $g(q)$. The resulting dynamics, as defined by Equations (2.16), (2.1), and (2.3), take the form

$$M\ddot{q} + g(q) = \psi(\theta_1 - q, \theta_2 - q) + \tau_{\text{ext}} \,, \tag{3.1}$$

$$B\ddot{\theta}_1 + \tau_1(\theta_1 - q) = u_1 \,, \tag{3.2}$$

$$B\ddot{\theta}_2 + \tau_2(\theta_2 - q) = u_2 \,, \tag{3.3}$$

where u_i denotes the torque input applied to the i-th motor and constitutes the only available control authority. A schematic representation of the open-loop dynamics is provided in Figure 3.1(a). Direct actuation is limited exclusively to the motor coordinates θ_1 and θ_2; the link coordinate q is influenced solely through the elastic coupling torque ψ. This structural underactuation poses a fundamental challenge for precise regulation of the link state $(q, \dot{q})$.

3.2.1 Control Objectives

The primary objective in the design of a controller is to endow the soft robotic system with a prescribed compliant behavior during physical interaction with a human operator. The desired closed-loop dynamics, illustrated schematically in Figure 3.1(b), are formulated as follows:

$$M\ddot{q} + D_q\dot{q} + K_q(q - q_d) = \psi(\eta_1 - q, \eta_2 - q) + \tau_{\text{ext}} \,, \tag{3.4}$$

$$B^\star\ddot{\eta}_1 + \tau_1(\eta_1 - q) = \tau_{0,1} - D_{\eta,1}\dot{\eta}_1, \tag{3.5}$$

$$B^\star\ddot{\eta}_2 + \tau_2(\eta_2 - q) = \tau_{0,2} - D_{\eta,2}\dot{\eta}_2, \tag{3.6}$$

$$\psi(\eta_1 - q, \eta_2 - q) = \tau_1(\eta_1 - q) + \tau_2(\eta_2 - q). \tag{3.7}$$

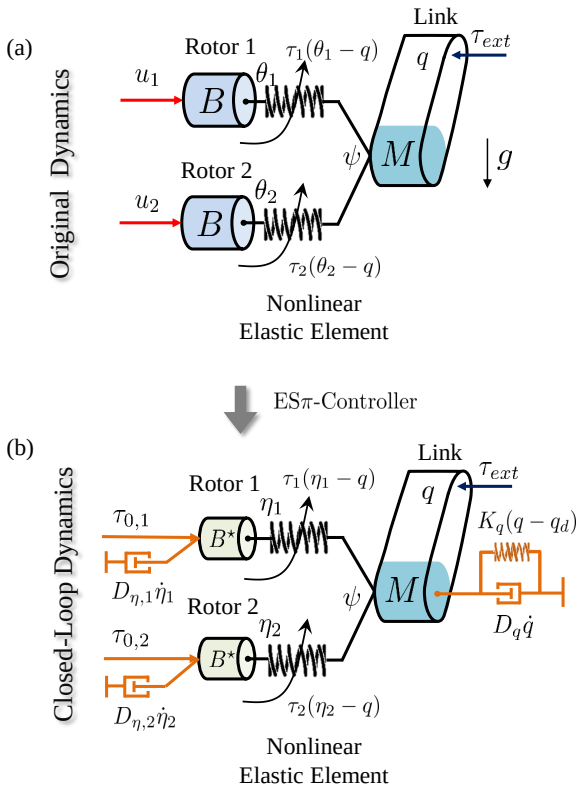


Figure 3.1: Schematic diagram of a simplified single joint implemented with a BAVS joint in (a) the original dynamics and (b) the closed-loop dynamics achieved by implementing the ESPi controller © 2021 IEEE.

The target link-side dynamics in (3.4) include the original inertial term M with a virtual spring of stiffness K_q and a positive damping term D_q, as depicted in Figure 3.1(b). The equilibrium of the link subsystem is defined by $q = q_d$ and $\dot{q} = 0$. The motor inertia is scaled by a factor $\beta \in (0, 1]$, yielding a modified inertia matrix $\boldsymbol{B}^\star = \beta \boldsymbol{B}$, consistent with the inertia-shaping methodology introduced in Section 2.3.2. Throughout this chapter, the following assumption is imposed on the impedance parameters:

Assumption 3. *The stiffness gain K_q and damping gain D_q are constant.*

It is noteworthy that the desired dynamics employ a distinct set of motor coordinates, denoted η_1 and η_2, in place of the physical coordinates θ_1 and θ_2. Consequently, the virtual elastic torque ψ in Equation (3.7) is expressed in terms of these new coordinates. The precise transformation from θ_i to η_i is detailed in Section 3.2.2. Furthermore, the physical motor inertia B may be effectively reduced to $B^\star$ through appropriate control synthesis, as established in prior work [95].

An essential requirement for the closed-loop system is that the apparent stiffness at the link side, defined as

$$\left.\frac{\Delta \tau_{\text{ext}}}{\Delta q}\right|_{\substack{\dot{q}=0 \\ \dot{\eta}_i=0}},$$

must coincide with the specified stiffness K_q. The realization of this property is addressed in Section 3.2.2. Additionally, positive damping terms $D_{\eta,i}$ are introduced on the motor side to attenuate oscillatory modes. Constant feedforward torques $\tau_{0,1}$ and $\tau_{0,2}$ are incorporated to establish internal pretension within the antagonistic pair. To ensure that variations in internal pretension do not perturb the desired link-side dynamics in Equation (3.4), the constraint

$$\tau_{0,1} + \tau_{0,2} = 0 \tag{3.8}$$

must be strictly satisfied. The complete state vector of the closed-loop system is defined as

$$\boldsymbol{z} = \begin{bmatrix} q & \eta_1 & \eta_2 & \dot{q} & \dot{\eta}_1 & \dot{\eta}_2 \end{bmatrix}^T .$$

In the absence of external torque ($\tau_{\text{ext}} = 0$), the system admits a unique equilibrium point given by

$$\boldsymbol{z}_{\text{eq}} = \begin{bmatrix} q_d & \eta_{1,d} & \eta_{2,d} & 0 & 0 & 0 \end{bmatrix}^T . \tag{3.9}$$

3.2.2 Controller Design

This section presents the synthesis of a control law that renders the original system dynamics, given by Equations (3.1)–(3.3), equivalent to the desired closed-loop dynamics specified in Equations (3.4), (3.6). The design proceeds in two principal stages: first, a coordinate transformation from the physical motor coordinates θ_i to virtual motor coordinates η_i is introduced; second, a feedback control law is derived to enforce the target dynamics in the new coordinates. Throughout this section, the overbar notation $\bar{(\cdot)}$ denotes a function that retains the same analytical form as its unbarred counterpart but is evaluated using the virtual coordinates η_i instead of the physical coordinates θ_i, thereby simplifying notation.

Coordinate transformation

A comparison between the original link dynamics (3.1) and the desired closed-loop dynamics (3.4) yields the following relationship

$$\psi(\theta_1 - q, \theta_2 - q) := \bar{\psi}(\eta_1 - q, \eta_2 - q) + \underbrace{g(q) - K_q(q - q_d) - D_q\dot{q}}_{=:\,\tau_d} , \tag{3.10}$$

where the gravitational term $g(q)$ is explicitly compensated, and τ_d assumes the structure of a standard impedance control law with gravity compensation, commonly employed in rigid robotic systems. The virtual coordinates η_1 and η_2 encode the desired mechanical behavior at the link side. However, Equation (3.10) alone does not uniquely determine η_1 and η_2, as it constitutes a single scalar constraint for two unknowns.

To ensure a well-posed mapping from (θ_1, θ_2) to (η_1, η_2), an additional kinematic constraint is imposed. Noting that the motor stiffness preset $\sigma = \theta_1 - \theta_2$ governs the internal pretension in the antagonistic actuator (as discussed in Section 2.2.1), it is natural to preserve this quantity under the coordinate transformation. Accordingly, the following constraint is enforced

$$\eta_1 - \eta_2 := \theta_1 - \theta_2 . \tag{3.11}$$

Together, Equations (3.10) and (3.11) uniquely define the virtual coordinates η_1 and η_2 as functions of the physical states and the desired equilibrium q_d.

Differentiating these relations with respect to time yields the velocity-level transformation

$$\underbrace{\begin{bmatrix} \dot{\theta}_1 \\ \dot{\theta}_2 \end{bmatrix}}_{\dot{\boldsymbol{\theta}}} = \begin{bmatrix} \frac{\partial \psi}{\partial \theta_1} & \frac{\partial \psi}{\partial \theta_2} \\ 1 & -1 \end{bmatrix}^{-1} \left(\begin{bmatrix} \frac{\partial \bar{\psi}}{\partial \eta_1} & \frac{\partial \bar{\psi}}{\partial \eta_2} \\ 1 & -1 \end{bmatrix} \underbrace{\begin{bmatrix} \dot{\eta}_1 \\ \dot{\eta}_2 \end{bmatrix}}_{\dot{\boldsymbol{\eta}}} + \begin{bmatrix} \frac{\partial \bar{\psi}}{\partial q}\dot{q} - \frac{\partial \psi}{\partial q}\dot{q} - \dot{\tau}_d \\ 0 \end{bmatrix} \right) . \tag{3.12}$$

A second time derivative provides the acceleration-level mapping:

$$\underbrace{\begin{bmatrix}\ddot{\theta}_1\\ \ddot{\theta}_2\end{bmatrix}}_{\ddot{\boldsymbol{\theta}}} = \underbrace{\begin{bmatrix}\frac{\partial\psi}{\partial\theta_1} & \frac{\partial\psi}{\partial\theta_2}\\ 1 & -1\end{bmatrix}^{-1}\begin{bmatrix}\frac{\partial\bar{\psi}}{\partial\eta_1} & \frac{\partial\bar{\psi}}{\partial\eta_2}\\ 1 & -1\end{bmatrix}}_{\boldsymbol{A}}\underbrace{\begin{bmatrix}\ddot{\eta}_1\\ \ddot{\eta}_2\end{bmatrix}}_{\ddot{\boldsymbol{\eta}}} + \underbrace{\begin{bmatrix}\frac{\partial\psi}{\partial\theta_1} & \frac{\partial\psi}{\partial\theta_2}\\ 1 & -1\end{bmatrix}^{-1}\begin{bmatrix}c_1 + \frac{\partial\bar{\psi}}{\partial q}\ddot{q} - c_2 - \frac{\partial\psi}{\partial q}\ddot{q} - \ddot{\tau}_d\\ 0\end{bmatrix}}_{\boldsymbol{a}}, \tag{3.13}$$

where the scalar terms c_1 and c_2 account for Coriolis- and centrifugal-like effects arising from the nonlinear elastic coupling:

$$c_1 = \begin{bmatrix}\frac{\partial^2\bar{\psi}}{\partial\eta_1^2}\dot{\eta}_1 + \frac{\partial^2\bar{\psi}}{\partial\eta_1\partial\eta_2}\dot{\eta}_2 + \frac{\partial^2\bar{\psi}}{\partial\eta_1\partial q}\dot{q}\\ \frac{\partial^2\bar{\psi}}{\partial\eta_1\partial\eta_2}\dot{\eta}_1 + \frac{\partial^2\bar{\psi}}{\partial\eta_2^2}\dot{\eta}_2 + \frac{\partial^2\bar{\psi}}{\partial\eta_2\partial q}\dot{q}\\ \frac{\partial^2\bar{\psi}}{\partial\eta_1\partial q}\dot{\eta}_1 + \frac{\partial^2\bar{\psi}}{\partial\eta_2\partial q}\dot{\eta}_2 + \frac{\partial^2\bar{\psi}}{\partial q^2}\dot{q}\end{bmatrix}^T\begin{bmatrix}\dot{\eta}_1\\ \dot{\eta}_2\\ \dot{q}\end{bmatrix}, \tag{3.14}$$

$$c_2 = \begin{bmatrix}\frac{\partial^2\psi}{\partial\theta_1^2}\dot{\theta}_1 + \frac{\partial^2\psi}{\partial\theta_1\partial\theta_2}\dot{\theta}_2 + \frac{\partial^2\psi}{\partial\theta_1\partial q}\dot{q}\\ \frac{\partial^2\psi}{\partial\theta_1\partial\theta_2}\dot{\theta}_1 + \frac{\partial^2\psi}{\partial\theta_2^2}\dot{\theta}_2 + \frac{\partial^2\psi}{\partial\theta_2\partial q}\dot{q}\\ \frac{\partial^2\psi}{\partial\theta_1\partial q}\dot{\theta}_1 + \frac{\partial^2\psi}{\partial\theta_2\partial q}\dot{\theta}_2 + \frac{\partial^2\psi}{\partial q^2}\dot{q}\end{bmatrix}^T\begin{bmatrix}\dot{\theta}_1\\ \dot{\theta}_2\\ \dot{q}\end{bmatrix}. \tag{3.15}$$

Substituting the acceleration transformation (3.13) into the original motor dynamics (3.2)–(3.3) yields, in matrix form,

$$\underbrace{\begin{bmatrix}B & 0\\ 0 & B\end{bmatrix}}_{\boldsymbol{B}}(\boldsymbol{A}\ddot{\boldsymbol{\eta}} + \boldsymbol{a}) + \underbrace{\begin{bmatrix}\tau_1(\theta_1, q)\\ \tau_2(\theta_2, q)\end{bmatrix}}_{\boldsymbol{\tau}} = \underbrace{\begin{bmatrix}u_1\\ u_2\end{bmatrix}}_{\boldsymbol{u}}. \tag{3.16}$$

The control input is then selected as

$$\boldsymbol{u} = \boldsymbol{B}\boldsymbol{a} + \boldsymbol{\tau} - \boldsymbol{B}\boldsymbol{A}\boldsymbol{B}^{\star-1}\left(\underbrace{\begin{bmatrix}\bar{\tau}_1(\eta_1, q)\\ \bar{\tau}_2(\eta_2, q)\end{bmatrix}}_{\bar{\boldsymbol{\tau}}} + \boldsymbol{D}_\eta\dot{\boldsymbol{\eta}} - \underbrace{\begin{bmatrix}\bar{\tau}_{0,1}\\ \bar{\tau}_{0,2}\end{bmatrix}}_{\bar{\boldsymbol{\tau}}_0}\right), \tag{3.17}$$

where $\boldsymbol{D}_\eta = \mathrm{diag}(D_{\eta,1}, D_{\eta,2}) \in \mathbb{R}^{2\times2}$ is a positive definite diagonal damping matrix, and $\bar{\boldsymbol{\tau}}_0$ represents a constant feedforward torque vector used to establish internal pretension. The term $\boldsymbol{B}\boldsymbol{A}\boldsymbol{B}^{\star-1}$ implements inertia shaping by scaling the feedback signals, namely, the virtual elastic torques $\bar{\boldsymbol{\tau}}$ and motor-side damping forces $\boldsymbol{D}_\eta\dot{\boldsymbol{\eta}}$, according to the desired scaled inertia $\boldsymbol{B}^\star$. With this control law, the closed-loop dynamics are rendered exactly equivalent to the target model given in Equations (3.4)–(3.6).

Setting motor pretension via σ_d and q_d

The desired internal pretension in the antagonistic actuator is specified through a commanded stiffness preset σ_d. Substituting the equilibrium state (3.9) into the closed-loop motor dynamics (3.5)–(3.6) yields the required feedforward torques:

$$\bar{\tau}_{0,1} = \bar{\tau}_1(\eta_{1,d} - q_d)\,, \tag{3.18}$$

$$\bar{\tau}_{0,2} = \bar{\tau}_2(\eta_{2,d} - q_d)\,. \tag{3.19}$$

Enforcing the pretension neutrality condition (3.8), i.e., $\bar{\tau}_{0,1} + \bar{\tau}_{0,2} = 0$, leads to

$$\bar{\psi}_0(\eta_{1,d} - q_d, \eta_{2,d} - q_d) = \bar{\tau}_{0,1} + \bar{\tau}_{0,2} = 0\,. \tag{3.20}$$

Assuming symmetric elastic characteristics, this condition implies

$$\eta_{1,d} + \eta_{2,d} = 2q_d \, . \tag{3.21}$$

In addition, the desired stiffness preset is imposed as

$$\eta_{1,d} - \eta_{2,d} = \sigma_d \, , \tag{3.22}$$

which, by virtue of the kinematic constraint (3.11), is equivalent to prescribing $\theta_1 - \theta_2 = \sigma_d$ in the physical domain. Solving the linear system formed by (3.21) and (3.22) yields the equilibrium virtual coordinates as explicit functions of the commanded pose and stiffness preset:

$$\eta_{1,d} = q_d + \tfrac{1}{2}\sigma_d \, , \tag{3.23}$$

$$\eta_{2,d} = q_d - \tfrac{1}{2}\sigma_d \, . \tag{3.24}$$

Since the virtual elastic torque $\bar{\psi}$ retains the same functional form as the physical torque ψ, the equilibrium condition (3.21) corresponds geometrically to the intersection of the zero-torque contour $\bar{\psi} = 0$ (depicted as a black dashed line in Figure 2.2) with the line defined by the prescribed σ_d. For instance, when $\sigma_d = 0.1$ rad, the equilibrium point is located at the intersection of the purple line ($\eta_1 - \eta_2 = 0.1$) and the black dashed line, fully determining the closed-loop equilibrium state (3.9).

Achieving desired link-side stiffness

A critical requirement of the controller is that the apparent stiffness at the link side, defined as $\frac{\Delta\tau_{\text{ext}}}{\Delta q}\Big|_{q=q_d,\dot{q}=0,\dot{\eta}_i=0}$, must equal the commanded stiffness K_q. This property is established by the following procedures.

Consider the application of a constant external torque $\tau_{\text{ext}} \neq 0$ to a stable closed-loop system. The system settles to a new static equilibrium $(q = q^*, \eta_1 = \eta_1^*, \eta_2 = \eta_2^*, \dot{q} = \ddot{q} = 0, \dot{\eta}_i = \ddot{\eta}_i = 0)$. Substitution into the closed-loop link dynamics (3.4) gives

$$K_q(q^* - q_d) - \bar{\psi}(\eta_1^* - q^*, \eta_2^* - q^*) = \tau_{\text{ext}} \, . \tag{3.25}$$

Because the feedforward terms $\bar{\tau}_{0,1}$ and $\bar{\tau}_{0,2}$ remain unchanged, the internal pretension condition (3.20) continues to hold, implying

$$\bar{\psi}(\eta_1^* - q^*, \eta_2^* - q^*) = 0 \, . \tag{3.26}$$

Substituting (3.26) into (3.25) yields

$$K_q(q^* - q_d) = \tau_{\text{ext}} \, . \tag{3.27}$$

Defining $\Delta q = q^* - q_d$ and $\Delta\tau_{\text{ext}} = \tau_{\text{ext}} - 0$, it follows directly that

$$\frac{\Delta\tau_{\text{ext}}}{\Delta q} = K_q \, . \tag{3.28}$$

Thus, the closed-loop system exhibits precisely the commanded stiffness K_q at the link side under static conditions, as required.

3.2.3 Passivity and Stability Analysis

Output-strict passivity

The passivity of the closed-loop system under external interaction forces $\tau_{\text{ext}} \neq 0$ is now examined. Following an energy-based physical design methodology, storage functions are constructed for both the link and motor subsystems, referenced to the desired equilibrium dynamics specified in Equations (3.4)–(3.6). These storage functions are defined as

$$S_q = \frac{1}{2} M \dot{q}^2 + \frac{1}{2} K_q (q - q_d)^2 \,, \tag{3.29}$$

$$S_\eta = \frac{1}{2} B \dot{\eta}_1^2 + \frac{1}{2} B \dot{\eta}_2^2 + \bar{U}(\tilde{\eta}_1, \tilde{\eta}_2, \tilde{q}) \,, \tag{3.30}$$

where $\tilde{\eta}_i := \eta_i - \eta_{i,d}$ and $\tilde{q} := q - q_d$ denote deviations from the equilibrium configuration, and $\bar{U}(\tilde{\eta}_1, \tilde{\eta}_2, \tilde{q})$ represents the potential energy associated with the virtual elastic coupling expressed in deviation coordinates. The total stored energy of the closed-loop system is given by $S = S_q + S_\eta$. The time derivatives of the individual storage functions are computed as

$$\dot{S}_q = \dot{q}\, \tau_{\text{ext}} - D_q \dot{q}^2 + \bar{\psi}\, \dot{q} \,, \tag{3.31}$$

$$\dot{S}_\eta = \dot{q}(\bar{\tau}_{0,1} + \bar{\tau}_{0,2}) - D_{\eta,1} \dot{\eta}_1^2 - D_{\eta,2} \dot{\eta}_2^2 - \bar{\psi}\, \dot{q} \,. \tag{3.32}$$

By virtue of the pretension neutrality condition (3.8), which enforces $\bar{\tau}_{0,1} + \bar{\tau}_{0,2} = 0$, the feedforward terms cancel identically, yielding

$$\dot{S}_\eta = -D_{\eta,1} \dot{\eta}_1^2 - D_{\eta,2} \dot{\eta}_2^2 - \bar{\psi}\, \dot{q} \,.$$

The term $\bar{\psi}\, \dot{q}$ represents internal power exchange between the motor and link subsystems, while $\dot{q}\, \tau_{\text{ext}}$ corresponds to power injected by the environment through the external torque. Summing the two derivatives gives

$$\dot{S} = \dot{S}_q + \dot{S}_\eta = \dot{q}\, \tau_{\text{ext}} - D_q \dot{q}^2 - D_{\eta,1} \dot{\eta}_1^2 - D_{\eta,2} \dot{\eta}_2^2 \leq \dot{q}\, \tau_{\text{ext}} \,.$$

This inequality establishes the following result.

Proposition 1. *The closed-loop system described by Equations* (3.4)–(3.6) *constitutes an output-strictly passive mapping from the external torque input τ_{ext} to the link velocity output $\dot{q}$.*

Proof. The inequality $\dot{S} \leq \dot{q}\, \tau_{\text{ext}}$ directly satisfies the definition of output-strict passivity, with the storage function S serving as a valid Lyapunov-like energy function. The dissipation terms $D_q \dot{q}^2$, $D_{\eta,1} \dot{\eta}_1^2$, and $D_{\eta,2} \dot{\eta}_2^2$ ensure strict energy loss in the absence of external input, thereby confirming output-strict passivity. □

Global asymptotical stability

The stability properties of the closed-loop system in the absence of external interaction ($\tau_{\text{ext}} = 0$) are now addressed.

Proposition 2. *The equilibrium point $\boldsymbol{z}_{eq}$ defined in Equation* (3.9) *is globally asymptotically stable when $\tau_{ext} = 0$.*

Proof. Consider the Lyapunov function candidate $V(\boldsymbol{z}) = S = S_q + S_\eta$. By construction, $V(\boldsymbol{z})$ is positive definite with respect to the equilibrium $\boldsymbol{z}_{\text{eq}}$, and radially unbounded, i.e., $V(\boldsymbol{z}) \to \infty$ as $\|\boldsymbol{z}\| \to \infty$, due to the quadratic kinetic terms of the potential energy $\bar{U}$. With $\tau_{\text{ext}} = 0$, the time derivative of V reduces to

$$\dot{V} = -D_q \dot{q}^2 - D_{\eta,1} \dot{\eta}_1^2 - D_{\eta,2} \dot{\eta}_2^2 \leq 0 \,,$$

which is negative semi-definite. Application of LaSalle's invariance principle reveals that the largest invariant set contained in $\{\boldsymbol{z} \mid \dot{V} = 0\}$ is characterized by

$$\dot{q} = 0, \quad \dot{\eta}_1 = 0, \quad \dot{\eta}_2 = 0 \,.$$

Substituting these conditions into the closed-loop dynamics (3.4)–(3.6) with $\tau_{\text{ext}} = 0$ yields $q = q_d$, $\eta_1 = \eta_{1,d}$, and $\eta_2 = \eta_{2,d}$, corresponding precisely to the equilibrium $\boldsymbol{z}_{\text{eq}}$. Hence, all trajectories converge to $\boldsymbol{z}_{\text{eq}}$, establishing global asymptotic stability. □

3.3 Tendon-Coupled Multi-Joint System with FAS Actuation

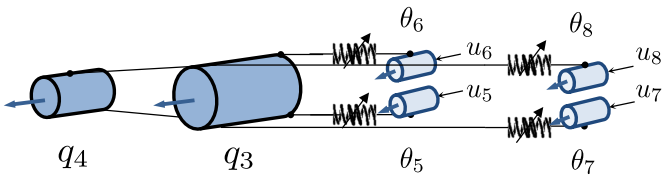
The dynamics of the tendon-coupled multi-joint system under consideration are revisited from Equations (2.17a)–(2.17b), and restated here for completeness as

$$\boldsymbol{M}(\boldsymbol{q})\ddot{\boldsymbol{q}} + \boldsymbol{C}(\boldsymbol{q}, \dot{\boldsymbol{q}})\dot{\boldsymbol{q}} + \boldsymbol{g}(\boldsymbol{q}) = \boldsymbol{\psi}(\boldsymbol{\theta}, \boldsymbol{q}) + \boldsymbol{\psi}_{\text{ext}}, \tag{3.33a}$$

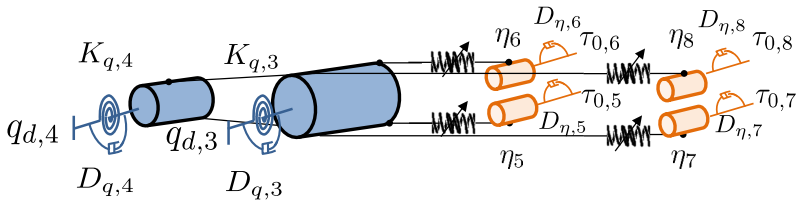
$$\boldsymbol{B}\ddot{\boldsymbol{\theta}} + \boldsymbol{\tau}(\boldsymbol{\theta}, \boldsymbol{q}) = \boldsymbol{u}, \tag{3.33b}$$

where $\boldsymbol{q} \in \mathbb{R}^n$ denotes the vector of joint positions, $\boldsymbol{\theta} \in \mathbb{R}^{n_\theta}$ represents the motor (or actuator) coordinates, $\boldsymbol{\psi}_{\text{ext}} \in \mathbb{R}^n$ is the vector of external interaction torques applied at the joints, and $\boldsymbol{u} \in \mathbb{R}^{n_\theta}$ constitutes the control input vector applied at the motor side. The matrix $\boldsymbol{M}(\boldsymbol{q}) \in \mathbb{R}^{n \times n}$ is the configuration-dependent joint inertia matrix, assumed symmetric and positive definite; $\boldsymbol{C}(\boldsymbol{q}, \dot{\boldsymbol{q}}) \in \mathbb{R}^{n \times n}$ encapsulates Coriolis and centrifugal effects; and $\boldsymbol{g}(\boldsymbol{q}) \in \mathbb{R}^n$ accounts for gravitational torques. The constant diagonal matrix $\boldsymbol{B} \in \mathbb{R}^{n_\theta \times n_\theta}$ represents the reflected motor inertia, assumed identical for all actuators for notational simplicity, though this assumption may be relaxed without loss of generality. When the Coriolis matrix $\boldsymbol{C}(\boldsymbol{q}, \dot{\boldsymbol{q}})$ is constructed from the Christoffel symbols of the first kind associated with $\boldsymbol{M}(\boldsymbol{q})$, the well-known property that $\dot{\boldsymbol{M}}(\boldsymbol{q}) - 2\boldsymbol{C}(\boldsymbol{q}, \dot{\boldsymbol{q}})$ is skew-symmetric holds [120]. This property plays a fundamental role in energy-based control design and passivity analysis.

The elastic coupling between motors and joints is mediated through nonlinear tendon transmissions, giving rise to the joint-side elastic torque $\boldsymbol{\psi}(\boldsymbol{\theta}, \boldsymbol{q}) \in \mathbb{R}^n$ and the motor-side elastic torque $\boldsymbol{\tau}(\boldsymbol{\theta}, \boldsymbol{q}) \in \mathbb{R}^{n_\theta}$, which are defined respectively in Equations (2.6) and (2.7). These torques arise from the deformation of compliant elements, such as series elastic actuators or tendon springs, and encode the geometric and mechanical properties of the transmission architecture. A schematic representation of the open-loop system dynamics is provided in Figure 3.2(a), illustrating the physical separation between the underactuated link dynamics and the fully actuated motor dynamics, coupled solely through the elastic transmission network.



(a) Original dynamics



(b) Closed-loop dynamics

Figure 3.2: (a) The original system dynamics of the last two joints in the index finger of the DLR *neoDavid* Hand, corresponding to the mechanism shown in Figure 2.3 (a). (b) The resulting closed-loop dynamics when the proposed controller is applied. This figure is adapted from [117].

3.3.1 Target Closed-Loop Dynamics

The control objectives for the tendon-coupled multi-joint system are formulated to achieve compliant, stable, and physically interpretable interaction behavior while preserving the intrinsic mechanical structure of the actuation architecture. Specifically, the design aims to:

(a) Impart desired stiffness $\boldsymbol{K}_q$ and damping $\boldsymbol{D}_q$ at the link side;

(b) Ensure asymptotic convergence of the joint configuration to a reference trajectory $\boldsymbol{q}_d$, i.e., $\boldsymbol{q}(t) \to \boldsymbol{q}_d$ as $t \to \infty$;

(c) Minimally alter the natural dynamics, elastic coupling, and transmission geometry of the physical system;

(d) Reduce the effective reflected motor inertia through scaling.

To realize these objectives, a target closed-loop dynamics model is prescribed, as illustrated schematically in Figure 3.2(b). This model takes the form

$$\boldsymbol{M}(\boldsymbol{q})\ddot{\boldsymbol{q}} + \boldsymbol{C}(\boldsymbol{q},\dot{\boldsymbol{q}})\dot{\boldsymbol{q}} = \boldsymbol{L}^\top \boldsymbol{f}_{te}(\boldsymbol{\eta},\boldsymbol{q}) - \boldsymbol{K}_q(\boldsymbol{q}-\boldsymbol{q}_d) - \boldsymbol{D}_q\dot{\boldsymbol{q}} + \boldsymbol{\psi}_{\text{ext}}, \tag{3.34a}$$

$$\boldsymbol{B}^\star\ddot{\boldsymbol{\eta}} + \boldsymbol{E}\boldsymbol{f}_{te}(\boldsymbol{\eta},\boldsymbol{q}) = -\boldsymbol{D}_\eta\dot{\boldsymbol{\eta}} + \boldsymbol{\tau}_0, \tag{3.34b}$$

where $\boldsymbol{K}_q, \boldsymbol{D}_q \in \mathbb{R}^{n\times n}$ and $\boldsymbol{D}_\eta \in \mathbb{R}^{n_\theta \times n_\theta}$ are symmetric, positive definite, and bounded gain matrices. The scaled motor inertia is defined as $\boldsymbol{B}^\star = \beta\boldsymbol{B}$ with scaling factor $\beta \in (0,1]$, consistent with the inertia-shaping methodology introduced in Section 2.3.2. The virtual motor coordinates $\boldsymbol{\eta} \in \mathbb{R}^{n_\theta}$ are introduced to decouple the specification of link-side impedance from the physical motor states; their construction is detailed in Section 3.3.2.

The feedforward torque vector $\boldsymbol{\tau}_0 = \boldsymbol{E}\boldsymbol{f}_{t0}$, where $\boldsymbol{f}_{t0} \in \mathbb{R}^{n_\theta}$ denotes the desired tendon tension profile, is selected to maintain positive tension in all tendons and thereby avoid slack. Notably, gravitational effects are omitted from the target dynamics, as they are implicitly compensated by

the equilibrium condition rather than explicitly canceled. This formulation achieves the desired interactive behavior through minimal structural modification of the original dynamics given in Equations (3.33a)–(3.33b).

Defining the extended state vector as

$$\boldsymbol{z} = \begin{bmatrix} \boldsymbol{q} \\ \dot{\boldsymbol{q}} \\ \boldsymbol{\eta} \\ \dot{\boldsymbol{\eta}} \end{bmatrix},$$

the equilibrium of the closed-loop system is obtained by imposing $\dot{\boldsymbol{z}} = \boldsymbol{0}$ and $\boldsymbol{\psi}_{\text{ext}} = \boldsymbol{0}$ in Equations (3.34a)–(3.34b), yielding

$$\begin{aligned} \boldsymbol{L}^\top \boldsymbol{f}_{te}(\boldsymbol{\eta}, \boldsymbol{q}) - \boldsymbol{K}_q(\boldsymbol{q} - \boldsymbol{q}_d) &= \boldsymbol{0}, \\ \boldsymbol{E}\boldsymbol{f}_{te}(\boldsymbol{\eta}, \boldsymbol{q}) &= \boldsymbol{\tau}_0. \end{aligned} \tag{3.35}$$

If the target tendon force vector $\boldsymbol{f}_{tp}$ satisfies $\boldsymbol{f}_{tp} \in \mathcal{N}(\boldsymbol{L}^\top)$, i.e., $\boldsymbol{L}^\top \boldsymbol{f}_{tp} = \boldsymbol{L}^\top \boldsymbol{E}^{-1}\boldsymbol{\tau}_0 = \boldsymbol{0}$, then the unique equilibrium point of the system is given by

$$\boldsymbol{z}_{\text{eq}} = \begin{bmatrix} \boldsymbol{q}_d \\ \boldsymbol{0} \\ \boldsymbol{\eta}_d \\ \boldsymbol{0} \end{bmatrix}, \tag{3.36}$$

where $\boldsymbol{\eta}_d$ is the solution to $\boldsymbol{f}_{te}(\boldsymbol{q}_d, \boldsymbol{\eta}_d) = \boldsymbol{f}_{tp}$. This equilibrium reflects a configuration in which the link is positioned at the desired pose $\boldsymbol{q}_d$, all velocities vanish, and internal tendon tensions are maintained at a feasible pretension level that ensures the controllability of the transmission.

3.3.2 Control Design

This section presents the control strategy that enforces the target closed-loop dynamics specified in Equations (3.34a)–(3.34b). The design is structured in two sequential stages: (i) a coordinate transformation from the physical motor coordinates $\boldsymbol{\theta}$ to a set of virtual motor coordinates $\boldsymbol{\eta}$, which enables independent specification of the desired link-side impedance; and (ii) the synthesis of a feedback control law that renders the closed-loop system equivalent to the target dynamics while ensuring stability and passivity.

Coordinate transformation

To reconcile the original link dynamics (3.33a) with the desired form (3.34a), equality is imposed between the generalized elastic torques acting on the link side:

$$\underbrace{\boldsymbol{L}^\top \boldsymbol{f}_{te}(\boldsymbol{\theta}, \boldsymbol{q})}_{\boldsymbol{\psi}(\boldsymbol{\theta}, \boldsymbol{q})} := \underbrace{\boldsymbol{L}^\top \boldsymbol{f}_{te}(\boldsymbol{\eta}, \boldsymbol{q})}_{\boldsymbol{\psi}(\boldsymbol{\eta}, \boldsymbol{q})} + \boldsymbol{\tau}_d(\boldsymbol{q}, \dot{\boldsymbol{q}}, \boldsymbol{q}_d), \tag{3.37}$$

where the desired feedback torque is defined as

$$\boldsymbol{\tau}_d(\boldsymbol{q}, \dot{\boldsymbol{q}}, \boldsymbol{q}_d) := \boldsymbol{g}(\boldsymbol{q}) - \boldsymbol{K}_q(\boldsymbol{q} - \boldsymbol{q}_d) - \boldsymbol{D}_q\dot{\boldsymbol{q}}. \tag{3.38}$$

Equation (3.37) provides n scalar constraints relating the physical and virtual motor coordinates. However, since the number of motor degrees of freedom satisfies $n_\theta > n$, this system is underdetermined and does not yield a unique mapping from $\boldsymbol{\theta}$ to $\boldsymbol{\eta}$. To resolve this indeterminacy, an additional $n_\theta - n$ independent constraints are introduced by preserving the component of the tendon force vector that lies in the nullspace of $\boldsymbol{L}^\top$:

$$\underbrace{\boldsymbol{N}^\top \boldsymbol{f}_{te}(\boldsymbol{\eta}, \boldsymbol{q})}_{\boldsymbol{\psi}_N(\boldsymbol{\eta},\boldsymbol{q})} = \underbrace{\boldsymbol{N}^\top \boldsymbol{f}_{te}(\boldsymbol{\theta}, \boldsymbol{q})}_{\boldsymbol{\psi}_N(\boldsymbol{\theta},\boldsymbol{q})}, \tag{3.39}$$

where $\boldsymbol{N} \in \mathbb{R}^{n_\theta \times (n_\theta - n)}$ is a full-rank matrix whose columns span $\mathcal{N}(\boldsymbol{L}^\top)$. Under Assumption 2, which ensures that $\boldsymbol{L}$ has constant rank, the combined set of equations is well-posed and yields n_θ independent relationships. Collecting both sets of constraints, the full transformation is expressed as a system of nonlinear equations:

$$\left.\begin{aligned} \boldsymbol{\psi}(\boldsymbol{\eta}, \boldsymbol{q}) - \boldsymbol{\psi}(\boldsymbol{\theta}, \boldsymbol{q}) + \boldsymbol{\tau}_d(\boldsymbol{q}, \dot{\boldsymbol{q}}, \boldsymbol{q}_d) = \boldsymbol{0}, \\ \boldsymbol{\psi}_N(\boldsymbol{\eta}, \boldsymbol{q}) - \boldsymbol{\psi}_N(\boldsymbol{\theta}, \boldsymbol{q}) = \boldsymbol{0}, \end{aligned}\right\} \quad \Rightarrow \quad \boldsymbol{h}(\boldsymbol{q}, \dot{\boldsymbol{q}}, \boldsymbol{q}_d, \boldsymbol{\theta}, \boldsymbol{\eta}) = \boldsymbol{0}. \tag{3.40}$$

The following proposition establishes the existence and uniqueness of this mapping.

Proposition 3. *The system of equations* (3.40) *defines a unique coordinate transformation from* $(\boldsymbol{\theta}, \boldsymbol{q})$ *to* $(\boldsymbol{\eta}, \boldsymbol{q})$.

Proof. The Implicit Function Theorem is applied to the mapping (3.40). Consider a solution point $(\boldsymbol{q}_0, \dot{\boldsymbol{q}}_0, \boldsymbol{q}_d, \boldsymbol{\theta}_0, \boldsymbol{\eta}_0)$, where $\boldsymbol{q}_d$ is constant due to the regulation setting. The theorem guarantees a unique local solution $\boldsymbol{\eta} = \boldsymbol{\eta}(\boldsymbol{q}, \dot{\boldsymbol{q}}, \boldsymbol{\theta})$ provided that:

(a) $\boldsymbol{h}(\cdot)$ in (3.40) is continuously differentiable ($\mathcal{C}^1$);

(b) the Jacobian $\frac{\partial \boldsymbol{h}}{\partial \boldsymbol{\eta}}$ is non-singular at the solution point.

Condition (a) holds under Assumption 1, which ensures the smoothness and convexity of the elastic potential energy, and hence the $\mathcal{C}^1$ continuity of $\boldsymbol{\psi}$ and $\boldsymbol{\psi}_N$. For condition (b), the Jacobian is computed using the chain rule and the definitions of $\boldsymbol{\psi}$ and $\boldsymbol{\psi}_N$:

$$\det\left(\frac{\partial \boldsymbol{h}}{\partial \boldsymbol{\eta}}\right) = \det\left(\begin{bmatrix} \boldsymbol{L}^\top \\ \boldsymbol{N}^\top \end{bmatrix}\right) \det\left(\frac{\partial \boldsymbol{f}_{te}(\boldsymbol{\eta}, \boldsymbol{q})}{\partial \boldsymbol{\eta}}\right). \tag{3.41}$$

The first determinant is nonzero because $\boldsymbol{L}^\top$ and $\boldsymbol{N}^\top$ form a full-rank decomposition of $\mathbb{R}^{n_\theta}$, a consequence of Assumption 2 and the orthogonality between the row space of $\boldsymbol{L}^\top$ and its nullspace. The second determinant is nonzero by Assumption 1, which implies strict monotonicity (and hence invertibility) of the tendon force map with respect to motor deformation. Therefore, the Jacobian is nonsingular, and the transformation is locally unique and invertible. If these conditions hold globally over the admissible configuration space, the mapping is globally well-defined. □

With the coordinate transformation established, the corresponding velocity-level relationship is obtained by differentiating (3.40) with respect to time. After algebraic rearrangement, the physical motor velocity is expressed as

$$\dot{\boldsymbol{\theta}} = \boldsymbol{A}(\boldsymbol{q}, \boldsymbol{\theta}, \boldsymbol{\eta})\dot{\boldsymbol{\eta}} + \boldsymbol{a}(\boldsymbol{q}, \dot{\boldsymbol{q}}, \ddot{\boldsymbol{q}}, \boldsymbol{q}_d, \boldsymbol{\theta}, \boldsymbol{\eta}), \tag{3.42}$$

where the matrices $\boldsymbol{A}$ and $\boldsymbol{a}$ are defined as

$$\boldsymbol{A} = \begin{bmatrix} \frac{\partial \psi(\boldsymbol{\theta},\boldsymbol{q})}{\partial \boldsymbol{\theta}} \\ \frac{\partial \psi_N(\boldsymbol{\theta},\boldsymbol{q})}{\partial \boldsymbol{\theta}} \end{bmatrix}^{-1} \begin{bmatrix} \frac{\partial \psi(\boldsymbol{\eta},\boldsymbol{q})}{\partial \boldsymbol{\eta}} \\ \frac{\partial \psi_N(\boldsymbol{\eta},\boldsymbol{q})}{\partial \boldsymbol{\eta}} \end{bmatrix}, \tag{3.43}$$

$$\boldsymbol{a} = \begin{bmatrix} \frac{\partial \psi(\boldsymbol{\theta},\boldsymbol{q})}{\partial \boldsymbol{\theta}} \\ \frac{\partial \psi_N(\boldsymbol{\theta},\boldsymbol{q})}{\partial \boldsymbol{\theta}} \end{bmatrix}^{-1} \left(\begin{bmatrix} \frac{\partial \psi(\boldsymbol{\eta},\boldsymbol{q})}{\partial \boldsymbol{q}} - \frac{\partial \psi(\boldsymbol{\theta},\boldsymbol{q})}{\partial \boldsymbol{q}} \\ \frac{\partial \psi_N(\boldsymbol{\eta},\boldsymbol{q})}{\partial \boldsymbol{q}} - \frac{\partial \psi_N(\boldsymbol{\theta},\boldsymbol{q})}{\partial \boldsymbol{q}} \end{bmatrix} \dot{\boldsymbol{q}} + \begin{bmatrix} \dot{\boldsymbol{\tau}}_d(\boldsymbol{q},\dot{\boldsymbol{q}},\boldsymbol{q}_d) \\ \boldsymbol{0} \end{bmatrix} \right). \tag{3.44}$$

The invertibility of the block matrix in (3.43) follows directly from Proposition 3. A second time differentiation of (3.42) yields the acceleration-level mapping:

$$\ddot{\boldsymbol{\theta}} = \boldsymbol{A}\ddot{\boldsymbol{\eta}} + \dot{\boldsymbol{A}}\dot{\boldsymbol{\eta}} + \dot{\boldsymbol{a}}. \tag{3.45}$$

This relationship provides the foundation for the subsequent synthesis of the control law, enabling the substitution of physical motor accelerations in the original dynamics with expressions in terms of the virtual coordinates and their derivatives.

Control law

Upon applying the CT to (3.33a), the link-side dynamics transforms into (3.34a). Substituting (3.45) into (3.33b) produces:

$$\boldsymbol{B}\boldsymbol{A}\ddot{\boldsymbol{\eta}} + \boldsymbol{B}\dot{\boldsymbol{a}} + \boldsymbol{B}\dot{\boldsymbol{A}}\dot{\boldsymbol{\eta}} + \boldsymbol{E}\boldsymbol{f}_{te}(\boldsymbol{\theta},\boldsymbol{q}) = \boldsymbol{u}. \tag{3.46}$$

Implementation of the control strategy:

$$\boldsymbol{u} = \boldsymbol{B}\dot{\boldsymbol{a}} + \boldsymbol{B}\dot{\boldsymbol{A}}\dot{\boldsymbol{\eta}} + \boldsymbol{E}\boldsymbol{f}_{te}(\boldsymbol{\theta},\boldsymbol{q}) + \boldsymbol{B}\boldsymbol{A}\boldsymbol{B}^{\star -1}(-\boldsymbol{E}\boldsymbol{f}_{te}(\boldsymbol{\eta},\boldsymbol{q}) - \boldsymbol{D}_\eta\dot{\boldsymbol{\eta}} + \boldsymbol{\tau}_0) \tag{3.47}$$

eliminates undesired terms. Multiplying both sides by $\boldsymbol{B}^\star(\boldsymbol{B}\boldsymbol{A})^{-1}$ yields the target dynamics (3.34a)-(3.34b). A block diagram representation is shown in Figure 3.3.

3.3.3 Stability and Passivity Analysis

Global asymptotic stability

The stability properties of the equilibrium point defined in Equation (3.36) are now analyzed. Consider the following candidate Lyapunov function:

$$\begin{aligned} V &= T(\boldsymbol{q},\dot{\boldsymbol{q}},\dot{\boldsymbol{\eta}}) + U_q(\boldsymbol{q}) + \bar{U}_e(\boldsymbol{\eta},\boldsymbol{q}) \\ &= \frac{1}{2}\dot{\boldsymbol{q}}^\top \boldsymbol{M}(\boldsymbol{q})\dot{\boldsymbol{q}} + \frac{1}{2}\dot{\boldsymbol{\eta}}^\top \boldsymbol{B}\dot{\boldsymbol{\eta}} + \frac{1}{2}(\boldsymbol{q}-\boldsymbol{q}_d)^\top \boldsymbol{K}_q(\boldsymbol{q}-\boldsymbol{q}_d) + \bar{U}_e(\boldsymbol{\eta},\boldsymbol{q}), \end{aligned} \tag{3.48}$$

where the constituent terms are defined as

$$T(\boldsymbol{q},\dot{\boldsymbol{q}},\dot{\boldsymbol{\eta}}) = \frac{1}{2}\dot{\boldsymbol{q}}^\top \boldsymbol{M}(\boldsymbol{q})\dot{\boldsymbol{q}} + \frac{1}{2}\dot{\boldsymbol{\eta}}^\top \boldsymbol{B}\dot{\boldsymbol{\eta}}, \tag{3.49}$$

$$U_q(\boldsymbol{q}) = \frac{1}{2}(\boldsymbol{q}-\boldsymbol{q}_d)^\top \boldsymbol{K}_q(\boldsymbol{q}-\boldsymbol{q}_d), \tag{3.50}$$

$$\bar{U}_e(\boldsymbol{\eta},\boldsymbol{q}) = U_e(\boldsymbol{\eta},\boldsymbol{q}) - U_0, \tag{3.51}$$

with the constant offset

$$U_0 := (\boldsymbol{E}\boldsymbol{\eta} - \boldsymbol{L}\boldsymbol{q})^\top \boldsymbol{f}_{t0} = -\Delta\boldsymbol{l}(\boldsymbol{\eta},\boldsymbol{q})^\top \boldsymbol{f}_{t0}.$$

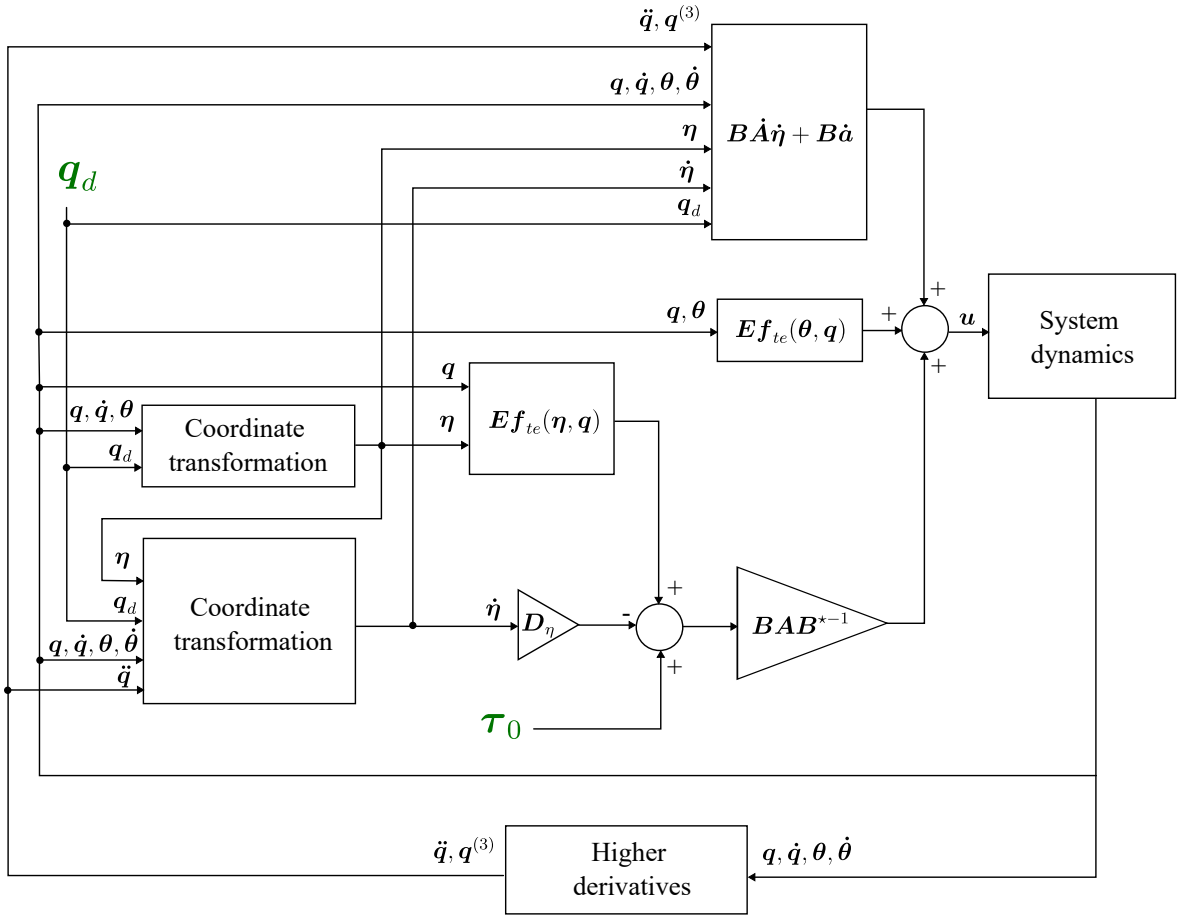


Figure 3.3: Block diagram of the proposed control law (3.47).

Here, T represents the total virtual kinetic energy of the link and motor subsystems, U_q is the potential energy associated with the desired impedance, and $\bar{U}_e$ denotes the elastic potential energy of the tendon network relative to a reference pretension state defined by $\boldsymbol{f}_{t0}$. The term U_0 accounts for the work done by the constant internal tendon forces $\boldsymbol{f}_{t0}$ and ensures that the net torque contribution from $\tau_0 = \boldsymbol{E}\boldsymbol{f}_{t0}$ vanishes at the link side when $\boldsymbol{f}_{t0} \in \mathcal{N}(\boldsymbol{L}^\top)$. Under Assumption 1, which guarantees strict convexity and smoothness of the elastic potential, the partial derivatives of $\bar{U}_e$ satisfy

$$\left(\frac{\partial \bar{U}_e(\boldsymbol{\eta}, \boldsymbol{q})}{\partial \boldsymbol{q}}\right)^\top = -\boldsymbol{L}^\top \boldsymbol{f}_{te}(\boldsymbol{\eta}, \boldsymbol{q}) + \underbrace{\boldsymbol{L}^\top \boldsymbol{f}_{t0}}_{=\mathbf{0}}, \tag{3.52}$$

$$\left(\frac{\partial \bar{U}_e(\boldsymbol{\eta}, \boldsymbol{q})}{\partial \boldsymbol{\eta}}\right)^\top = \boldsymbol{E}\boldsymbol{f}_{te}(\boldsymbol{\eta}, \boldsymbol{q}) - \boldsymbol{E}\boldsymbol{f}_{t0}. \tag{3.53}$$

These identities reflect the physical consistency of the energy model with the force transmission structure.

Proposition 4. *In the absence of external interaction torques ($\psi_{ext} = \mathbf{0}$), the equilibrium point $\boldsymbol{z}_{eq}$ given in Equation* (3.36) *is globally asymptotically stable for the closed-loop dynamics* (3.34a)–(3.34b).

Proof. The proof relies on LaSalle's Invariance Principle (see, e.g., Theorem 3.5 in [150]). The Lyapunov function candidate V is continuously differentiable and, under Assumption 1, radially unbounded due to the positive definiteness of $\boldsymbol{M}(\boldsymbol{q})$, $\boldsymbol{B}$, $\boldsymbol{K}_q$, and the coercivity of $\bar{U}_e$.

The time derivative of V along system trajectories is computed as

$$\dot{V} = \dot{\boldsymbol{\eta}}^\top \boldsymbol{B}\ddot{\boldsymbol{\eta}} + \dot{\boldsymbol{q}}^\top \boldsymbol{K}_q(\boldsymbol{q}-\boldsymbol{q}_d) + \dot{\boldsymbol{q}}^\top \left(\frac{\partial \bar{U}_e}{\partial \boldsymbol{q}}\right)^\top + \dot{\boldsymbol{\eta}}^\top \left(\frac{\partial \bar{U}_e}{\partial \boldsymbol{\eta}}\right)^\top + \dot{\boldsymbol{q}}^\top \boldsymbol{M}(\boldsymbol{q})\ddot{\boldsymbol{q}} + \frac{1}{2}\dot{\boldsymbol{q}}^\top \dot{\boldsymbol{M}}(\boldsymbol{q})\dot{\boldsymbol{q}}. \quad (3.54)$$

Substituting the closed-loop dynamics (3.34a)–(3.34b) and invoking the well-known property that $\dot{\boldsymbol{M}}(\boldsymbol{q}) - 2\boldsymbol{C}(\boldsymbol{q},\dot{\boldsymbol{q}})$ is skew-symmetric (when $\boldsymbol{C}$ is derived from Christoffel symbols), the expression simplifies to

$$\begin{aligned}\dot{V} &= \dot{\boldsymbol{q}}^\top \big(-\boldsymbol{C}\dot{\boldsymbol{q}} + \boldsymbol{L}^\top \boldsymbol{f}_{te} - \boldsymbol{K}_q(\boldsymbol{q}-\boldsymbol{q}_d) - \boldsymbol{D}_q\dot{\boldsymbol{q}} + \boldsymbol{\psi}_{\text{ext}}\big) \\ &\quad + \dot{\boldsymbol{\eta}}^\top \big(-\boldsymbol{D}_\eta\dot{\boldsymbol{\eta}} + \boldsymbol{\tau}_0 - \boldsymbol{E}\boldsymbol{f}_{te}\big) + \dot{\boldsymbol{q}}^\top \boldsymbol{K}_q(\boldsymbol{q}-\boldsymbol{q}_d) \\ &\quad + \dot{\boldsymbol{q}}^\top \big(-\boldsymbol{L}^\top \boldsymbol{f}_{te}\big) + \dot{\boldsymbol{\eta}}^\top \big(\boldsymbol{E}\boldsymbol{f}_{te} - \boldsymbol{\tau}_0\big) + \frac{1}{2}\dot{\boldsymbol{q}}^\top \dot{\boldsymbol{M}}\dot{\boldsymbol{q}} \\ &= -\dot{\boldsymbol{q}}^\top \boldsymbol{D}_q\dot{\boldsymbol{q}} - \dot{\boldsymbol{\eta}}^\top \boldsymbol{D}_\eta\dot{\boldsymbol{\eta}} + \dot{\boldsymbol{q}}^\top \boldsymbol{\psi}_{\text{ext}},\end{aligned} \quad (3.55)$$

where all elastic and potential terms cancel exactly due to the energy-consistent design of the target dynamics. In the free-motion case ($\boldsymbol{\psi}_{\text{ext}} = \boldsymbol{0}$), it follows that $\dot{V} \leq 0$, with equality if and only if $\dot{\boldsymbol{q}} = \boldsymbol{0}$ and $\dot{\boldsymbol{\eta}} = \boldsymbol{0}$. Define the invariant set

$$\mathcal{R} = \left\{ \boldsymbol{z} \in \mathbb{R}^{2n+2n_\theta} \mid \dot{V}(\boldsymbol{z}) = 0 \right\}.$$

Any trajectory remaining in $\mathcal{R}$ must satisfy $\dot{\boldsymbol{q}} \equiv \boldsymbol{0}$, $\dot{\boldsymbol{\eta}} \equiv \boldsymbol{0}$, and hence $\ddot{\boldsymbol{q}} \equiv \boldsymbol{0}$, $\ddot{\boldsymbol{\eta}} \equiv \boldsymbol{0}$. Substitution into the closed-loop dynamics yields

$$\boldsymbol{L}^\top \boldsymbol{f}_{te}(\boldsymbol{\eta},\boldsymbol{q}) = \boldsymbol{K}_q(\boldsymbol{q}-\boldsymbol{q}_d), \quad \boldsymbol{E}\boldsymbol{f}_{te}(\boldsymbol{\eta},\boldsymbol{q}) = \boldsymbol{\tau}_0.$$

Given that $\boldsymbol{f}_{t0} \in \mathcal{N}(\boldsymbol{L}^\top)$, the unique solution to this system is $\boldsymbol{q} = \boldsymbol{q}_d$ and $\boldsymbol{f}_{te}(\boldsymbol{\eta},\boldsymbol{q}) = \boldsymbol{f}_{t0}$, which corresponds precisely to the equilibrium $\boldsymbol{z}_{\text{eq}}$ in (3.36). Thus, $\boldsymbol{z}_{\text{eq}}$ is the largest invariant subset of $\mathcal{R}$, and global asymptotic stability follows from LaSalle's principle. □

Remark 1. *The stability of the equilibrium in the virtual coordinates* $(\boldsymbol{\eta},\boldsymbol{q})$ *implies stability in the original physical coordinates* $(\boldsymbol{\theta},\boldsymbol{q})$. *This equivalence holds because the coordinate transformation defined by* (3.40) *and its velocity-level counterpart* (3.42) *are smooth and unique mapping under the conditions of Proposition 3.*

Output-strict passivity

The passivity of the closed-loop system with respect to external interaction is now established. Since V is radially unbounded and bounded from below, there exists a constant $c \in \mathbb{R}$ such that the shifted storage function $V_s = V + c$ is positive semi-definite and suitable for passivity analysis.

Proposition 5. *The closed-loop dynamics* (3.34a)–(3.34b) *define an output-strictly passive mapping from the external torque input* $\boldsymbol{\psi}_{ext}$ *to the joint velocity output* $\dot{\boldsymbol{q}}$.

Proof. Differentiating V_s along system trajectories and applying the same simplifications as in the stability proof yields

$$\dot{V}_s = -\dot{\boldsymbol{q}}^\top \boldsymbol{D}_q\dot{\boldsymbol{q}} - \dot{\boldsymbol{\eta}}^\top \boldsymbol{D}_\eta\dot{\boldsymbol{\eta}} + \dot{\boldsymbol{q}}^\top \boldsymbol{\psi}_{\text{ext}}. \quad (3.56)$$

Since $\boldsymbol{D}_q$ is symmetric positive definite, there exists $\epsilon > 0$ such that $\dot{\boldsymbol{q}}^\top \boldsymbol{D}_q\dot{\boldsymbol{q}} \geq \epsilon\, \dot{\boldsymbol{q}}^\top\dot{\boldsymbol{q}}$. Consequently,

$$\dot{V}_s \leq \dot{\boldsymbol{q}}^\top \boldsymbol{\psi}_{\text{ext}} - \epsilon \left\|\dot{\boldsymbol{q}}\right\|^2,$$

which satisfies the definition of output-strict passivity from $\boldsymbol{\psi}_{\text{ext}}$ to $\dot{\boldsymbol{q}}$. □

This passivity property ensures robustness against unmodeled dynamics and guarantees stable interaction with passive environments, including human operators.

3.4 Experiment: Interaction Test on a Single BAVS Joint

This section presents an experimental validation of the proposed impedance controller during physical interaction between a human operator and a single-joint BAVS system. The test platform consists of the forearm rotation axis of the elastic robot DLR *neoDavid*, which integrates a BAVS joint as its actuation mechanism. The experimental setup is illustrated in Figure 3.4. To isolate the dynamics of the tested joint, the shoulder and elbow joints are regulated using a previously developed controller [151], thereby preventing spurious oscillations from other degrees of freedom.

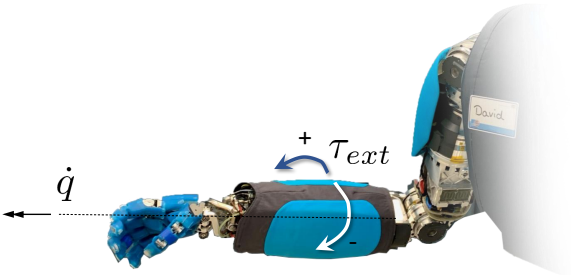


Figure 3.4: Experimental setup for evaluating impedance behavior under human interaction. The forearm of the elastic robot DLR *neoDavid* is initialized at the desired configuration $q = q_d$. The remaining joints (shoulder and elbow) are stabilized using the ESPi controller reported in [151] to suppress undesired motion coupling © 2021 IEEE.

Damping parameters for both the link and motor subsystems are selected following the modal damping approach described in [151]. Specifically, the link-side damping gain is set as $D_q = 2\xi_q\sqrt{K_q M}$, and the motor-side damping gains are defined by $D_{\eta,i} = 2\xi_\eta\sqrt{\bar{k}_i B^\star}$, where $\bar{k}_i$ denotes the local stiffness expressed in the virtual motor coordinates η_i, and ξ_q, ξ_η are prescribed damping ratios. A motor friction observer [152, 153] is implemented throughout all trials to compensate for unmodeled dissipative effects.

The external torque τ_{ext} exerted by the human subject on the link is estimated in real time using a momentum-based disturbance observer [153]; an example of the estimated interaction torque is shown in Figure 3.5. Experiments are conducted across four commanded link stiffness values, $K_q \in \{5, 15, 25, 50\}$ N m/rad, under two distinct stiffness presets: $\sigma_d = 0.1$ rad and $\sigma_d = 0.3$ rad. The complete set of control parameters is summarized in Table 3.1.

Table 3.1: Controller Parameters Used in Experiments

No.	K_q [N m/rad]	σ_d [rad]	ξ_q	ξ_η	β
1	5	0.1 / 0.3	0.5	0.1	0.3
2	15	0.1 / 0.3	0.5	0.1	0.3
3	25	0.1 / 0.3	0.5	0.1	0.3
4	50	0.1 / 0.3	0.5	0.1	0.3

It is observed that larger values of the stiffness preset σ_d result in reduced peak magnitudes of the achievable external torque τ_{ext}. This limitation arises because increasing σ_d narrows the feasible operating range of the link-side elastic torque ψ, as illustrated in Figure 2.2 by comparing the torque envelopes for $\sigma_d = 0$ (red curve) and $\sigma_d = 0.1$ (purple curve). Concurrently, the instantaneous physical joint stiffness $\kappa(\theta_1 - q, \theta_2 - q)$ is recorded throughout each trial, as depicted in Figure 3.7.

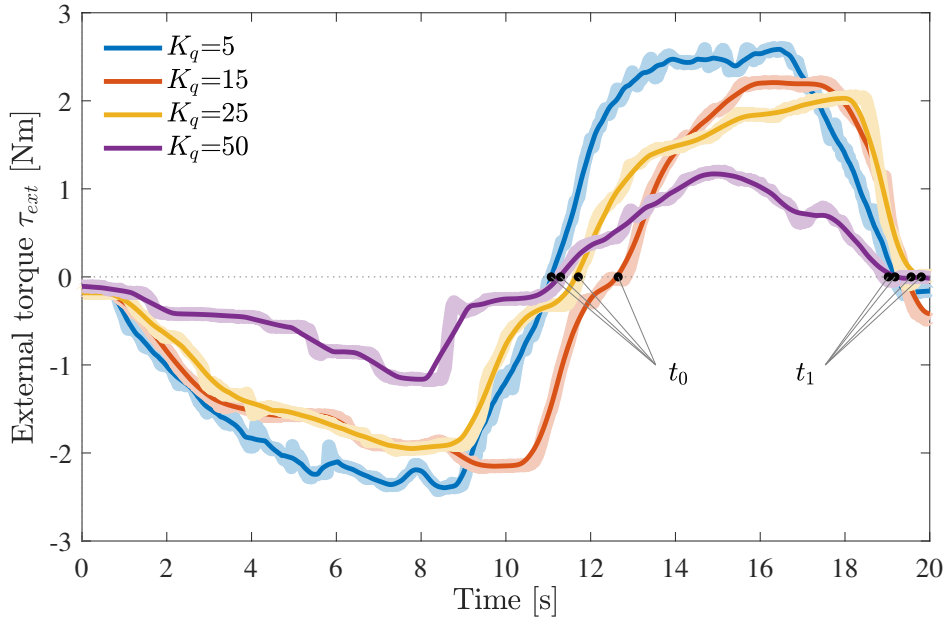


Figure 3.5: Estimated external torque τ_{ext} acting on the BAVS joint for $\sigma_d = 0.3$ rad. Colored traces correspond to different commanded stiffness values K_q. For each trial, the interval $[t_0, t_1]$ denotes the duration over which τ_{ext} remains positive © 2021 IEEE.

The relationship between the external torque τ_{ext} and the link deflection error $\tilde{q} = q - q_d$ is presented in Figure 3.6. The apparent link-side stiffness, approximated as the slope $\Delta\tau_{\text{ext}}/\Delta\tilde{q}$, is obtained via linear regression (black dashed lines) over the quasi-static interaction segments. The resulting stiffness estimates and their relative errors with respect to the commanded K_q are summarized in Table 3.2. The consistently low relative errors, within $\pm 2.6\%$ across all conditions, support the first key conclusion: the realized link-side stiffness is governed exclusively by the controller parameter K_q and is decoupled from the underlying physical joint stiffness κ.

Furthermore, the feasible range of link deflection $\tilde{q}$ is demonstrably constrained by the choice of σ_d. As evident in Figure 3.6, trials with $\sigma_d = 0.3$ rad (gray curves in the blue-shaded region) exhibit a significantly smaller deflection envelope compared to those with $\sigma_d = 0.1$ rad (colored curves), confirming that σ_d modulates the operational workspace without affecting the commanded impedance.

Figure 3.7 compares the commanded stiffness K_q with the instantaneous physical stiffness κ over the interaction intervals defined in Figure 3.5. A second important observation emerges: the effective link-side stiffness can be rendered either softer or significantly stiffer than the intrinsic physical stiffness of the joint. For instance, when $K_q = 50\ \text{N m/rad}$ and $\sigma_d = 0.3$ rad, the achieved stiffness exceeds the physical baseline by approximately a factor of three. Additionally, the stiffness preset σ_d directly limits the dynamic range of the physical joint stiffness κ. This effect is visible in the amplitude disparity between the upper plot ($\sigma_d = 0.1$ rad) and the lower plot ($\sigma_d = 0.3$ rad) in Figure 3.7, where higher pretension reduces the variability of κ during interaction.

These results collectively confirm that the proposed controller successfully realizes independent regulation of link-side impedance and internal pretension, enabling versatile and predictable physical human–robot interaction.

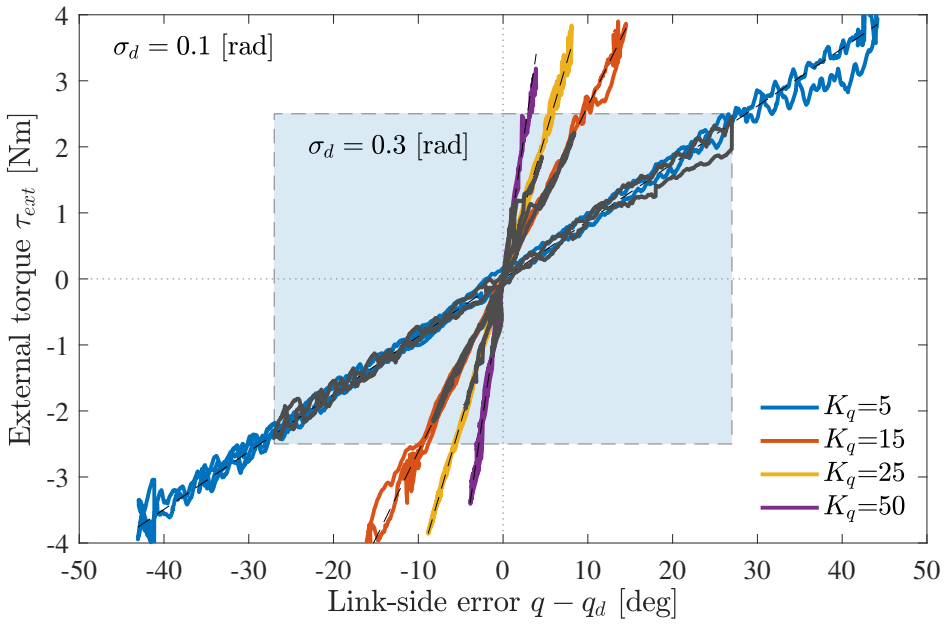


Figure 3.6: External torque τ_{ext} versus link deflection $\tilde{q} = q - q_d$. Colored curves correspond to $\sigma_d = 0.1$ rad; gray curves (within the blue region) correspond to $\sigma_d = 0.3$ rad. The stiffness preset influences only the admissible range of deflection (and thus maximal torque), while the slope, which reflects the achieved stiffness, remains consistent with the commanded K_q, validating the impedance control objective © 2021 IEEE.

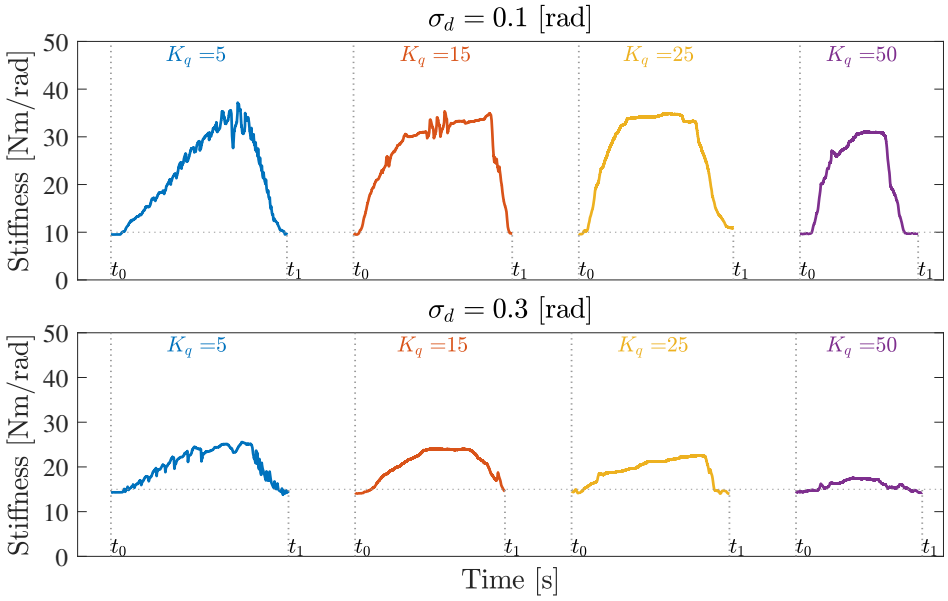


Figure 3.7: Comparison between physical joint stiffness $\kappa(\theta_1 - q, \theta_2 - q)$ and commanded stiffness K_q. Four stiffness profiles are shown for each preset: the top panel corresponds to $\sigma_d = 0.1$ rad, the bottom panel to $\sigma_d = 0.3$ rad. Data are extracted over the time intervals indicated in Figure 3.5 © 2021 IEEE.

3.5 Simulations on Elastic Tendon-Driven Fingers

This section presents simulation-based validation of the proposed control strategy on the tendon-driven index finger of the DLR *neoDavid* Hand [31, 44]. As illustrated in Figure 2.3(b), the finger mechanism comprises 4 DoFs and eight degrees of actuation (DoA), with nonlinear tendon coupling between motors and joints. The dynamic and elastic parameters used in the system model, Equa-

Table 3.2: Experimental Results: Achieved Link-Side Stiffness

Desired K_q [Nm/rad]	Desired σ_d [rad]	$\Delta\tau_{\text{ext}}/\Delta\tilde{q}$ [Nm/rad]	Relative Error [%]
5.0	0.10	4.87	-2.60
15.0	0.10	15.13	0.86
25.0	0.10	25.14	0.56
50.0	0.10	49.10	-1.80
5.0	0.30	4.92	-1.60
15.0	0.30	14.89	-0.73
25.0	0.30	24.52	-1.92
50.0	0.30	49.63	-0.74

tions (3.33a)–(3.33b), are taken directly from the physical robot's specifications.

All simulations are implemented in MATLAB & SIMULINK using a variable-step Runge–Kutta ODE45 solver. The damping matrices $\boldsymbol{D}_q$ and $\boldsymbol{D}_\eta$ are synthesized via modal damping ratios $\boldsymbol{\xi}_q$ and $\boldsymbol{\xi}_\eta$, following the methodology in [101, Eq. (85)]. Derivatives of the inertia and Coriolis matrices are computed using algorithmic differentiation techniques as described in [154]. Joint acceleration $\ddot{\boldsymbol{q}}$ and jerk $\boldsymbol{q}^{(3)}$ are derived from the dynamic model and require an estimate of the external torque $\boldsymbol{\psi}_{\text{ext}}$, as detailed in Remark 2.

Remark 2. *The joint acceleration and jerk are computed as:*

$$\begin{aligned}\ddot{\boldsymbol{q}} &= \boldsymbol{M}^{-1}\left(\boldsymbol{\psi} - \boldsymbol{C}\dot{\boldsymbol{q}} - \boldsymbol{g} + \boldsymbol{\psi}_{ext}\right),\\ \boldsymbol{q}^{(3)} &= \boldsymbol{M}^{-1}\left(\dot{\boldsymbol{\psi}} - \dot{\boldsymbol{M}}\ddot{\boldsymbol{q}} - \boldsymbol{C}\ddot{\boldsymbol{q}} - \dot{\boldsymbol{C}}\dot{\boldsymbol{q}} - \dot{\boldsymbol{g}} + \dot{\boldsymbol{\psi}}_{ext}\right).\end{aligned}$$

The coordinate transformation defined implicitly by Equation (3.40) is solved numerically at each time step using the `fmincon` interior-point optimization algorithm. To emulate realistic sensing conditions, zero-mean band-limited white noise (sampled at 1 kHz) is added to the measured joint positions q_i and motor angles θ_j. This noise propagates through numerical differentiation, resulting in approximate variances of $1\ \mathrm{rad/s^2}$ for joint accelerations and $10^3\ \mathrm{rad/s^3}$ for jerks. Two simulation scenarios are conducted: (i) regulation to a desired configuration $\boldsymbol{q}_d$, and (ii) verification of the commanded link-side stiffness $\boldsymbol{K}_q$ under interaction.

3.5.1 Regulatory Behavior

The first simulation evaluates the regulatory performance of the proposed ESPi controller. For comparative assessment, the ESPi controller is benchmarked against the cascaded-structure (CS) controller introduced by Chalon et al. [97], which addresses similar impedance control objectives for elastic actuators. The CS control law for the open-loop dynamics (3.33a)–(3.33b) is given by

$$\begin{aligned}\boldsymbol{u} &= \boldsymbol{\tau}_d - \boldsymbol{K}_\tau(\boldsymbol{\tau} - \boldsymbol{\tau}_d) - \boldsymbol{D}_\theta\dot{\boldsymbol{\theta}}\\ &\overset{(3.38)}{=} \boldsymbol{g} - \boldsymbol{K}_q(\boldsymbol{q} - \boldsymbol{q}_d) - \boldsymbol{D}_q\dot{\boldsymbol{q}} - \boldsymbol{K}_\tau\Big[\boldsymbol{E}\boldsymbol{f}_{te} - (\boldsymbol{g} - \boldsymbol{K}_q(\boldsymbol{q} - \boldsymbol{q}_d) - \boldsymbol{D}_q\dot{\boldsymbol{q}})\Big] - \boldsymbol{D}_\theta\dot{\boldsymbol{\theta}},\end{aligned} \tag{3.57}$$

where $\boldsymbol{\tau}_d$ denotes the desired link-side torque (i.e., the outer-loop impedance command) as defined in Equation (3.38).

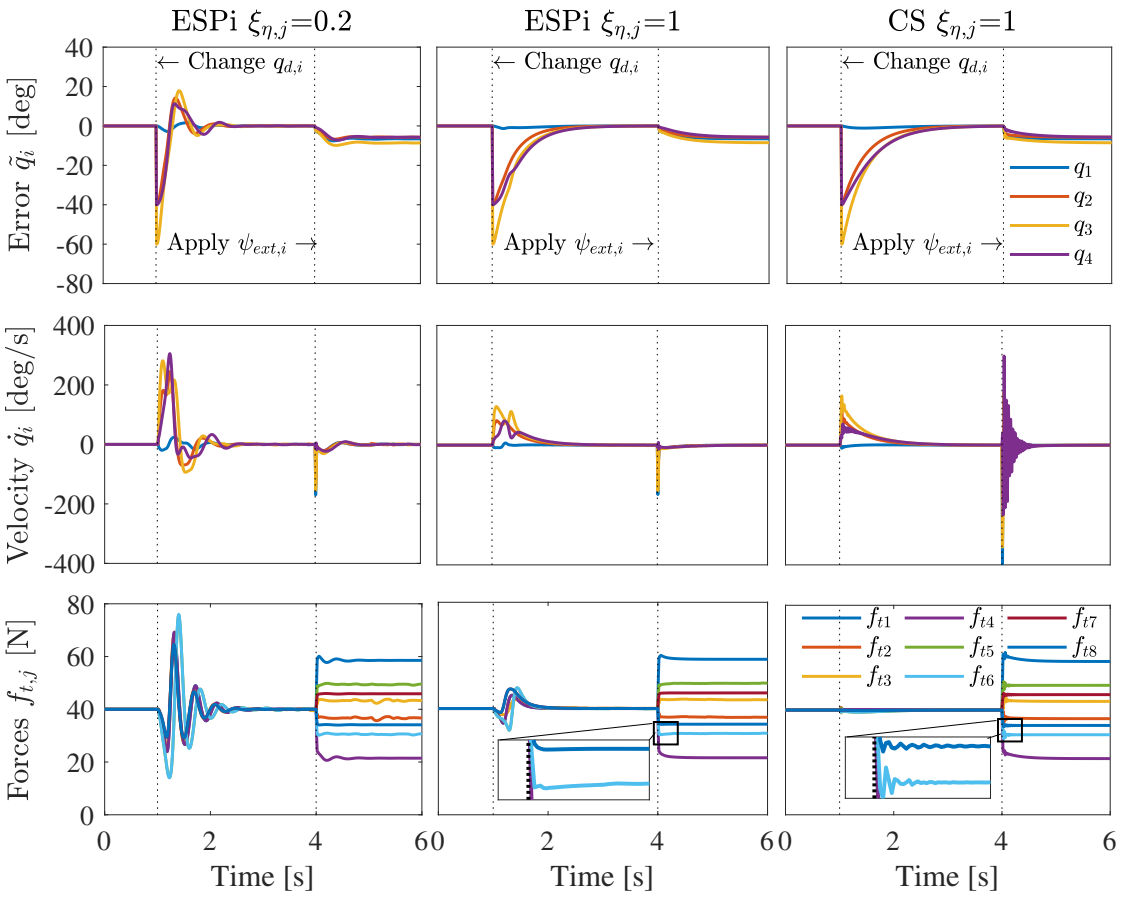


Figure 3.8: Regulation performance comparison between the ESPi controller (with motor-side modal damping ratios $\xi_{\eta_j} = 0.2$ and $\xi_{\eta_j} = 1.0$) and the cascaded-structure (CS) controller ($\xi_{\theta_j} = 1.0$). From top to bottom: joint position error $\tilde{\boldsymbol{q}} = \boldsymbol{q} - \boldsymbol{q}_d$, joint velocities $\dot{\boldsymbol{q}}$, and tendon forces $\boldsymbol{f}_{te}(\boldsymbol{\theta}, \boldsymbol{q})$. At $t = 1$ s, the reference configuration $\boldsymbol{q}_d$ is updated; at $t = 4$ s, a constant external torque $\boldsymbol{\psi}_{\text{ext}}$ is applied. The CS controller exhibits high-frequency oscillations in tendon forces, as visible in the bottom subplot of the third column © 2022 IEEE.

Test setup

The test scenario begins with the finger in an open configuration ($\boldsymbol{q}_0 = \boldsymbol{0}^\circ$). At $t = 1$ s, the reference configuration is stepped to a semi-closed pose $\boldsymbol{q}_d = [0, 40, 60, 40]^\top$ deg, as depicted in Figure 3.9. At $t = 4$ s, a constant external torque $\boldsymbol{\psi}_{\text{ext}} = [-0.4, -0.25, -0.15, -0.05]^\top$ N m is applied to assess disturbance rejection. This sequence emulates natural finger closure followed by environmental contact. Due to the significantly smaller link inertia relative to motor inertia, variations in the link-side damping ratio ξ_{q_i} have negligible impact on overall transient behavior. Consequently, $\xi_{q_i} = 0.6$ is held constant across all trials. Motor-side damping is evaluated under two settings: $\xi_{\eta_j} = 0.2$ (underdamped) and $\xi_{\eta_j} = 1.0$ (critically damped). The commanded stiffness matrix is set to $\boldsymbol{K}_q = \text{diag}(3.5, 2.5, 1.0, 0.5)$ N m/rad, approximating the mean intrinsic joint stiffness of the mechanism. All tendons are initialized and maintained at a pretension force of $f_{t_{p,j}} = 40$ N, corresponding to one-third of the maximum allowable tendon load and satisfying $\boldsymbol{f}_{t0} \in \mathcal{N}(\boldsymbol{L}^\top)$.

For a fair comparison, the CS controller employs identical $\boldsymbol{K}_q$ and $\boldsymbol{D}_q$ as the ESPi controller. The inner-loop gain $\boldsymbol{K}_\tau$ is tuned to match the steady-state regulation error of the ESPi controller over $t \in [1, 4]$ s. Furthermore, the motor-side damping matrices are aligned: $\boldsymbol{D}_\theta$ in (3.57) is set equal to $\boldsymbol{D}_\eta$ from the ESPi law.

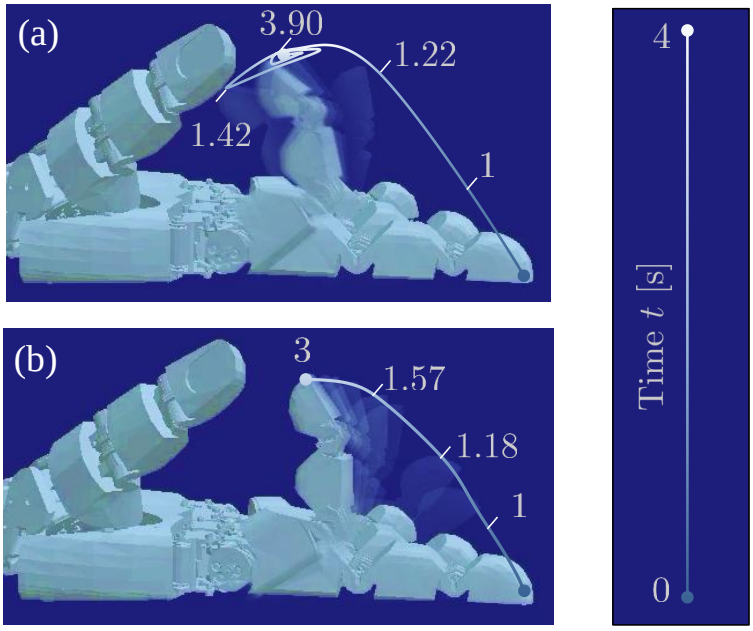


Figure 3.9: Regulation test for the 4-DoF finger: (a) ESPi with $\xi_{\eta_j} = 0.2$; (b) ESPi with $\xi_{\eta_j} = 1.0$. The timestamps correspond to the faded time axis in Figure 3.8. Adapted from [117].

Results and analysis

Simulation results are shown in Figure 3.8. Comparing the two ESPi configurations, the critically damped case ($\xi_{\eta_j} = 1.0$) eliminates overshoot in joint position error (first row) and significantly reduces peak velocities (second row) relative to the underdamped case ($\xi_{\eta_j} = 0.2$). Tendon forces remain strictly positive throughout, with smoother convergence to the target pretension under higher damping (third row). The motion sequences in Figure 3.9 visually confirm the absence of oscillations in the critically damped case.

During the regulation phase ($t \in [1, 4]$ s), the tracking error $\tilde{\boldsymbol{q}}$ converges asymptotically to zero, consistent with the global asymptotic stability result in Proposition 4. Upon application of the disturbance at $t = 4$ s, the system settles to a new equilibrium $\boldsymbol{q}^\star$ satisfying $\boldsymbol{K}_q(\boldsymbol{q}^\star - \boldsymbol{q}_d) = \boldsymbol{\psi}_{\text{ext}}$, yielding $\boldsymbol{q}^\star = [-6.55, -5.73, -8.59, -5.73]^\circ$, in agreement with theoretical prediction.

Comparative assessment

While both controllers achieve comparable steady-state accuracy and disturbance rejection (Figure 3.8, third column), their transient behaviors differ markedly. The CS controller exhibits high-frequency oscillations in joint velocities and tendon forces during transients, attributable to aggressive inner-loop torque tracking without explicit energy shaping. Such oscillations may induce fatigue in tendon materials and reduce mechanical longevity [155].

In contrast, the ESPi controller produces smoother tendon force profiles, despite slightly larger initial force excursions at $t = 1$ s. Both controllers demonstrate robustness to sensor noise and effective regulation under perturbation. These results corroborate the theoretical stability and passivity properties established earlier and highlight the practical advantage of the ESPi architecture in promoting mechanical durability through energetically consistent control.

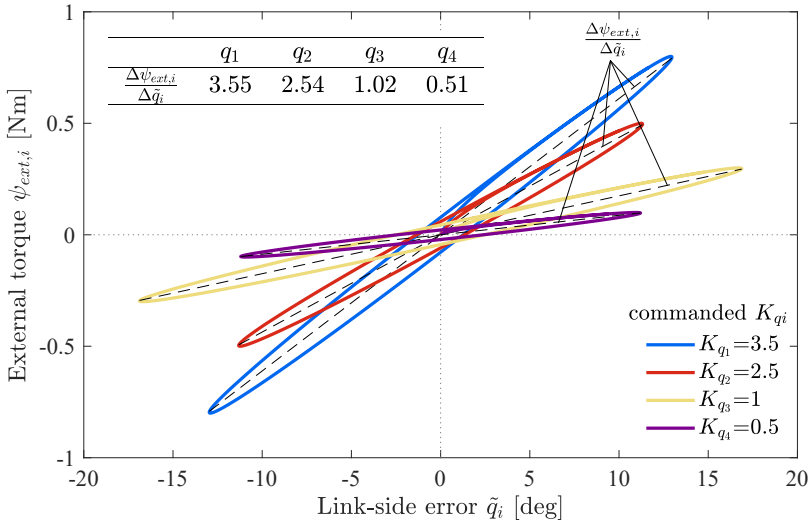


Figure 3.10: Relationship between external torques $\boldsymbol{\psi}_{\text{ext}}$ and link-side position errors $\tilde{\boldsymbol{q}} = \boldsymbol{q} - \boldsymbol{q}_d$. Colored curves correspond to different commanded stiffness values K_{q_i} (in $[\mathrm{N\,m/rad}]$). Dashed black lines indicate ideal stiffness slopes. Achieved stiffness estimates $\Delta\psi_{\text{ext},i}/\Delta\tilde{q}_i$ are reported in the top-left corner of each subplot. Adapted from [117].

3.5.2 Interaction Behavior

The second simulation validates the controller's ability to realize prescribed impedance characteristics during dynamic interaction. The finger is held at a fixed reference pose $\boldsymbol{q}_d$, while sinusoidal external torques $\boldsymbol{\psi}_{\text{ext}}$ are applied. The achieved stiffness is estimated via linear regression of $\psi_{\text{ext},i}$ versus $\tilde{q}_i$, yielding the slope $\Delta\psi_{\text{ext},i}/\Delta\tilde{q}_i$ for each joint i.

Test setup

The same parameter set as in the regulation test is employed:

- $\xi_{q_i} = 0.6$,
- $\xi_{\eta_j} = 1.0$,
- $\boldsymbol{q}_d = [0, 40, 60, 40]^\top$ deg, and
- $\boldsymbol{K}_q = \mathrm{diag}(3.5, 2.5, 1.0, 0.5)\ \mathrm{N\,m/rad}$.

Sinusoidal external torques of amplitude $[0.8, 0.5, 0.3, 0.1]^\top\ \mathrm{N\,m}$ are applied at 1 Hz, a frequency representative of typical human manipulation speeds. Tendon pretension remains fixed at $40\ \mathrm{N}$.

Results and analysis

Figure 3.10 shows that the achieved stiffness closely matches the commanded values across all joints. However, the data points deviate slightly from the ideal linear relationship (dashed black lines), forming elliptical hysteresis loops rather than straight lines. This behavior arises because the sinusoidal excitation maintains non-zero velocity and acceleration throughout most of the cycle; quasi-static conditions, required for pure stiffness characterization, are only momentarily satisfied at the extrema of the sinusoid.

Consequently, the measured torque–deflection relationship reflects a combination of elastic and inertial/damping effects, manifesting as phase-shifted ellipses. Despite these dynamic contributions, the major axis of each ellipse aligns closely with the commanded stiffness slope, confirming that the dominant impedance behavior is accurately imposed. This demonstrates the controller's effectiveness in achieving desired interactive compliance even under continuous, dynamic interaction.

3.6 Summary

This chapter introduces an Elastic Structure Preserving impedance (ESPi) control framework for BAVS actuators and tendon-driven systems with nonlinear elastic couplings. Building on the ESPi concept from [137], the controller imposes desired link-side stiffness and damping while preserving the system's intrinsic inertial and elastic properties.

For BAVS actuators, motor pretension is achieved via constant internal torques with opposing signs, ensuring link-side torque invariance under stiffness modulation. Motor-side damping suppresses oscillations, and stability and passivity are rigorously analyzed using physically motivated storage functions. Experimental validation on the DLR *neoDavid* forearm joint demonstrated robust compliance during human interaction.

While the design for the BAVS joint highlights the proposed controller's ability to impose desired impedance behavior for actuators with symmetric antagonistic drives, tendon-driven mechanisms introduce additional challenges due to nonlinear elastic couplings. Extending the controller to this domain requires reinterpreting motor coordinates to encode link-side impedance, allowing the closed-loop dynamics to preserve the underlying elastic structure with minimal shaping. This generalization enables global asymptotic set-point regulation and output-strict passivity, enhancing energy efficiency and robustness. Simulations on a tendon-driven finger validated set-point accuracy and disturbance rejection, though friction (unmodeled) may induce steady-state errors without compensation. Practical implementation requires motor position sensing, tendon elongation estimation, and external torque measurement.

4

Finger Flow (FF): Reactive Reach-While-Grasp Motion Generation

Humans exhibit a remarkable capacity to grasp both static and dynamically moving objects through seamless, one-shot motions. They adapt fluidly to external perturbations and recover autonomously from failed attempts without explicit planning. In stark contrast, robotic systems equipped with multi-fingered hands typically employ rigid, precomputed "reach-then-grasp" pipelines. These sequential strategies not only produce slow and unnatural motion patterns but also severely limit the robot's responsiveness to unexpected changes in object pose. Moreover, open-loop execution, common in such approaches, often culminates in grasp failure when real-world conditions deviate from assumptions.

Driven by this disparity, this work addresses **(Gap 2)**, as outlined in Section 1.3, which encompasses two specific gaps:

(**a**) **Dynamic grasping of objects undergoing unpredictable motion in free space**: Despite advances in robotic manipulation, no existing method has demonstrated robust, real-time grasping of freely moving objects with arbitrary trajectories using a fully actuated hand–arm system.

(**b**) **A lightweight geometric abstraction for high-DoF hands that enables real-time, finger-aware reaching**: The intricate geometry of anthropomorphic hands impedes rapid motion planning. To date, there exists no computationally efficient representation that facilitates online collision avoidance between fingers and the target object during reaching.

Figure 4.1 provides a conceptual illustration of these challenges. From a hand-centric viewpoint, the task of reactive reach-and-grasp can be interpreted as guiding an object, whose motion is uncertain, toward a stable attractor within the hand's configuration space. This attractor lies within a *basin of attraction* (denoted by the green dot), where successful grasping occurs while actively avoiding collisions with the fingers and palm. To bridge these gaps and fulfill the research objectives outlined as (**G2**)–(**G3**) in the introduction, this chapter introduces the following contributions (**C3**)–(**C4**):

1) *Finger Flow (FF)*: A reactive motion generation framework that unifies reaching and grasping into a single, continuous action. Leveraging real-time visual estimates of object pose and proprioceptive feedback from finger joints, FF dynamically coordinates both arm and hand motions. Crucially, the embedded hand motion controller continuously modulates end-effector

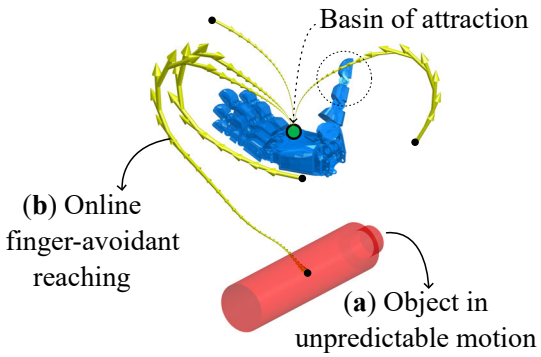


Figure 4.1: From a hand-centric perspective, the reactive reaching motion can be viewed as guiding an object displaying unpredictable motion toward an attractor, where it eventually settles within the basin of attraction (green dot) while avoiding fingers and palm.

pose to prevent premature contact between fingers and the object during approach. The entire algorithm operates at over 3 kHz on low-power mobile processors, enabling true real-time responsiveness.

2) Formal theoretical guarantees establishing both asymptotic convergence to the target and guaranteed avoidance of finger-object collisions, specifically for stationary spherical objects.

3) Extensive real-world validation on the DLR robot *neoDavid* [44], including: (i) more than 130 trials grasping a static object on a tabletop; (ii) dynamic interception and grasping of cylindrical bottles moving unpredictably in 3D space, with median peak velocities exceeding 0.7 m/s; and (iii) 58 successful human-to-robot handovers under diverse interaction modes, ranging from cooperative to adversarial, without task-specific reconfiguration.

4) Comprehensive simulation-based evaluations, including quantitative comparisons against Position-Based Visual Servoing (PBVS) and open-loop variants of FF, as well as parametric studies examining the influence of hand hull simplification, object dimensions (cylindrical geometries), and surface friction properties.

To guide the reader through the chapter, Section 4.2 introduces the proposed methods and gives an overview of the proposed framework. Section 4.3 introduces the concept of the hand hull, which serves as the foundation for Section 4.4, where the first thread, a hand motion generation, is presented. The second thread, finger motion generation, is detailed in Section 4.5. Section 4.6 validates our approach through real-world experiments on the DLR robot *neoDavid*, with discussions of the experimental results and supporting simulation studies. The chapter closes with concluding remarks in Section 4.7.

Publication Note

The content of this chapter is based on the following publication

- [156] **X. Meng**, H. Maurenbrecher, A. Albu-Schäffer, and M. Keppler, "Finger flow: Reactive Reach-while-Grasp Generation for Robotic Arms with Multi-Fingered Hands", in *Robotics and Autonomous Systems*, 2025.

Parts of this chapter reuse figures from publications by the author that are licensed under Creative Commons Attribution 4.0.

4.1 Challenges

Robust and fluid robotic manipulation demands dynamic, reactive reaching and grasping capabilities. Key objectives include: (1) enabling reliable interception of moving objects [70]; (2) improving grasp success through real-time adaptation to perturbations in object or robot states [20]; and (3) supporting natural human–robot interaction via integrated strategies such as simultaneous reach-and-grasp during dynamic handovers [8]. Achieving these goals hinges on three pillars: reliable mechatronic design, high-bandwidth sensing and control [157], and computationally efficient online re-planning frameworks [3, 17] that allow continuous adaptation to evolving task conditions.

Conventional robotic grasping systems typically adhere to the classic "sense–plan–act" paradigm [13], a framework consistently observed across decades, from early work by [2] to recent studies like [3]. In this paradigm, grasping unfolds in two sequential phases: first, the arm moves to a precomputed grasp pose near the object; second, the fingers close to secure the object. These stages are often executed open-loop using time-parameterized trajectories: sampling-based planners (e.g., [158]) generate collision-free arm motions, followed by interpolated or optimized finger motions, with transitions governed by event-triggered logic. While conceptually simple, this decoupled strategy is brittle under uncertainty. Unforeseen disturbances, whether from object motion, sensor noise, or actuation delays, frequently invalidate the initial plan, leading to grasp failure unless rapid replanning or reactive correction is possible.

Although recent advances in real-time grasp synthesis, such as [66, 67, 159], have enabled end-to-end generation of grasp poses and finger configurations at up to 50 Hz on physical hardware (spanning parallel-jaw grippers to 15-DoF anthropomorphic hands), a critical gap persists: the lack of efficient online motion planning that can track a continuously evolving grasp target in real time.

Fast online reaching planning for arms

Most methods for grasping moving objects assume predictable trajectories, e.g., via learned motion models [5] or dynamical systems (DS) that anticipate interception points [4, 72]. These fail when motion is erratic or perturbed. While Position-Based Visual Servoing (PBVS) [68] offers reactive correction using pose feedback, it often ignores hand geometry, which can lead to finger–object collisions with dexterous hands. Lightweight planning tools (e.g., potential fields, navigation functions, DS controllers) exist but are typically limited to simple end-effectors. A real-time, finger-aware reaching framework for high-DoF hands under unpredictable motion remains absent.

Finger-arm coordination in fluid grasping and reaching

Human reach-and-grasp involves tightly coupled arm and finger coordination [73], enabling fluid adaptation. Although joint control via deep reinforcement learning has been explored [3], practical deployment is hindered by sim-to-real gaps and computational cost. Most real-world systems still employ decoupled strategies, where fingers close only after the arm reaches a trigger condition (time- or distance-based). These lack geometric awareness and frequently collide with fast-moving objects, undermining robustness.

Maximizing grasp success despite sensing uncertainties and execution errors

Dynamic grasping must tolerate sensing noise and actuation errors. Rather than demanding perfect state estimation, systems can exploit geometric constraints, such as the bean-bowl principle [160],

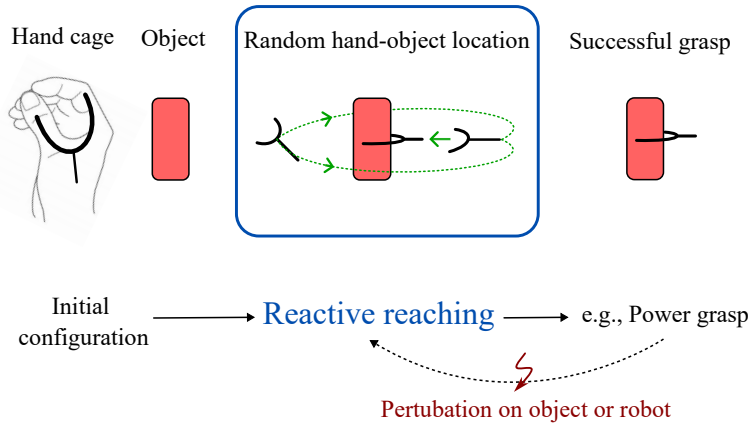


Figure 4.2: Finger Flow: achieving grasp-while-reaching behavior. The fingers form a U-shaped cage (adapted from [162, Fig. 3]) during reaching.

where environment shape passively guides objects into stable poses. Recent work extends this via dynamic caging [161], using evolving hand configurations to topologically constrain object motion without full immobilization. Such strategies significantly enhance grasp reliability under uncertainty but are underutilized in reactive manipulation pipelines.

4.2 Methods and Framework Overview

To address gaps (**a**) and (**b**), we develop methods based on the following three core design ideas.

4.2.1 Core Ideas

Idea 1: Unidirectional object–to-finger-to-arm coordination

Tackling gap (**a**) demands tight coordination between finger and arm motions. Human prehension research shows that finger shaping often initiates before and actively shapes subsequent arm trajectory adjustments during reach [163, 164]. Guided by this insight, finger motion is generated by modulating finger aperture solely based on the distance between the object and a fixed attractor located on the palm. This enables automatic adaptation to varying approach speeds. Concurrently, hand motion planning integrates both the current object state and finger configuration to continuously reshape the reaching path. The result is a unidirectional coordination cascade—object $\rightarrow$ fingers $\rightarrow$ arm—in which the arm naturally adapts to both object dynamics and finger configuration without explicit timing or synchronization logic.

Idea 2: Hand cage — prioritizing robustness over optimality under uncertainty

Drawing from the conceptual framework in [160], a key strategy for addressing (**a**) is to prioritize robust, sub-optimal grasps over globally optimal but fragile ones[1]. The human hand inherently acts

[1] "Fragile grasps" refer to configurations that satisfy static criteria like force closure [23] but are prone to failure in dynamic or uncertain conditions.

as a *hand cage*, suggesting that fingers should be pre-shaped into a semi-enclosing configuration during approach.

From a hand-centric viewpoint, the manipulation task becomes one of guiding the object toward an attractor until it settles within its basin of attraction (see Figure 4.1). As the object nears the attractor, fingers progressively close, enabling a seamless transition from an initial caging posture, such as a U-shaped hand envelope, to a final enveloping grasp (e.g., a power grasp), as depicted in Figure 4.2.

Idea 3: Hand hull — enabling fast, finger-aware collision avoidance

To fulfill requirement (**b**), we introduce a unified, continuous, finger-dependent geometric abstraction termed the *hand hull*. This surrogate model compactly represents the combined shape of the palm and fingers across all configurations, offering a lightweight alternative to detailed mesh-based collision checking. Tailored for high-DoF, multi-fingered hands with complex kinematics, the hand hull supports real-time, collision-aware motion generation and directly enables the coordination scheme outlined in (**Idea 1**).

This chapter focuses on spherical and cylindrical objects. These primitives are selected for two primary reasons:

- They represent a broad class of convex objects that can be accurately approximated by a single spherical or ellipsoidal bounding volume.
- They permit rigorous theoretical analysis of convergence and collision avoidance while retaining analytical tractability.

In Section 4.6.5, we outline a pathway for generalizing the proposed framework to more complex object geometries—a direction left for future investigation.

4.2.2 Overview

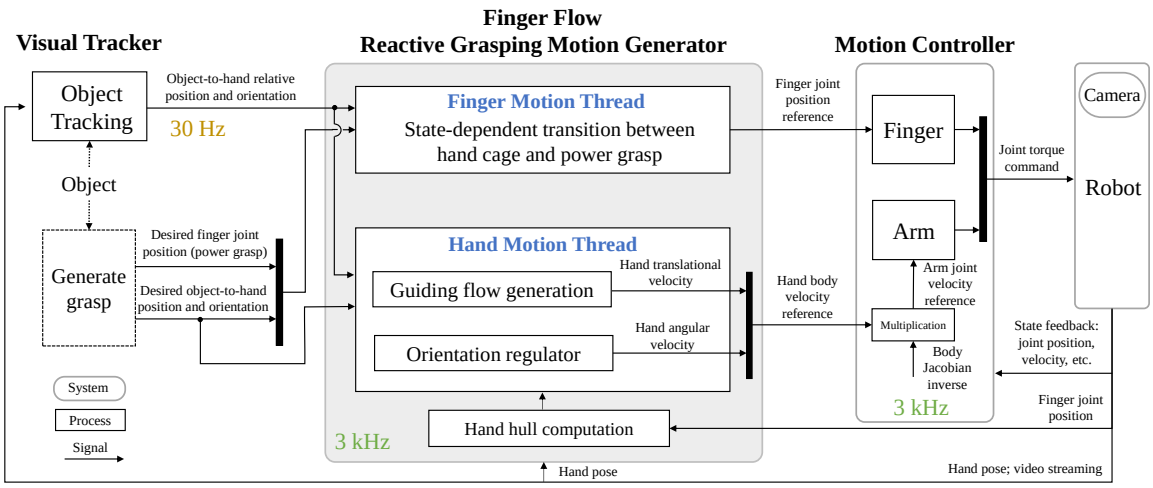


Figure 4.3: The block diagram of Finger Flow (FF) framework, where the middle block is the main contribution. In Motion Controller: [101, 103] are used for arm control, [165] for finger control; In Visual Tracker, [166] is implemented for object pose visual tracking.

Figure 4.3 presents the complete architecture of the proposed system, organized into three principal modules that jointly process real-time feedback from both the robot's proprioceptive sensors and an external vision system.

Visual tracker

A real-time visual object tracker provides continuous estimates of the 6D relative pose (position and orientation) between the target object and the robotic hand at a rate of 30 Hz. This component builds upon the framework described in [166] and serves as the primary perceptual input for downstream motion generation. Accurate and low-latency pose estimation is critical to enabling reactive behavior in dynamic scenarios.

Finger Flow – A reactive motion generator

The core of the proposed approach is implemented through two parallel execution threads:

- The **Hand Motion Thread** computes a collision-aware body velocity command for the end-effector. It integrates real-time measurements of finger joint angles, the current 6D hand pose, and the visually estimated object pose (see Section 4.4 for details). This ensures that the hand trajectory continuously adapts to avoid premature contact between fingers and the object during approach.
- The **Finger Motion Thread** synthesizes adaptive finger trajectories based on the distance between the object and a fixed attractor on the palm, a mechanism grounded in design (**Idea 1**) and elaborated in Section 4.5. The resulting joint position references are forwarded to the low-level finger controller for execution.

Together, these threads realize a unified, reactive reach-and-grasp motion generation that operates without discrete planning phases or explicit state machines.

Motion controller

This module translates high-level motion references into executable torque commands. Specifically, it receives: (i) desired finger joint positions for grasp execution [165], and (ii) a reference body velocity for the arm, derived from the Hand Motion Thread. The latter is converted into joint-space velocity via left-multiplication with the inverse of the body Jacobian. These joint velocities are then processed by an impedance-based arm controller [101, 103], which, alongside the finger controller, outputs joint torque commands dispatched directly to the actuators.

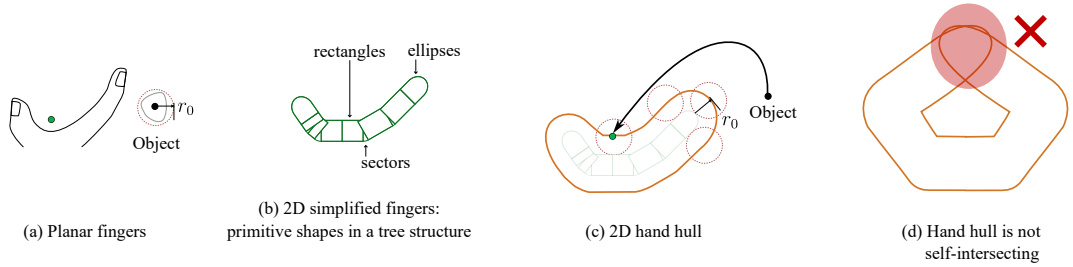
Remark 3. *The grasp synthesis component ("Generate grasp" in the diagram) lies outside the scope of this contribution. Throughout this work, we assume that a target power-grasp configuration, specified as desired finger joint angles, and the corresponding object-to-hand relative pose are provided a priori. For approaches to grasp pose generation, whether model-based [167] or data-driven [112], the reader is directed to the broader literature on grasp planning.*

4.3 Hand Hull: A Simplified Hand Mesh

The objective is to derive a computationally efficient yet geometrically accurate mesh approximation suitable for hand-reaching motion generation, enabling real-time collision avoidance between fingers

and an approaching object. Given that fingers, rigidly attached to the palm, can be represented as primitive shapes arranged in tree-like kinematic structures, a single continuous 3D hull is introduced as a unified obstacle representation. In the subsequent development, the following assumption is adopted regarding the target object:

Assumption 4. *The object is modeled as a sphere with radius r_o.*



(a) Planar fingers

(b) 2D simplified fingers: primitive shapes in a tree structure

(c) 2D hand hull

(d) Hand hull is not self-intersecting

Figure 4.4: Illustration of the 2D hand hull concept. (**a**) Planar fingers and a circular object of radius r_0. (**b**) Fingers approximated by primitive shapes (ellipses, rectangles, and circular sectors). (**c**) The extended hand hull incorporates the object radius r_0, effectively reducing the object to a point. (**d**) The hull remains non-self-intersecting even when fingers cross.

4.3.1 2D Hand Hull

To convey the underlying principle, a planar configuration is considered wherein two fingers are approximated by a single 2D hull.

Approximation of planar fingers through primitive shapes Under Assumption 4, the object is treated as a circle of radius r_0, as shown in Figure 4.4(a). Each finger is decomposed into three categories of primitive geometric elements: ellipses for fingertips, rectangles for finger links and palm segments, and circular sectors for articulation junctions, illustrated in Figure 4.4(b). These primitives are organized into a kinematic tree structure, with their placement and orientation updated based on current joint angles. The dimensions of each segment, specifically width and length, are calibrated to ensure complete coverage of the original hand geometry while minimizing unnecessary voids between the hull and the actual mesh; detailed design criteria are provided in Appendix B.1.

2D Hull: Approximation via an extended hull To simplify collision detection between the object and finger primitives, the problem is reformulated by expanding the finger hull outward by a margin equal to the object radius r_0, as depicted in Figure 4.4(c). Under this transformation, the spherical object is reduced to a point, and collision avoidance is recast as maintaining separation between this point and the expanded hull. This geometric reinterpretation facilitates the construction of a guiding vector field that directs the object toward a designated attractor (indicated by the green dot in Figure 4.4(c)). The formulation of this vector field is detailed in Section 4.4.

4.3.2 3D Hand Hull

While the planar finger model offers a useful simplification, anthropomorphic hands exhibit inherently non-planar kinematics due to multi-finger arrangements and higher degrees of freedom. Nevertheless,

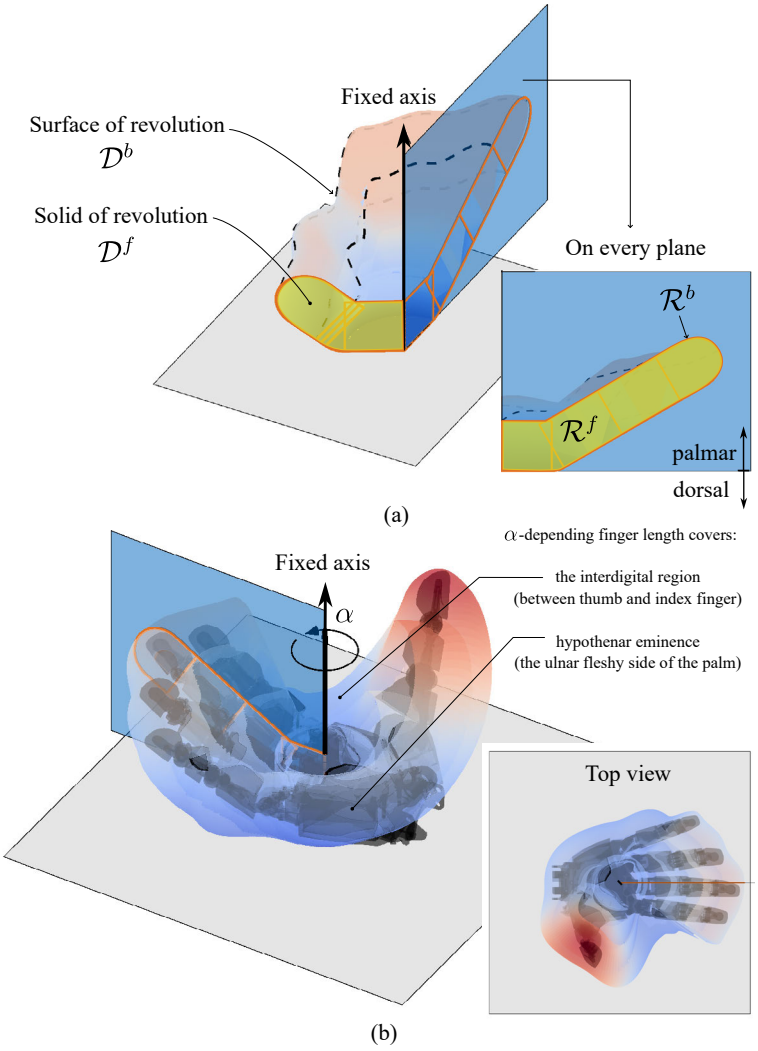


Figure 4.5: (a) The spatial hand hull $\mathcal{D}$ is defined as a surface of revolution generated by rotating a 2D kinematic tree, dependent on a rotation angle, about a fixed hand-aligned axis. Regions interior to and on the hull are annotated. (b) Full 360° revolution of the generatrix, with color encoding height variation along the axis of revolution.

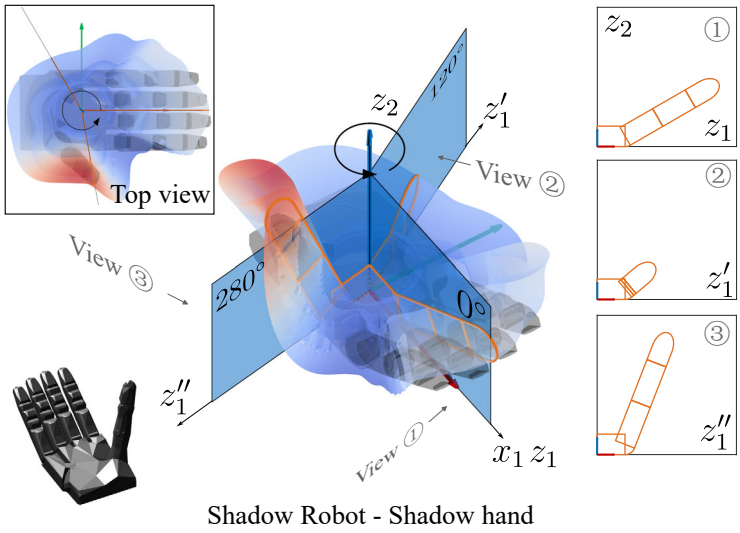


Figure 4.6: Hand hull $\mathcal{D}$ constructed for the Shadow Dexterous Hand, showing three representative rotated planes.

the 2D hull concept can be extended to three dimensions through a surface-of-revolution approach, inspired by axially symmetric geometries such as cones.

Definition 3. *The hand hull $\mathcal{D}$ is defined as a surface of revolution [168], formed by rotating a set of 2D primitive shapes, rectangles, ellipses, and sectors, arranged in a single serial kinematic tree on a half-plane about a hand-fixed axis over the interval $\alpha \in [0, 2\pi)$. The resulting solid of revolution is denoted $\mathcal{D}^f$, and its boundary surface is denoted $\mathcal{D}^b$, consistent with the region classifications in Table B.4.*

This 3D representation consolidates multi-finger kinematic information into a unified tree structure. Each physical finger segment, including the palm, is encoded by the position and orientation of corresponding 2D primitives within the rotating plane. These primitives are parameterized not only by joint configurations but also by the rotation angle α, which identifies the meridional plane intersecting the actual fingers (see Appendix B.1.3 for implementation details). By allowing the lengths of the 2D primitives to vary with α, the hull accurately envelops complex anatomical features such as the hypothenar eminence and interdigital spaces, yielding a continuous 3D volume around the hand axis (further elaborated in Appendix B.1.2).

The formulation is agnostic to specific hand morphologies or kinematic architectures. Consequently, the hull can be adapted to diverse hand types and updated in real time based on joint feedback. An instance of the hull applied to the Shadow Dexterous Hand is shown in Figure 4.6. In certain configurations, such as during a power grasp, the hull may not fully enclose all finger segments, as illustrated in Figure 4.11(d). This behavior is intentional: it prevents self-intersections in the hull geometry (cf. Figure 4.4(d)) and ensures continuity of the guiding motion even as the fingers close around an object.

4.4 Hand Motion Generation

This section presents a guiding flow formulation for generating hand-reaching motions. The reaching-motion generation problem, introduced in Section 4.4.1, is cast as the design of two coupled dy-

namical systems that jointly realize a target pose, specified through grasp synthesis, by coordinating translational and rotational motion. In Section 4.4.2, a semi-tangent flow is proposed to generate object-centric translational motion relative to a given hand hull (see Definition 3). The corresponding hand motion command is then obtained by inverting this flow and augmenting it with an orientation regulator, as described in Section 4.4.3. A formal proof establishing convergence and collision avoidance for static, unperturbed spherical objects is provided in Section 4.4.4. Notably, finger motion during arm reaching is not considered in this formulation; the hand configuration, and thus the hull, is assumed fixed during the approach phase.

4.4.1 Problem Statement

The synthesis of an approaching motion is formulated as the concurrent design of two dynamical systems: one governing translational dynamics and another regulating rotational alignment.

Translational Motion Let $\boldsymbol{x} = (x_1, x_2, x_3) \in \Omega \subset \mathbb{R}^3$ denote the position of the object's geometric center (GC), denoted P, expressed in the hand-fixed frame $\{\mathcal{H}\}$. The domain $\Omega := B(\boldsymbol{x}^\star, c)$ is a bounded ball centered at the desired GC location $\boldsymbol{x}^\star$ (denoted P_d), as prescribed by a grasp planner, with radius $0 < c < \infty$. A first-order autonomous dynamical system is sought to govern the evolution of P:

$$\dot{\boldsymbol{x}} = \boldsymbol{f}_t(\boldsymbol{x}), \tag{4.1}$$

where $\boldsymbol{f}_t \colon \Omega \to \mathbb{R}^3$ satisfies the following objectives:

(O1) **Convergence**: The trajectory $\boldsymbol{x}(t)$ asymptotically approaches the attractor $\boldsymbol{x}^\star$, i.e., $\|\boldsymbol{x}(t) - \boldsymbol{x}^\star\| \to 0$ as $t \to \infty$.

(O2) **Collision-free guiding**: Throughout the motion, the object remains outside the hand hull $\mathcal{D}$ (see Definition 3), ensuring no penetration of the fingers during approach.

Rotational Motion Let ${}^{\mathcal{H}}\boldsymbol{R}_o \in SO(3)$ represent the orientation of the object-fixed frame relative to the hand frame $\{\mathcal{H}\}$. The goal is to define a dynamical system

$$\boldsymbol{\omega} = \boldsymbol{f}_r({}^{\mathcal{H}}\boldsymbol{R}_o), \tag{4.2}$$

where $\boldsymbol{f}_r \colon SO(3) \to \mathbb{R}^3$, such that ${}^{\mathcal{H}}\boldsymbol{R}_o(t) \to {}^{\mathcal{H}}\boldsymbol{R}_{o,d}$ as $t \to \infty$, with ${}^{\mathcal{H}}\boldsymbol{R}_{o,d} \in SO(3)$ specified by the grasp synthesis module. The translational flow field is developed in Section 4.4.2, while the orientation regulation strategy is detailed in Section 4.4.3.

4.4.2 Semi-tangent Flow: An Attractive and Collision-Avoiding Translational Velocity Field for the Object

A semi-tangent flow is introduced to generate a reference translational velocity field for the object, leveraging the hand hull $\mathcal{D}$ as a geometric representation of obstacles. This field guides the object toward the desired location P_d while guaranteeing avoidance of collisions with the fingers. The design integrates a globally attractive linear vector field with a locally reactive tangent component that deflects trajectories along the hull boundary.

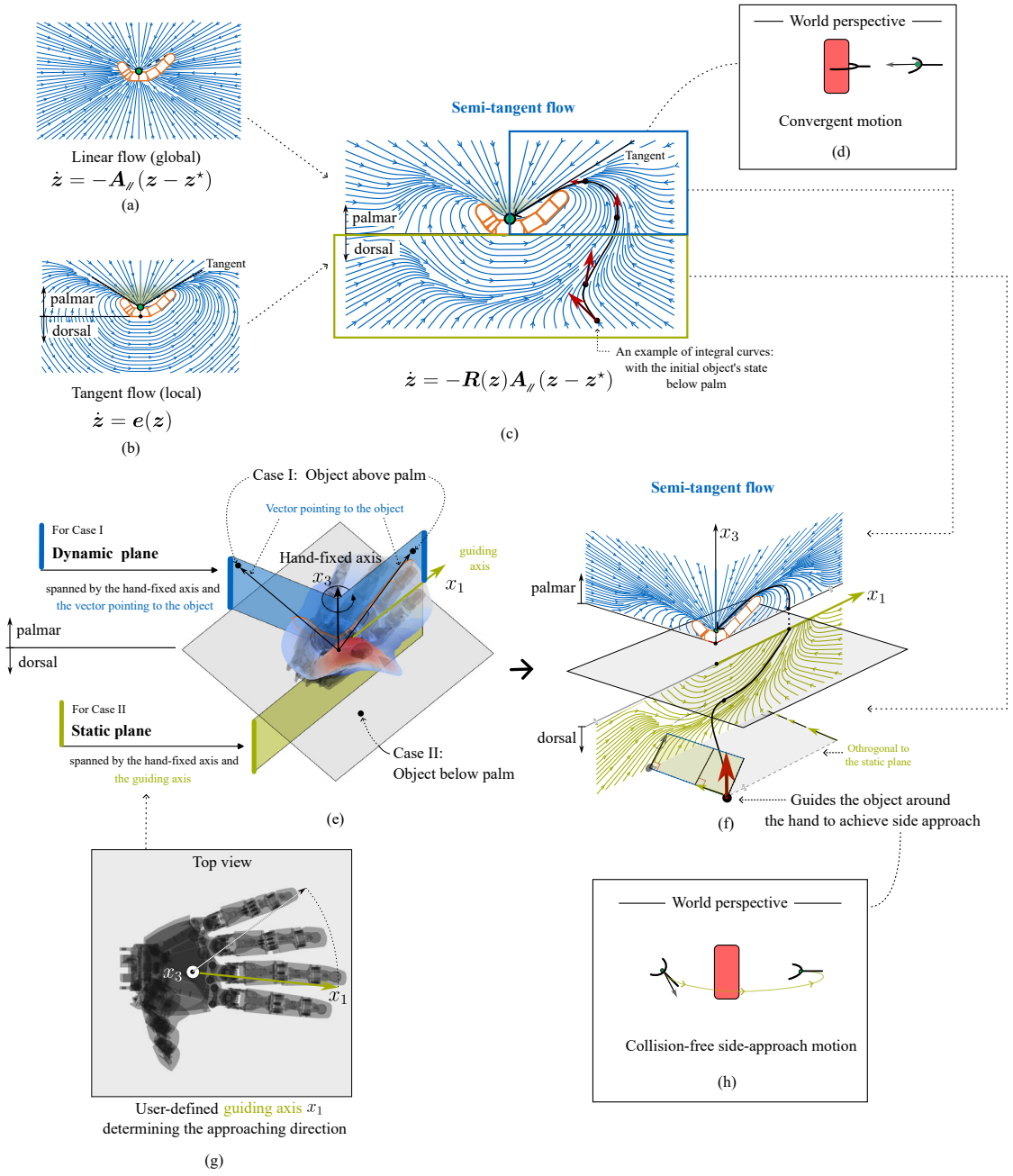


Figure 4.7: Overview of hand translational motion generation. (e) Two types of planes are defined based on the object's position relative to the dorsal plane (light grey), which separates the palmar and dorsal sides of the hand. The dynamic plane is spanned by the hand-fixed axis and a vector from the origin to the object's geometric center, whereas the static plane is fixed to the hand and spanned by the hand-fixed axis and a user-defined guiding axis (g). The semi-tangent flow (c) is constructed within these planes by combining a global linear attractor (a) with a local tangent component (b) that enforces collision avoidance along the hand hull. The spatial realization of the flow is shown in (f). For objects on the palmar side, the dynamic plane yields convergent motion (d). When the object lies below the palm and the static plane does not intersect it consistently, an orthogonal correction drives the object toward the plane, enabling a collision-free side approach (h) from the world frame perspective. The hand motion command is derived by reversing the semi-tangent flow.

Given that the hand hull $\mathcal{D}$ is constructed as a surface of revolution generated by rotating a 2D kinematic tree about a fixed axis, the synthesis of a 3D collision-avoiding flow can be reduced to the design of a 2D flow on each meridional (rotated) plane. This dimensional reduction holds when the object lies above the dorsal plane, as illustrated in Figure 4.7(e).

Guiding axis

When the object is positioned beneath the dorsal plane, a guiding axis must be explicitly defined (see Figure 4.7(g)). This axis encodes a preferred approach direction, enabling user-specified strategies such as lateral or side grasping, as demonstrated in Figure 4.7(h).

Remark 4. *For instance, when reaching toward a cylindrical object resting on a tabletop, a side approach typically yields higher success rates than a top-down motion. Such an approach reduces sensitivity to timing errors in finger closure and enhances robustness to pose estimation uncertainties, properties reminiscent of caging-based grasps.*

Accordingly, the formulation distinguishes between two geometric regimes: objects located on the palmar side (above the dorsal plane) and those on the dorsal side (below it).

Prior to addressing these cases, the hand-fixed coordinate frame $\{\mathcal{H}\}$ is formally defined, as depicted in Figure 4.8(a). The x_1x_2-plane coincides with the dorsal plane. The x_3-axis aligns with the rotational symmetry axis of the hand hull $\mathcal{D}$, oriented such that its positive direction points away from the palm. The origin O is placed at the intersection of the x_3-axis and the dorsal plane. The positive x_1-axis serves as the guiding axis: it lies within the dorsal plane, passes through the origin, and is directed toward the midpoint of the middle fingertip. This axis is user-configurable and reflects the intended approach semantics; an example consistent with a side-grasping strategy is illustrated in Figure 4.2.

Object on palmar side ($x_3 \geq 0$)

When the object is positioned above the palm ($x_3 \geq 0$), motion generation is formulated on a dynamically defined plane that adapts to the object's current location.

Definition 4 (*Dynamic plane*)**.** *Let $\boldsymbol{r}$ denote the vector from the origin O of the hand-fixed frame $\{\mathcal{H}\}$ to the object's center of mass (CoM) position $\boldsymbol{x}$. The plane spanned by $\boldsymbol{r}$ and the x_3-axis is referred to as the* Dynamic Plane *(DP), illustrated as the blue plane in Figure 4.8(a). The angle between the DP and the x_1x_3-plane is denoted by α.*

Remark 5. *The DP is undefined when $\boldsymbol{r}$ is collinear with the x_3-axis, that is, when the object lies directly on the hand-fixed symmetry axis. This degenerate case is explicitly handled in the final dynamical system design.*

Remark 6. *When the spherical object intersects the DP through its geometric center, the intersection yields a circular cross-section of radius r_0. Simultaneously, the DP slices the 3D hand hull $\mathcal{D}$ along the meridional plane corresponding to rotation angle α, reproducing the 2D generatrix used in the hull's construction.*

Within the DP, the object's geometric center is represented in a local 2D coordinate system $\boldsymbol{z} = \mathrm{col}[z_1\ z_2]^\top \in \Omega_z$, where $\Omega_z = B(\boldsymbol{z}^\star, c_z) \subset \mathbb{R}^2$ with $0 < c_z < \infty$. The planar semi-tangent flow is constructed in three sequential stages.

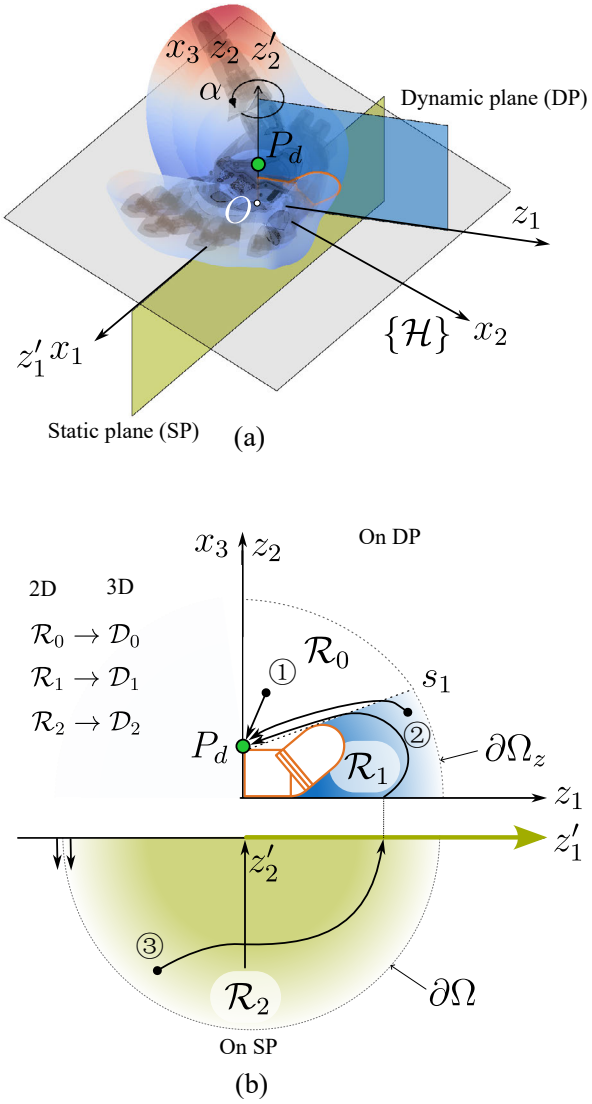


Figure 4.8: (a) Definition of the hand-fixed coordinate system $\{\mathcal{H}\}$ and associated planes. (b) Owing to the rotational symmetry of the hand hull, only half of the dynamic plane (DP) is displayed for clarity. Key regions on the DP include $\mathcal{R}_0$, whose solid of revolution constitutes the interior of the hull $\mathcal{D}_0$, and $\mathcal{R}_1$, representing the exterior region; its solid of revolution is denoted $\mathcal{D}_1$. Sample integral curves are shown for three initial object positions (①, ②, ③).

Stage 1: Global linear attractive flow A globally attractive linear vector field is first defined on the DP:

$$\dot{\boldsymbol{z}} = \boldsymbol{f}_{t,w}(\boldsymbol{z}) = -\boldsymbol{A}_{/\!/}\tilde{\boldsymbol{z}} = -\begin{bmatrix} a_1\tilde{z}_1 \\ a_3\tilde{z}_2 \end{bmatrix}, \tag{4.3}$$

where the tracking error is $\tilde{\boldsymbol{z}} = \boldsymbol{z} - \boldsymbol{z}^\star$, and the attractor P_d is placed on the hand-fixed axis such that $\boldsymbol{z}^\star = \mathrm{col}[0\ z_2^\star]^\top$. The gain matrix

$$\boldsymbol{A}_{/\!/} = \mathrm{diag}(a_1, a_3) \succ 0, \quad \text{with } a_1 \geq a_3, \tag{4.4}$$

ensures that convergence along the z_2-direction (parallel to the symmetry axis) is no faster than along z_1. This property is instrumental in the convergence analysis presented in Lemma 2.

Stage 2: Region partitioning and tangent Flow A critical region $\mathcal{R}_0$ is defined on the DP, as shown in Figure 4.8(b). This region is constructed by rotating a line, initially aligned with the z_2-axis and passing through the attractor P_d, clockwise about P_d until it first contacts the hand hull boundary. The resulting supporting line is denoted s_1 (see (B.32) for its analytic form). The area bounded by the z_2-axis, the line s_1, and the domain boundary $\partial\Omega_z$ (including all edges) constitutes $\mathcal{R}_0$ (see (B.17)). The adjacent exterior region between s_1 and the z_1-axis, lying outside the hull, is denoted $\mathcal{R}_1$, while the region below the palm is labeled $\mathcal{D}_2$ (see Table B.4 for full set definitions). Since potential collisions are confined to $\mathcal{R}_0$ during approach, the linear flow (4.3) is retained unchanged within this region.

In $\mathcal{R}_1$, a *tangent flow* $\boldsymbol{e}(\boldsymbol{z}) \in \mathbb{R}^2$ is introduced (see Figure 4.7(b)). This flow assigns to each point $\boldsymbol{z} \in \mathcal{R}_1$ a unit vector tangent to the hand hull boundary, providing a local direction that avoids penetration. Closed-form expressions for $\boldsymbol{e}(\boldsymbol{z})$ are given in (B.21) and derived in Appendix B.2. The flow is constructed to ensure continuity across the interface s_1, as evidenced by the integral curve originating from initial position ② in Figure 4.8(b); further details are provided in Appendix B.2.3.

Stage 3: Semi-tangent flow construction A composite flow, termed the *semi-tangent flow*, is synthesized to blend the global attraction of $\boldsymbol{f}_{t,w}$ with the local collision-avoidance behavior of $\boldsymbol{e}(\boldsymbol{z})$. This is achieved by locally rotating the linear flow via a state-dependent rotation matrix $\boldsymbol{R}(\gamma(\boldsymbol{z})) \in SO(2)$, where

$$\boldsymbol{R}(\gamma) = \begin{bmatrix} \cos\gamma & -\sin\gamma \\ \sin\gamma & \cos\gamma \end{bmatrix}.$$

The rotation angle $\gamma(\boldsymbol{z}) \in (-\pi, \pi)$ modulates the influence of the tangent direction based on proximity to the hull, yielding the final planar dynamics:

$$\dot{\boldsymbol{z}} = -\boldsymbol{R}^\top(\gamma(\boldsymbol{z}))\boldsymbol{A}_{/\!/}\tilde{\boldsymbol{z}} = -\begin{bmatrix} \cos(\gamma)a_1\tilde{z}_1 + \sin(\gamma)a_3\tilde{z}_2 \\ -\sin(\gamma)a_1\tilde{z}_1 + \cos(\gamma)a_3\tilde{z}_2 \end{bmatrix}, \tag{4.5}$$

where $\gamma(\boldsymbol{z})$ is defined as

$$\gamma(\boldsymbol{z}) = \eta(\Gamma(\boldsymbol{z})) \cdot \gamma_0(\boldsymbol{z}). \tag{4.6}$$

Here, $\Gamma(\boldsymbol{z})$ is a smooth distance function measuring the signed distance from $\boldsymbol{z}$ to the nearest finger segment center (see (B.35) and Figure 4.9(a–b)). The transition function $\eta(\cdot) \in [0, 1]$ is user-configurable and smoothly interpolates between the linear and tangent regimes; an example is provided in (B.34), with implementation details in Appendix B.2.4.

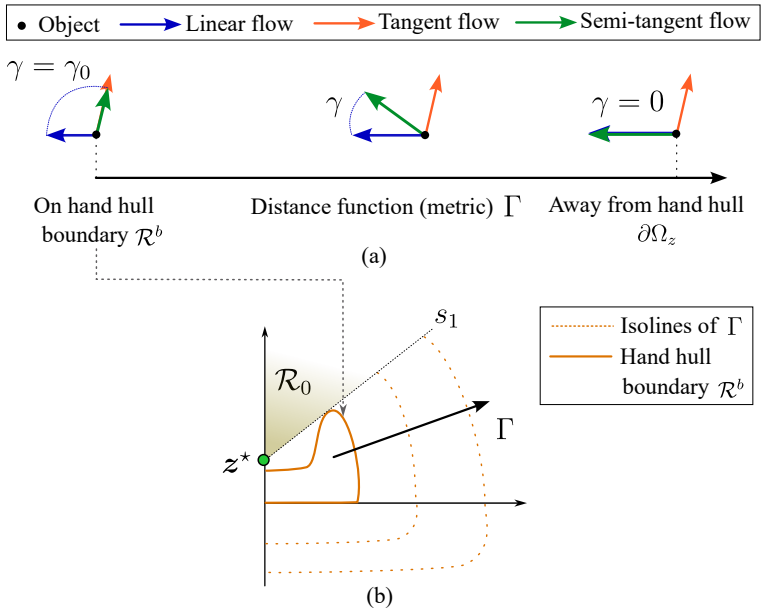


Figure 4.9: (a) Illustration of the modulation angle $\gamma(\Gamma)$, which partially rotates the linear flow toward the tangent direction based on the distance metric Γ. (b) Isolines of the distance function $\Gamma(\boldsymbol{z})$ near the hand hull. Note that Γ is undefined in $\mathcal{R}_0$, as no rotation is applied in this region.

The base rotation angle $\gamma_0(\boldsymbol{z})$ encodes the angular deviation between the linear flow and the tangent direction at $\boldsymbol{z}$:

$$\gamma_0(\boldsymbol{z}) := \operatorname{sgn}\left(\boldsymbol{f}_{t,w}(\boldsymbol{z}) \wedge \boldsymbol{e}(\boldsymbol{z})\right) \arccos\left(\frac{\boldsymbol{f}_{t,w}(\boldsymbol{z})^\top \boldsymbol{e}(\boldsymbol{z})}{\|\boldsymbol{f}_{t,w}(\boldsymbol{z})\|}\right), \tag{4.7}$$

where $\wedge$ denotes the 2D exterior (wedge) product, generalizing the scalar cross product. The denominator is non-zero for all $\boldsymbol{z} \in \mathcal{R}_1$, ensuring well-definedness.

The resulting semi-tangent flow exhibits two key properties:

- On the hull boundary ($\boldsymbol{z} \in \mathcal{R}^b$), the flow aligns with the tangent direction while preserving the magnitude of the linear field: $\dot{\boldsymbol{z}} = \boldsymbol{e}(\boldsymbol{z}) \cdot \|\boldsymbol{f}_{t,w}(\boldsymbol{z})\|$, with $\gamma(\boldsymbol{z}) = \gamma_0(\boldsymbol{z})$ (see left panel of Figure 4.9(a)).
- Far from the hull ($\boldsymbol{z} \to \partial\Omega_z$), the flow reverts to the pure linear attractor, i.e., $\gamma(\boldsymbol{z}) \to 0$ (see right panel of Figure 4.9(a)).

The complete planar dynamical system for the palmar side is thus defined as a piecewise-smooth map $\boldsymbol{g} : \Omega_z \to \mathbb{R}^2$:

$$\dot{\boldsymbol{z}} = \boldsymbol{g}(\boldsymbol{z}) = \begin{cases} \boldsymbol{f}_{t,w}(\boldsymbol{z}) & \text{if } \boldsymbol{z} \in \mathcal{R}_0, \\ -\boldsymbol{R}^\top(\gamma(\boldsymbol{z}))\boldsymbol{A}_{/\!/}\tilde{\boldsymbol{z}} & \text{if } \boldsymbol{z} \in \mathcal{R}_1. \end{cases} \tag{4.8}$$

Remark 7. *By construction, the tangent flow $\boldsymbol{e}(\boldsymbol{z})$ aligns with the linear flow $\boldsymbol{f}_{t,w}(\boldsymbol{z})$ along the interface s_1. Consequently, $\gamma_0(\boldsymbol{z}) = 0$ on s_1, and the two expressions in* (4.8) *coincide. This ensures continuity of the vector field over $\mathcal{R}_0 \cup \mathcal{R}_1$.*

Object on dorsal side ($x_3 < 0$)

When the object lies below the dorsal plane ($x_3 < 0$), motion generation is defined relative to a fixed reference plane tied to the hand's geometry.

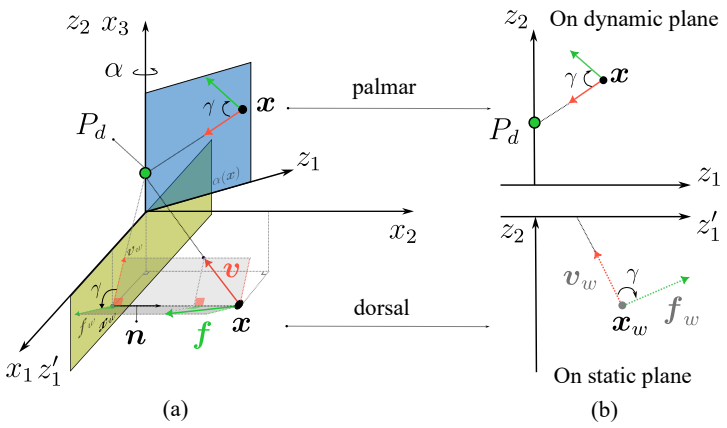


Figure 4.10: Geometric interpretation of the 3D semi-tangent flow: the global linear velocity $\boldsymbol{v}$ is rotated about the normal vector $\boldsymbol{n}(\boldsymbol{x})$ of the dynamic or static plane by angle γ.

Definition 5 (*Static Plane*)**.** *The hand-fixed* Static Plane *(SP) is defined as the plane spanned by the x_1- and x_3-axes, illustrated as the green plane in Figure 4.8(a).*

A globally attractive linear dynamical system is first prescribed in the full 3D space:

$$\dot{\boldsymbol{x}} = -\boldsymbol{A}\tilde{\boldsymbol{x}}, \quad \tilde{\boldsymbol{x}} = \boldsymbol{x} - \boldsymbol{x}^\star, \tag{4.9}$$

where the attractor $\boldsymbol{x}^\star = (0, 0, x_3^\star)$ corresponds to the spatial embedding of the planar target $\boldsymbol{z}^\star = (0, z_2^\star)$ from (4.3), with $x_3^\star = z_2^\star$. The gain matrix is chosen as

$$\boldsymbol{A} = \mathrm{diag}(a_1, a_1, a_3) \succ 0, \tag{4.10}$$

ensuring isotropic attraction in the x_1–x_2 plane and potentially slower convergence along the symmetry axis x_3.

For objects not lying within the static plane, the velocity field is modified only in the component parallel to the SP (x_1x_3-plane). The orthogonal component—along the x_2-axis—remains governed by the original linear dynamics. Specifically, the in-plane velocity vector $(\dot{x}_1, \dot{x}_3)^\top$ is rotated by an angle $\gamma(x_1, x_3)$, constructed analogously to the palmar case via (4.6), with the mapping $z_1 = x_1$ and $z_2 = x_3$. This rotation preserves the magnitude of the in-plane flow while redirecting it to avoid the hand hull.

The resulting 3D semi-tangent flow $\boldsymbol{f} : \Omega \to \mathbb{R}^3$ is given by

$$\dot{\boldsymbol{x}} = -\begin{bmatrix} \cos(\gamma)a_1\tilde{x}_1 + \sin(\gamma)a_3\tilde{x}_3 \\ a_1\tilde{x}_2 \\ -\sin(\gamma)a_1\tilde{x}_1 + \cos(\gamma)a_3\tilde{x}_3 \end{bmatrix} = -\boldsymbol{R}_{\boldsymbol{n}}(\gamma)\boldsymbol{A}\tilde{\boldsymbol{x}}, \tag{4.11}$$

where $\boldsymbol{R}_{\boldsymbol{n}}(\gamma)$ denotes the rotation matrix about the normal vector $\boldsymbol{n}$ of the static plane. The normal is

$$\boldsymbol{n} = \mathrm{col}[0\ 1\ 0]^\top, \tag{4.12}$$

and the rotation is computed using Rodrigues' formula:

$$\boldsymbol{R}_{\boldsymbol{n}}(\gamma) = \boldsymbol{I}_{3\times 3} + \sin\gamma\,[\boldsymbol{n}]_\times + (1 - \cos\gamma)\,[\boldsymbol{n}]_\times^2, \tag{4.13}$$

with the skew-symmetric operator

$$[\boldsymbol{n}]_\times = \begin{bmatrix} 0 & -n_3 & n_2 \\ n_3 & 0 & -n_1 \\ -n_2 & n_1 & 0 \end{bmatrix}.$$

Geometrically, this operation rotates the linear velocity vector $\boldsymbol{v} = -\boldsymbol{A}\tilde{\boldsymbol{x}}$ (shown in red in Figure 4.10) about the SP normal $\boldsymbol{n}$ (black arrow) to produce the semi-tangent flow $\boldsymbol{f}$ (light green), as visualized in Figure 4.10. Notably, when the object is initialized below the dorsal plane ($x_3 < 0$), the integral curves of this vector field drive it toward the plane $x_3 = 0$, after which the motion transitions into the palmar regime. This behavior is illustrated in Figure 4.7(f).

Figure 4.11 presents the full spatial realization of the semi-tangent flow for two representative hand configurations: open (a–c) and closed (d–f). The left and right columns show the hand hull $\mathcal{D}$ overlaid with dynamic planes (blue, labeled by rotation angle α) and the static plane (green). Streamlines depict the integral curves of the designed vector field on each respective plane, demonstrating consistent collision-free guidance across diverse postures.

4.4.3 Guiding flow for the hand

This section presents the complete dynamical systems that realize the objectives stated in (4.1) and (4.2), culminating in a velocity reference for hand motion generation.

For objects located on the palmar side ($x_3 \geq 0$), the mapping from the 3D hand-fixed coordinates $\boldsymbol{x}$ to the 2D dynamic plane coordinates $\boldsymbol{z}$ is defined as

$$\boldsymbol{z} = \begin{bmatrix} z_1 \\ z_2 \end{bmatrix} = \underbrace{\begin{bmatrix} \cos\alpha & \sin\alpha & 0 \\ 0 & 0 & 1 \end{bmatrix}}_{\boldsymbol{N}} \boldsymbol{x}, \tag{4.14}$$

where the rotation angle α is computed as

$$\alpha = \operatorname{mod}\big(\operatorname{atan2}(x_2, x_1), 2\pi\big),$$

with $\operatorname{atan2}(y, x) \in [-\pi, \pi)$ denoting the four-quadrant arctangent and $\operatorname{mod}(\cdot, 2\pi)$ ensuring $\alpha \in [0, 2\pi)$. This mapping is valid for all $\boldsymbol{x} \in \mathcal{D}_1 \cup \mathcal{D}_0 \setminus \mathcal{D}_a$, where the set

$$\mathcal{D}_a = \{\boldsymbol{x} \in \Omega \mid x_1 = 0,\, x_2 = 0,\, x_3 \geq x_3^\star\} \tag{4.15}$$

excludes configurations where the object lies on the hand-fixed symmetry axis above the attractor—precisely the degenerate case in which the dynamic plane is undefined (see Remark 5).

Since the object remains confined to its associated dynamic plane during motion on the palmar side, the angular coordinate α is constant along trajectories, i.e., $\dot{\alpha} = 0$. Furthermore, the matrix $\boldsymbol{N}$ satisfies $\boldsymbol{N}\boldsymbol{N}^\top = \boldsymbol{I}_{2\times 2}$. Differentiating (4.14) with respect to time and substituting the planar dynamics from (4.3) and (4.5) yields the 3D representation of the palmar-side flow:

$$\dot{\boldsymbol{x}} = -\underbrace{\boldsymbol{N}^\top \boldsymbol{R}^\top(\gamma(\boldsymbol{N}\boldsymbol{x}))\boldsymbol{A}_{/\!/}\boldsymbol{N}}_{\boldsymbol{S}(\boldsymbol{x})}\tilde{\boldsymbol{x}}. \tag{4.16}$$

Consequently, the full 3D dynamical system for the palmar regime is expressed as

$$\dot{\boldsymbol{x}} = \begin{cases} -\operatorname{col}\big[0,\ 0,\ a_3(x_3 - x_3^\star)\big]^\top & \text{if } \boldsymbol{x} \in \mathcal{D}_a, \\ -\boldsymbol{S}(\boldsymbol{x})\tilde{\boldsymbol{x}} & \text{if } \boldsymbol{x} \in \mathcal{D}_0 \cup \mathcal{D}_1 \setminus \mathcal{D}_a. \end{cases} \tag{4.17}$$

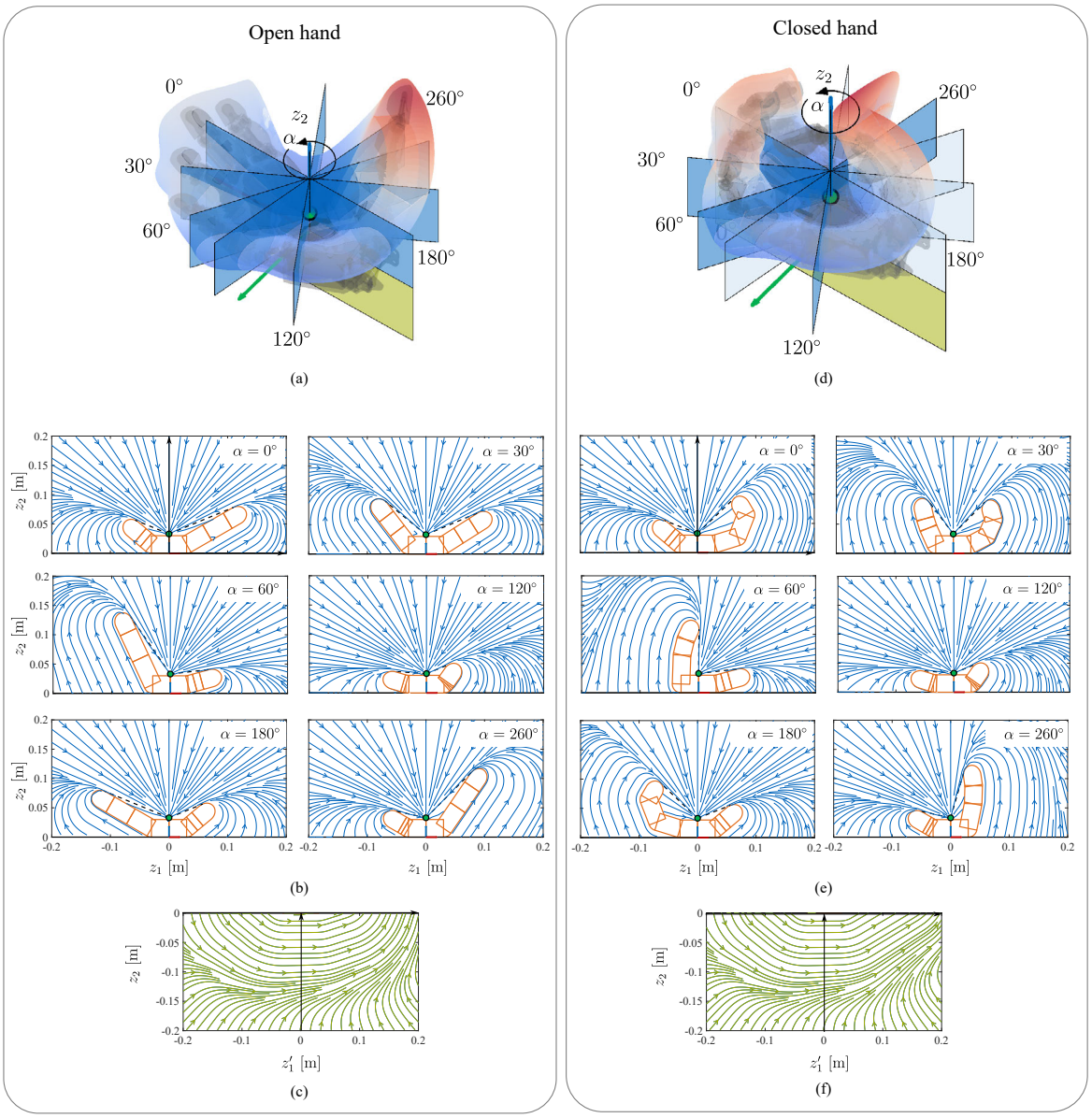


Figure 4.11: Semi-tangent flow visualized for two finger configurations: open hand (a–c) and closed hand (d–f). The left column (a–c) and right column (d–f) display the hand hull $\mathcal{D}$ with dynamic planes (blue, annotated with rotation angle α) and the static plane (green). Streamlines represent integral curves of the vector field on each plane.

Combining this with the dorsal-side dynamics from (4.11) leads to a unified definition of the semi-tangent flow over the entire domain Ω:

Definition 6 (*Semi-Tangent Flow*)**.** *The semi-tangent flow $\boldsymbol{f}_t : \Omega \to \mathbb{R}^3$, governing the evolution of the object's geometric center $\boldsymbol{x}$, is defined as*

$$\dot{\boldsymbol{x}} = \boldsymbol{f}_t(\boldsymbol{x}) = \begin{cases} -\boldsymbol{A}\tilde{\boldsymbol{x}} & \text{if } \boldsymbol{x} \in \mathcal{D}_a, \\ -\boldsymbol{S}(\boldsymbol{x})\tilde{\boldsymbol{x}} & \text{if } \boldsymbol{x} \in \mathcal{D}_0 \cup \mathcal{D}_1 \setminus \mathcal{D}_a, \\ -\boldsymbol{R}_{\boldsymbol{n}}(\gamma(\boldsymbol{x}))\boldsymbol{A}\tilde{\boldsymbol{x}} & \text{otherwise}, \end{cases} \tag{4.18}$$

where: $\boldsymbol{A} = \mathrm{diag}(a_1, a_1, a_3) \succ 0$ is given in (4.10)*, $\boldsymbol{S}(\boldsymbol{x})$ is defined in* (4.16)*, $\boldsymbol{R}_{\boldsymbol{n}}(\cdot)$ is the rotation matrix from Rodrigues' formula* (4.13)*, $\boldsymbol{n} = [0\ 1\ 0]^\top$ is the normal to the static plane* (4.12)*, $\gamma(\boldsymbol{x})$ is the modulation angle from* (4.6)*.*

Velocity reversal

The semi-tangent flow $\boldsymbol{f}_t(\boldsymbol{x})$ prescribes a desired velocity for the object under the assumption that the hand remains stationary. To generate a corresponding motion command for the hand, the object's reference velocity is reversed:

$$\boldsymbol{v}_r = -\boldsymbol{f}_t(\boldsymbol{x}). \tag{4.19}$$

This reversal yields a translational velocity reference that drives the hand toward the object while respecting collision constraints encoded in the hand hull.

Orientation regulator

To ensure rapid alignment of the hand's orientation with the desired grasp pose, an orientation regulator is designed to converge significantly faster than the translational dynamics. This fast rotational response is physically realizable through low-inertia actuation modes (e.g., forearm or wrist rotation) and ensures that the assumption of a circular cross-section remains valid not only for spherical objects but also for cylindrical ones when viewed along the approach direction.

Following the potential-field approach in [169, 170], the desired angular velocity is defined as

$$\boldsymbol{\omega}_r = \mathrm{asym}\left({}^{\mathcal{H}}\boldsymbol{R}_{o,d}\boldsymbol{G}\right), \tag{4.20}$$

where $\mathrm{asym}(\boldsymbol{M}) = \frac{1}{2}(\boldsymbol{M} - \boldsymbol{M}^\top)$ extracts the skew-symmetric part of a matrix, and the co-stiffness matrix is

$$\boldsymbol{G} = \tfrac{1}{2}\,\mathrm{tr}(\boldsymbol{K})\boldsymbol{I} - \boldsymbol{K}, \quad \boldsymbol{K} = \mathrm{diag}(k_1, k_2, k_3) \succ 0.$$

The desired orientation ${}^{\mathcal{H}}\boldsymbol{R}_{o,d} \in SO(3)$ is obtained via hand-eye calibration from the grasp generator and real-time object pose estimates (see footnote in original text for transformation details). Stacking the translational and rotational components yields the full body-frame velocity reference for the hand:

$$\boldsymbol{\chi}_r = \begin{bmatrix} \boldsymbol{v}_r \\ \boldsymbol{\omega}_r \end{bmatrix}. \tag{4.21}$$

In scenarios where the object exhibits measurable motion, denoted by its body velocity $\boldsymbol{\chi}_o$, the hand reference is augmented to maintain relative pose consistency:

$$\boldsymbol{\chi}_{\text{hand}} = \boldsymbol{\chi}_r + \boldsymbol{\chi}_o.$$

Here, $\boldsymbol{\chi}_r$ generates the attractive, collision-free reaching motion, while $\boldsymbol{\chi}_o$ synchronizes the hand with the object's motion induced by external dynamics.

Remark 8. *In practice, accurate estimation of $\boldsymbol{\chi}_o$ is challenging due to limited sensor refresh rates and noise in numerical differentiation of pose measurements, particularly in dynamic interaction scenarios such as human-to-robot handovers, tethered objects, or unpredictable disturbances. For the experimental validation presented in this work, the object is assumed stationary, i.e., $\boldsymbol{\chi}_o = \mathbf{0}$, and $\boldsymbol{\chi}_r$ from* (4.21) *is used as the final motion reference.*

A summary of the overall flow computation is provided in pseudocode form in Algorithm 1.

Joint velocity reference

The body-frame velocity reference $\boldsymbol{\chi}_r$ is mapped to joint-space via the hand's body Jacobian $\boldsymbol{J} \in \mathbb{R}^{6\times n}$ (expressed relative to frame $\{\mathcal{H}\}$) to yield the arm joint velocity command:

$$\dot{\boldsymbol{q}}_{a,r} = \boldsymbol{J}^{\#}\boldsymbol{\chi}_r + (\boldsymbol{I} - \boldsymbol{J}^{\#}\boldsymbol{J})\,\dot{\boldsymbol{q}}_{\text{null}}, \tag{4.22}$$

where $\boldsymbol{J}^{\#} = \boldsymbol{J}^{\top}(\boldsymbol{J}\boldsymbol{J}^{\top})^{-1}$ denotes the right Moore–Penrose pseudoinverse, and $\dot{\boldsymbol{q}}_{\text{null}} \in \mathbb{R}^n$ represents a nullspace velocity component. The design of nullspace behaviors is outside the scope of this work and is assumed to be either zero or governed by secondary tasks.

Algorithm 1 Hand Motion Generation via Semi-Tangent Flow

Input: Current object pose in the hand-fixed frame $({}^{\mathcal{H}}\boldsymbol{R}_O, \boldsymbol{x})$, desired grasp pose $({}^{\mathcal{H}}\boldsymbol{R}_{O,d}, \boldsymbol{x}^\star)$, and current finger joint configuration $\boldsymbol{q}_f$.
Output: Body-frame velocity reference for the hand, $\boldsymbol{\chi}_r = [\boldsymbol{v}_r^\top\ \boldsymbol{\omega}_r^\top]^\top$.

while A stable grasp has not been confirmed. **do**
  $\mathcal{D} \leftarrow$ Update hand hull using $\boldsymbol{q}_f$ ▷ See Definition 3
  $\boldsymbol{f}_t \leftarrow -\boldsymbol{A}(\boldsymbol{x} - \boldsymbol{x}^\star)$ ▷ Initialize global linear field, (4.9)
  if $\boldsymbol{x} \in \mathcal{D}_0 \cup \mathcal{D}_1 \setminus \mathcal{D}_a$ **then**
    $\boldsymbol{z} \leftarrow \boldsymbol{N}\boldsymbol{x}$ ▷ Map to dynamic plane, (4.14)
    $\boldsymbol{e} \leftarrow$ Tangent flow at $\boldsymbol{z}$ ▷ (B.21)
    $\gamma \leftarrow \eta(\Gamma(\boldsymbol{z})) \cdot \gamma_0(\boldsymbol{z})$ ▷ Modulation angle, (4.6)
    $\boldsymbol{f}_t \leftarrow -\boldsymbol{S}(\boldsymbol{x})(\boldsymbol{x} - \boldsymbol{x}^\star)$ ▷ Palmar semi-tangent flow, (4.16)
  else if $\boldsymbol{x} \in \mathcal{D}_a$ **then**
    $\boldsymbol{f}_t \leftarrow -\boldsymbol{A}(\boldsymbol{x} - \boldsymbol{x}^\star)$ ▷ Axial linear flow
  else
    $\boldsymbol{f}_t \leftarrow -\boldsymbol{R}_{\boldsymbol{n}}(\gamma(\boldsymbol{x}))\boldsymbol{A}(\boldsymbol{x} - \boldsymbol{x}^\star)$ ▷ Dorsal semi-tangent flow, (4.11)
  end if
  $\boldsymbol{v}_r \leftarrow -\boldsymbol{f}_t$ ▷ Velocity reversal, (4.19)
  $\boldsymbol{\omega}_r \leftarrow \operatorname{asym}\left({}^{\mathcal{H}}\boldsymbol{R}_{O,d}\boldsymbol{G}\right)$ ▷ Orientation regulator, (4.20)
  $\boldsymbol{\chi}_r \leftarrow [\boldsymbol{v}_r^\top\ \boldsymbol{\omega}_r^\top]^\top$ ▷ Compose body velocity, (4.21)
end while

4.4.4 Convergence and Collision Avoidance

The dynamical systems defined in (4.8) and (4.11) are shown to satisfy the objectives (O1) convergence and (O2) collision avoidance stated in Section 4.4.1. The analysis is restricted to translational dynamics, as rotational regulation is decoupled and assumed to operate on a faster timescale.

Uniqueness of integral curves

Lemma 1. *Consider the autonomous dynamical systems governed by* (4.8) *and* (4.11)*. For any bounded initial condition* $\boldsymbol{x}(0) \in \Omega$ *(or* $\boldsymbol{z}(0) \in \Omega_z$*), there exists a unique integral curve* $\boldsymbol{x}(t)$ *(respectively,* $\boldsymbol{z}(t)$*).*

Proof. The proof follows the framework established in [131, pp. 388] and proceeds in two steps: (1) establishing Lipschitz continuity of the vector fields, and (2) verifying uniqueness of solutions across switching surfaces in the sense of Filippov [131, 135, 136].

Step 1: Lipschitz continuity Consider two states $\boldsymbol{x}, \boldsymbol{x}'$ belonging to the same region of the domain partition (e.g., both in $\mathcal{D}_2$). It suffices to show that the vector field $\boldsymbol{f}$ satisfies

$$\|\boldsymbol{f}(\boldsymbol{x}) - \boldsymbol{f}(\boldsymbol{x}')\| \leq L\|\boldsymbol{x} - \boldsymbol{x}'\| \tag{4.23}$$

for some finite constant $L > 0$.

For the dorsal-side flow (4.11), the difference between vector field evaluations is

$$\|\boldsymbol{f}(\boldsymbol{x}) - \boldsymbol{f}(\boldsymbol{x}')\| = \|\boldsymbol{R_n}(\gamma(\boldsymbol{x}))\boldsymbol{A}\tilde{\boldsymbol{x}} - \boldsymbol{R_n}(\gamma(\boldsymbol{x}'))\boldsymbol{A}\tilde{\boldsymbol{x}}'\|. \tag{4.24}$$

Applying the triangle inequality yields

$$\begin{aligned}\|\boldsymbol{f}(\boldsymbol{x}) - \boldsymbol{f}(\boldsymbol{x}')\| \leq \|[\boldsymbol{R_n}(\gamma(\boldsymbol{x})) - \boldsymbol{R_n}(\gamma(\boldsymbol{x}'))]\boldsymbol{A}\tilde{\boldsymbol{x}}\| \\ + \|\boldsymbol{R_n}(\gamma(\boldsymbol{x}'))\boldsymbol{A}(\boldsymbol{x} - \boldsymbol{x}')\|.\end{aligned} \tag{4.25}$$

The modulation angle $\gamma(\boldsymbol{x})$, defined in (4.6), is Lipschitz continuous; this is established in Appendix B.2.5. Thus, there exists $L_\gamma > 0$ such that

$$|\gamma(\boldsymbol{x}) - \gamma(\boldsymbol{x}')| \leq L_\gamma\|\boldsymbol{x} - \boldsymbol{x}'\|. \tag{4.26}$$

By the mean value theorem for matrix-valued functions [171, Theorem 5.9] and the smooth dependence of $\boldsymbol{R_n}(\gamma)$ on γ via trigonometric terms in Rodrigues' formula (4.13), there exists $L_R > 0$ satisfying

$$\|\boldsymbol{R_n}(\gamma(\boldsymbol{x})) - \boldsymbol{R_n}(\gamma(\boldsymbol{x}'))\| \leq L_R|\gamma(\boldsymbol{x}) - \gamma(\boldsymbol{x}')|. \tag{4.27}$$

Since $\boldsymbol{x} \in \Omega = B(\boldsymbol{x}^\star, c)$, the tracking error is bounded: $\|\tilde{\boldsymbol{x}}\| \leq c < \infty$, and thus $\|\boldsymbol{A}\tilde{\boldsymbol{x}}\| \leq c\|\boldsymbol{A}\|$. Combining these bounds,

$$\|[\boldsymbol{R_n}(\gamma(\boldsymbol{x})) - \boldsymbol{R_n}(\gamma(\boldsymbol{x}'))]\boldsymbol{A}\tilde{\boldsymbol{x}}\| \leq 2cL_\gamma L_R\|\boldsymbol{A}\|\|\boldsymbol{x} - \boldsymbol{x}'\|. \tag{4.28}$$

For the second term in (4.25), the orthogonality of rotation matrices implies

$$\|\boldsymbol{R_n}(\gamma(\boldsymbol{x}'))\boldsymbol{A}(\boldsymbol{x} - \boldsymbol{x}')\| \leq \|\boldsymbol{A}\|\|\boldsymbol{x} - \boldsymbol{x}'\|. \tag{4.29}$$

Substituting (4.28) and (4.29) into (4.25) establishes (4.23) with Lipschitz constant

$$L = (2cL_\gamma L_R + 1)\|\boldsymbol{A}\| = (2cL_\gamma L_R + 1)a_1, \tag{4.30}$$

since $\|\boldsymbol{A}\| = a_1$ for $\boldsymbol{A} = \mathrm{diag}(a_1, a_1, a_3)$ with $a_1 \geq a_3 > 0$.

An analogous argument applies to the planar vector field $\boldsymbol{g}(\boldsymbol{z})$ in (4.8) over $\mathcal{R}_0 \cup \mathcal{R}_1$, confirming its Lipschitz continuity.

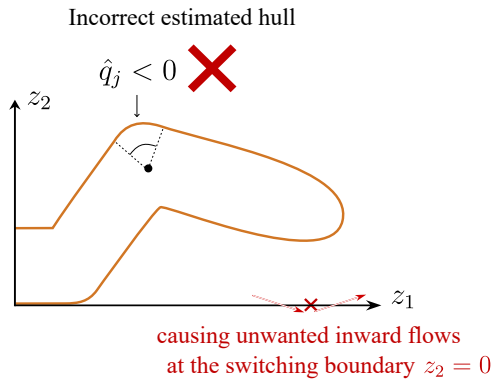


Figure 4.12: When the estimated configuration of the finger joint is smaller than the lower bound, this may create a tangent flow that crosses the switching boundary $z_2 = 0$ from the palmar side to the dorsal side.

Step 2: Uniqueness across switching surfaces Consider an initial state $\boldsymbol{x}(0) \in \mathcal{D}_2$ (i.e., below the palm). The hand hull construction assumes a lower-bounded finger joint configuration ($\hat{q}_j > q_{\text{min}}$), as detailed in Appendix B.1.3 and illustrated in Figure 4.12. This ensures that the hull does not degenerate and that no spurious outward or inward flows arise near the switching plane $x_3 = 0$.

To verify solution uniqueness in the Filippov sense, the consistency of the flow across the interface $x_3 = 0$ is examined. Let $\boldsymbol{n}_{x_3} = [0\ 0\ 1]^\top$ denote the normal to the switching plane. The inner products of the velocity field with this normal satisfy:

$$\dot{\boldsymbol{x}}^\top \boldsymbol{n}_{x_3} > 0 \quad \text{as } x_3 \to 0^- \quad \text{(dorsal side)},$$

$$\dot{\boldsymbol{z}}^\top \boldsymbol{n}_{z_2} > 0 \quad \text{as } z_2 \to 0^+ \quad \text{(palmar side, with } \boldsymbol{n}_{z_2} = [0\ 1]^\top).$$

Thus, the vector field points strictly from the dorsal to the palmar side across $x_3 = 0$, and no sliding mode or ambiguity arises. This directional consistency guarantees a unique Filippov solution through the switching surface.

Combining Lipschitz continuity within regions and uniqueness across boundaries concludes the proof. □

Proof of objective (O1): Convergence to the attractor

The convergence of trajectories to the desired attractor P_d (i.e., $\boldsymbol{x}^\star$ or $\boldsymbol{z}^\star$) is established through the following auxiliary result and main theorem.

Lemma 2. *The region $\mathcal{R}_0$ is an invariant set under the dynamics defined in* (4.8).

Proof. See Appendix B.3.1. □

Theorem 1. *Consider the autonomous dynamical systems defined by* (4.8) *and* (4.11). *For any initial condition $\boldsymbol{x}(0) \in \Omega$, the corresponding trajectory $\boldsymbol{x}(t)$ converges to the attractor $\boldsymbol{x}^\star$ as $t \to \infty$.*

Proof. The proof proceeds by partitioning the domain Ω into three disjoint cases based on the initial object position, as illustrated in Figure 4.8(b):

(C1) $\boldsymbol{z}(0) \in \mathcal{R}_0$ (e.g., ①),

(C2) $\boldsymbol{z}(0) \in \mathcal{R}_1$ (e.g., ②),

(C3) $\boldsymbol{x}(0) \in \mathcal{D}_2 = \{\boldsymbol{x} \in \Omega \mid x_3 < 0\}$ (e.g., ③).

It is shown that all trajectories eventually enter the invariant set $\mathcal{R}_0$ and subsequently converge exponentially to $\boldsymbol{z}^\star$. The regions are traversed in a fixed sequence: $\mathcal{D}_2 \to \mathcal{R}_1 \to \mathcal{R}_0$, ensuring global convergence.

Case (C1): Initial state in $\mathcal{R}_0$. Within $\mathcal{R}_0$, the dynamics reduce to the linear system (4.3):

$$\dot{\boldsymbol{z}} = -\boldsymbol{A}_{/\!/}(\boldsymbol{z} - \boldsymbol{z}^\star),$$

where $\boldsymbol{A}_{/\!/} = \mathrm{diag}(a_1, a_3) \succ 0$ with $a_1 \geq a_3$. Since $-\boldsymbol{A}_{/\!/}$ is Hurwitz, the origin of the error dynamics is exponentially stable. Consequently, $\boldsymbol{z}(t) \to \boldsymbol{z}^\star$ as $t \to \infty$.

Moreover, by Lemma 2, $\mathcal{R}_0$ is invariant. This invariance is guaranteed by the design choice $a_1 \geq a_3$, which ensures that convergence along the z_1-direction is at least as fast as along z_2, preventing trajectories from exiting $\mathcal{R}_0$ through the boundary s_1.

Case (C2): Initial state in $\mathcal{R}_1$. Three properties ensure finite-time convergence to $\mathcal{R}_0$:

- No crossing of the switching plane $x_3 = 0$: The lower-bounded finger joint configuration ($\hat{q}_j > q_{\min}$, see Appendix B.1.3 and Figure 4.12) ensures that the hand hull remains well-defined and that the vector field (4.5) does not drive the object across $x_3 = 0$.
- Attraction toward the interface s_1: The tangent flow $\boldsymbol{e}(\boldsymbol{z})$ (defined in (B.21) and detailed in Appendix B.2) is constructed such that trajectories in $\mathcal{R}_1$ are guided toward the boundary s_1.
- Uniform lower bound on velocity magnitude: The norm of the semi-tangent flow satisfies

  $$\left\| \boldsymbol{R}(\gamma(\boldsymbol{z}))\boldsymbol{A}_{/\!/}(\boldsymbol{z} - \boldsymbol{z}^\star) \right\| \geq a_3 |z_2^\star| > 0,$$

  for all $\boldsymbol{z} \in \mathcal{R}_1$, since $z_2^\star = x_3^\star > 0$ by construction. This guarantees that the object reaches s_1 in finite time $t_1 < \infty$.

Upon reaching s_1, the trajectory enters $\mathcal{R}_0$, after which convergence to $\boldsymbol{z}^\star$ follows from Case (C1).

Case (C3): Initial state in $\mathcal{D}_2$ ($x_3 < 0$). Analogous reasoning applies:

- The lower-bounded joint configuration and the design of the dorsal-side flow (4.11) prevent pathological behaviors near the fingertip.
- The velocity field is uniformly bounded below in magnitude:

  $$\left\| \boldsymbol{R}_{\boldsymbol{n}}(\gamma(\boldsymbol{x}))\boldsymbol{A}(\boldsymbol{x} - \boldsymbol{x}^\star) \right\| \geq a_3 |x_3^\star| > 0, \quad \forall \boldsymbol{x} \in \mathcal{D}_2,$$

  ensuring that the object reaches the switching plane $x_3 = 0$ in finite time $t_f < \infty$.
- By the consistency of the vector field across $x_3 = 0$ (established in Step 2 of Lemma 1), the trajectory crosses into the palmar half-space ($x_3 > 0$) immediately after t_f, entering either $\mathcal{R}_1$ or $\mathcal{R}_0$. Subsequent convergence follows from Cases (C2) or (C1), respectively.

Thus, for any $\boldsymbol{x}(0) \in \Omega$, the trajectory $\boldsymbol{x}(t)$ converges to $\boldsymbol{x}^\star$ as $t \to \infty$, satisfying Objective (O1). □

Proof of objective (O2): Collision avoidance

Collision avoidance is guaranteed by ensuring that the object trajectory never penetrates the interior of the hand hull $\mathcal{D}$. Since the regions $\mathcal{R}_0$ and $\mathcal{D}_2$ (formerly denoted $\mathcal{R}_2$) are defined to lie entirely outside the hull or within safe convergence zones (see Figure 4.8(b) and Table B.4), it suffices to analyze trajectories initialized in $\mathcal{R}_1$, where the object is in proximity to the hull boundary.

Theorem 2. *Consider the dynamical system defined by* (4.5). *Let the initial state satisfy* $\boldsymbol{z}(0) \in \mathcal{R}_1$, *with* $\boldsymbol{z}(0)$ *lying on or outside the hand hull* $\mathcal{D}$ *(as per Definition 3). Then, for all* $t \geq 0$, *the trajectory* $\boldsymbol{z}(t)$ *remains outside the interior of* $\mathcal{D}$; *i.e.,* $\boldsymbol{z}(t) \notin \mathcal{D}^f$.

Proof. Collision avoidance is established by verifying that the vector field does not point into the hull at any point on its boundary. Let $\boldsymbol{z}_b \in \mathcal{R}^b \cap \mathcal{R}_1$ denote a point on the boundary of the hand hull within the region $\mathcal{R}_1$, and let $\boldsymbol{n}(\boldsymbol{z}_b)$ be the outward-pointing unit normal vector to $\mathcal{D}$ at $\boldsymbol{z}_b$ (defined in (B.22)).

A sufficient condition for non-penetration is that the velocity vector $\boldsymbol{g}(\boldsymbol{z}_b)$ satisfies

$$\boldsymbol{n}^\top(\boldsymbol{z}_b)\boldsymbol{g}(\boldsymbol{z}_b) \geq 0,$$

which ensures that the flow is either tangent to or directed away from the hull—consistent with standard conditions in obstacle avoidance literature [53, 54, 172].

By construction of the semi-tangent flow (4.5), at any boundary point $\boldsymbol{z}_b$, the velocity aligns with the local tangent direction:

$$\boldsymbol{g}(\boldsymbol{z}_b) = -\|\boldsymbol{A}_{/\!/}(\boldsymbol{z}_b - \boldsymbol{z}^\star)\|\, \boldsymbol{e}(\boldsymbol{z}_b),$$

where $\boldsymbol{e}(\boldsymbol{z}_b)$ is the unit tangent vector (see Figure 4.9(a), left panel). Since the normal vector $\boldsymbol{n}(\boldsymbol{z}_b)$ is orthogonal to the tangent vector by definition,

$$\boldsymbol{n}^\top(\boldsymbol{z}_b)\boldsymbol{e}(\boldsymbol{z}_b) = 0.$$

It follows that

$$\boldsymbol{n}^\top(\boldsymbol{z}_b)\boldsymbol{g}(\boldsymbol{z}_b) = -\|\boldsymbol{A}_{/\!/}(\boldsymbol{z}_b - \boldsymbol{z}^\star)\| \cdot \underbrace{\boldsymbol{n}^\top(\boldsymbol{z}_b)\boldsymbol{e}(\boldsymbol{z}_b)}_{=0} = 0.$$

Thus, the flow is everywhere tangent to the hull boundary in $\mathcal{R}_1$, and no trajectory can enter the interior $\mathcal{D}^f$. Combined with the fact that initial conditions are assumed to lie outside or on $\mathcal{D}$, this guarantees collision-free motion for all $t \geq 0$, satisfying the objective (O2). □

4.5 Finger Motion Generation

Reactive finger motions are generated through an object-state-dependent transition function $\epsilon(\boldsymbol{x}) \in [0, 1]$, which smoothly interpolates between a hand-cage configuration $\boldsymbol{q}_{f,o}$ (defined in Section 4.5.1) and a target power-grasp configuration $\boldsymbol{q}_{f,d}$ (assumed to be provided by a grasp planner; see Remark 3). The interpolation is modulated by the Euclidean distance between the object's current position $\boldsymbol{x}$ and the attractor $\boldsymbol{x}^\star$. This behavior is illustrated in Figure 4.13.

The resulting finger joint reference is given by

$$\boldsymbol{q}_{f,r}(\boldsymbol{x}) = \epsilon(\boldsymbol{x})\, \boldsymbol{q}_{f,d} + \big(1 - \epsilon(\boldsymbol{x})\big)\, \boldsymbol{q}_{f,o}, \tag{4.31}$$

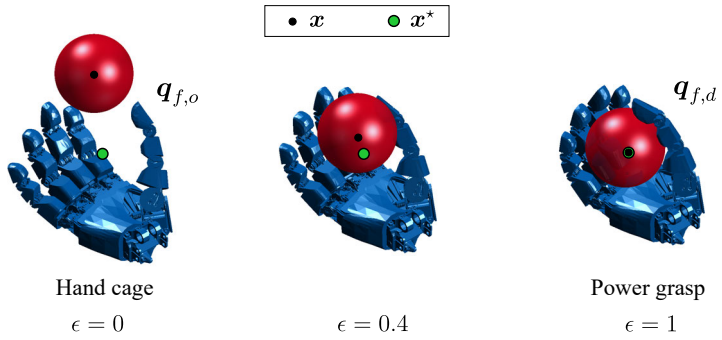


Figure 4.13: The transition function $\epsilon(\boldsymbol{x})$ enables smooth interpolation between the hand-cage and power-grasp configurations based on object proximity to the attractor.

which is relayed to the low-level finger controller (e.g., as implemented in [165]). The overall signal flow is depicted in Figure 4.3.

The transition function is designed as

$$\epsilon(\boldsymbol{x}) = \exp\Big(-(\boldsymbol{x} - \boldsymbol{x}^\star)^\top \boldsymbol{Q}_f (\boldsymbol{x} - \boldsymbol{x}^\star)\Big), \tag{4.32}$$

where $\boldsymbol{Q}_f \succ 0$ is a constant positive-definite matrix that governs the sensitivity of grip aperture to the object-to-attractor distance. The matrix $\boldsymbol{Q}_f$ is selected heuristically to ensure that the object is fully enclosed within the hand cage before significant finger closure occurs.

By construction, as the object recedes from the attractor ($\|\boldsymbol{x} - \boldsymbol{x}^\star\| \to c$, with $\boldsymbol{x} \in B(\boldsymbol{x}^\star, c)$), the transition function satisfies $\epsilon \to 0$, and the reference converges to the open hand-cage posture: $\boldsymbol{q}_{f,r} \to \boldsymbol{q}_{f,o}$. Conversely, as the object approaches the attractor ($\|\boldsymbol{x} - \boldsymbol{x}^\star\| \to 0$), it follows that $\epsilon \to 1$, and the reference transitions to the power-grasp configuration: $\boldsymbol{q}_{f,r} \to \boldsymbol{q}_{f,d}$.

Remark 9. *In practice, the selection of $\boldsymbol{Q}_f$ must account for uncertainties in object pose estimation, arising from visual tracking latency or noise, as well as mechanical effects such as joint friction, which may delay actual finger response relative to the commanded reference.*

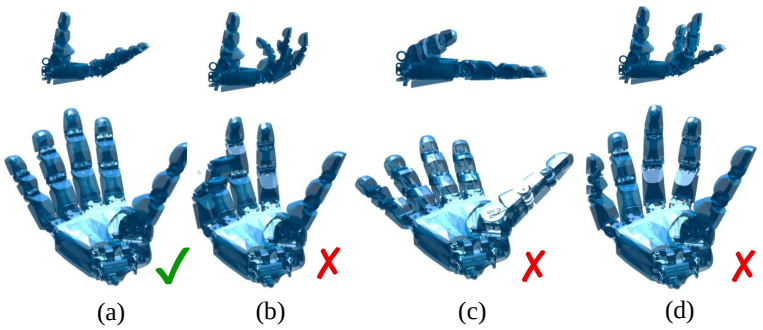


Figure 4.14: (**a**) A valid hand-cage configuration forming a concave, bowl-like enclosure. (**b–d**) Invalid configurations: (b) irregular finger placement lacking coherence, (c) excessive thumb abduction disrupting cage continuity, and (d) fragmented finger arrangement yielding disjoint sub-cages.

4.5.1 Selection of the Hand-Cage Configuration

The hand-cage configuration $\boldsymbol{q}_{f,o}$ defines the finger posture during the approach phase. While no universal mathematical definition exists due to variations in anthropomorphic hand kinematics and object geometry, the primary design criterion is to form a geometrically coherent, concave workspace around the palm that facilitates reliable object capture during motion.

A common and effective choice is a bowl-shaped configuration, in which the index finger, the little finger, and the thumb together form a smooth, continuous concavity. This is illustrated by a five-fingered humanoid hand with 20 degrees of freedom (4 per finger: 3 for flexion/extension and 1 for abduction/adduction). The following guidelines are adopted:

- Minimal or no abduction/adduction for the index to little fingers, with slight flexion at the metacarpophalangeal (MCP) joints to initiate curvature.
- Significant abduction of the thumb at its base joint to oppose the fingers and complete the cage structure.
- All joint angles are maintained above a lower bound ($\boldsymbol{q}_{f,o} \geq \boldsymbol{q}_{\min} > 0$) to preserve hull validity and avoid degenerate postures, consistent with the assumptions in Figure 4.12.

This configuration is illustrated in Figure 4.14(a). In contrast, Figure 4.14(b)–(d) depict non-viable alternatives: (b) lacks structural coherence, (c) features a hyper-abducted thumb that breaks cage continuity, and (d) results in two isolated sub-cavities rather than a unified enclosure—each failing to satisfy the functional requirements of a hand cage.

4.6 Experimental Validation, Simulation Study, and Discussion

Three experimental scenarios were conducted to evaluate whether the proposed Finger Flow (FF) framework satisfies the stated objectives of convergence, collision avoidance, and robust grasp execution. The experimental outcomes are analyzed to highlight key insights, while the practical strengths and limitations of the framework are critically discussed.

The evaluation encompasses the following scenarios:

1. **Stationary tabletop object**: The robot performs a grasp on a static ketchup bottle placed at random positions and heights on a table.
2. **Unpredictably moving object**: The robot attempts to grasp a bottle suspended from a rope, subjected to external perturbations that induce irregular spatial motion.
3. **Interactive human-to-robot handover**: A human operator hands over the bottle to the robot under two conditions, cooperative (unpredictable motion) and adversarial (evasive or disturbed motion), to assess robustness in dynamic interaction.

In all experiments, a standard ketchup bottle (mass: 500 g, height: 30 cm, diameter: 5 cm) with homogeneous mass distribution is used as the target object. Its 3D mesh (OBJ format) is assumed known and provided to the visual tracking system. The object remains within the robot's reachable workspace and is continuously visible within the camera's field of view throughout each trial.

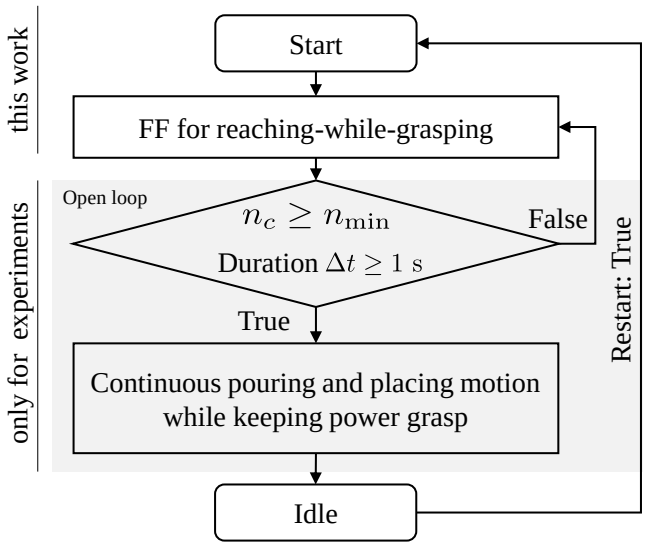


Figure 4.15: Post-grasp continuous pouring motion used to validate grasp stability. This sequence follows the framework in Figure 4.3 and is executed only in physical experiments. Parameters are listed in Appendix B.4.2.

Grasp stability assessment

Grasp success is evaluated through a post-grasp pouring motion that transitions smoothly from the final power-grasp configuration. A grasp is deemed stable if the object remains securely held throughout the entire pouring sequence without slippage or loss of contact.

As illustrated in Figure 4.15, this motion serves as a functional verification of grasp integrity and is applied exclusively in experimental validation (not in simulation). During the final approach phase, visual pose estimation becomes unreliable due to occlusion between the object and the hand. To address this, grasp confirmation is based on proprioceptive feedback: specifically, the estimated external joint torques $\tau_{i,\text{ext}}$ must exceed a minimum threshold $\tau_{i,\min}$ for at least 1 second, and the number of engaged finger joints n_c must satisfy $n_c \geq n_{\min}$. Once this condition is met, the system transitions to the pouring action in open-loop mode, assuming a stable grasp has been achieved. Implementation details of the pouring motion are provided in Appendix B.4.2.

System setup

The FF framework is implemented on the right arm (5 active degrees of freedom) and right hand (20 degrees of freedom) of the DLR humanoid robot *neoDavid* [44], which features variable stiffness actuators (VSAs) across its kinematic chain [118]. The wrist joints (DoFs 6–7) and torso are fixed during experimentation to simplify control and reduce computational load. A summary of system parameters is provided in Table B.5.

Two reference signals are generated in real time:

- Arm joint velocity reference $\dot{\boldsymbol{q}}_{a,r}$ (see (4.22), with Jacobian $\boldsymbol{J}_T \in \mathbb{R}^{3\times5}$ reflecting the 5 active arm joints);
- Finger joint position reference $\boldsymbol{q}_{f,r}$ (see (4.31)).

These references are dispatched to dedicated low-level controllers. The arm controller is implemented within a unified MATLAB/Simulink model using the Elastic-Space Programming (ESP)

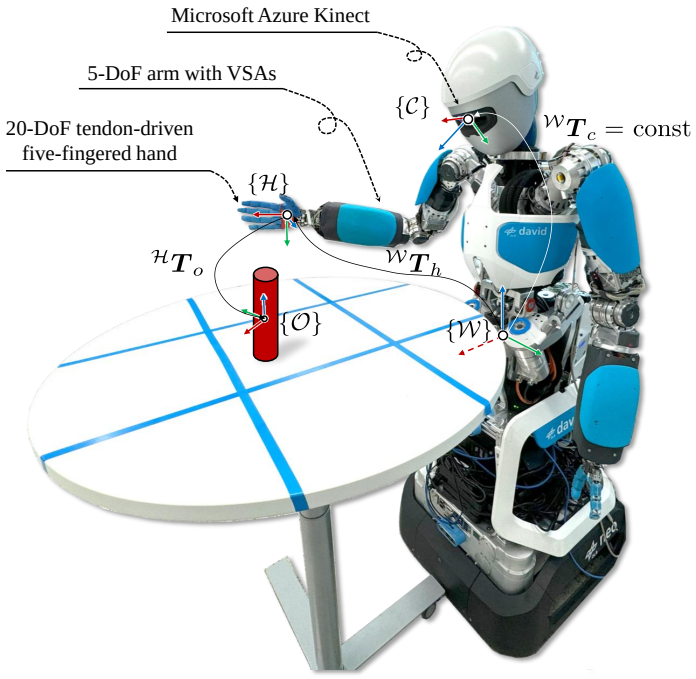


Figure 4.16: Experimental setup on the DLR robot *neoDavid*. The Azure Kinect camera is head-mounted. The right arm has five active DoFs; the hand has twenty. The torso is fixed. Coordinate frames: world ($\mathcal{W}$), camera ($\mathcal{C}$), hand ($\mathcal{H}$), object ($\mathcal{O}$). Axes (x_1, x_2, x_3) are colored red, green, and blue, respectively.

framework [101, 103]. The hand controller employs a cascaded architecture comprising an inner-loop tendon force regulator and an outer-loop joint-space impedance controller. Both models are auto-generated into C code and executed on two real-time PCs (Intel® Core™ i7-1185G7 @ 3.00 GHz) at a control frequency of 3 kHz. Forward kinematics and dynamics computations for *neoDavid* are performed at 1 kHz using the libraries described in [173].

Visual perception is enabled by an Azure Kinect RGB-D camera mounted on the robot's head in an eye-to-hand configuration (see Figure 4.16). Object pose estimation leverages the M3T library [166][2], which fuses 3D mesh models and kinematic priors to robustly estimate the 6-DoF pose of rigid and articulated objects under partial occlusion and motion blur. In this setup, the ketchup bottle's pose, comprising position $\boldsymbol{x}$ and orientation $^{\mathcal{H}}\boldsymbol{R}_o$, is tracked at 30 Hz using the provided OBJ mesh, running on a separate workstation (Intel® Core™ i9-11900K @ 3.50 GHz).

4.6.1 Experiment 1: Grasping a Stationary Tabletop Object

The ketchup bottle was placed at random positions on a circular table of diameter 0.8 m, arranged in a 9×9 grid as shown in Figure 4.17. The table height was varied across three levels: 0.90 m, 1.00 m, and 1.10 m. The robot arm was initialized in random configurations above the table, ensuring the object remained visible to the camera throughout the approach. A total of 150 trials were conducted, 50 at each height, with trials discarded if the visual tracker lost the object during the approaching phase. After filtering, 132 valid trials were retained for analysis. Representative successful trials are

[2]https://github.com/DLR-RM/3DObjectTracking

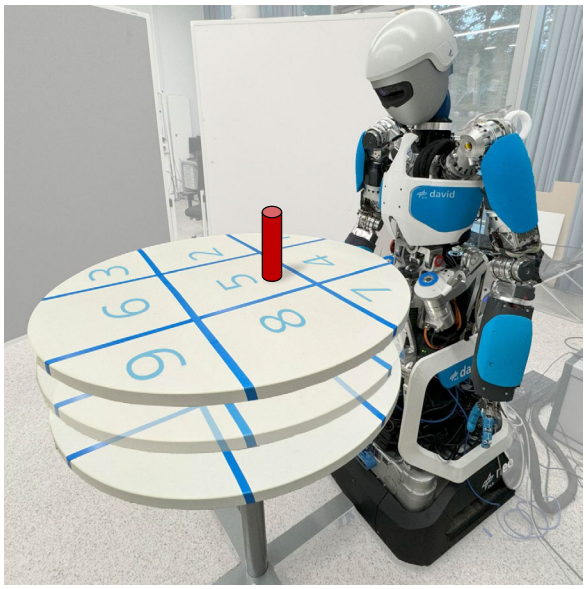


Figure 4.17: Placement regions for the stationary tabletop experiment. The bottle is randomly positioned within one of nine marked zones (1–9) at heights between 0.9 m and 1.1 m.

illustrated in Figure 4.20, while a detailed failure case is analyzed in Figure 4.21.

Grasp success rate

The spatial distribution of outcomes is shown in Figure 4.18, where green markers denote successful grasps and red markers indicate failures. An overall success rate of **87.3%** (115 out of 132 trials) was achieved. Performance across regions and heights is summarized in Figure 4.19.

Notably, the closed-loop nature of the Finger Flow (FF) framework enabled recovery from transient disturbances. For instance, in the failed trial depicted in Figure 4.21, the system re-engaged the moving object after an initial collision, a behavior not possible under open-loop control. However, once grasp confirmation was erroneously triggered (based on torque estimates), the subsequent pouring motion proceeded in open-loop mode, preventing further correction and ultimately leading to object drop. This highlights a key limitation: while FF ensures a robust approach and collision avoidance, final grasp verification remains sensitive to proprioceptive sensing fidelity.

Transient object motion within the hand cage

A core design principle of the semi-tangent flow is to tolerate sub-optimal intermediate grasps to maximize overall success under real-world uncertainties, including perceptual noise, unmodeled object dynamics, and actuation errors. To evaluate this, the object's transient motion within the hand cage was analyzed across all successful trials using kinematic data and video verification.

As shown in Figure 4.22, the object typically exhibited either *sliding* or *rolling* toward an in-cage equilibrium as the hand advanced and fingers closed. Rolling, characterized by significant rotation about the bottle's principal axis, occurred in 57% of successful trials, often when the arm operated near singular configurations. In these cases, limited hand mobility allowed fingers to gently "hook" the object into the cage, promoting stable contact formation and yielding a smaller final position error relative to the attractor (2.7 ± 1.8 cm). Sliding, occurring in 43% of trials, was observed when the object entered the cage aligned with the symmetry axis, resulting in slightly larger errors ($3.2 \pm$

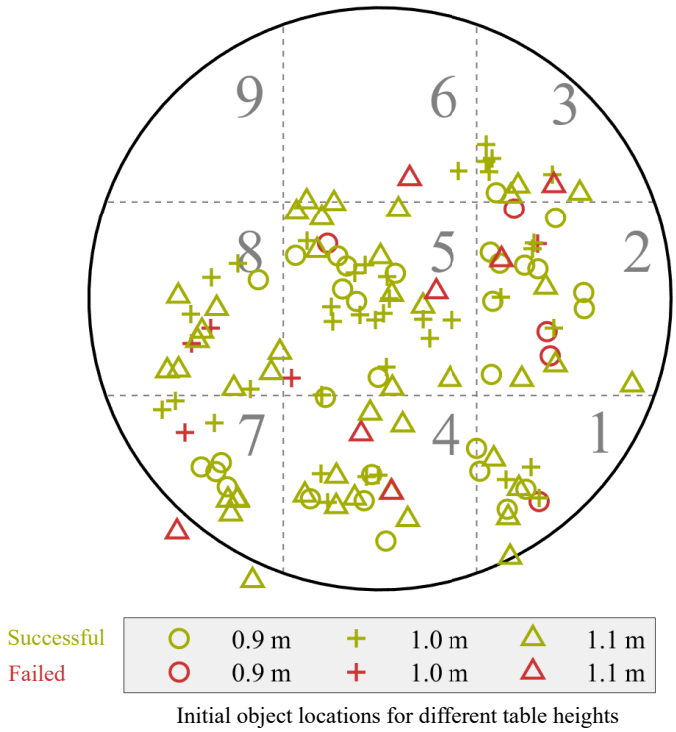


Figure 4.18: Spatial distribution of initial object positions (projected onto the horizontal plane) for Experiment 1. Green: successful grasps; red: failures. Due to perception noise in the world frame, some projections appear outside the physical table boundary. Overall success rate: 87.3% (115/132).

2.5 cm). Despite these variations, both behaviors led to functional grasps, validating the robustness of the proposed approach.

Failure analysis

Of the 17 failed trials (13%), two primary failure modes were identified, often co-occurring:

Collision during approach (14/17 trials). Most collisions involved the thumb sliding against or adhering to the bottle surface. These incidents stemmed from inaccuracies in the hand hull approximation, primarily due to uncertainties in elastic joint position estimation. The DLR *neoDavid* hand employs tendon-driven variable stiffness actuators, for which joint position is inferred indirectly via tendon length and force models. This introduces greater uncertainty compared to rigid hands with

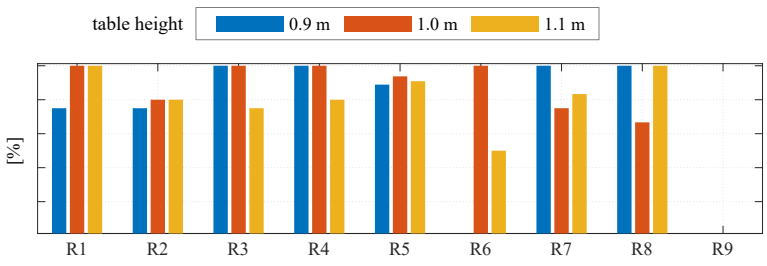


Figure 4.19: Grasp success rate by region and table height. Regions near the table center exhibit higher reliability, whereas edge regions exhibit higher failure rates due to arm kinematic constraints.

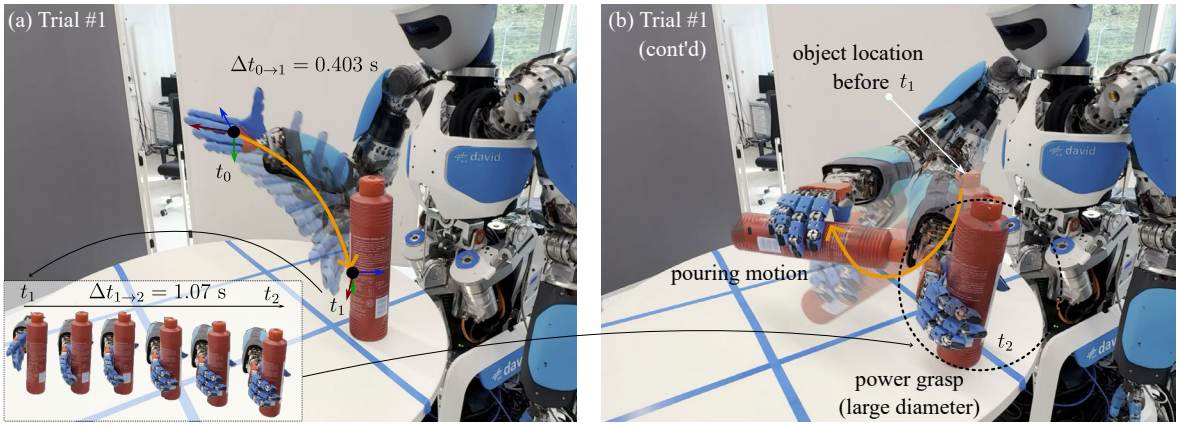


Figure 4.20: Selected moments from three successful trials in Experiment 1. The orange arrow indicates the trajectory of the hand-fixed attractor P_d. **(a)** Trial #1: Rapid approach ($\Delta t = 0.403$ s) with concurrent orientation alignment and synchronized finger closure. Bottom left: Sequence showing the object sliding into the hand cage during finger closure, accompanied by rotation about the vertical axis. **(b)** Continuation of Trial #1: Stable power grasp (classified as "large diameter" per [162]) confirmed, followed by continuous pouring motion (not the focus of this work).

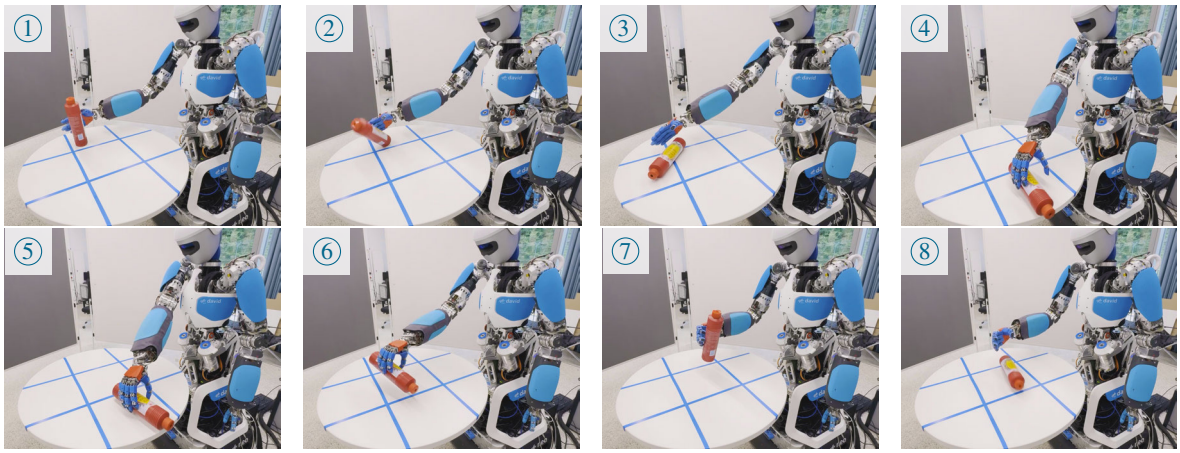


Figure 4.21: Analysis of a failed trial in Experiment 1. ①→②: Collision with the thumb causes object displacement. ③→⑤: Closed-loop tracking enables the arm to follow the rolling object as it temporarily exits the reachable workspace. ⑤→⑥: Erroneous torque-based grasp confirmation leads to premature transition to a precision (fingertip) grasp. ⑦→⑧: Open-loop pouring motion begins; the unstable fingertip grasp fails under dynamic loading, resulting in object drop.

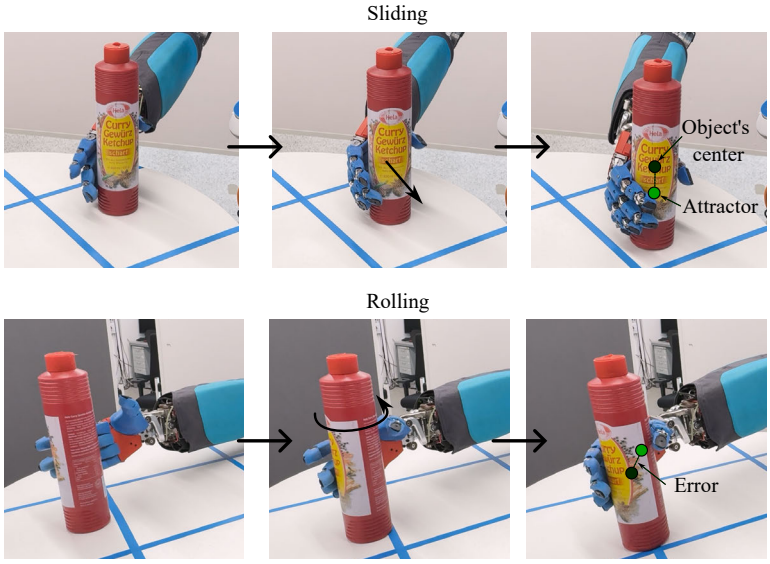


Figure 4.22: Transient in-cage motion of the object during successful grasps. The error is quantified as the Euclidean distance between the object's center and the attractor P_d.

Table 4.1: In-cage motion characteristics across all successful trials ($n = 115$).

Behavior	Sliding (43%)	Rolling (57%)
Distance to attractor	3.2 ± 2.5 cm	2.7 ± 1.8 cm

direct joint encoders. Although the hand hull includes safety margins to account for such errors, residual inaccuracies, particularly in thumb configuration, can still lead to unintended contacts.

The silicone fingertip covering enhances friction, aiding grasp stability in imperfect configurations (see Figure 4.21(c)). However, this same property can inhibit necessary in-cage adjustments (e.g., rolling or sliding), causing the object to become trapped in unstable equilibria and eventually fall, even on smooth surfaces like the plastic bottle.

Premature grasp confirmation (5/17 trials). Grasp confirmation relied on estimated external joint torques derived from tendon force measurements and a tendon-to-joint coupling matrix [117, 165]. Unlike systems equipped with dedicated joint torque sensors [174] or tactile arrays, this indirect method is susceptible to static bias from stiction, tendon friction, and configuration-dependent calibration errors, especially at the thumb base joint. In several cases, these errors caused the torque condition ($\tau_{i,\text{ext}} \geq \tau_{i,\text{min}}$ for > 1 s) to be falsely satisfied before a stable power grasp was established. Subsequent open-loop execution of the pouring motion then led to failure.

Developing a more robust grasp verification mechanism lies beyond the scope of this work but represents a critical direction for future improvement.

4.6.2 Experiment 2: Grasping an Unpredictably Moving Object

This experiment evaluates the robustness of the Finger Flow (FF) framework under highly dynamic conditions, where the target object undergoes continuous, unstructured motion. A ketchup bottle is suspended from a rope and persistently perturbed in random directions with varying amplitudes, inducing Cartesian velocities of up to 0.8 m/s in the world frame. The test is conducted continuously for

20 minutes, with each successful grasp triggering an automatic reset to restart the swinging motion.

Compared to Experiment 1, this scenario introduces three key challenges:

1. **Unpredictable object dynamics**: External disturbances cause non-smooth, high-acceleration motion that cannot be modeled a priori.

2. **Limited visual tracking bandwidth**: The M3T tracker [166] operates at 30 Hz, which constrains the system's ability to resolve fast-moving states accurately.

3. **Pose estimation uncertainty**: Transient occlusions, caused by the robot's own arm or fingers, introduce intermittent errors in the object's 6-DoF pose feedback.

A representative successful trial is illustrated in Figure 4.23, with key phases annotated by timestamped frames. By design, the magnitude of the semi-tangent flow $\boldsymbol{f}_t(\boldsymbol{x})$ in (4.18) preserves the norm of the underlying linear field (4.9), ensuring that hand velocity scales with object distance from the attractor. This property enables the robot to respond more aggressively when the object is far away, facilitating real-time adaptation.

Despite these mechanisms, high-speed motion remains challenging. As shown in frames ②–⑤, the bottle occasionally collides with the palm and rebounds before the control loop can react, a limitation primarily attributed to the 30 Hz visual feedback rate. In such cases, incorporating a predictive estimate of the object's motion ($\boldsymbol{\chi}_o \neq \mathbf{0}$) could enhance responsiveness, provided low-latency, low-noise state predictions are available.

Quantitative analysis across all successful trials is presented in Figure 4.24. The median peak velocity of the bottle exceeds 0.7 m/s, confirming the highly dynamic nature of the task. Nevertheless, the guiding vector field consistently drives the hand toward the moving attractor, achieving spatial convergence even during motion. At the moment of grasp confirmation ($t = 0$, aligned across trials), the object is rarely stationary; however, the median distance between the bottle's center and the attractor is approximately 0.02 m, indicating accurate alignment despite dynamic conditions.

These results confirm that the FF framework maintains both convergence (Objective O1) and collision avoidance (Objective O2) even under significant motion uncertainty, validating its suitability for real-world robotic manipulation in unstructured environments.

4.6.3 Experiment 3: Interactive and Adversarial Human-to-Robot Handover

This experiment evaluates the Finger Flow (FF) framework in a human-in-the-loop scenario, where a human operator hands over a ketchup bottle to the robot under varying levels of cooperation. The human is instructed to either assist the robot (cooperative mode) or actively challenge it by introducing evasive motions, sudden pose changes, or resistance during the approach phase (adversarial mode). Throughout the interaction, the object's pose is continuously perturbed, requiring the robot to react in real time while maintaining collision-free motion and convergence to a stable grasp.

A representative sequence of interactions is shown in Figure 4.25, illustrating both cooperative and adversarial behaviors. In cooperative trials (①→②), the human presents the object steadily, enabling smooth convergence. In adversarial cases (③→⑤), the human moves the bottle unpredictably, pulling away, rotating, or repositioning it mid-approach, to test the system's robustness. Despite these disturbances, the closed-loop nature of FF enables continuous adaptation, culminating in successful power grasps in the majority of trials.

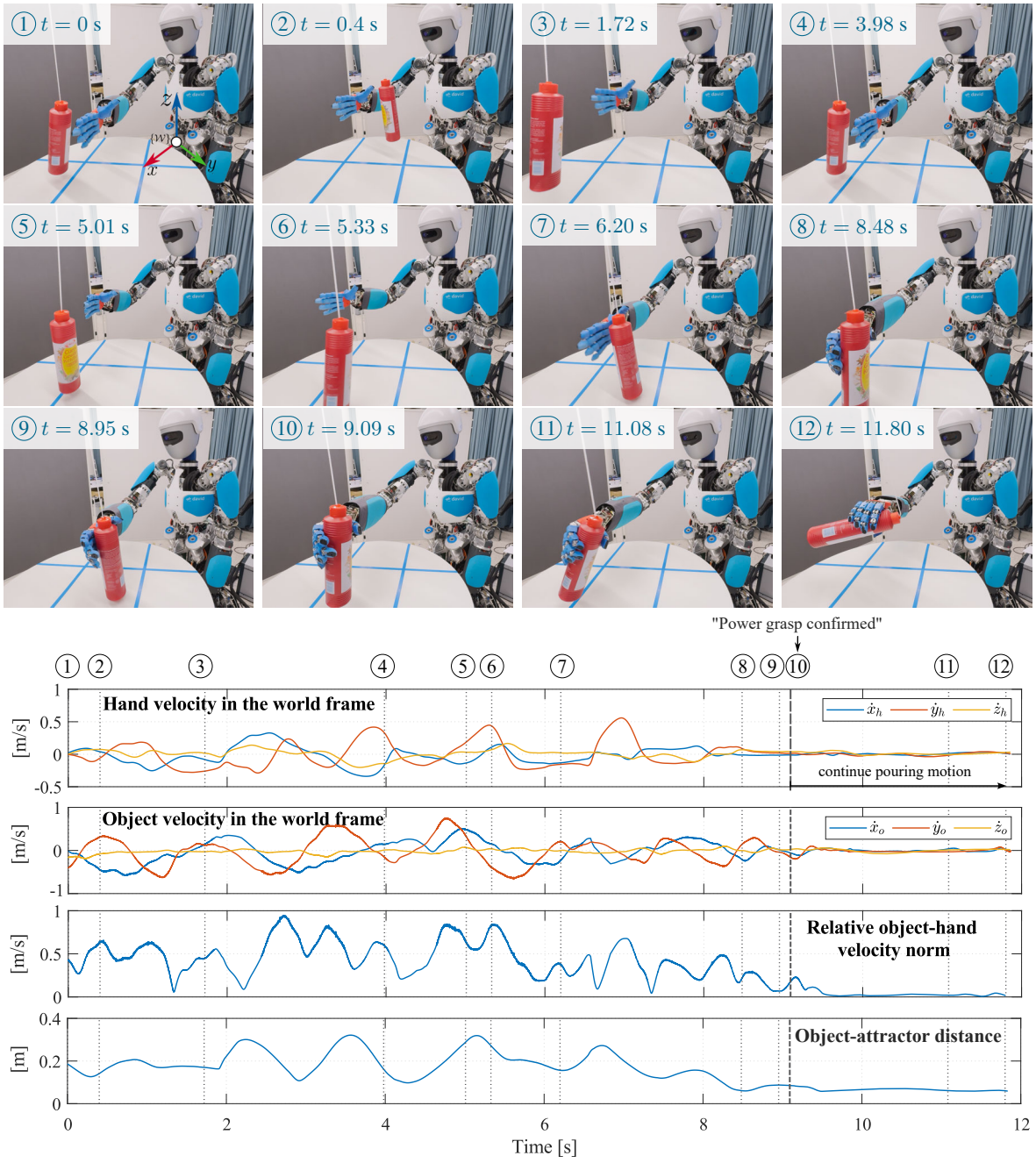


Figure 4.23: Experiment 2: Grasping a bottle undergoing persistent, unpredictable motion due to external disturbances. ①: Object moves behind the thumb; hand retracts to avoid collision. ②→③ ($\Delta t = 1.32$ s): Object motion exceeds robot response capability. ④→⑤: Object approaches dorsal side; hand adjusts to maintain safe distance. ⑥→⑦ ($\Delta t = 0.87$ s): Rapid approach executed as object enters capture zone. ⑧→⑨: Slight slippage during finger closure triggers transient reopening. ⑩→⑫: Stable power grasp achieved, followed by pouring and placement. Bottom panel: Time evolution of relative object–attractor distance, relative velocity norm, and absolute translational velocities in the world frame.

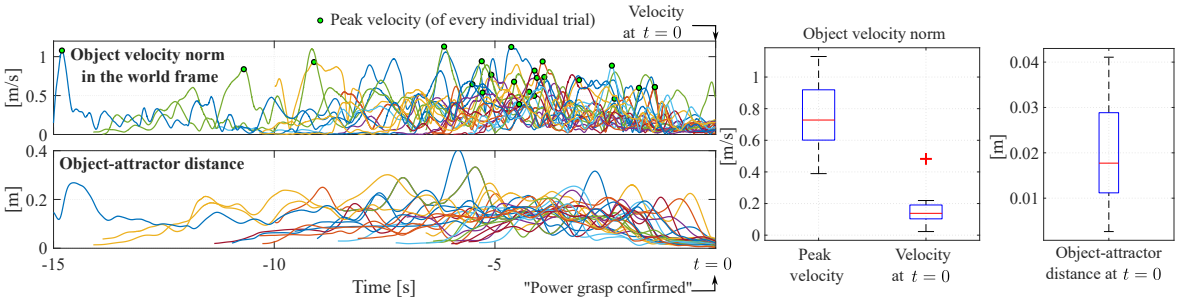


Figure 4.24: Statistical analysis of successful dynamic grasps. **Left**: Upper plot shows absolute translational velocity of the object over time; lower plot shows object–attractor distance. All trials are time-aligned at $t = 0$, defined as the onset of the pouring motion (grasp confirmation). **Middle**: Box plots of peak object velocity and velocity at $t = 0$. **Right**: Distribution of object–attractor distance at $t = 0$, with median near 2 cm, demonstrating consistent convergence despite motion.

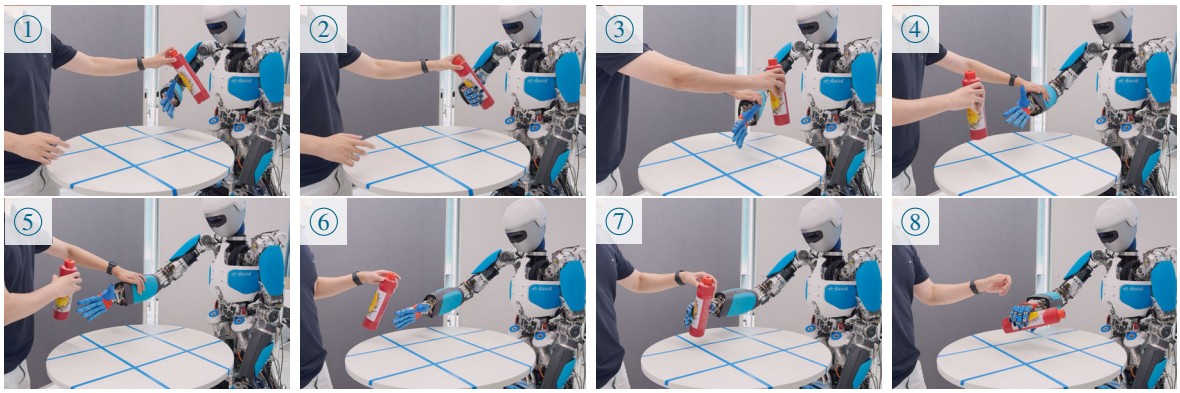


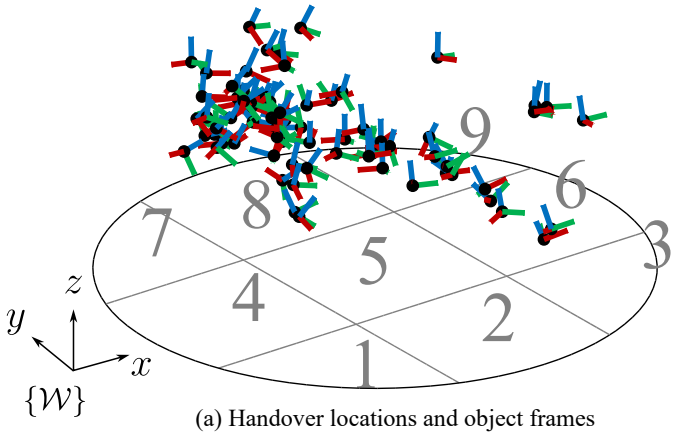
Figure 4.25: Experiment 3: Interactive and adversarial human-to-robot handover. ①→②: Cooperative handover with a stationary object. ③→⑤: Adversarial handover with active object motion by the human. ⑥→⑦: Dynamic handover involving rapid changes in object orientation and position. ⑧: Stable power grasp confirmed, followed by pouring motion to verify grasp integrity.

Out of 63 total attempts, 60 resulted in successful handovers, yielding a success rate of 95%. The spatial distribution of grasp confirmation points, expressed in the object-fixed frame, is shown in Figure 4.26. Successful grasps are predominantly concentrated in the regions above R4 and R5. It offers sufficient clearance for finger closure, aligns well with the palm curvature, and lies within a region of high visual observability from the head-mounted camera. This concentration reflects both robotic kinematic preferences and implicit human behavioral adaptation; participants unconsciously adjusted their handover poses based on tactile feedback (e.g., contact forces) and visual cues (e.g., observing the robot's approach trajectory), often converging toward configurations that facilitate successful grasping.

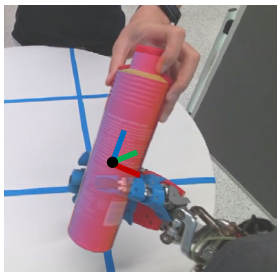
Guiding the robot by shared holding an object

When the object enters the vicinity of the attractor, or when visual uncertainty causes the estimated state to lie inside the hand hull, the reference hand velocity $\boldsymbol{v}_r$ approaches zero (see (4.19)). In this regime, the closed-loop arm controller effectively behaves as if operating in a low-impedance or near-zero-gravity mode. Consequently, the human can physically guide the robot's end-effector by manipulating the shared object, while the fingers maintain a compliant yet stable grip governed by the reactive finger generator (Section 4.5).

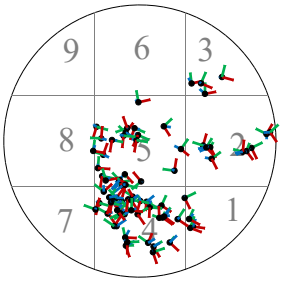
This capability is illustrated in Figure 4.27, where the human applies an interaction force $\boldsymbol{F}_{\text{inter}}$ to



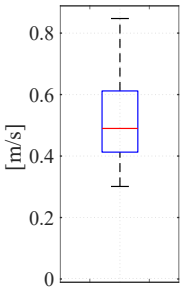
(a) Handover locations and object frames



(b) Object-fixed frame



(c) Top view



(d) Object peak velocity

Figure 4.26: Analysis of successful handovers ($n = 60$). (a) Spatial distribution of grasp confirmation points in the world frame. (b) Same points expressed in the object-fixed frame. (c) Top-down view highlighting clustering near the region above R4–R5. (d) Distribution of peak translational velocities during handover, demonstrating the dynamic nature of adversarial trials.

steer the robot during co-manipulation. The system remains passive and responsive, enabling intuitive physical collaboration without explicit mode switching or teleoperation commands. This property enhances usability in human-robot teamwork scenarios, where seamless role transitions between autonomous action and human guidance are essential.

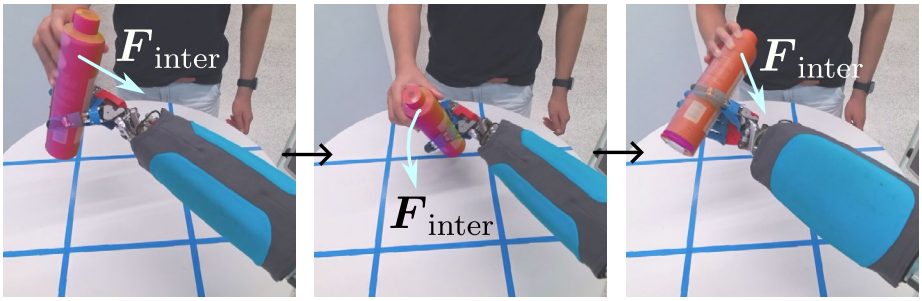


Figure 4.27: Shared control during co-manipulation: a human and robot jointly hold the object, with the human guiding the robot's motion through physical interaction. The interaction force $\boldsymbol{F}_{\text{inter}}$ is applied by the human to direct the arm.

4.6.4 Simulation Study

Recent reinforcement learning (RL) approaches have demonstrated impressive reactive grasping capabilities with high-degree-of-freedom hands [11, 175]. However, such methods rely on extensive offline training in high-fidelity simulators and embed implicit horizon-based optimization within their policies. In contrast, the proposed Finger Flow (FF) framework is a purely model-based, fully reactive controller that operates without preview, policy pretraining, or simulation-to-reality adaptation. A direct comparison with RL-based systems would conflate differences in training paradigms, data requirements, and planning horizons, thereby obscuring the core contribution.

To isolate the effect of closed-loop reactivity and geometric reasoning, baseline comparisons are restricted to two alternatives that share the same modeling assumptions and computational footprint:

- **Position-Based Visual Servoing (PBVS)**: A classical 6D visual servoing method using a linear control law with gain matrix $\boldsymbol{A}$ from (4.9), combined with the same orientation regulator (4.20).
- **Open-loop FF**: The full FF trajectory is computed once from the initial object state $\boldsymbol{x}_0 = \boldsymbol{x}(t=0)$ and executed without subsequent updates, ignoring all motion for $t > 0$.

To further investigate the influence of geometric and physical parameters, such as hand hull fidelity, object diameter, and surface friction, additional ablation studies are conducted in simulation. These conditions are difficult to control systematically on physical hardware but can be precisely varied in a physics engine.

The simulation environment replicates the DLR *neoDavid* platform: a 7-DoF arm equipped with a 20-DoF anthropomorphic hand, modeled in the MuJoCo physics engine. To decouple reaching performance from grasp synthesis, a fixed power-grasp pose is used across all trials. A cylindrical object with a lowered center of mass (mimicking a Roly-Poly toy) is placed on a table and assigned a random initial horizontal velocity, inducing persistent swinging motion. The robot hand is initialized at diverse poses around the object, ensuring no initial collisions.

Comparison of PBVS, open-Loop, and closed-loop FF

A total of 294 trials were conducted per method, with success defined strictly by the outcome of the first grasp attempt; subsequent recovery motions are not counted. Initial object positions are categorized based on their location relative to the hand's dorsal plane ($x_3 < 0$) or palmar side ($x_3 \geq 0$).

As summarized in Table 4.2 and visualized in Figure 4.28, PBVS succeeds only when the object starts directly above the palm ($\mathcal{D}_0$), achieving a 62% success rate in this region but failing entirely on the dorsal side. This validates the design choice of preserving a pure linear flow in $\mathcal{D}_0$, where collision risk is minimal.

Open-loop FF performs marginally better overall (27%) but struggles with dynamic objects, as its trajectory cannot adapt to motion after initialization. In contrast, closed-loop FF leverages continuous feedback from both object pose and finger configuration to adjust the hand trajectory in real time, avoiding collisions and maintaining convergence. It achieves a near-perfect success rate of 99.7% (293/294), demonstrating robustness across both palmar and dorsal regimes.

Table 4.2: Grasp success rates across baseline methods in simulation. Trials are grouped by initial object position relative to the hand-fixed frame.

Method	Object center at $t = 0$		
	Dorsal ($x_3 < 0$)	Palmar ($x_3 \geq 0$)	Total
PBVS	0/134 (0%)	62/160 (39%)	62/294 (21%)
Open-loop FF	30/134 (22%)	49/160 (31%)	79/294 (27%)
FF (proposed)	134/134 (**100%**)	159/160 (**99%**)	293/294 (**99.7%**)

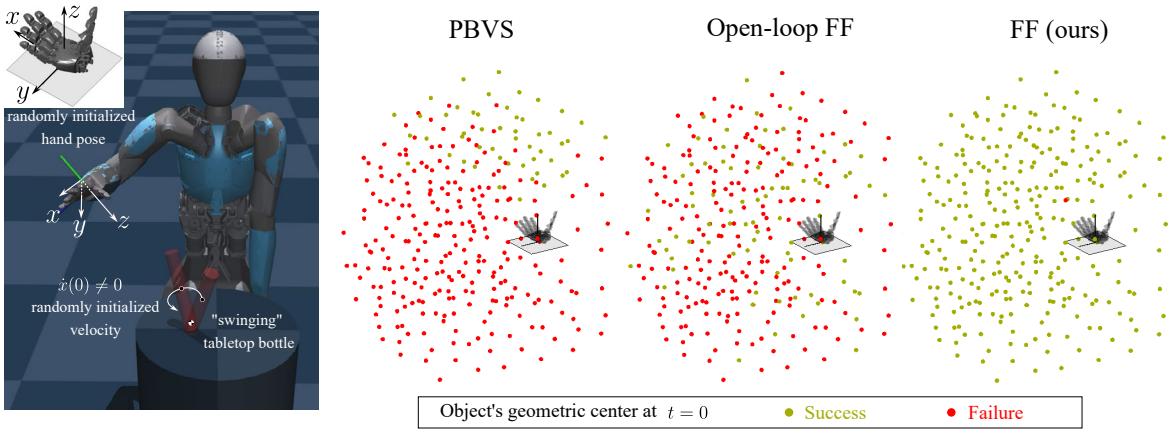


Figure 4.28: Baseline comparison in simulation. (Left) Experimental setup: 294 randomized hand poses around a swinging cylindrical object. (Right) Initial object positions (in hand-fixed frame) color-coded by success (green) or failure (red) for each method. PBVS fails on the dorsal side; open-loop FF lacks adaptivity; closed-loop FF succeeds universally.

Effect by changing object's geometry and surface friction

To assess sensitivity to physical properties, grasp success is evaluated under variations in bottle diameter (small: 4 cm, large: 8 cm) and surface friction (low/high, corresponding to halved or doubled MuJoCo `geom/friction` values). The hand hull remains unchanged, and all trials initialize with the object in $\mathcal{D}_0$ at ≥ 40 cm from the attractor.

Results from 60 trials per condition (Table 4.3) show high success rates across all settings, with minor degradation for large, high-friction bottles (80%). Smaller, low-friction objects exhibit smoother in-cage motion (sliding/rolling toward the attractor), consistent with the "bean-in-bowl" dynamical model. Failures in the large/high-friction regime arise from excessive stiction between fingers and object, which inhibits necessary adjustments and leads to slippage during closure.

Table 4.3: Grasp success rate under varying object diameter and surface friction.

Diameter \ Friction	Low	High
Small	98%	97%
Large	89%	80%

Sensitivity to hand hull parameterization

The accuracy of the hand hull representation critically influences performance. Two key parameters are varied: (1) hull thickness (distance between inner and outer contours in Figure 4.4(c)), and (2) thumb coverage extent. As shown in Figure 4.30, deviations from the nominal hull lead to performance degradation.

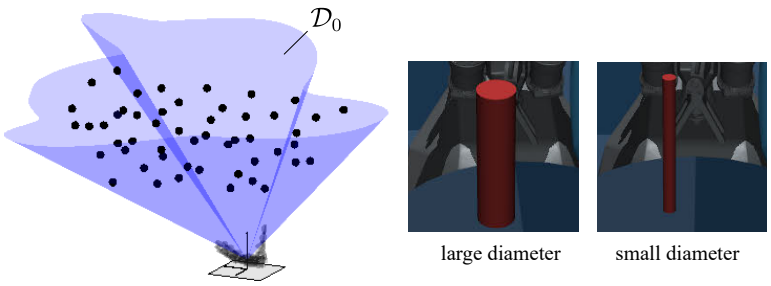
Using the same swinging bottle and 102 randomized trials per configuration, success rates are compared against the baseline (98% with nominal hull). Results in Table 4.4 reveal two failure modes:

- **Insufficient coverage** (e.g., partial thumb hull): Causes early collisions before caging, leading to up to 34% drop in success.
- **Excessive hull volume** (e.g., double thickness or over-coverage): Creates hollow regions where the object is misclassified as "inside" the hull, causing the controller to halt motion prematurely, even without physical contact.

These findings underscore the importance of *tight yet complete* hull approximation: it must cover all potential finger configurations without introducing unnecessary voids that disrupt the vector field logic. Together, these simulation studies validate the robustness, adaptivity, and geometric sensitivity of the FF framework, confirming that its performance hinges on accurate hand modeling and tight integration of perception, dynamics, and control.

Table 4.4: Change in grasp success rate relative to the nominal hand hull (98%). Negative values indicate performance loss.

Thickness	Double	Half
Difference	–27%	–9%
Thumb coverage	Partial	Over
Difference	–34%	–19%



(a) Initial bottle's center locations (b) Test bottles

Figure 4.29: (a) Initial object centers (black dots) confined to $\mathcal{D}_0$, the solid of revolution generated by rotating the tangent line s_1. (b) Test bottles of small and large diameters used in friction/diameter ablation.

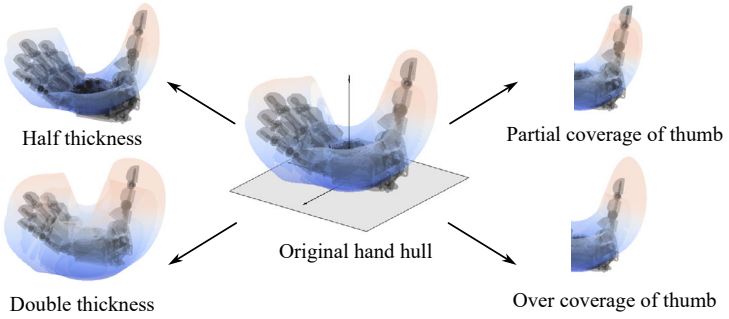


Figure 4.30: Variants of the hand hull used in parameter sensitivity analysis: (left) nominal, (middle) increased thickness, (right) altered thumb coverage.

4.6.5 Limitations and Outlook

While the Finger Flow framework demonstrates robust performance in reactive grasping across diverse experimental conditions, several limitations remain, pointing to promising avenues for future research.

Non-smooth arm velocity transitions

The current formulation exhibits discontinuities in the arm velocity field when the object crosses the switching plane $x_3 = 0$ (i.e., the dorsal–palmar interface). Although solution uniqueness is guaranteed in the Filippov sense (Lemma 1), the resulting non-smooth velocity profiles can challenge low-level tracking controllers on physical hardware, particularly those requiring continuous derivatives. A natural extension is to redesign the vector field to be continuously differentiable across all regions, e.g., via smooth blending functions or higher-order modulation schemes, thereby improving compatibility with industrial-grade motion control systems.

Scalar-driven finger closure strategy

Finger motion is currently governed by a single scalar transition function $\epsilon(\boldsymbol{x})$ dependent solely on the Euclidean distance to the attractor (see (4.32)). While effective for canonical objects like cylinders, this simplification lacks adaptivity to complex geometries, surface properties, or task-specific grasp requirements. Future work could incorporate multi-dimensional feedback, such as local curvature, contact normals, or tactile signals, to modulate finger trajectories in a more nuanced, shape-aware manner.

Absence of dynamical modeling

The FF framework is purely kinematic: it does not account for the dynamics of either the robot or the object. Consequently, performance may degrade in highly dynamic scenarios involving rapid accelerations or external forces (e.g., catching an object moving at speeds exceeding 3 m/s). Incorporating dynamical priors, such as object inertia, momentum, or environmental constraints—would require tighter integration with high-bandwidth perception (e.g., > 100 Hz tracking) and model-predictive control. Such an extension remains a compelling direction for applications demanding high-speed interaction.

Generalization to different object geometries

The current design assumes the object admits a circular cross-section of fixed radius r_o in any plane through its geometric center (Assumption 4). This limits applicability to non-cylindrical or irregularly shaped objects. A principled generalization involves redefining the dynamic plane to pass through the point on the object's surface closest to the 2D hand hull, rather than its centroid. The intersection of this plane with the object yields a convex 2D silhouette, which can be tightly enclosed by an oriented ellipse. The hand hull thickness can then be modulated locally based on this ellipse's semi-axes, replacing the fixed-radius assumption.

This approach would relax Assumption 4 and improve geometric fidelity. For mildly non-convex objects, a convex hull approximation may suffice; however, pronounced concavities (e.g., handles, hooks) remain challenging. Conservative convexification risks introducing excessive empty space around the object, potentially triggering premature motion arrest or suboptimal caging. Extending FF to handle arbitrary non-convex geometries, possibly through learned shape embeddings or hierarchical decomposition, constitutes an important open problem.

Integration with global motion generators

The semi-tangent flow is inherently local: it activates only when the object lies within a predefined reactivity margin (e.g., 30 cm from the attractor). Beyond this range, the flow reverts to a global linear attractor. This property enables seamless composition with other motion generators via smooth activation functions (e.g., sigmoids).

As a proof of concept, FF was integrated with a Gaussian Mixture Model (GMM)-based imitation learning framework—specifically, the Stable Estimator of Dynamical Systems (SEDS) [78] —to generate collision-free reaching motions around environmental obstacles such as tables. The GMM was trained on human demonstrations of table-avoiding reaches toward a bottle. The final arm velocity reference combines both systems:

$$\boldsymbol{v}_r = \sigma(d) \cdot \boldsymbol{v}_{\text{FF}} + (1 - \sigma(d)) \cdot \boldsymbol{v}_{\text{GMM}},$$

where $d = \|\boldsymbol{x} - \boldsymbol{x}^\star\|$ and $\sigma(d)$ is a smooth switching function that activates FF only when $d < 0.3$ m.

Figure 4.31 illustrates this hybrid behavior: the hand starts below the table (①), follows a GMM-generated trajectory to avoid collision (①→②), and transitions smoothly to FF for final approach and grasp (②→④). This demonstrates FF's compatibility with data-driven motion planners, enabling end-to-end reactive manipulation that respects both environmental and self-collision constraints.

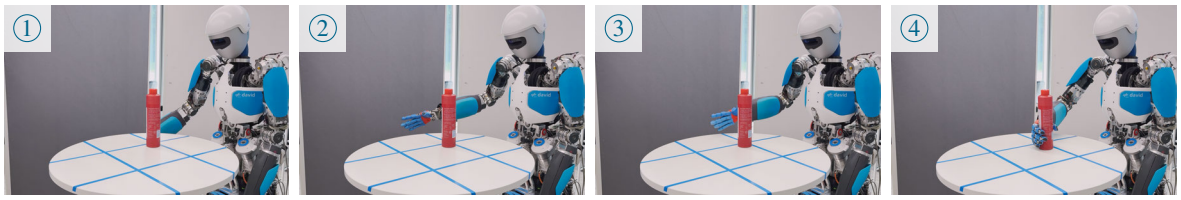


Figure 4.31: Hybrid motion generation combining FF with GMM-based SEDS. ①: Initial hand position below the table. ①→②: GMM guides the hand around the table. ②→④: Smooth transition to FF for final approach and grasp.

4.7 Summary

This chapter introduced Finger Flow (FF), a reactive reach-while-grasp generation framework that leverages visual and proprioceptive feedback to instantaneously provide velocity references to lower-level controllers of a robot arm and a multi-fingered hand. FF enables robust grasping of both stationary and unpredictably moving objects. By design, the framework accounts for finger location and geometry in real time, continuously guiding the hand to avoid collisions with the object during the approach phase and adjusting finger opening and closure based on the relative pose between the object and the hand. This purely state-dependent behavior allows automatic recovery from failed grasp attempts. Formal proofs of convergence and collision avoidance were also established for the case of grasping a stationary spherical object.

The FF framework was implemented on the DLR robot *neoDavid* equipped with a multi-fingered hand and evaluated through a series of fast pick-and-catch tasks involving both stationary and randomly moving objects. Operating in closed loop at 3 kHz, FF achieved a grasp success rate exceeding 87 % for stationary objects placed at random locations across 130 trials. In addition, interactive and adversarial handover experiments demonstrated the robustness and safety of the proposed approach in human–robot interaction scenarios.

At present, FF guarantees only piecewise smooth arm motion generation and relies on simplified finger-closing strategies. Future research directions include extending the framework to handle a broader range of object geometries, including concave and irregular shapes. Moreover, the current formulation generates body velocities based on object-to-hand poses in $SO(3)$ and $\mathbb{R}^3$ separately, rather than directly operating on the non-Euclidean manifold $SE(3)$. Additional practical considerations remain to be addressed, such as the explicit incorporation of sensing uncertainties arising from visual object perception and finger position and torque measurements. Overall, the results presented in this work demonstrate that the model-based FF motion generator is not restricted to humanoid platforms and is equally applicable to manipulators equipped with arbitrary multi-fingered hands.

5

Passivity-based Motion and Force Tracking Control

In this chapter, the focus is shifted to the phase following the completion of the reaching motion, where the robotic hand establishes contact with the target object and wraps around it. At this stage, the system can be viewed as a kinematically constrained system. Using the multifingered grasping as an example, the contact points between the hand and the object are assumed to remain fixed relative to the object's surface. For simplicity without the loss of generality, all contacts are assumed either point contacts with friction or soft-finger contacts, which provides a physical justification for the assumption of fixed contact locations [120, Chapter 6].

Aligned with the goal **G5** outlined in Section 1.3, this chapter introduces a control strategy that combines PD+ task-space tracking with integral force control. Importantly, this approach maintains the intrinsic inertial and elastic properties of the robot system. A passivity analysis is conducted to demonstrate the uniform asymptotic stability of the equilibrium point. The effectiveness of the proposed control law is demonstrated through simulations on a planar two-armed robotic system subject to constraints.

The contributions corresponding to **C5** in Section 1.4 are detailed as follows:

- A passivity-based control framework is developed for elastic joint robots, enabling simultaneous precise motion tracking and force regulation during object manipulation. This is achieved by employing a dynamically consistent projection operator while preserving the system's inherent inertial and elastic structure.

- To eliminate steady-state errors caused by constant disturbances within the constrained space, an integral of force error is integrated in the feedback loop. This enhancement ensures output strict passivity in physical interactions and guarantees uniform asymptotic stability during unconstrained motion phases.

The chapter is structured as follows. Following the introduction in Section 5.1, the dynamics of the constrained robotic system with serial elastic actuators are formulated in Section 5.2. The control problem is then stated, and the proposed control law is derived in Section 5.3. The passivity and stability properties of the resulting closed-loop system are rigorously analyzed in Section 5.4. To validate the theoretical developments, simulation results for a planar two-arm robotic system, subject to a holonomic distance constraint between its end-effectors, are presented in Section 5.5,

using smooth motion and force reference trajectories. Finally, Section 5.6 provides a summary of this chapter.

Publication Note

The content of this chapter is based on the following publication:

> [129]: **X. Meng**, M. Keppler and C. Ott, "Passivity-Based Motion and Force Tracking Control for Constrained Elastic Joint Robots," in *IEEE Control Systems Letters*, vol. 7, pp. 217-222, 2023.

5.1 Introduction

Constrained elastic joint robots can be viewed as multi-body systems with closed-loop topologies, such as cooperative manipulators, multifingered hands, or humanoid robots. This raises a central question: How can one achieve robust, simultaneous motion and force control for constrained elastic joint robots?

In the domain of hybrid motion and force control for such systems, early approaches like those by Spong [104] and Mills [105] employed a two-loop structure based on integral manifolds and corrective control to address joint flexibility, requiring fast inner loops due to the singularly perturbed system dynamics. Later, Ahmad et al. [176] proposed a single-loop framework that canceled nonlinearities in the projected end-effector dynamics without relying on acceleration or force measurements. To handle dynamic uncertainties and unknown stiffness, adaptive and sliding mode strategies were introduced in [177–179].

Later on, Aghili [106] introduced a projected inverse-dynamics approach for rigid-joint robots, decoupling the dynamics into orthogonal subspaces using kinematic projections. This method was extended to operational space control by Mistry et al. [107, 108], enabling applications in underactuated systems like humanoid robots. Subsequent works (e.g., [109–111]) validated similar projection-based controllers in multi-arm and legged robotic platforms, achieving effective decoupled motion and force control.

Although the aforementioned approaches have demonstrated strong performance, control laws developed for rigid-joint manipulators [106, 111] are not directly applicable to robots with elastic joints. A common workaround is to introduce an additional inner control loop, such as a cascaded or dual-loop architecture [104, 105], to bridge this gap. However, this practice unavoidably alters the original system dynamics, thereby complicating the control design and analysis. Moreover, several methods, including [106, 108], rely on inverse-dynamics or feedback-linearization techniques in at least one subsystem, typically the unconstrained subspace. Such strategies explicitly cancel or reshape the inherent mechanical properties of the robot, which may be undesirable from both robustness and physical interpretability perspectives. In addition, the extent to which passivity is preserved in these designs is not always evident. In contrast, passivity-based control has long been recognized as a principled framework for robot control [180, 181]. Building upon this paradigm, Keppler et al. [101, 113] introduced a control approach for elastic-joint robots that enforces a desired interaction behavior at either the motor side or the link side, while explicitly retaining the robot's intrinsic elastic characteristics.

This chapter builds upon these foundations to propose a novel control strategy that achieves simultaneous motion and force tracking in constrained elastic joint robots while preserving their intrinsic

inertial and elastic structure.

5.2 Open-Loop Task-Space Dynamics

Consider the system dynamics (2.20a), (2.20c), and (2.20c) with all rotational joints implemented by SEAs. The system considers n rigid links with $n - m$ linearly independent kinematic constraints, expressed by a set of algebraic equations [128].

$$\boldsymbol{M}(\boldsymbol{q})\ddot{\boldsymbol{q}} + \boldsymbol{C}(\boldsymbol{q}, \dot{\boldsymbol{q}})\dot{\boldsymbol{q}} + \boldsymbol{g}(\boldsymbol{q}) = \boldsymbol{K}(\boldsymbol{\theta} - \boldsymbol{q}) + \boldsymbol{J}_c(\boldsymbol{q})^\top \boldsymbol{\lambda} + \boldsymbol{\tau}_{ext}, \tag{5.1a}$$

$$\boldsymbol{B}\ddot{\boldsymbol{\theta}} + \boldsymbol{K}(\boldsymbol{\theta} - \boldsymbol{q}) = \boldsymbol{u}, \tag{5.1b}$$

$$\boldsymbol{J}_c(\boldsymbol{q})\dot{\boldsymbol{q}} = \boldsymbol{0}, \tag{5.1c}$$

where $\boldsymbol{q} \in \mathbb{R}^n$ represents link position. $\boldsymbol{M}(\boldsymbol{q})$ is a symmetric positive definite link inertia matrix. Te Coriolis/centrifugal matrix $\boldsymbol{C}(\boldsymbol{q}, \dot{\boldsymbol{q}})$ is chosen such that $\dot{\boldsymbol{M}}(\boldsymbol{q}) - 2\boldsymbol{C}(\boldsymbol{q}, \dot{\boldsymbol{q}})$ is skew-symmetric [120]. $\boldsymbol{g}(\boldsymbol{q})$ denotes the gravity torque, $\boldsymbol{\tau}_{ext} \in \mathbb{R}^n$ the generalized external torques on the link, $\boldsymbol{\theta} \in \mathbb{R}^n$ the motor coordinate. The positive diagonal matrix $\boldsymbol{B}$ includes the reflected motor inertia, with the following Assumption 5

Assumption 5. *The joint elasticity is modeled by a constant, positive-definite diagonal stiffness matrix $\boldsymbol{K} \succ 0$, representing ideal linear torsional springs between each motor shaft and its corresponding link. The inertia matrix $\boldsymbol{M}(\boldsymbol{q})$ is symmetric, uniformly positive definite, and satisfies*

$$0 < \underline{m} \leq \sigma_{\min}\big(\boldsymbol{M}(\boldsymbol{q})\big) \leq \sigma_{\max}\big(\boldsymbol{M}(\boldsymbol{q})\big) \leq \overline{m} < \infty,$$

for all $\boldsymbol{q} \in \mathbb{R}^n$, where $\underline{m}, \overline{m}$ are finite positive constants and $\sigma_{\min}(\cdot)$, $\sigma_{\max}(\cdot)$ denote the minimum and maximum singular values, respectively. Similarly, the motor inertia matrix $\boldsymbol{B}$ is constant, symmetric, and positive definite, with its singular values bounded away from zero and infinity. Consequently, both $\boldsymbol{M}(\boldsymbol{q})^{-1}$ and $\boldsymbol{B}^{-1}$ exist for all $\boldsymbol{q}$ and are uniformly bounded. Moreover, the Coriolis and centrifugal matrix $\boldsymbol{C}(\boldsymbol{q}, \dot{\boldsymbol{q}})$ is continuous in $(\boldsymbol{q}, \dot{\boldsymbol{q}})$ and satisfies the property that, for any bounded $\dot{\boldsymbol{q}}$, the norm $\|\boldsymbol{C}(\boldsymbol{q}, \dot{\boldsymbol{q}})\|$ remains bounded uniformly in $\boldsymbol{q}$.

The motor input $\boldsymbol{u} \in \mathbb{R}^n$ is the control input. Recap that $\boldsymbol{\lambda}$ is a Lagrange multiplier that denotes the constraint force. The constraint Jacobian matrix $\boldsymbol{J}_c(\boldsymbol{q})$ is given in (2.19), where the constraint function $\boldsymbol{\phi}(\boldsymbol{q})$ is assumed fulfilling Assumption 6:

Assumption 6. *The system is subject to a set of holonomic constraints described by the vector-valued function $\boldsymbol{\phi}(\boldsymbol{q}) : \mathbb{R}^n \to \mathbb{R}^m$, which is assumed to be at least four times continuously differentiable ($\boldsymbol{\phi} \in \mathcal{C}^4$). The associated constraint Jacobian matrix, defined as $\boldsymbol{J}_c(\boldsymbol{q}) := \frac{\partial \boldsymbol{\phi}(\boldsymbol{q})}{\partial \boldsymbol{q}}(\boldsymbol{q}) \in \mathbb{R}^{m \times n}$, has constant full row rank equal to m (equivalently, the nullspace of $\boldsymbol{J}_c(\boldsymbol{q})$ has dimension $n - m$) for all configurations $\boldsymbol{q}$ in the domain of interest. Furthermore, $\boldsymbol{J}_c(\boldsymbol{q})$ and its derivatives up to the required order are uniformly bounded with respect to $\boldsymbol{q}$.*

Remark 10. *The $\mathcal{C}^4$ continuity ensures that time derivatives of the constraints up to the fourth order exist and are continuous—a condition often required in higher-order control designs (e.g., feedback linearization, differential flatness, or observer-based schemes). The full-rank condition guarantees that the constraints are independent and that the constrained configuration manifold is a smooth embedded submanifold of $\mathbb{R}^n$.*

Owing to the presence of holonomic kinematic constraints, the configuration vector $\boldsymbol{q} \in \mathbb{R}^n$ no longer constitutes a set of minimal coordinates; the true degrees of freedom of the system are reduced to $m < n$. To work within the constrained tangent space, it is common practice to introduce a projection operator that maps arbitrary velocities onto the nullspace of the constraint Jacobian $\boldsymbol{J}_c(\boldsymbol{q}) := \partial\boldsymbol{\phi}/\partial\boldsymbol{q}$. Following the approach of Aghili [106] and Mistry [108], such a projector $\boldsymbol{P}$ satisfies

$$\dot{\boldsymbol{q}} = \boldsymbol{P}(\boldsymbol{q})\dot{\boldsymbol{q}}, \quad \forall\, \dot{\boldsymbol{q}} \in \mathcal{N}(\boldsymbol{J}_c),$$

though it is important to note that $\boldsymbol{P}$ is not unique.

As discussed in Table 2.2, the choice of projector has significant implications for the preservation of the system's inertial structure. In contrast to the geometric projectors employed in [106, 108], a *dynamically consistent* projector is adopted that respects the kinetic energy metric induced by the inertia matrix $\boldsymbol{M}(\boldsymbol{q})$. Specifically, the following is defined:

$$\boldsymbol{P}(\boldsymbol{q}) = \boldsymbol{I} - \boldsymbol{J}_c(\boldsymbol{q})^{M+}\boldsymbol{J}_c(\boldsymbol{q}), \tag{5.2}$$

where $\boldsymbol{J}_c^{M+}(\boldsymbol{q})$ denotes the inertia-weighted (or $\boldsymbol{M}(\boldsymbol{q})$-weighted) pseudoinverse of $\boldsymbol{J}_c(\boldsymbol{q})$, defined by

$$\boldsymbol{J}_c^{M+}(\boldsymbol{q}) = \boldsymbol{M}^{-1}\boldsymbol{J}_c^\top\left(\boldsymbol{J}_c\boldsymbol{M}^{-1}\boldsymbol{J}_c^\top\right)^{-1}. \tag{5.3}$$

For notational brevity, the explicit dependence of $\boldsymbol{P}$, $\boldsymbol{J}_c$, and related matrices on $\boldsymbol{q}$ is omitted in what follows (see footnote[1]).

This projector is idempotent ($\boldsymbol{P}^2 = \boldsymbol{P}$) and satisfies the orthogonality condition $\boldsymbol{J}_c\boldsymbol{P} = \boldsymbol{0}$ (with $\boldsymbol{J}_c$ denoting the constraint force direction, ensuring that projected dynamics remain consistent with the underlying Lagrangian structure of the constrained mechanical system.

To achieve task-space control objectives, a smooth task mapping is introduced as follows:

$$\boldsymbol{x} := \boldsymbol{f}(\boldsymbol{q}), \quad \boldsymbol{f} : \mathbb{Q} \subseteq \mathbb{R}^n \to \mathbb{R}^m,$$

which maps each configuration $\boldsymbol{q}$ to a point $\boldsymbol{x}$ in the task space. The corresponding task-space velocity is given by the standard Jacobian relationship

$$\dot{\boldsymbol{x}} = \boldsymbol{J}(\boldsymbol{q})\dot{\boldsymbol{q}} = \boldsymbol{J}(\boldsymbol{q})\boldsymbol{P}\dot{\boldsymbol{q}}, \tag{5.4}$$

where $\boldsymbol{J}(\boldsymbol{q}) = \partial\boldsymbol{f}/\partial\boldsymbol{q} \in \mathbb{R}^{m\times n}$ denotes the task Jacobian, and $\boldsymbol{P}$ is the dynamically consistent projector defined in (5.2), ensuring that only velocities compatible with the holonomic constraints are considered.

To standardize the treatment of constraints and task variables, an *extended task vector* is defined by combining the constraint functions with the task mapping:

$$\bar{\boldsymbol{x}} := \begin{bmatrix}\boldsymbol{0}\\ \boldsymbol{x}\end{bmatrix} = \underbrace{\begin{bmatrix}\boldsymbol{\phi}(\boldsymbol{q})\\ \boldsymbol{f}(\boldsymbol{q})\end{bmatrix}}_{\bar{\boldsymbol{f}}(\boldsymbol{q})}. \tag{5.5}$$

Differentiating with respect to time yields the extended velocity relation

$$\dot{\bar{\boldsymbol{x}}} = \begin{bmatrix}\boldsymbol{0}\\ \dot{\boldsymbol{x}}\end{bmatrix} = \underbrace{\begin{bmatrix}\boldsymbol{J}_c(\boldsymbol{q})\\ \boldsymbol{J}(\boldsymbol{q})\boldsymbol{P}\end{bmatrix}}_{\bar{\boldsymbol{J}}(\boldsymbol{q})}\dot{\boldsymbol{q}}, \tag{5.6}$$

[1] The argument $\boldsymbol{q}$ is suppressed in $\boldsymbol{P}(\boldsymbol{q})$, $\boldsymbol{J}_c(\boldsymbol{q})$, and $\bar{\boldsymbol{J}}(\boldsymbol{q})$ throughout this chapter for conciseness.

where $\bar{\boldsymbol{J}}(\boldsymbol{q}) \in \mathbb{R}^{n\times n}$ is referred to as the *augmented task Jacobian*. Here, $\bar{\boldsymbol{x}}$, $\dot{\bar{\boldsymbol{x}}}$, and $\bar{\boldsymbol{f}}(\boldsymbol{q})$ collectively represent the extended task position, velocity, and configuration-to-task mapping, respectively.

The following structural assumption ensures that this augmented representation is well-posed and free of kinematic singularities:

Assumption 7 (Full-Rank Extended Task Mapping)**.** *The mapping $\bar{\boldsymbol{f}}(\boldsymbol{q})$ is injective over the set*

$$\bar{\mathbb{Q}} := \left\{ \boldsymbol{q} \in \mathbb{Q} \,\middle|\, \sigma_l < \sigma_{\min}\big(\bar{\boldsymbol{J}}(\boldsymbol{q})\big) \le \sigma_{\max}\big(\bar{\boldsymbol{J}}(\boldsymbol{q})\big) < \sigma_u \right\},$$

for some constants $0 < \sigma_l < \sigma_u < \infty$. Consequently, $\bar{\boldsymbol{J}}(\boldsymbol{q})$ has full rank n for all $\boldsymbol{q} \in \bar{\mathbb{Q}}$, and is therefore invertible. This implies that (i) the task variables $\{x_i\}$ are mutually independent, (ii) each task variable is independent of the constraint functions $\{\phi_j\}$, and (iii) the combined set $\bar{\boldsymbol{x}}$ spans the entire constrained configuration manifold. Moreover, $\bar{\boldsymbol{f}}$ is assumed to be continuously differentiable with respect to $\boldsymbol{q}$.

This singularity-free workspace assumption is standard in task-space control analysis (see, e.g., [182]) and guarantees that the inverse kinematics and dynamics can be uniquely resolved. Under Assumption 7, the inverse of the augmented Jacobian admits the explicit block structure

$$\bar{\boldsymbol{J}}^{-1} = \begin{bmatrix} \boldsymbol{J}_c^{M+} & \boldsymbol{P}(\boldsymbol{J}\boldsymbol{P})^{+} \end{bmatrix}, \tag{5.7}$$

where the inertia-weighted constraint pseudoinverse $\boldsymbol{J}_c^{M+}$ is defined as in (5.3), and the task-space pseudoinverse is given by

$$\boldsymbol{P}(\boldsymbol{J}\boldsymbol{P})^{+} = \boldsymbol{P}\boldsymbol{P}^{\top}\boldsymbol{J}^{\top}\big(\boldsymbol{J}\boldsymbol{P}\boldsymbol{P}^{\top}\boldsymbol{J}^{\top}\big)^{-1}. \tag{5.8}$$

Using this inverse, joint velocities and accelerations can be expressed in terms of extended task-space variables:

$$\dot{\boldsymbol{q}} = \bar{\boldsymbol{J}}^{-1}\dot{\bar{\boldsymbol{x}}}, \tag{5.9}$$

$$\ddot{\boldsymbol{q}} = \bar{\boldsymbol{J}}^{-1}\ddot{\bar{\boldsymbol{x}}} - \bar{\boldsymbol{J}}^{-1}\dot{\bar{\boldsymbol{J}}}\bar{\boldsymbol{J}}^{-1}\dot{\bar{\boldsymbol{x}}}. \tag{5.10}$$

Substituting (5.10) into the joint-space dynamics of the compliant actuated system (cf. (5.1a)) and premultiplying by $\bar{\boldsymbol{J}}^{-\top}$ yields the intermediate task-space dynamics:

$$\boldsymbol{M}\bar{\boldsymbol{J}}^{-1}\ddot{\bar{\boldsymbol{x}}} + \Big(-\boldsymbol{M}\bar{\boldsymbol{J}}^{-1}\dot{\bar{\boldsymbol{J}}} + \boldsymbol{C}\Big)\bar{\boldsymbol{J}}^{-1}\dot{\bar{\boldsymbol{x}}} = \boldsymbol{\tau} - \boldsymbol{g} + \boldsymbol{J}_c^{\top}\boldsymbol{\lambda} + \boldsymbol{\tau}_{\text{ext}}. \tag{5.11}$$

Introducing the transformed inertia and Coriolis/centrifugal matrices,

$$\boldsymbol{\Lambda}(\boldsymbol{q}) := \bar{\boldsymbol{J}}^{-\top}\boldsymbol{M}\bar{\boldsymbol{J}}^{-1}, \quad \boldsymbol{\mu}(\boldsymbol{q},\dot{\boldsymbol{q}}) := \bar{\boldsymbol{J}}^{-\top}\big(-\boldsymbol{M}\bar{\boldsymbol{J}}^{-1}\dot{\bar{\boldsymbol{J}}} + \boldsymbol{C}\big)\bar{\boldsymbol{J}}^{-1},$$

the full open-loop task-space dynamics can be compactly written as

$$\boldsymbol{\Lambda}(\boldsymbol{q})\ddot{\bar{\boldsymbol{x}}} + \boldsymbol{\mu}(\boldsymbol{q},\dot{\boldsymbol{q}})\dot{\bar{\boldsymbol{x}}} = \bar{\boldsymbol{J}}^{-\top}\big[\boldsymbol{K}(\boldsymbol{\theta}-\boldsymbol{q}) - \boldsymbol{g} + \boldsymbol{J}_c^{\top}\boldsymbol{\lambda} + \boldsymbol{\tau}_{\text{ext}}\big]. \tag{5.12}$$

Owing to the particular structure of $\bar{\boldsymbol{J}}$, which separates constrained and unconstrained directions, the transformed inertia matrix $\boldsymbol{\Lambda}$ is block-diagonal:

$$\boldsymbol{\Lambda} = \begin{bmatrix} \boldsymbol{\Lambda}_{cc} & \boldsymbol{0} \\ \boldsymbol{0} & \boldsymbol{\Lambda}_{xx} \end{bmatrix},$$

while the Coriolis/centrifugal matrix assumes the general block form

$$\boldsymbol{\mu} = \begin{bmatrix} \boldsymbol{\mu}_{cc} & \boldsymbol{\mu}_{cx} \\ \boldsymbol{\mu}_{xc} & \boldsymbol{\mu}_{xx} \end{bmatrix}.$$

These blocks satisfy the well-known properties of mechanical systems: $\dot{\boldsymbol{\Lambda}}_{xx} = \boldsymbol{\mu}_{xx} + \boldsymbol{\mu}_{xx}^\top$ and $\boldsymbol{\mu}_{cx} = -\boldsymbol{\mu}_{xc}^\top$ (see, e.g., [95, Sec. 4.4]).

Decomposing (5.12) into constrained and unconstrained subspaces yields the following pair of equations:

$$\boldsymbol{\lambda} = \boldsymbol{\mu}_{cx}\dot{\boldsymbol{x}} - (\boldsymbol{J}_c^{M+})^\top \big[\boldsymbol{K}(\boldsymbol{\theta} - \boldsymbol{q}) - \boldsymbol{g}\big] - \boldsymbol{\lambda}_{\text{ext}}, \tag{5.13a}$$

$$\boldsymbol{\Lambda}_{xx}\ddot{\boldsymbol{x}} + \boldsymbol{\mu}_{xx}\dot{\boldsymbol{x}} = [\boldsymbol{P}(\boldsymbol{J}\boldsymbol{P})^+]^\top \big[\boldsymbol{K}(\boldsymbol{\theta} - \boldsymbol{q}) - \boldsymbol{g}\big] + \boldsymbol{F}_{\text{ext}}. \tag{5.13b}$$

Here, the generalized external joint torque $\boldsymbol{\tau}_{\text{ext}}$ is decomposed according to the dual spaces induced by the constraints and the task:

$$\boldsymbol{\tau}_{\text{ext}} = \boldsymbol{J}_c^\top \boldsymbol{\lambda}_{\text{ext}} + (\boldsymbol{J}\boldsymbol{P})^\top \boldsymbol{F}_{\text{ext}}, \tag{5.14}$$

where $\boldsymbol{F}_{\text{ext}} \in \mathbb{R}^m$ and $\boldsymbol{\lambda}_{\text{ext}} \in \mathbb{R}^{n-m}$ represent $\mathcal{C}^1$-continuous disturbances acting in the unconstrained (task) and constrained subspaces, respectively.

5.3 Control Objectives and Design

The control strategy developed in this work aims to simultaneously achieve three key objectives:

(i) Passive, asymptotically stable task-space motion tracking,

(ii) Robust force tracking with rejection of constant disturbances, and

(iii) Preservation of the system's intrinsic elastic and inertial structure throughout the closed-loop dynamics,

These goals are pursued within a framework that respects the physical nature of elastic-joint mechanical systems, avoiding aggressive cancellation of natural dynamics while ensuring performance through structural augmentation.

5.3.1 Desired Closed-Loop Dynamics

The proposed control architecture follows the Elastic Structure Preserving (ESP) philosophy introduced in [113], which transforms an underactuated flexible-joint system into a quasi fully-actuated one by leveraging its inherent elasticity rather than suppressing it. Within this paradigm, the reference trajectories for task position and constraint force are assumed to satisfy the following regularity condition:

Assumption 8 (Smoothness and Boundedness of Reference Trajectories)**.** *The desired task trajectory $\boldsymbol{x}_d(t)$ is four times continuously differentiable ($\boldsymbol{x}_d \in \mathcal{C}^4$) with uniformly bounded derivatives up to the fourth order:*

$$\|\dot{\boldsymbol{x}}_d(t)\|, \ldots, \|\boldsymbol{x}_d^{(4)}(t)\| \leq c_x < \infty.$$

Similarly, the desired constraint force trajectory $\boldsymbol{\lambda}_d(t)$ is twice continuously differentiable ($\boldsymbol{\lambda}_d \in \mathcal{C}^2$) with bounded first and second time derivatives:

$$\|\dot{\boldsymbol{\lambda}}_d(t)\|, \|\ddot{\boldsymbol{\lambda}}_d(t)\| \leq c_\lambda < \infty.$$

Under this assumption, the desired closed-loop dynamics is prescribed by:

$$\tilde{\boldsymbol{\lambda}} = -\boldsymbol{K}_I \int_0^t \tilde{\boldsymbol{\lambda}}(\tau)\, d\tau - (\boldsymbol{J}_c^{M+})^\top \boldsymbol{\psi}(\boldsymbol{\eta}, \tilde{\boldsymbol{x}}) + \boldsymbol{\mu}_{cx}\dot{\tilde{\boldsymbol{x}}} - \boldsymbol{\lambda}_{\text{ext}}, \quad (5.15a)$$

$$\boldsymbol{\Lambda}_{xx}\ddot{\tilde{\boldsymbol{x}}} + (\boldsymbol{\mu}_{xx} + \boldsymbol{D}_x)\dot{\tilde{\boldsymbol{x}}} + \boldsymbol{K}_x\tilde{\boldsymbol{x}} = [\boldsymbol{P}(\boldsymbol{J}\boldsymbol{P})^+]^\top \boldsymbol{\psi}(\boldsymbol{\eta}, \tilde{\boldsymbol{x}}) + \boldsymbol{F}_{\text{ext}}, \quad (5.15b)$$

$$\boldsymbol{B}\ddot{\boldsymbol{\eta}} + \boldsymbol{\psi}(\boldsymbol{\eta}, \tilde{\boldsymbol{x}}) = -\boldsymbol{D}_\eta\dot{\boldsymbol{\eta}}, \quad (5.15c)$$

where $\boldsymbol{K}_I, \boldsymbol{K}_x, \boldsymbol{D}_x, \boldsymbol{D}_\eta \succ 0$ are positive-definite gain matrices, and the elastic torque error is defined as

$$\boldsymbol{\psi}(\boldsymbol{\eta}, \tilde{\boldsymbol{x}}) := \boldsymbol{K}\big(\boldsymbol{\eta} - \boldsymbol{G}(\tilde{\boldsymbol{x}})\big).$$

Here, $\boldsymbol{\eta} \in \mathbb{R}^n$ denotes a *virtual motor coordinate*, whose role will be clarified in Section 5.3.3. The tracking errors are defined as

$$\tilde{\boldsymbol{x}} := \boldsymbol{f}(\boldsymbol{q}) - \boldsymbol{x}_d, \quad (5.16)$$

$$\tilde{\boldsymbol{\lambda}} := \boldsymbol{\lambda} - \boldsymbol{\lambda}_d, \quad (5.17)$$

with corresponding velocity and acceleration errors given by

$$\dot{\tilde{\boldsymbol{x}}} = \boldsymbol{J}\dot{\boldsymbol{q}} - \dot{\boldsymbol{x}}_d,$$
$$\ddot{\tilde{\boldsymbol{x}}} = \boldsymbol{J}\ddot{\boldsymbol{q}} + \dot{\boldsymbol{J}}\dot{\boldsymbol{q}} - \ddot{\boldsymbol{x}}_d.$$

To express the dynamics solely in terms of the error variable $\tilde{\boldsymbol{x}}$, an implicit inverse kinematics mapping $\boldsymbol{G} : \mathbb{R}^m \to \bar{\mathbb{Q}}$ is introduced, which is defined as

$$\boldsymbol{G}(\tilde{\boldsymbol{x}}) := \bar{\boldsymbol{f}}^{-1}\big(\operatorname{col}[\boldsymbol{0}, \boldsymbol{x}]\big) - \bar{\boldsymbol{f}}^{-1}\big(\operatorname{col}[\boldsymbol{0}, \boldsymbol{x}_d]\big), \quad (5.18)$$

where $\bar{\boldsymbol{f}}(\boldsymbol{q}) = \operatorname{col}[\boldsymbol{\phi}(\boldsymbol{q}), \boldsymbol{f}(\boldsymbol{q})]$. By Assumption 7, $\bar{\boldsymbol{f}}$ is locally invertible, ensuring that $\boldsymbol{G}$ is well-defined in a neighborhood of the desired trajectory. Importantly, $\boldsymbol{G}$ is used only for conceptual clarity in formulating the desired dynamics; no explicit computation of $\boldsymbol{G}$ is required in the final controller implementation.

The motion control objective (i) is realized by augmenting the open-loop task dynamics (5.13b) with a linear spring-damper pair $(\boldsymbol{K}_x, \boldsymbol{D}_x)$ and pseudo-feedforward terms that ensure asymptotic tracking without altering the underlying inertia structure. Similarly, the force control objective (ii) addresses the fundamental challenge posed by flexible joints: unlike rigid-joint systems, the elastic coupling $\boldsymbol{K}(\boldsymbol{\theta} - \boldsymbol{q})$ cannot be directly commanded, making exact force tracking infeasible without high-gain or derivative feedback. To circumvent this, a robust integral action on the force error is adopted, introducing the term $-\boldsymbol{K}_I \int \tilde{\boldsymbol{\lambda}}\, dt$ to reject constant disturbances, while retaining the cross-coupling Coriolis term $\boldsymbol{\mu}_{cx}\dot{\tilde{\boldsymbol{x}}}$ to preserve dynamic consistency. Feedforward of $\boldsymbol{\lambda}_d$ and $\boldsymbol{\mu}_{cx}\dot{\boldsymbol{x}}_d$ further enhances tracking fidelity. The resulting closed-loop equations (5.15a)–(5.15c) retain the original system's:

- Inertial properties (via $\boldsymbol{\Lambda}_{xx}, \boldsymbol{\mu}_{xx}$),
- Elastic coupling structure (via $\boldsymbol{\psi}$),

- Natural motion-force interaction (via $\boldsymbol{\mu}_{cx}$).

Finally, the motor dynamics (5.15c) are augmented with viscous damping $\boldsymbol{D}_\eta$ to enhance robustness against motor-side disturbances, completing the passive stabilization of the full cascade. For notational convenience, the extended reference vector is defined as $\bar{\boldsymbol{x}}_d := \mathrm{col}[\boldsymbol{0}, \boldsymbol{x}_d]$.

5.3.2 Equilibrium Analysis

To facilitate stability analysis, differentiating (5.15a) leads to a first-order representation of the force error dynamics:

$$\dot{\tilde{\boldsymbol{\lambda}}} + \boldsymbol{K}_I \tilde{\boldsymbol{\lambda}} = \boldsymbol{h}_2(\tilde{\boldsymbol{x}}, \dot{\tilde{\boldsymbol{x}}}, \boldsymbol{\eta}, \dot{\boldsymbol{\eta}}) - \dot{\boldsymbol{\lambda}}_{\text{ext}}, \tag{5.19}$$

where

$$\boldsymbol{h}_2 = \boldsymbol{\mu}_{cx}\ddot{\tilde{\boldsymbol{x}}} + \dot{\boldsymbol{\mu}}_{cx}\dot{\tilde{\boldsymbol{x}}} - \frac{d}{dt}\Big[(\boldsymbol{J}_c^{M+})^\top \boldsymbol{\psi}(\boldsymbol{\eta}, \tilde{\boldsymbol{x}})\Big].$$

Notably, substituting $\ddot{\tilde{\boldsymbol{x}}}$ from (5.15b) ensures that $\boldsymbol{h}_2$ depends only on positions and velocities. Define the composite state vector

$$\boldsymbol{z} := \mathrm{col}\left[\tilde{\boldsymbol{x}},\, \dot{\tilde{\boldsymbol{x}}},\, \boldsymbol{\eta},\, \dot{\boldsymbol{\eta}},\, \tilde{\boldsymbol{\lambda}}\right].$$

Setting $\dot{\boldsymbol{z}} = \boldsymbol{0}$ and assuming zero external disturbances ($\boldsymbol{F}_{\text{ext}} = \boldsymbol{0}$, $\dot{\boldsymbol{\lambda}}_{\text{ext}} = \boldsymbol{0}$), the equilibrium conditions reduce to:

$$\boldsymbol{K}_I \tilde{\boldsymbol{\lambda}} = \boldsymbol{0}, \tag{5.20}$$

$$\boldsymbol{\psi}(\boldsymbol{\eta}, \tilde{\boldsymbol{x}}) = \boldsymbol{0}, \tag{5.21}$$

$$\boldsymbol{K}_x \tilde{\boldsymbol{x}} = [\boldsymbol{P}(\boldsymbol{J}\boldsymbol{P})^+]^\top \boldsymbol{\psi}(\boldsymbol{\eta}, \tilde{\boldsymbol{x}}). \tag{5.22}$$

From (5.20), $\tilde{\boldsymbol{\lambda}} = \boldsymbol{0}$. Equation (5.21) implies $\boldsymbol{\eta} = \boldsymbol{G}(\tilde{\boldsymbol{x}})$. Substituting into (5.22) yields $\boldsymbol{K}_x \tilde{\boldsymbol{x}} = \boldsymbol{0}$, and since $\boldsymbol{K}_x \succ 0$, it follows that $\tilde{\boldsymbol{x}} = \boldsymbol{0}$. By definition of $\boldsymbol{G}$ in (5.18), $\boldsymbol{G}(\boldsymbol{0}) = \boldsymbol{0}$, hence $\boldsymbol{\eta} = \boldsymbol{0}$. Therefore, the unique equilibrium of the closed-loop system is the origin:

$$\boldsymbol{z} = \boldsymbol{0}.$$

5.3.3 Coordinate Transformation

The controller is constructed via a change of variables from the physical motor coordinates $\boldsymbol{\theta}$ to the virtual coordinates $\boldsymbol{\eta}$. This transformation is designed so that the actual open-loop dynamics (5.13a)–(5.13b) match the desired closed-loop dynamics (5.15a)–(5.15b) when expressed in terms of $\boldsymbol{\eta}$. Specifically, the equivalence is imposed by

$$\boldsymbol{K}(\boldsymbol{\theta} - \boldsymbol{q}) := \boldsymbol{\psi}(\boldsymbol{\eta}, \tilde{\boldsymbol{x}}) + \boldsymbol{\tau}_d, \tag{5.23}$$

where the auxiliary term $\boldsymbol{\tau}_d$ encapsulates the control actions necessary to achieve tracking:

$$\boldsymbol{\tau}_d = \boldsymbol{J}_c^\top \Big[-\boldsymbol{\lambda}_d + \boldsymbol{K}_I \int_0^t \tilde{\boldsymbol{\lambda}}(\tau)\,\mathrm{d}\tau + \boldsymbol{\mu}_{cx}\dot{\boldsymbol{x}}_d \Big] + (\boldsymbol{J}\boldsymbol{P})^\top \Big[\boldsymbol{\Lambda}_{xx}\ddot{\boldsymbol{x}}_d + \boldsymbol{\mu}_{xx}\dot{\boldsymbol{x}}_d - \boldsymbol{K}_x\tilde{\boldsymbol{x}} - \boldsymbol{D}_x\dot{\tilde{\boldsymbol{x}}} \Big] + \boldsymbol{g}. \tag{5.24}$$

This term comprises three physically interpretable components:

1. A force controller (integral action + feedforward) acting in the constrained subspace,

2. A task-space PD+ controller acting in the unconstrained subspace,

3. Joint-space gravity compensation.

Differentiating (5.23) requires care due to the implicit dependence of $\boldsymbol{G}(\tilde{\boldsymbol{x}})$ on $\boldsymbol{q}$. Utilizing the chain rule and the identity $\dot{\tilde{\boldsymbol{x}}} = \bar{\boldsymbol{J}}\dot{\boldsymbol{q}}$ leads to

$$\dot{\boldsymbol{G}}(\tilde{\boldsymbol{x}}) = \bar{\boldsymbol{J}}^{-1}\dot{\tilde{\boldsymbol{x}}} - \bar{\boldsymbol{J}}^{-1}\dot{\tilde{\boldsymbol{x}}}_d = \dot{\boldsymbol{q}} - \boldsymbol{a},$$

where the reference velocity is written as

$$\boldsymbol{a} := \bar{\boldsymbol{J}}^{-1}\dot{\tilde{\boldsymbol{x}}}_d, \quad \dot{\boldsymbol{a}} = -\bar{\boldsymbol{J}}^{-1}\dot{\bar{\boldsymbol{J}}}\bar{\boldsymbol{J}}^{-1}\dot{\tilde{\boldsymbol{x}}}_d + \bar{\boldsymbol{J}}^{-1}\ddot{\tilde{\boldsymbol{x}}}_d,$$

with $\ddot{\tilde{\boldsymbol{x}}}_d = \mathrm{col}[\boldsymbol{0}, \ddot{\boldsymbol{x}}_d]$.

Consequently, the physical motor velocity and acceleration are related to the virtual ones by

$$\dot{\boldsymbol{\theta}} = \dot{\boldsymbol{\eta}} + \boldsymbol{a} + \boldsymbol{K}^{-1}\dot{\boldsymbol{\tau}}_d, \tag{5.25a}$$

$$\ddot{\boldsymbol{\theta}} = \ddot{\boldsymbol{\eta}} + \dot{\boldsymbol{a}} + \boldsymbol{K}^{-1}\ddot{\boldsymbol{\tau}}_d. \tag{5.25b}$$

Implementation of this transformation requires access to higher-order derivatives and constraint forces, which are obtained via model-based reconstruction, as detailed in the following remark.

Remark 11 (Computation of Higher-Order Signals)**.** *The term $\ddot{\boldsymbol{n}}$ involves the task jerk $\boldsymbol{x}^{(3)} = \boldsymbol{J}\boldsymbol{q}^{(3)} + 2\dot{\boldsymbol{J}}\ddot{\boldsymbol{q}} + \ddot{\boldsymbol{J}}\dot{\boldsymbol{q}}$. The joint jerk $\boldsymbol{q}^{(3)}$ is computed by differentiating the joint-space dynamics:*

$$\boldsymbol{q}^{(3)} = \boldsymbol{M}^{-1}\Big[\boldsymbol{K}(\dot{\boldsymbol{\theta}} - \dot{\boldsymbol{q}}) + \dot{\boldsymbol{J}}_c^\top\boldsymbol{\lambda} + \boldsymbol{J}_c^\top\dot{\boldsymbol{\lambda}} + \dot{\boldsymbol{\tau}}_{ext} - \dot{\boldsymbol{M}}\ddot{\boldsymbol{q}} - \dot{\boldsymbol{C}}\dot{\boldsymbol{q}} - \boldsymbol{C}\ddot{\boldsymbol{q}} - \dot{\boldsymbol{g}}\Big].$$

The constraint force $\boldsymbol{\lambda}$ may be measured directly or estimated from the dynamics:

$$\boldsymbol{\lambda} = (\boldsymbol{J}_c\boldsymbol{M}^{-1}\boldsymbol{J}_c^\top)^{-1}\boldsymbol{J}_c\boldsymbol{M}^{-1}\big[\boldsymbol{C}\dot{\boldsymbol{q}} + \boldsymbol{g} - \boldsymbol{K}(\boldsymbol{\theta} - \boldsymbol{q}) - \boldsymbol{\tau}_{ext}\big] - (\boldsymbol{J}_c\boldsymbol{M}^{-1}\boldsymbol{J}_c^\top)^{-1}\dot{\boldsymbol{J}}_c\dot{\boldsymbol{q}}.$$

These computations rely only on measurable or reconstructable signals and known model parameters, ensuring practical implementability.

5.3.4 Controller Design

The complete control architecture is illustrated in Figure 5.1. The scheme implements the coordinate transformation and dynamic augmentation described in the previous sections, with all higher-order derivatives (e.g., jerk, force rates) computed via model-based reconstruction as detailed in Remark 11. Analytical differentiation blocks (denoted by $\frac{\mathrm{d}}{\mathrm{d}t}$) operate on reference or error signals, ensuring compatibility with the desired closed-loop structure without reliance on numerical differentiation. To derive the control law, substituting the motor acceleration transformation (5.25b) into the original motor dynamics (cf. (5.1b)), yields the intermediate expression

$$\boldsymbol{B}\ddot{\boldsymbol{\eta}} + \boldsymbol{B}\dot{\boldsymbol{a}} + \boldsymbol{B}\boldsymbol{K}^{-1}\ddot{\boldsymbol{\tau}}_d + \boldsymbol{K}(\boldsymbol{\theta} - \boldsymbol{q}) = \boldsymbol{u}. \tag{5.26}$$

Recalling the elastic coupling identity (5.23), namely $\boldsymbol{K}(\boldsymbol{\theta} - \boldsymbol{q}) = \psi(\boldsymbol{\eta}, \tilde{\boldsymbol{x}}) + \boldsymbol{\tau}_d$, and selecting the control input as

$$\boldsymbol{u} = \boldsymbol{B}\boldsymbol{K}^{-1}\ddot{\boldsymbol{\tau}}_d + \boldsymbol{B}\dot{\boldsymbol{a}} + \boldsymbol{\tau}_d - \boldsymbol{D}_\eta\dot{\boldsymbol{\eta}}, \tag{5.27}$$

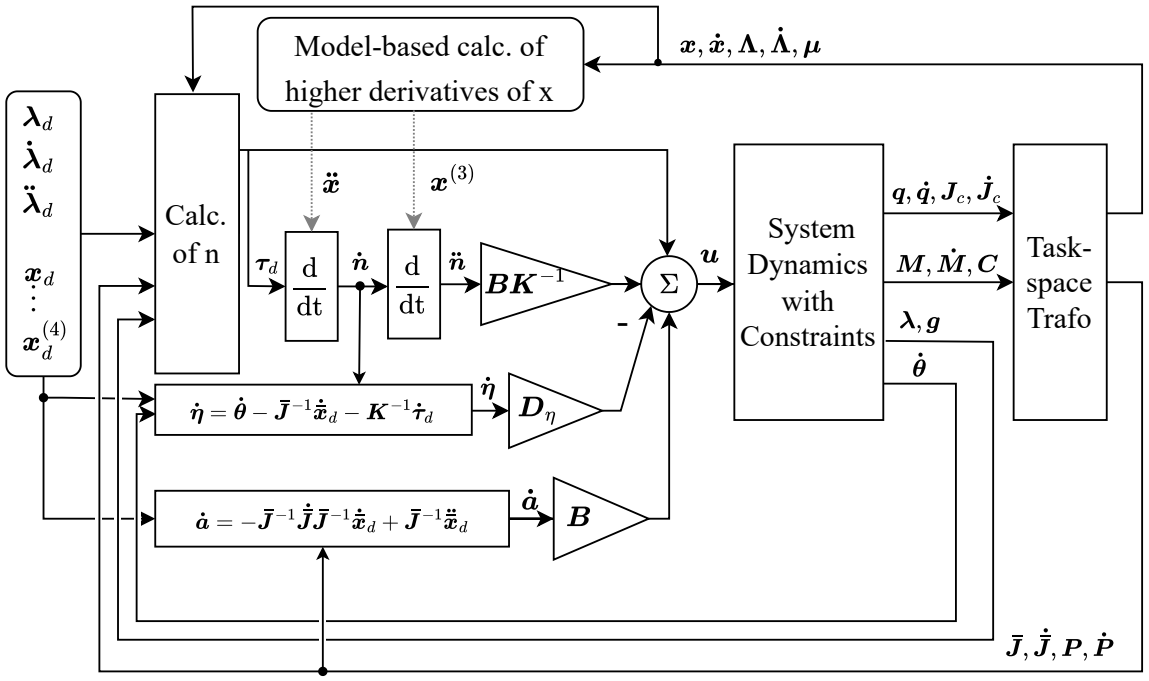


Figure 5.1: Proposed control architecture. The block $\frac{\mathrm{d}}{\mathrm{d}t}$ represents analytical time differentiation of its input signal. Higher-order derivatives required for implementation are obtained through model-based computation, as outlined in Remark 11.

the intermediate dynamics (5.26) simplify precisely to the desired motor equation (5.15c):

$$\boldsymbol{B}\ddot{\boldsymbol{\eta}} + \boldsymbol{\psi}(\boldsymbol{\eta}, \tilde{\boldsymbol{x}}) = -\boldsymbol{D}_\eta \dot{\boldsymbol{\eta}}.$$

The complete control architecture is illustrated in Figure 5.1. Notably, the only free design parameters are the stiffness-like gains $\boldsymbol{K}_I$ (for force error integral action) and $\boldsymbol{K}_x$ (for task-space position regulation). The damping matrices $\boldsymbol{D}_x$ and $\boldsymbol{D}_\eta$ are not tuned heuristically but are instead computed via the modal damping method [183], which relates damping to the closed-loop inertia and stiffness properties through a dimensionless modal damping factor $\xi \in [0, 1]$. In practice, $\xi = 1$ is chosen, corresponding to critical damping of the dominant error modes. Under this choice:

- The convergence rate of the task-position error $\tilde{\boldsymbol{x}}$ and the virtual motor error $\boldsymbol{\eta}$ is primarily governed by $\boldsymbol{K}_x$,
- The convergence rate of the constraint-force error $\tilde{\boldsymbol{\lambda}}$ is predominantly determined by $\boldsymbol{K}_I$ and also affected by the convergence rate of the task-position error.

This systematic tuning procedure eliminates the need for ad hoc damping selection and ensures well-damped transient responses without oscillatory behavior, consistent with the passive design philosophy underpinning the ESP framework.

5.4 Passivity and Stability Analysis

This section establishes the passivity properties and asymptotic stability of the closed-loop system formed by the original flexible-joint dynamics (cf. (5.1a)–(5.1c)) under the proposed control

law (5.27). The analysis proceeds in two parts: First, it is shown that the closed-loop system is *output strictly passive* concerning physically meaningful input-output pairs. Additionally, the *uniform asymptotic stability* of the equilibrium is established under zero external disturbances.

5.4.1 Output Strict Passivity (OSP)

The process begins by constructing a storage function that effectively captures the total energy of the error dynamics in both task and virtual motor coordinates. Consider the candidate Lyapunov-like function

$$S = \frac{1}{2}\dot{\tilde{\boldsymbol{x}}}^\top \boldsymbol{\Lambda}_{xx}\dot{\tilde{\boldsymbol{x}}} + \frac{1}{2}\dot{\boldsymbol{\eta}}^\top \boldsymbol{B}\dot{\boldsymbol{\eta}} + \frac{1}{2}\tilde{\boldsymbol{x}}^\top \boldsymbol{K}_x\tilde{\boldsymbol{x}} + U_e(\boldsymbol{\eta} - \boldsymbol{G}(\tilde{\boldsymbol{x}})), \tag{5.28}$$

where the elastic potential energy is defined as

$$U_e(\boldsymbol{\eta} - \boldsymbol{G}(\tilde{\boldsymbol{x}})) := \frac{1}{2}(\boldsymbol{\eta} - \boldsymbol{G}(\tilde{\boldsymbol{x}}))^\top \boldsymbol{K}(\boldsymbol{\eta} - \boldsymbol{G}(\tilde{\boldsymbol{x}})).$$

This function aggregates kinetic energy in the task and motor error velocities, potential energy from the regulation springs, and stored energy in the closed-loop elastic coupling. The following proposition characterizes the passivity of the resulting closed-loop system.

Proposition 6 (Output Strict Passivity)**.** *The closed-loop dynamics* (5.15b)–(5.15c) *define an output strictly passive map from the external disturbance input* $\boldsymbol{F}_{ext}$ *to the task-velocity tracking error output* $\dot{\tilde{\boldsymbol{x}}}$*.*

Proof. Differentiating the storage function S along trajectories of the closed-loop system yields

$$\dot{S} = \dot{\tilde{\boldsymbol{x}}}^\top \boldsymbol{\Lambda}_{xx}\ddot{\tilde{\boldsymbol{x}}} + \frac{1}{2}\dot{\tilde{\boldsymbol{x}}}^\top \dot{\boldsymbol{\Lambda}}_{xx}\dot{\tilde{\boldsymbol{x}}} + \dot{\boldsymbol{\eta}}^\top \boldsymbol{B}\ddot{\boldsymbol{\eta}} + \tilde{\boldsymbol{x}}^\top \boldsymbol{K}_x\dot{\tilde{\boldsymbol{x}}} - \left(\dot{\boldsymbol{\eta}} - \dot{\boldsymbol{G}}(\tilde{\boldsymbol{x}})\right)^\top \boldsymbol{\psi},$$

where $\boldsymbol{\psi} = \boldsymbol{K}(\boldsymbol{\eta} - \boldsymbol{G}(\tilde{\boldsymbol{x}}))$. Using the identity $\dot{\boldsymbol{\Lambda}}_{xx} = \boldsymbol{\mu}_{xx} + \boldsymbol{\mu}_{xx}^\top$ (cf. [95, Sec. 4.4]), and substituting the closed-loop dynamics (5.15b) and (5.15c) leads to

$$\dot{S} = \dot{\tilde{\boldsymbol{x}}}^\top \boldsymbol{F}_{\text{ext}} - \dot{\tilde{\boldsymbol{x}}}^\top \boldsymbol{D}_x\dot{\tilde{\boldsymbol{x}}} - \dot{\boldsymbol{\eta}}^\top \boldsymbol{D}_\eta\dot{\boldsymbol{\eta}} + \dot{\boldsymbol{G}}^\top \boldsymbol{\psi}.$$

Crucially, the term $\dot{\boldsymbol{G}}^\top \boldsymbol{\psi}$ represents the power exchanged through the implicit kinematic mapping. Recalling that

$$\dot{\boldsymbol{G}}(\tilde{\boldsymbol{x}}) = \bar{\boldsymbol{J}}^{-1}\begin{bmatrix}\boldsymbol{0}\\ \dot{\tilde{\boldsymbol{x}}}\end{bmatrix}, \quad \bar{\boldsymbol{J}}^{-1} = \begin{bmatrix}\boldsymbol{J}_c^{M+} & \boldsymbol{P}(\boldsymbol{J}\boldsymbol{P})^+\end{bmatrix},$$

it follows that

$$\dot{\boldsymbol{G}}^\top \boldsymbol{\psi} = \dot{\tilde{\boldsymbol{x}}}^\top [\boldsymbol{P}(\boldsymbol{J}\boldsymbol{P})^+]^\top \boldsymbol{\psi}. \tag{5.29}$$

This term appears with opposite sign in the expression for $\dot{S}$ and precisely cancels the corresponding elastic coupling term in the task dynamics (5.15b). After cancellation, the time derivative of the storage function is then:

$$\dot{S} = \dot{\tilde{\boldsymbol{x}}}^\top \boldsymbol{F}_{\text{ext}} - \dot{\tilde{\boldsymbol{x}}}^\top \boldsymbol{D}_x\dot{\tilde{\boldsymbol{x}}} - \dot{\boldsymbol{\eta}}^\top \boldsymbol{D}_\eta\dot{\boldsymbol{\eta}} \leq \dot{\tilde{\boldsymbol{x}}}^\top \boldsymbol{F}_{\text{ext}}, \tag{5.30}$$

since $\boldsymbol{D}_x, \boldsymbol{D}_\eta \succ 0$. This inequality confirms that the system is *output strictly passive* from $\boldsymbol{F}_{\text{ext}}$ to $\dot{\tilde{\boldsymbol{x}}}$, with strict dissipation in the absence of external disturbances. □

Remark 12. *In the regulation case (*$\dot{\boldsymbol{x}}_d = \boldsymbol{0}$*), the term* $\dot{\tilde{\boldsymbol{x}}}^\top \boldsymbol{F}_{ext}$ *corresponds to the physical power injected into the system through environmental interaction.*

5.4.2 Uniform Asymptotic Stability (UAS)

The local uniform asymptotic stability of the equilibrium $\boldsymbol{z} = \mathbf{0}$ is established under the assumption that external disturbances vanish, specifically, $\boldsymbol{F}_{\text{ext}} = \mathbf{0}$ and $\dot{\boldsymbol{\lambda}}_{\text{ext}} = \mathbf{0}$. Due to the requirement of a non-singular task Jacobian (Assumption 7), the domain of attraction is necessarily restricted to a neighborhood of the desired trajectory within the singularity-free workspace $\bar{\mathbb{Q}}$, a standard limitation in task-space control (see, e.g., [182]).

To facilitate the analysis, the full state vector is partitioned as

$$\boldsymbol{z} = \text{col}[\boldsymbol{z}_1,\ \boldsymbol{z}_2] \in \mathbb{R}^{3n+m}, \tag{5.31}$$

with

$$\boldsymbol{z}_1 := \text{col}[\tilde{\boldsymbol{x}},\ \dot{\tilde{\boldsymbol{x}}},\ \boldsymbol{\eta},\ \dot{\boldsymbol{\eta}}] \in \mathbb{R}^{2n+2m}, \tag{5.32}$$

$$\boldsymbol{z}_2 := \tilde{\boldsymbol{\lambda}} \in \mathbb{R}^{n-m}. \tag{5.33}$$

The closed-loop dynamics can then be expressed as a cascaded (or hierarchical) system:

$$\dot{\boldsymbol{z}}_1 = \boldsymbol{f}_1(t, \boldsymbol{z}_1), \tag{5.34}$$

$$\dot{\boldsymbol{z}}_2 = -\boldsymbol{K}_I \boldsymbol{z}_2 + \boldsymbol{h}_2(t, \boldsymbol{z}_1), \tag{5.35}$$

where $\boldsymbol{h}_2(t, \boldsymbol{z}_1)$ is continuous and vanishes at the origin (cf. (5.19)). This structure matches the form considered in Vidyasagar's framework for interconnected systems [184, Eq. (2.2)].

Proposition 7 (Uniform Asymptotic Stability)**.** *Under Assumptions 7–8, the equilibrium $\boldsymbol{z} = \mathbf{0}$ of the closed-loop system* (5.34)–(5.35) *is uniformly asymptotically stable when $(\boldsymbol{F}_{ext}, \dot{\boldsymbol{\lambda}}_{ext}) = (\mathbf{0}, \mathbf{0})$.*

Proof. The proof follows from Theorem 3.1 in [184] (see Appendix A.1), which provides sufficient conditions for UAS of cascaded systems. The following steps are required to verify:

1. *Continuous differentiability*: The vector fields $\boldsymbol{f}_1$ and $\boldsymbol{h}_2$ are continuously differentiable in a neighborhood of the origin due to the smoothness of the robot dynamics and the $\mathcal{C}^4$ continuity of the reference trajectories (Assumption 8).

2. *Uniform asymptotic stability of the driving subsystem*: The subsystem (5.34) is autonomous and isolated. Using Matrosov's theorem [185], and leveraging the strict dissipation established in (5.30) (with $\boldsymbol{F}_{\text{ext}} = \mathbf{0}$), one can construct a Matrosov function to show that $\boldsymbol{z}_1 = \mathbf{0}$ is uniformly asymptotically stable within the domain $\bar{\mathbb{Q}}$. A concise proof is provided in Appendix A.2.

3. *Uniform asymptotic stability of the driven subsystem*: Setting $\boldsymbol{z}_1 = \mathbf{0}$ in (5.35) yields $\boldsymbol{h}_2(t, \mathbf{0}) = \mathbf{0}$, reducing the force-error dynamics to

$$\dot{\boldsymbol{z}}_2 = -\boldsymbol{K}_I \boldsymbol{z}_2.$$

   Since $\boldsymbol{K}_I \succ 0$, this linear system is exponentially (hence uniformly asymptotically) stable.

By Vidyasagar's theorem [184], the cascade is uniformly asymptotically stable at the origin, completing the proof. □

5.5 Case Study: A Constrained Dual-Arm System

To validate the proposed control framework, a planar dual-manipulator system subject to a holonomic kinematic constraint is examined, as depicted in Figure 5.2. Each arm is actuated by series elastic actuators (SEAs), represented by the large red dots, with identical joint stiffnesses. The mechanical structure consists of four rigid links: two proximal links (AB and EF) of mass 6 kg each, and two distal links (BC and DE) of mass 1 kg each. All links have uniform mass distribution, so their centers of mass lie at their geometric midpoints. The total length of each link is 0.3 m.

The motion of the two end-effectors, which are denoted C and D, is constrained by a massless rigid bar, enforcing a fixed distance between them. This introduces a single scalar holonomic constraint,

$$\phi(\boldsymbol{q}) = \left\|\boldsymbol{x}_C(\boldsymbol{q}) - \boldsymbol{x}_D(\boldsymbol{q})\right\| - \ell_0 = 0, \tag{5.36}$$

where ℓ_0 is the prescribed constant length. As a result, the originally unconstrained system with $n = 4$ DoFs is reduced to $m = n - 1 = 3$ independent DoFs. The associated Lagrange multiplier λ represents the internal reaction force transmitted through the constraint bar—interpreted physically as the manipulation force along the connecting rod. The task space is defined by the Cartesian coordinates that specify both the position and orientation of the end-effector C:

$$\boldsymbol{x} = \begin{bmatrix} f_x(\boldsymbol{q}) \\ f_y(\boldsymbol{q}) \\ q_1 + q_2 + q_\alpha(\boldsymbol{q}) \end{bmatrix} \in \mathbb{R}^3, \tag{5.37}$$

where $q_\alpha(\boldsymbol{q})$ accounts for the relative orientation induced by the closed-loop kinematics. The full schematic, including sample configurations along an elliptical reference trajectory, is shown in Figure 5.2(b).

All joints are equipped with SEAs characterized by identical diagonal stiffness

$$\boldsymbol{K} = \mathrm{diag}(K_1, K_2, K_3, K_4), \quad K_i = 800\ \mathrm{Nm/rad}, \quad i = 1, \ldots, 4.$$

The system dynamics—including inertia, Coriolis, and Jacobian matrices—are computed using the recursive algorithms described in [186].

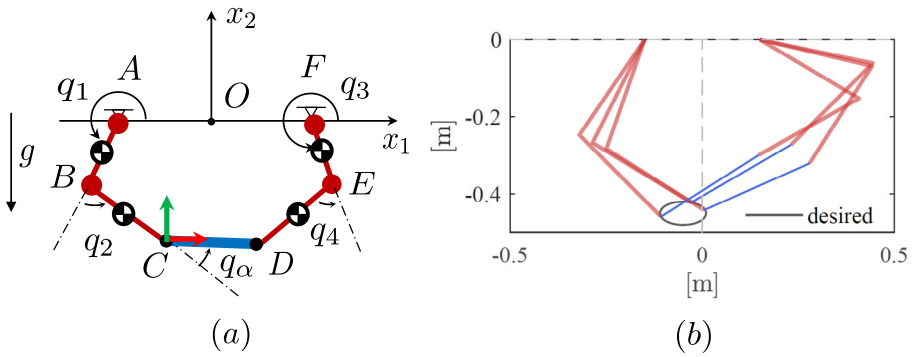


Figure 5.2: (a) Schematic of the constrained two-arm system with SEAs (red dots). Links AB and EF have mass 6 kg; BC and DE have mass 1 kg. A massless rigid bar enforces a constant distance between end-effectors C and D. (b) Sequence of configurations tracking an elliptical reference trajectory (black curve). © 2022 IEEE

5.5.1 Reference Trajectories and Disturbance

The desired motion and force trajectories are designed to be sufficiently smooth to satisfy Assumption 8:

1. *Task-space motion*: The end-effector follows a frequency-modulated elliptical path with time-varying angular velocity:
$$\boldsymbol{x}_d(t) = \begin{bmatrix} r_a \cos(\omega(t)t) + c_a \\ r_b \sin(\omega(t)t) + c_b \\ \Delta\alpha_0 \sin(\omega_0 t) + \alpha_0 \end{bmatrix}, \tag{5.38}$$
where the instantaneous frequency is given by a smooth sigmoidal transition:
$$\omega(t) = \frac{\Delta\omega_0}{1 + e^{\left(-(t-h_0)\right)}} + \omega_0.$$

2. *Constraint force*: The desired internal force is a sinusoidal signal:
$$\lambda_d(t) = \lambda_0 \sin(\omega_\lambda t). \tag{5.39}$$

The numerical values of all trajectory parameters are listed in Table 5.1.

Table 5.1: Parameters for the desired motion and force trajectories.

$r_a = 0.06$ m	$r_b = 0.03$ m	$c_a = -0.05$ m	$c_b = -0.45$ m
$\alpha_0 = 6.64$ rad	$\Delta\alpha_0 = 0.2$ rad	$\Delta\omega_0 = 2.5\pi$ rad/s	$\omega_0 = 0.2\pi$ rad/s
$h_0 = 4$ s	$\lambda_0 = 10$ N	$\omega_\lambda = 2\pi$ rad/s	

To evaluate robustness, external disturbances are injected into both the constrained and unconstrained subspaces. The disturbance in the constraint force channel is modeled as a smoothed step function:
$$\lambda_{\text{ext}}(t) = \begin{cases} \dfrac{a_0}{\sigma_0\sqrt{2\pi}} e^{\left(-\frac{1}{2}\left(\frac{t-h_0}{\sigma_0}\right)^2\right)} & t < h_0, \\ a_0 & \text{otherwise}, \end{cases} \tag{5.40}$$
ensuring $\mathcal{C}^1$-continuity at $t = h_0$. The task-space disturbance is a damped oscillatory signal:
$$\boldsymbol{F}_{\text{ext}}(t) = \begin{bmatrix} a_1 \\ a_2 \\ a_3 \end{bmatrix} \frac{1}{\sigma_1\sqrt{2\pi}} e^{\left(-\frac{1}{2}\left(\frac{t-h_1}{\sigma_1}\right)^2\right)} \sin(\omega_e t), \tag{5.41}$$
which is inherently $\mathcal{C}^1$-smooth due to the product of analytic functions.

The disturbance parameters are summarized in Table 5.2. The temporal evolution of these disturbances defines four distinct experimental phases (see Figure 5.3, shaded regions):

Table 5.2: Parameters for the external disturbances $\boldsymbol{F}_{\text{ext}}(t)$ and $\lambda_{\text{ext}}(t)$.

$a_0 = 20$ N	$a_3 = 10$ Nm	$\sigma_0 = 0.4$
$a_1 = -20$ N	$h_0 = 8.0$ s	$\sigma_1 = 0.5$
$a_2 = 40$ N	$h_1 = 6.5$ s	$\omega_e = \pi$ rad/s

a. $t \in [0.0, 5.0)$ s: nominal operation (no disturbance);

b. $t \in [5.0, 6.5)$ s (yellow): task-space disturbance $\boldsymbol{F}_{\text{ext}}$ only;

c. $t \in [6.5, 8.0)$ s (lime): simultaneous disturbances in both subspaces;

d. $t \in [8.0, 10.0]$ s (gray): pure constraint-force disturbance λ_{ext}.

5.5.2 Parameter and Simulation Setup

The control gains are selected as follows:

- Task-space stiffness: $\boldsymbol{K}_x = \text{diag}(5\,000, 5\,000, 1\,000)$ in units of $\text{N/m}, \text{N/m}, \text{Nm/rad}$;
- Force integral gain: $K_I = 10$.

A practical guideline for selecting $\boldsymbol{K}_x$ is provided in the following remark.

Remark 13 (Initial Gain Selection via Stiffness Mapping)**.** *An informed initial estimate for the task-space stiffness gain $\boldsymbol{K}_x$ can be obtained by mapping the intrinsic joint-space elasticity into the task space using the static stiffness transformation [187, Eq. (5.3)]:*

$$\boldsymbol{K}_x \approx \left[\bar{\boldsymbol{J}}(\boldsymbol{q}_0)\, \boldsymbol{K}\, \bar{\boldsymbol{J}}^{\top}(\boldsymbol{q}_0)\right]^{-1},$$

where $\bar{\boldsymbol{J}}(\boldsymbol{q}_0)$ is the augmented task Jacobian evaluated at the initial configuration $\boldsymbol{q}_0$. Since $\bar{\boldsymbol{J}}$ is square and nonsingular under Assumption 7, this inverse is well-defined and can be computed numerically (e.g., using the methods in [154]).

Prior to each simulation, the system is initialized at a configuration satisfying the exact constraint $\phi(\boldsymbol{q}) = 0$. All simulations are conducted in MATLAB/SIMULINK using a fourth-fifth-order Runge–Kutta (RK45) solver with a fixed integration step of 1 ms. The results are presented in Section 5.5.3, followed by a discussion on numerical sensitivity to solver choice and sampling time in Section 5.5.4.

5.5.3 Results and Discussion

The closed-loop performance is illustrated in Figures 5.3 and 5.4. Figure 5.3 shows the reference trajectories (dashed black) alongside the actual system responses (colored lines) for task position, velocity, and constraint force. The external disturbances, comprising three components of $\boldsymbol{F}_{\text{ext}}$ (two translational and one rotational) and the scalar constraint disturbance λ_{ext}, are plotted in the bottom row. Figure 5.4 presents the corresponding tracking errors, control inputs, and the storage function S defined in (5.28). The system behavior is analyzed across four distinct phases, each characterized by a different disturbance regime:

- *Phase a (0.0–5.0 s, white background)*: In the absence of external disturbances, the system exhibits critically damped convergence of the task-position and velocity errors to zero, consistent with the modal damping design ($\xi = 1$). The constraint force error also decays asymptotically, confirming stable regulation in both subspaces.

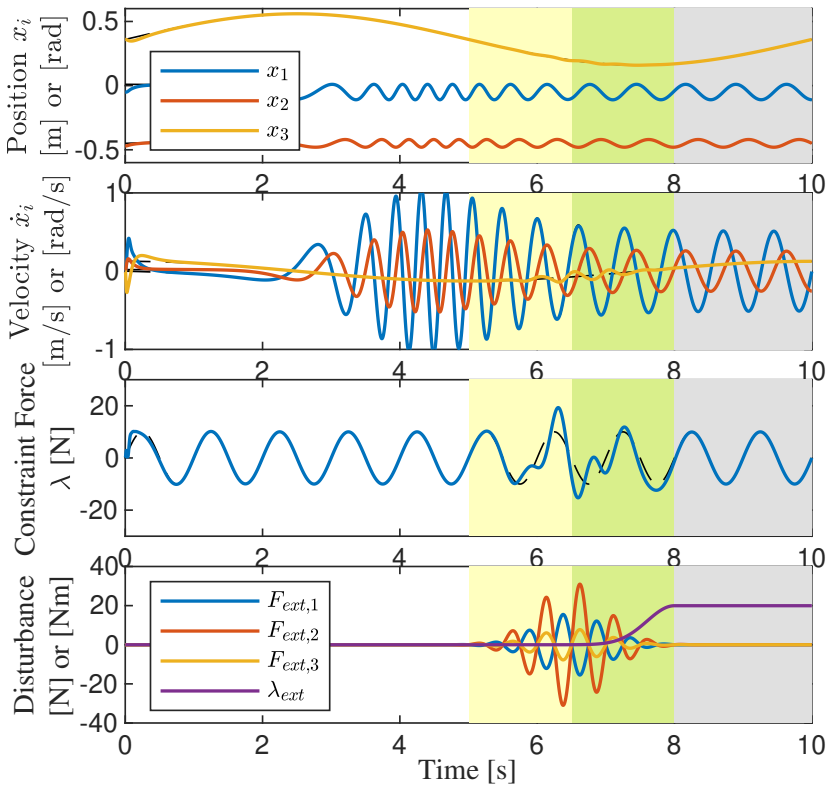


Figure 5.3: Reference (dashed black) and actual (colored) trajectories for task position, velocity, and constraint force. Bottom row: external disturbances—$F_{\text{ext},1}$, $F_{\text{ext},2}$, $F_{\text{ext},3}$ (task space) and λ_{ext} (constrained space). © 2022 IEEE

- *Phase b (5.0–6.5 s, yellow background)*: The introduction of the task-space disturbance $\boldsymbol{F}_{\text{ext}}$ induces transient deviations in both the unconstrained and constrained dynamics (visible in position, velocity, and force responses). Crucially, the storage function S increases during this interval, reflecting the physical power injection $\dot{\tilde{\boldsymbol{x}}}^{\top} \boldsymbol{F}_{\text{ext}} > 0$ as predicted by the passivity analysis in (5.30).

- *Phase c (6.5–8.0 s, lime background)*: Both $\boldsymbol{F}_{\text{ext}}$ and λ_{ext} are active. Notably, while λ_{ext} affects the constraint force trajectory, it does not excite the task-space dynamics or increase the storage function S. This observation aligns with the theoretical result that disturbances in the constrained subspace do not inject energy into the passive closed-loop system, only task-space disturbances contribute to $\dot{S}$.

- *Phase d (8.0–10.0 s, gray background)*: The task-space disturbance is removed, leaving only a constant bias $\lambda_{\text{ext}} = 20$ N in the constrained channel. Thanks to the integral action in (5.15a), the constraint force error $\tilde{\lambda}$ converges asymptotically to zero, demonstrating effective rejection of constant disturbances. Meanwhile, the storage function S monotonically decreases, indicating that all previously injected energy has been dissipated through the inherent damping terms $\boldsymbol{D}_x$ and $\boldsymbol{D}_\eta$, a direct consequence of the system's output strict passivity.

These results collectively validate the three core design objectives: (i) asymptotically stable motion tracking, (ii) robust force regulation with integral disturbance rejection, and (iii) preservation of the system's passive energetic structure.

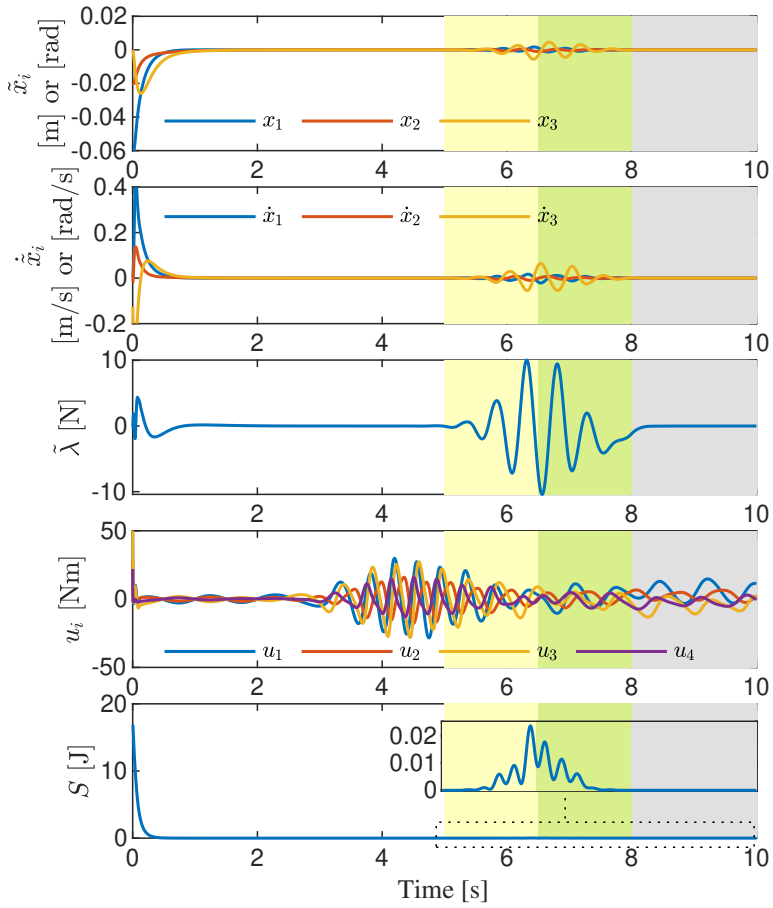


Figure 5.4: Tracking errors in position ($\tilde{\boldsymbol{x}}$), velocity ($\dot{\tilde{\boldsymbol{x}}}$), and constraint force ($\tilde{\boldsymbol{\lambda}}$); control input $\boldsymbol{u}$; and storage function S.
© 2022 IEEE

5.5.4 Robustness to Numerical Integration Solver Settings

The controller is derived in continuous time; however, practical implementation requires discretization. To assess sensitivity to numerical approximation, simulation results are compared using different solvers and sampling intervals while keeping all physical and control parameters unchanged.

The baseline simulation employs a fourth-fifth-order Runge–Kutta (RK45, ODE45) solver with a fixed step size of 1 ms, providing a high-fidelity approximation of the continuous-time dynamics. For comparison, the experiment is repeated using a third-order Bogacki–Shampine (ODE3) solver with coarser sampling rates of 5 ms and 10 ms, which correspond to integration steps that are 5× and 10× larger, respectively.

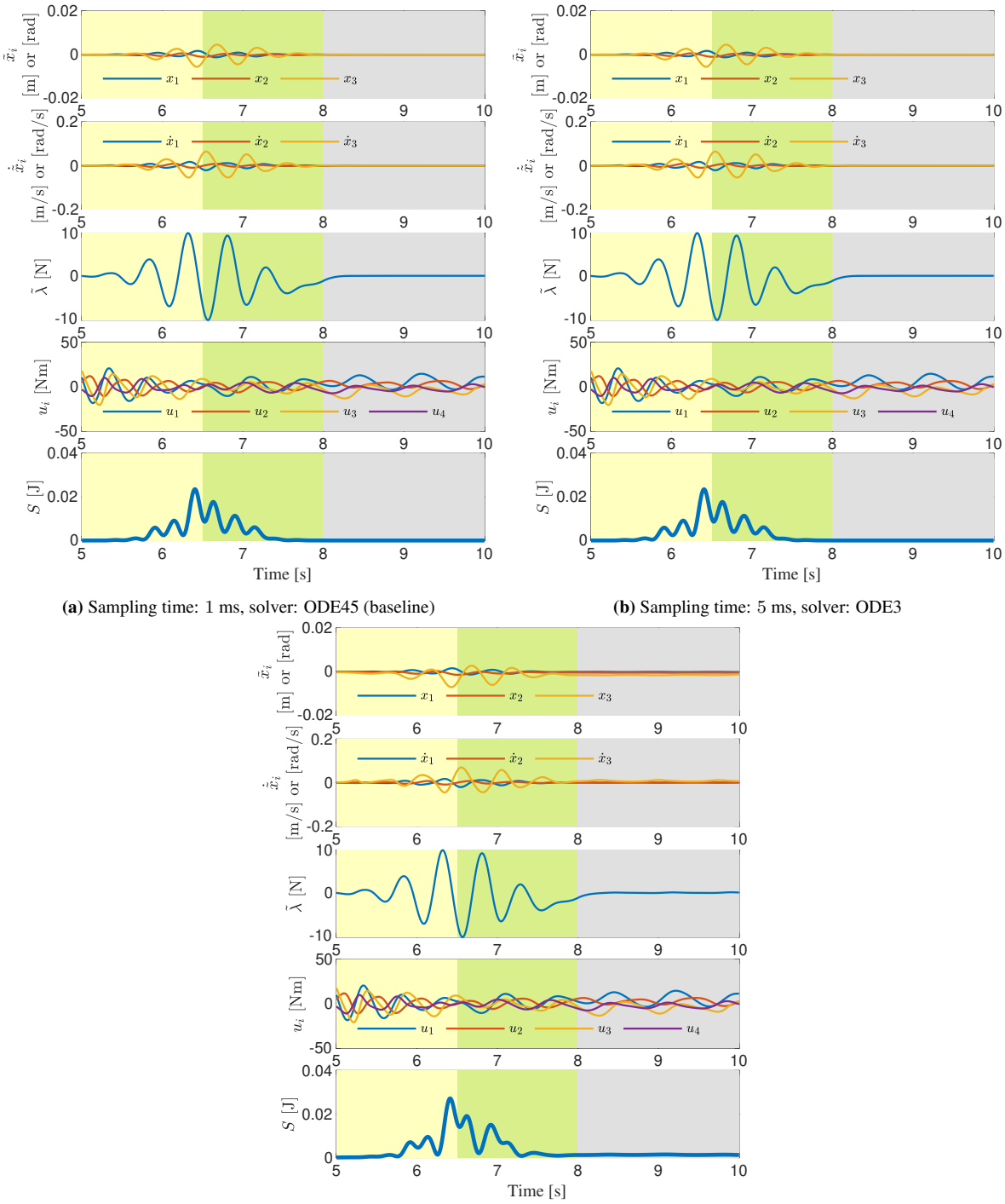
As shown in Figure 5.5, the tracking performance remains largely unaffected at 5 ms (Figure 5.5b), with errors nearly indistinguishable from the baseline (Figure 5.5a). At 10 ms (Figure 5.5c), minor deviations appear in the position and velocity errors during the peak disturbance interval ($t \approx 6.5$–7.0 s), where the system experiences the highest dynamic excitation. Nevertheless, stability and passivity are preserved: the errors remain bounded, converge after disturbance removal, and no retuning of gains is required.

This robustness to discretization parameters underscores the structural integrity of the control law; its performance is not critically dependent on ultra-fine sampling, which is advantageous for real-time embedded implementations. The results suggest that even modest computational resources can support effective deployment of the proposed ESP framework, provided the sampling rate satisfies basic Nyquist criteria for the dominant disturbance frequencies.

5.6 Summary

This chapter presented a task-space motion and force tracking controller for constrained robotic systems with elastic joints. In contrast to conventional approaches, such as inverse dynamics linearization [106, 188] or strategies that enforce complete decoupling between motion and force, the proposed framework deliberately preserves the system's intrinsic inertial and elastic structure. This structure-preserving design aligns with a passive control philosophy, thereby enhancing robustness while preserving the system's intrinsic inertial and elastic properties.

Rather than relying on aggressive cancellation of nonlinear dynamics, the force control component employs an integral action that ensures asymptotic tracking accuracy in the presence of constant disturbances acting in the constrained subspace. Crucially, the closed-loop system retains uniform asymptotic stability at the origin even when subjected to such persistent force disturbances, provided no external perturbations act in the task space. This result underscores the effectiveness of the controller in achieving stable, accurate, and energetically consistent simultaneous motion and force tracking for elastic-joint robots under holonomic constraints.



(a) Sampling time: 1 ms, solver: ODE45 (baseline)

(b) Sampling time: 5 ms, solver: ODE3

(c) Sampling time: 10 ms, solver: ODE3

Figure 5.5: Tracking error under disturbances ($t = 5$–10 s) for varying numerical settings. All other parameters and references are identical.

6

Conclusion and Discussion

The final chapter of this thesis provides a comprehensive summary and discussion of the main contributions presented throughout the work. The limitations of the current approach are examined, along with the challenges encountered during the implementation of real-world controllers for tendon-driven systems. Particular attention is given to the insights gained from these difficulties, and potential research directions are suggested to further enhance and extend the proposed framework. The chapter concludes with the author's forward-looking perspective on the vision for future robotics research.

6.1 Conclusion

Biological systems possess a remarkable ability to merge motion planning and control through the interplay of musculoskeletal elasticity and reflexive neural responses. This integration enables seamless, anticipatory adjustments during object interaction, without the need for explicit re-planning. In contrast, most contemporary robotic systems remain constrained by rigid, sequential behaviors—typically executing reaching and grasping as two separate stages, which limits their adaptability and fluidity in dynamic environments. Motivated by the natural agility of human motor systems, this thesis explores how reactivity, compliance, and dynamic control can be combined to enable more adaptive robotic grasping.

The thesis addresses these limitations through three key contributions: specialized control systems for antagonistic actuators, responsive motion planning algorithms, and integrated motion-force control under constraints. These advances enable high-degree-of-freedom robotic systems with compliant actuation to perform smooth, continuous approach-and-grasp movements in a single fluid motion.

In Chapter 3, controllers are designed for both unilateral and bidirectional types of antagonistic actuators, commonly employed in elastic-joint robotic systems, particularly multi-fingered hands. To enable impedance control on such systems, the Elastic Structure-Preserving Impedance (ESPi) control is extended to preserve intrinsic inertial and elastic elements while imposing desired link-side stiffness and damping. For BAVS actuators, ESPi ensures physical motor-side pretension during link-side stiffness modulation, while motor-side damping suppresses oscillations. Extending this philosophy to a multi-DoF tendon-coupled system, desired link-side impedance behavior is achieved with minimal perturbation to the underlying dynamics and elastic coupling arising from tendon routing. Global asymptotic stability and output-strict passivity are established for both actuator types. Simulations on

the DLR *neoDavid* hand and experiments on its forearm joint validate these properties. These results underscore the importance of preserving physical system dynamics to enhance robustness and energy efficiency in uncertain interactions.

Following the investigation of joint-level impedance control, Chapter 4 introduces Finger Flow (FF), a reactive motion generation paradigm that synthesizes visual and proprioceptive feedback into continuous velocity commands for coordinated hand-arm motion. By encoding real-time finger and spherical object geometry into a computationally efficient representation, the hand hull, FF generates finger-avoidant trajectories for the arm in real time. FF enables the grasping-while-reaching behavior and has the intrinsic nature of recovering from failed attempts. Formal convergence proofs are provided for stationary spherical objects, and experimental success rates exceed 87 % on dynamic pick-and-catch tasks. Implemented on the *neoDavid* platform, FF operates at 3 kHz, enabling safe and responsive interaction during adversarial human-robot scenarios. This demonstrates the critical value of state-dependent, closed-loop control in dynamic grasping.

Once a stable grasp is established, Chapter 5 presents a task-space motion and force tracking controller that preserves the system's intrinsic elastic structure under constraints, such as when stably holding an object. Unlike inverse-dynamics approaches, this method avoids full decoupling or cancellation of dynamics in constrained and unconstrained subspaces. Instead, it leverages closed-loop passive dynamics to enhance robustness. An integral term in the force controller ensures accurate force tracking under constant disturbances, with formal guarantees of uniform asymptotic stability even during prolonged constrained interactions. A case study simulating a two-arm constrained manipulation scenario validates the approach.

Collectively, these contributions establish a "scene-act" paradigm that unifies compliance, reactivity, and dynamic control, enabling fluid transitions between reaching, grasping, and force regulation. By synthesizing insights from human motor control and advancing elastic robotics through novel control and planning frameworks, this thesis provides a principled pathway toward reactive, human-like grasping in robots. Experimental validation on the complex hardware platform of the DLR *neoDavid* robot underscores the practical viability of preserving physical system dynamics while achieving robustness in dynamic environments—and maintaining safety in human-shared settings.

6.2 Limitations and Lessons Learned

In this section, the limitations and remaining gaps in the control of tendon-driven hands, as well as the reactive control strategy employed in Finger Flow, are elaborated upon. The lessons learned, based on the author's current observations and intuition, are summarized.

6.2.1 Tendon-Driven Hand Control: Gaps in Real World

Chapter 3 presented a mathematical foundation for antagonistic actuator control, including formal passivity and stability proofs. For BAVS actuations, the controller's effectiveness was demonstrated through real-world experiments on the underarm joint of the DLR robot *neoDavid*. However, as summarized in Chapter 3, a notable discrepancy persists between simulation predictions and real-system performance when applying the proposed control strategy.

The current approach relies heavily on accurate kinematic models of finger joints and tendon routing, as well as precise state estimation, particularly tendon elongation and force calibration via FAS.

In systems such as the *neoDavid* hand or other tendon-driven platforms like the Clash Hand [189] and hybrid compliant grippers [190], tendons serve dual roles: acting not only as actuators but also as indirect sensors, since no physical position or force/torque sensors are embedded within the fingers or fingertips, especially in compact configurations. Consequently, accumulated modeling errors propagate into critical state estimates, such as joint position and link-side torque. This becomes particularly problematic in tasks requiring high precision, such as trajectory tracking or constrained force regulation, where model-based controllers are inherently sensitive to identification inaccuracies.

Lesson Learned

A central question to myself was: *Can the performance of finger control be enhanced without altering the mechatronic setup?*

Past efforts focused on improving two key aspects:

- **Finger (joint) position accuracy**, which is crucial given that advanced multi-fingered manipulation strategies depend on precise Cartesian or joint-space trajectory execution;
- **Joint torque estimation**, which plays a pivotal role in the feedback loop of ESPi control and enables contact localization in the absence of tactile sensing, critical for object stabilization or reorientation within the hand.

To mitigate modeling and sensing errors, a recalibration routine for tendon elongation in the FAS component was implemented. While a comprehensive ablation study isolating the impact of tendon-force calibration was not feasible, a measurable reduction in static error during impedance control experiments was observed following recalibration.

Efforts were also made to refine tendon elongation estimation by incorporating wrist forward kinematics into the model, motivated by the known influence of wrist motion on finger joint estimation[1]. However, this approach was abandoned due to insufficient measurement fidelity in abduction and flexion angles. The resulting noise would have degraded, not improved, the overall estimation quality.

From a control design perspective, multiple avenues were explored to improve set-point regulation. An observer-based friction estimation scheme proposed by works [180, 191] was applied to estimate both motor-side and link-side friction. The latter was found to dominate system dynamics, approximately 100 times larger than combined inertial and gravitational effects, at intermediate movement speeds. Yet, compensating for this estimated friction via a quasi-feedforward term added to the ESPi control yielded only marginal improvements.

Alternative control structures were also tested. An integral term with anti-windup was introduced into the ESPi controller[2]. However, this led to delayed response dynamics: once accumulated error finally overcame the dead zone, overshoot and oscillations ensued. The presence of this dead zone is attributed to stiction between tendons and the bent routing within the wrist's parallel mechanism [39], as observed empirically. No systematic friction identification protocol was pursued beyond these observations. Similarly, implementation of the decoupled control scheme from [95, Sec. 6.1], designed to minimize steady-state error in set-point regulation, did not yield significant gains in precision.

Ultimately, a cascaded control architecture [149] was adopted: an inner loop maintains minimal tendon pretension to ensure tautness, while an outer loop performs classical joint-level impedance

[1] See prior work on wrist kinematic modeling in [165]

[2] Think of adding an integral term of error $\boldsymbol{K}_I \int \tilde{\boldsymbol{q}}(\tau)\mathrm{d}\tau$ in (3.47)

control in regulation mode. This structure proved most effective in practice, balancing robustness and simplicity.

This iterative process revealed several key insights: In lightweight, highly frictional systems, structure-preserving control approaches inherently preserve unmodeled dynamics, particularly friction and related nonlinearities, that can severely degrade real-world performance if not explicitly addressed. It appears that, under conditions of poor modeling fidelity, high-gain feedback may be unavoidable to achieve acceptable tracking accuracy.

Can enhanced sensing or mechanical design help? An alternative path forward could involve augmenting the sensing architecture, for instance, by integrating direct joint encoders or mechanically decoupling tendon elongation from wrist motion. However, adding sensors introduces challenges in cabling, signal conditioning, and system integration, potentially compromising the platform's compactness and passive compliance, which define its value.

While future work may explore such enhancements, the conclusion drawn from this phase is clear: achieving robust, high-performance finger control in tendon-driven systems will require a careful balance between mechanical design sophistication and control algorithm resilience.

6.2.2 Hand-Arm Coordination and Human Motor Control Parallels

The FF framework adopts a unidirectional finger-arm coordination strategy, where arm motion adapts in response to finger positioning rather than establishing bidirectional coupling between these subsystems. This design choice stems from the fundamental kinematic and manipulation advantages inherent to multi-fingered robotic hands. Unlike simple parallel grippers that provide limited contact configurations for a given grasp pose, multi-fingered hands offer significantly larger solution spaces for achieving force closure grasps [120, 192].

Meanwhile, research in human motor control also reveals that individuals employ diverse reaction strategies when reaching for or catching perturbed targets, strategically leveraging the dexterity of fingers, arms, or coordinated combinations of both systems [73].

6.2.3 Reactive Control but Non-predictive

The vector-field-based feedback planning employed in FF operates under a history-invariant, non-predictive paradigm, processing instantaneous sensory feedback without incorporating preview information or receding-horizon optimization techniques commonly used in model predictive control (MPC) frameworks [49] or trajectory optimization methods [193, 194]. This temporal myopia presents both advantages and limitations in reactive grasping scenarios. The absence of predictive modeling eliminates the computational overhead associated with forward simulation and optimization over future time horizons, enabling the 3 kHz control frequency demonstrated in the DLR *neoDavid* implementation. This high-frequency operation proves crucial for handling adversarial human-robot interactions and dynamic object trajectories where rapid response times supersede optimal long-term planning. The history-invariant nature may constrain the system's ability to anticipate and prepare for predictable disturbances or object motion patterns. Unlike MPC-based approaches that can preemptively adjust control actions based on predicted system evolution, FF responds reactively to sensory feedback, potentially missing opportunities for smoother, more efficient motion generation. Recent advances in real-time MPC [195] and learning-based predictive models [196] suggest potential path-

ways for incorporating limited-horizon preview capabilities while maintaining computational traceability.

6.2.4 Assumption on Constraint Modeling in Force Tracking Control

Chapter 5 has only considered an ideally simplified manipulation scenario where a contact is assumed invariant and can be simply described by a finite number of deterministic analytical algebraic relations. The work assumes the constraint models (Pfaffian and holonomic constraints) are consistently satisfied and analytically tractable. This represents a significant barrier to real-world implementation, where constraints cannot always be precisely described analytically. Complex environments, manufacturing tolerances, and sensor uncertainties challenge the reliability of exact mathematical constraint representations. Depending on the constraint modeling uncertainties, different force control schemes (direct vs. indirect) in the constrained space may apply.

Force control trade-offs: indirect versus direct approaches

Indirect force control through an impedance control scheme offers robustness when constraint modeling contains uncertainties, as the robot maintains compliant behavior and reduces damage risk from excessive contact forces. "Indirect" means this approach converts force control problems to motion tracking problems without explicit knowledge of the environment (or constraints) [59, 197]. Impedance control facilitates stable interaction even without precise environmental models. However, indirect force control provides only approximate force regulation through motion control mechanisms rather than direct force feedback [198]. This limitation becomes critical for tasks requiring precise force control, where accurate force tracking is essential rather than merely maintaining safe interaction.

Our current work prioritizes direct force control over the indirect approach. The former scheme utilizes explicit force feedback in compliant environments while maintaining passivity in the closed loop for elastic-joint systems. This choice balances precision and robustness, acknowledging that applications such as precision assembly or grasping require exact force control that indirect methods cannot adequately provide.

6.3 Future Directions

The findings and limitations of this work reveal several promising avenues for advancing reactive robotic grasping systems. These directions span from fundamental improvements in uncertainty handling to the development of more sophisticated planning and control paradigms.

Learning-augmented structure-preserving control

The limitations of model-based control in systems with unmodeled friction, tendon compliance nonlinearities, and sensorimotor uncertainty motivate a paradigm shift toward learning-augmented architectures. Rather than replacing physical models, data-driven methods can be embedded as adaptive correctors that preserve the stability and passivity guarantees of structure-preserving frameworks like ESPi. Recent advances show that neural observers can learn residual dynamics without compromising closed-loop stability, for example, Lipschitz-constrained neural networks enable stable model-

reference adaptation under unmodeled disturbances [199], while episodic learning with control Lyapunov functions ensures stability despite uncertain dynamics [200]. Hybrid approaches, where a learned module compensates for unmodeled dynamics in real-time while an underlying structure-preserving controller enforces safety and energy efficiency, offer a principled path forward. Such architectures align with the emerging field of learning-augmented control [201] and physics-informed neural networks [202], where domain knowledge constrains the hypothesis space to ensure generalizability and robustness.

Stochastic reactive motion generation under sensor uncertainty

Current reactive motion generation frameworks, such as Finger Flow, often treat sensory inputs as deterministic signals, neglecting the stochastic nature of visual tracking, proprioceptive estimation, and force sensing. This simplifying assumption leads to instability under conditions like large-scale occlusion, rapid object motion, or low-confidence measurements. A critical advancement lies in embedding probabilistic reasoning into the feedback loop, explicitly modeling sensor outputs as random variables with known or learned uncertainty distributions [203, 204]. By maintaining belief states over object pose, finger configuration, and contact forces, the system can dynamically reweight evidence from complementary modalities (e.g., decreasing reliance on vision during occlusion while increasing trust in tendon tension signals). Recent work on stochastic motion planning [205, 206] provides mathematical foundations for collision-free trajectory generation under sensing uncertainty, while Bayesian filtering and Gaussian-process-based approaches enable real-time tracking of evolving belief states in robotic manipulation [207, 208]. Together, these methods enable graceful degradation under degraded sensing conditions, preventing oscillatory or divergent behaviors common in deterministic reactive controllers when confronted with corrupted input.

Adaptive hybrid planning: From reactive to predictive execution

The dichotomy between purely reactive control and computationally intensive predictive planning suggests a more nuanced architecture: one that adaptively switches between paradigms based on environmental predictability. In stable or predictable scenarios, such as object free-fall, known manipulation patterns, or pre-learned interaction dynamics, a finite-horizon predictive planner could optimize motion sequences ahead of time, improving efficiency and precision. Conversely, during unpredictable interactions, the system reverts to the robust, history-invariant reactive framework. The challenge lies in defining trigger criteria for switching: metrics derived from prediction confidence, entropy of belief states, or rate of change in contact forces may serve as reliable indicators. Recent breakthroughs in diffusion policies [81], flow-matching generative models [209], and robotics foundation models [210] demonstrate that high-dimensional, multi-modal reactive behaviors can be learned from diverse datasets, enabling generalization across unseen scenarios without explicit planning. Future work will explore how these generative models can be conditioned on real-time context to produce hybrid plans, reactive when needed, predictive when beneficial, while maintaining real-time feasibility on embedded hardware.

Understanding contact for dexterous manipulation

A central obstacle to dexterous manipulation is the absence of compact, computationally feasible, and physically meaningful representations of contact. Traditional spring–damper abstractions fail to

capture the richness of multi-point and multi-modal interactions, while full-resolution contact mechanics remain computationally prohibitive for real-time control [211]. This motivates the search for intermediate representations that balance physical fidelity with online tractability.

One promising direction is the development of *stochastic contact models* that encode the intrinsic uncertainty of contact formation, dissipation, and slip. Rather than resolving material-level physics, such models would provide learned statistical summaries of interaction outcomes [212]. In practice, this could take the form of probability distributions over contact locations, feasible force directions, or effective friction coefficients. Inspired by domain randomization in reinforcement learning [213], these probabilistic models could serve as priors for both motion planning and impedance control, allowing the robot to operate within trust regions of plausible contact behavior rather than relying on brittle deterministic assumptions.

A natural next step is to integrate these stochastic models with *contact-implicit representations*. In such formulations, contact forces, object motions, and discrete contact events are jointly optimized through complementarity constraints, eliminating the need to enumerate contact modes a priori [211]. By embedding probabilistic contact models within contact-implicit MPC or trajectory optimization, one could achieve both robustness to model uncertainty and adaptability to unanticipated interactions. Moreover, coupling this approach with online constraint identification via machine learning [214] opens a pathway toward controllers that continuously refine their internal contact models during deployment, enabling reliable performance in contact-rich scenarios characterized by non-smooth dynamics, discontinuous gradients, and combinatorial explosion of feasible contact configurations.

Integration and system-level architectures

These future directions are inherently interconnected, suggesting that the most significant advances may come from integrated approaches that simultaneously address uncertainty handling, predictive planning, and contact understanding. The development of unified frameworks that seamlessly combine these elements while maintaining real-time performance represents a significant but potentially transformative research challenge. Additionally, the scalability of these approaches to more complex scenarios, involving multiple objects, collaborative manipulation, or long-horizon tasks, remains an open question that will require careful consideration of computational constraints and system architecture design.

A

Appendix: Stability Analysis for the Constrained System

A.1 Vidyasagar's Theorem on Hierarchical Systems

We recall the following result from Vidyasagar [184, Theorem 3.1], which provides sufficient conditions for uniform asymptotic stability of cascaded (hierarchical) nonlinear systems.

Theorem 3 (Vidyasagar, 1980)**.** *Consider a system in hierarchical form*

$$(\mathscr{S}) \quad \dot{\boldsymbol{z}}_i = \boldsymbol{f}_i(t, \boldsymbol{z}_1, \ldots, \boldsymbol{z}_i), \quad i = 1, \ldots, n,$$

and its associated collection of isolated subsystems

$$(\mathscr{S}_i) \quad \dot{\boldsymbol{z}}_i = \boldsymbol{f}_i(t, \boldsymbol{0}, \ldots, \boldsymbol{0}, \boldsymbol{z}_i).$$

Suppose the following assumptions hold:

(A1) Each vector field $\boldsymbol{f}_i$ is continuous and satisfies $\boldsymbol{f}_i(t, \boldsymbol{0}, \ldots, \boldsymbol{0}) = \boldsymbol{0}$ for all $t \geq 0$;

(A2) There exists a constant $c > 0$ such that

$$\sup_{t \geq 0} \sup_{\|\boldsymbol{w}_i\| \leq c} \|\nabla_{\boldsymbol{w}_i} \boldsymbol{f}_i(t, \boldsymbol{w}_i)\| < \infty, \quad \text{where } \boldsymbol{w}_i = \operatorname{col}[\boldsymbol{z}_1, \ldots, \boldsymbol{z}_i].$$

Then, the equilibrium $\boldsymbol{z} = \boldsymbol{0}$ of the full system $(\mathscr{S})$ is uniformly asymptotically stable (UAS) if and only if the origin $\boldsymbol{z}_i = \boldsymbol{0}$ is UAS for each isolated subsystem $(\mathscr{S}_i)$, for all $i = 1, \ldots, n$.

This theorem serves as the foundation for the stability analysis of the closed-loop dynamics presented in Section 5.4.

A.2 Proof of Uniform Asymptotic Stability

The stability of the driving subsystem $\dot{\boldsymbol{z}}_1 = \boldsymbol{f}_1(t, \boldsymbol{z}_1)$ (cf. (5.34)) is established using Matrosov's theorem, following the approach in [101]. Due to the local nature of the task-space parametrization (restricted to the singularity-free set $\bar{\mathbb{Q}}$), the result is necessarily local; hence, we prove (local) uniform asymptotic stability (UAS), rather than global.

Proof. Let $\boldsymbol{f}_1 : [0,\infty) \times \Omega \to \mathbb{R}^{4n-2m}$ be continuous, where $\Omega \subset \mathbb{R}^{4n-2m}$ is an open, connected neighborhood of the origin containing the initial conditions of interest.

We select the storage function $S(t, \boldsymbol{z}_1)$ defined in (5.28) as a Lyapunov candidate:

$$V(t, \boldsymbol{z}_1) := S(t, \boldsymbol{z}_1).$$

In the absence of external disturbances ($\boldsymbol{F}_{\text{ext}} = \boldsymbol{0}$), its time derivative along trajectories of $\dot{\boldsymbol{z}}_1 = \boldsymbol{f}_1(t, \boldsymbol{z}_1)$ is given by

$$\dot{V} = -\dot{\tilde{\boldsymbol{x}}}^\top \boldsymbol{D}_x \dot{\tilde{\boldsymbol{x}}} - \dot{\boldsymbol{\eta}}^\top \boldsymbol{D}_\eta \dot{\boldsymbol{\eta}} \le 0,$$

which is negative semi-definite due to the positive definiteness of $\boldsymbol{D}_x$ and $\boldsymbol{D}_\eta$.

To apply Matrosov's theorem (in the formulation of Paden and Panja [185]), we verify the following conditions:

Condition (1): Boundedness of V. Define the bounding functions

$$a_z(\|\boldsymbol{z}_1\|) := \tfrac{1}{2}\big(\lambda_{\min}(\boldsymbol{\Lambda}_{xx})\|\dot{\tilde{\boldsymbol{x}}}\|^2 + \lambda_{\min}(\boldsymbol{B})\|\dot{\boldsymbol{\eta}}\|^2 + \lambda_{\min}(\boldsymbol{K}_x)\|\tilde{\boldsymbol{x}}\|^2\big) + U_e(\boldsymbol{\eta} - \boldsymbol{G}(\tilde{\boldsymbol{x}})),$$
$$b_z(\|\boldsymbol{z}_1\|) := \tfrac{1}{2}\big(\lambda_{\max}(\boldsymbol{\Lambda}_{xx})\|\dot{\tilde{\boldsymbol{x}}}\|^2 + \lambda_{\max}(\boldsymbol{B})\|\dot{\boldsymbol{\eta}}\|^2 + \lambda_{\max}(\boldsymbol{K}_x)\|\tilde{\boldsymbol{x}}\|^2\big) + U_e(\boldsymbol{\eta} - \boldsymbol{G}(\tilde{\boldsymbol{x}})).$$

By Lemma 4.3 in [215], there exist class-$\mathcal{K}$ functions a, b such that

$$a(\|\boldsymbol{z}_1\|) \le V(t, \boldsymbol{z}_1) \le b(\|\boldsymbol{z}_1\|),$$

which implies that the origin is uniformly stable (US) and that $\boldsymbol{z}_1(t)$ remains bounded.

Condition (2)–(3): Auxiliary function and boundedness. Define the auxiliary function

$$W(t, \boldsymbol{z}_1) := \ddot{V}(t, \boldsymbol{z}_1) = -\big(2\dot{\tilde{\boldsymbol{x}}}^\top \boldsymbol{D}_x \ddot{\tilde{\boldsymbol{x}}} + \dot{\tilde{\boldsymbol{x}}}^\top \dot{\boldsymbol{D}}_x \dot{\tilde{\boldsymbol{x}}} + 2\dot{\boldsymbol{\eta}}^\top \boldsymbol{D}_\eta \ddot{\boldsymbol{\eta}} + \dot{\boldsymbol{\eta}}^\top \dot{\boldsymbol{D}}_\eta \dot{\boldsymbol{\eta}}\big).$$

Since $\boldsymbol{z}_1(t)$ is bounded and all system matrices are smooth, $|W(t, \boldsymbol{z}_1)|$ is uniformly bounded, satisfying Conditions (2) and (3) of Matrosov's theorem.

Condition (4): Non-vanishing derivative on the invariant set. Let $E = \{\boldsymbol{z}_1 \in \Omega \mid \dot{\tilde{\boldsymbol{x}}} = \boldsymbol{0}, \dot{\boldsymbol{\eta}} = \boldsymbol{0}\}$ be the largest invariant set contained in $\{\dot{V} = 0\}$. Differentiating W along the closed-loop dynamics (5.15b)–(5.15c) yields, for all $\boldsymbol{z}_1 \in E$,

$$\dot{W}(t, \boldsymbol{z}_1) = -2\big[\boldsymbol{T}\boldsymbol{\psi} - \boldsymbol{K}_x\tilde{\boldsymbol{x}}\big]^\top \boldsymbol{Q}\big[\boldsymbol{T}\boldsymbol{\psi} - \boldsymbol{K}_x\tilde{\boldsymbol{x}}\big] - 2\boldsymbol{\psi}^\top \boldsymbol{R}\boldsymbol{\psi}, \tag{A.1}$$

where

$$\boldsymbol{T} := [\boldsymbol{P}(\boldsymbol{J}\boldsymbol{P})^+]^\top, \quad \boldsymbol{Q} := \boldsymbol{\Lambda}_{xx}^{-\top} \boldsymbol{D}_x \boldsymbol{\Lambda}_{xx}^{-1} \succ 0, \quad \boldsymbol{R} := \boldsymbol{B}^{-\top} \boldsymbol{D}_\eta \boldsymbol{B}^{-1} \succ 0.$$

Here, symmetry of $\boldsymbol{Q}$ and $\boldsymbol{R}$ follows from the modal damping design [183], which ensures symmetric positive-definite damping matrices.

Equation (A.1) can be rewritten in quadratic form as

$$\dot{W} = -2 \begin{bmatrix} \boldsymbol{\psi} \\ \tilde{\boldsymbol{x}} \end{bmatrix}^\top \boldsymbol{H}(t, \boldsymbol{z}_1) \begin{bmatrix} \boldsymbol{\psi} \\ \tilde{\boldsymbol{x}} \end{bmatrix},$$

with

$$\boldsymbol{H} = \begin{bmatrix} \boldsymbol{T}^\top \boldsymbol{Q}\boldsymbol{T} + \boldsymbol{R} & -\boldsymbol{T}^\top \boldsymbol{Q}\boldsymbol{K}_x \\ -\boldsymbol{K}_x^\top \boldsymbol{Q}\boldsymbol{T} & \boldsymbol{K}_x^\top \boldsymbol{Q}\boldsymbol{K}_x \end{bmatrix} = \boldsymbol{Y}\boldsymbol{Y}^\top, \quad \boldsymbol{Y} = \begin{bmatrix} \boldsymbol{R}^{1/2} & -\boldsymbol{T}^\top \boldsymbol{Q}^{1/2} \\ \boldsymbol{0} & \boldsymbol{K}_x^\top \boldsymbol{Q}^{1/2} \end{bmatrix}.$$

Since $\boldsymbol{Y}$ has full column rank and depends continuously on $\boldsymbol{z}_1$, $\boldsymbol{H}(t, \boldsymbol{z}_1)$ is uniformly positive definite on compact subsets of Ω. Thus, there exists a class-$\mathcal{K}$ function γ such that

$$|\dot{W}(t, \boldsymbol{z}_1)| \geq \gamma(\|\boldsymbol{z}_1\|), \quad \forall \boldsymbol{z}_1 \in E \setminus \{\mathbf{0}\}.$$

This satisfies Condition (4) of Matrosov's theorem (see Lemma 1 in [101]).

Condition (5): Uniform stability. Already established in Condition (1).

Hence, by Matrosov's theorem, the equilibrium $\boldsymbol{z}_1 = \mathbf{0}$ is locally uniformly asymptotically stable. □

B

Appendix: Finger Flow

B.1 Hand Hull Generation

The hand hull is constructed by approximating the kinematic structure of each finger on a series of rotated planes parameterized by angle α. This approach is applicable to anthropomorphic multi-fingered hands. The process begins with the estimation of effective joint configurations from raw sensor feedback, as detailed in Appendix B.1.2, which serves as input to the forward kinematic model described in Appendix B.1.3.

B.1.1 Preliminaries: Rotated and Center-Shifted Ellipses

An ellipse with center $\boldsymbol{x}_c \in \mathbb{R}^2$ is defined implicitly by the quadratic distance function

$$\Gamma(\boldsymbol{x}) = (\boldsymbol{x} - \boldsymbol{x}_c)^\top \boldsymbol{Q} (\boldsymbol{x} - \boldsymbol{x}_c) = \Gamma_0, \tag{B.1}$$

where $\Gamma_0 > 0$ is a constant and $\boldsymbol{Q} \in \mathbb{R}^{2\times 2}$ is a symmetric positive-definite matrix. The matrix $\boldsymbol{Q}$ admits the eigendecomposition

$$\boldsymbol{Q} = \boldsymbol{R}(q) \boldsymbol{\Lambda} \boldsymbol{R}^\top(q), \tag{B.2}$$

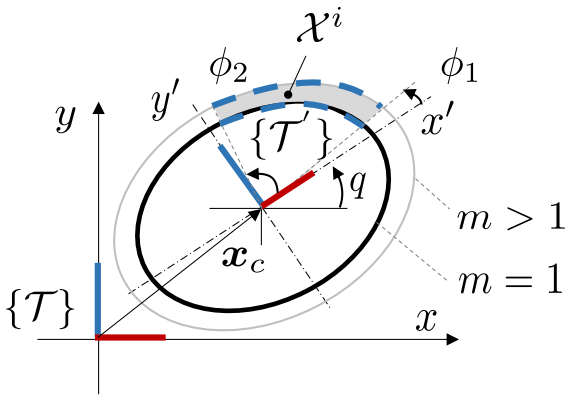


Figure B.1: Parametric representation of an elliptical sector or arc with center $\boldsymbol{x}_c$, rotation matrix $\boldsymbol{R}(q)$, and radial scaling factor m. The frame $\mathcal{T}'$ is obtained by rotating $\mathcal{T}$ by angle q.

Table B.1: Geometric explanation of different ϕ, u.

Geometric form	ϕ	u
Ellipse	$\in (0, 2\pi]$	u_0
Arc	$\in (\phi_1, \phi_2)$	u_0
Sector	$\in (\phi_1, \phi_2)$	$\in (0, u_0)$
Annulus	$\in (\phi_1, \phi_2)$	$\in (u_1, u_2)$

ϕ_1 and ϕ_2 are starting and ending angles, respectively. u_1 and u_2 are lower and upper bounds or radial scaling.

with rotation matrix

$$\boldsymbol{R}(q) = \begin{bmatrix} \cos q & -\sin q \\ \sin q & \cos q \end{bmatrix} \in SO(2),$$

and diagonal matrix

$$\boldsymbol{\Lambda} = \operatorname{diag}\left(l_a^{-2},\, l_b^{-2}\right), \tag{B.3}$$

where l_a and l_b denote the semi-major and semi-minor axes, respectively.

For the purpose of defining local regions around finger segments, a parametric set notation is introduced:

$$\mathcal{X}(\boldsymbol{x}_c, \boldsymbol{R}, \boldsymbol{\Lambda}, \phi, u) = \left\{ \boldsymbol{x} \in \mathbb{R}^2 \,\middle|\, \boldsymbol{x} = \boldsymbol{x}_c + u\boldsymbol{R}\boldsymbol{\Lambda}^{-1/2} \begin{bmatrix} \cos\phi \\ \sin\phi \end{bmatrix} \right\}, \tag{B.4}$$

where $\phi \in \mathbb{R}$ is the angular parameter and $u \in \mathbb{R}^+$ is a radial scaling factor. Different choices of ϕ and u yield distinct geometric primitives, as summarized in Table B.1.

Ellipse in second-order polynomial form

Expanding (B.1) yields the general conic form

$$a_1x^2 + a_2xy + a_3y^2 + a_4x + a_5y + a_6 = 0, \tag{B.5}$$

where the coefficients relate to $\boldsymbol{Q}$ and $\boldsymbol{x}_c$ as follows:

$$\boldsymbol{Q} = \begin{bmatrix} a_1 & \frac{1}{2}a_2 \\ \frac{1}{2}a_2 & a_3 \end{bmatrix}, \tag{B.6}$$

$$\boldsymbol{x}_c = \boldsymbol{Q}^{-1} \begin{bmatrix} -\frac{1}{2}a_4 \\ -\frac{1}{2}a_5 \end{bmatrix}, \tag{B.7}$$

$$\Gamma_0 = -\frac{\det \boldsymbol{Q}_q}{\det \boldsymbol{Q}}, \tag{B.8}$$

with the augmented matrix

$$\boldsymbol{Q}_q = \begin{bmatrix} a_1 & \frac{1}{2}a_2 & \frac{1}{2}a_4 \\ \frac{1}{2}a_2 & a_3 & \frac{1}{2}a_5 \\ \frac{1}{2}a_4 & \frac{1}{2}a_5 & a_6 \end{bmatrix}.$$

The conic represents a non-degenerate ellipse if and only if $\det \boldsymbol{Q} > 0$ and $\det \boldsymbol{Q}_q \neq 0$.

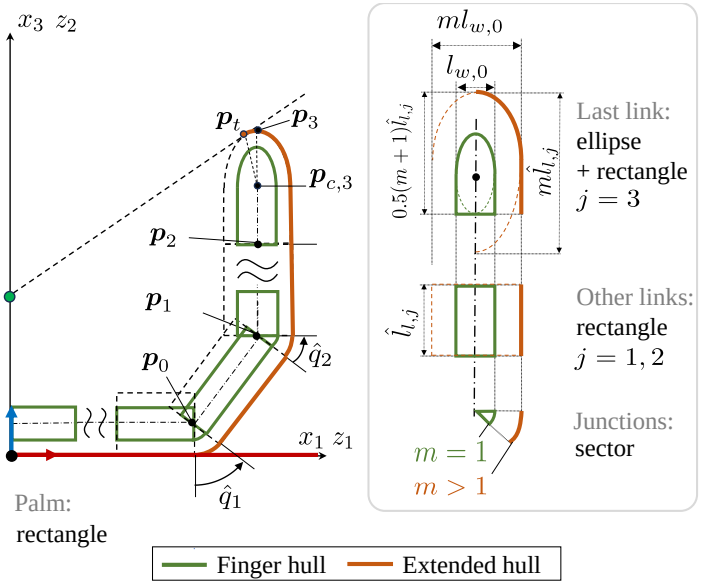


Figure B.2: Estimated kinematic chain of a single finger on a rotated plane. The extended hull (orange) incorporates object radius r_o per Assumption 4.

B.1.2 Estimation of Finger Configuration and Length

To balance fidelity and computational efficiency, the estimated finger model employs fewer degrees of freedom than the physical hand. As an example, a 3-DoF serial chain is used to represent flexion/extension at the metacarpophalangeal (MCP), proximal interphalangeal (PIP), and distal interphalangeal (DIP) joints, denoted $\hat{q}_j$ for $j = 1, 2, 3$. The base link is anchored to a fixed point representing half the palm width.

Joint configurations and segment lengths are modeled as piecewise third-order polynomials in the rotation angle α:

$$\hat{q}_j(\alpha, \boldsymbol{q}) = p_{q0,j} + p_{q1,j}\alpha + p_{q2,j}\alpha^2 + p_{q3,j}\alpha^3, \tag{B.9}$$

$$\hat{l}_{l,j}(\alpha, \boldsymbol{q}) = p_{l0,j} + p_{l1,j}\alpha + p_{l2,j}\alpha^2 + p_{l3,j}\alpha^3, \tag{B.10}$$

where coefficients are determined by boundary conditions at discrete angles corresponding to anatomical finger positions (thumb, index, middle, ring, little), as listed in Table B.2. For interval k, the conditions $\hat{q}_j(\alpha_k) = q_j^k$ and $\hat{q}_j(\alpha_{k+1}) = q_j^{k+1}$ yield standard cubic Hermite interpolation coefficients.

The estimated configuration vector is compactly denoted $\hat{\boldsymbol{q}} = \boldsymbol{f}_{\text{poly3}}(\alpha, \boldsymbol{q})$, with components bounded as

$$0 \leq q_{\min} \leq \hat{q}_j \leq q_{\max},$$

where $q_{\min}$ and $q_{\max}$ are functional limits (not mechanical joint stops). Violations of these bounds can lead to degenerate hulls, as illustrated in Figure 4.12 and Figure 4.4(d).

Physical parameters for the DLR *neoDavid* hand are provided in Table B.3.

B.1.3 Estimated Finger Kinematics

On each rotated plane, the finger is approximated using primitive shapes: rectangles for phalanges, circular sectors for joints, and ellipses for fingertips. The position of the j-th joint and the center of

Table B.2: Boundary conditions for polynomial interpolation of joint angles and segment lengths as a function of rotation angle α.

α^k [°]	0	20	40	100	180	240	310	340
$\hat{q}_j^k$	q_j^{middle}	q_j^{ring}	q_j^{little}	q_{min}	q_{min}	q_j^{thumb}	q_{min}	q_j^{index}
$\hat{l}_{l,j}^k$	$l_{l,j}^{\text{middle}}$	$l_{l,j}^{\text{ring}}$	$l_{l,j}^{\text{little}}$	$l_{l,j}^{\text{aux1}}$	$l_{l,j}^{\text{bottom}}$	$l_{l,j}^{\text{thumb}}$	$l_{l,j}^{\text{aux2}}$	$l_{l,j}^{\text{index}}$

Auxiliary lengths ($l^{\text{aux1}}, l^{\text{bottom}}, l^{\text{aux2}}$) span interdigital and hypothenar regions.

Table B.3: Segment lengths (m) and base thickness $l_{w,0}$ for the *neoDavid* hand, used in Table B.2.

Var.	Values [m]	Var.	Values [m]
$l_{l,j}^{\text{middle}}$	0.041, 0.041, 0.039	$l_{l,j}^{\text{bottom}}$	0.012, 0.012, 0.010
$l_{l,j}^{\text{ring}}$	0.032, 0.032, 0.025	$l_{l,j}^{\text{thumb}}$	0.050, 0.050, 0.040
$l_{l,j}^{\text{little}}$	0.028, 0.028, 0.022	$l_{l,j}^{\text{aux2}}$	0.004, 0.004, 0.003
$l_{l,j}^{\text{aux1}}$	0.002, 0.002, 0.002	—	—
$l_{w,0}$	0.02	—	—

the j-th segment are computed via forward kinematics:

$$\boldsymbol{p}_j = \boldsymbol{f}_{\text{fk}}(\hat{\boldsymbol{q}}, \hat{\boldsymbol{l}}) = \sum_{i=1}^{j} \begin{bmatrix} a_i \cos\left(\sum_{k=1}^{i} \hat{q}_k\right) \\ a_i \sin\left(\sum_{k=1}^{i} \hat{q}_k\right) \end{bmatrix} + \boldsymbol{p}_0, \tag{B.11}$$

$$\boldsymbol{p}_{c,j} = \frac{\boldsymbol{p}_j + \boldsymbol{p}_{j-1}}{2}, \tag{B.12}$$

where $\boldsymbol{p}_0$ is a fixed palm offset and segment lengths a_j are defined as

$$a_j = \begin{cases} \hat{l}_{l,j} & j = 1, 2, \\ 0.5(m+1)\hat{l}_{l,j} & j = 3, \end{cases} \tag{B.13}$$

with scaling factor

$$m = \frac{r_o + l_{w,0}}{l_{w,0}}, \tag{B.14}$$

accounting for object radius r_o per Assumption 4. A uniform thickness $b_j = m l_{w,0}$ is applied to all segments. The curvature at joints and tips is encoded via radius matrices:

$$\boldsymbol{Q}_{c,j} = \boldsymbol{R}(\theta_j)\,\text{diag}\left((0.5 m l_{w,0})^{-2}, (0.5 m l_{w,0})^{-2}\right)\boldsymbol{R}^\top(\theta_j), \tag{B.15}$$

$$\boldsymbol{Q}_t = \boldsymbol{R}(\theta_3)\,\text{diag}\left((0.5 m \hat{l}_{l,3})^{-2}, (0.5 m l_{w,0})^{-2}\right)\boldsymbol{R}^\top(\theta_3), \tag{B.16}$$

where $\theta_j = \sum_{k=1}^{j} \hat{q}_k$.

B.1.4 Closed Forms of Region Definitions

Figure B.3 illustrates the spatial partitioning (i.e., the regions) used in the dynamical system design. Formal set definitions are provided in Table B.4.

Table B.4: Definition of sets in the neighborhood of the hand hull $\mathcal{D}$.

Symbol	Category	Set Definition
$\mathcal{R}_r^b$	Rectangular boundary	$\{\boldsymbol{z} \in \Omega_z \mid \boldsymbol{G}_{[3]}^\top \boldsymbol{z} = b_{[3]},\ \boldsymbol{G}_{[1:2]}\boldsymbol{z} < \boldsymbol{b}_{[1:2]}\}$
$\mathcal{R}_c^b$	Circular boundary	$\mathcal{X}\big(\boldsymbol{p}_j, \boldsymbol{R}(-\sum_{i=1}^{j} q_i), \mathrm{diag}(l_{a,j}^{-2}, l_{b,j}^{-2}), [-\frac{\pi}{2} - q_j, -\frac{\pi}{2}), 1\big)$, $j = 1, 2$
$\mathcal{R}_t^b$	Fingertip boundary	$\mathcal{X}\big(\boldsymbol{p}_{c,3}, \boldsymbol{R}(-\sum_{i=1}^{3} q_i), \mathrm{diag}(l_{a,3}^{-2}, l_{b,3}^{-2}), [-\frac{\pi}{2}, \phi_t), 1\big)$
$\mathcal{R}_r^e$	Rectangular exterior	$\{\boldsymbol{z} \in \Omega_z \mid \boldsymbol{G}\boldsymbol{z} < \boldsymbol{b}\}$
$\mathcal{R}_c^e$	Circular exterior	$\mathcal{X}(\cdots, (1, c)),\ c > 1$
$\mathcal{R}_t^e$	Fingertip exterior	$\mathcal{X}(\cdots, (1, c)),\ c > 1$
$\mathcal{R}^b$	Boundary	$\{\boldsymbol{z} \in \Omega_z \mid \Gamma(\boldsymbol{z}) = 1\} = \mathcal{R}_r^b \cup \mathcal{R}_c^b \cup \mathcal{R}_t^b$
$\mathcal{R}^f$	Interior	$\{\boldsymbol{z} \in \Omega_z \mid \Gamma(\boldsymbol{z}) < 1\}$
$\mathcal{R}_0$	Cone set	$\{\boldsymbol{z} \in \Omega_z \mid \boldsymbol{G}\boldsymbol{z} \leq \boldsymbol{b}\}$
$\mathcal{R}_1$	Exterior set	$\{\boldsymbol{z} \in \Omega_z \mid \Gamma(\boldsymbol{z}) > 1\} = \mathcal{R}_r^e \cup \mathcal{R}_c^e \cup \mathcal{R}_t^e$
$\mathcal{D}^b$	Hull boundary	Surface of revolution of $\mathcal{R}^b$ about x_3-axis
$\mathcal{D}^f$	Hull interior	Solid of revolution of $\mathcal{R}^f$
$\mathcal{D}_0$	Spatial cone	Solid of revolution of $\mathcal{R}_0$
$\mathcal{D}_1$	Spatial exterior	Solid of revolution of $\mathcal{R}_1$
$\mathcal{D}_2$	Below palm	$\{\boldsymbol{x} \in \Omega \mid x_3 < 0\}$

The Cone-shaped Set $\mathcal{R}_0$

As shown in Figure B.3(a), $\mathcal{R}_0$ is a convex polyhedral cone defined by

$$\mathcal{R}_0 = \left\{ \boldsymbol{z} = (x, y) \,\middle|\, x \geq 0,\ y \leq p_{0,y},\ y \geq \frac{p_{t,y} - p_y^\star}{p_{t,x}} x + p_y^\star \right\}, \tag{B.17}$$

or equivalently $\boldsymbol{G}\boldsymbol{z} \leq \boldsymbol{b}$ with

$$\boldsymbol{G} = \begin{bmatrix} -1 & 0 \\ 0 & 1 \\ p_{t,y} - p_y^\star & -p_{t,x} \end{bmatrix}, \quad \boldsymbol{b} = \begin{bmatrix} 0 \\ p_{0,y} \\ -p_y^\star p_{t,x} \end{bmatrix}. \tag{B.18}$$

The tangent point $\boldsymbol{p}_t$ and supporting line s_1 are computed as described in Appendix B.2.2.

The Rectangular Set $\mathcal{R}_r$

The region adjacent to finger links is bounded by three half-planes (Figure B.3(b)):

$$\begin{aligned} \mathcal{R}_r = \big\{ \boldsymbol{z} = (x, y) \,\big|\, & n_{j,x} y \geq n_{j,y}(x - p_{j-1,x}) + p_{j-1,y}, \\ & n_{j,x} y \leq n_{j,y}(x - p_{j,x}) + p_{j,y}, \\ & l_{j,x} y \leq l_{j,y}(x - \bar{p}_{j,x}) + \bar{p}_{j,y} \big\}, \end{aligned} \tag{B.19}$$

where $\bar{p}_j = p_j + 0.5 m l_{w,0} \boldsymbol{n}_j$, and $\boldsymbol{n}_j = [n_{j,x}, n_{j,y}]^\top$ is the unit normal. In matrix form, $\boldsymbol{G}\boldsymbol{z} \leq \boldsymbol{b}$ with

$$\boldsymbol{G} = \begin{bmatrix} n_{j,y} & -n_{j,x} \\ n_{j,y} & -n_{j,x} \\ l_{j,y} & -l_{j,x} \end{bmatrix}, \quad \boldsymbol{b} = \begin{bmatrix} n_{j,y} p_{j-1,x} - p_{j-1,y} \\ n_{j,y} p_{j,x} - p_{j,y} \\ l_{j,y} \bar{p}_{j,x} - \bar{p}_{j,y} \end{bmatrix}. \tag{B.20}$$

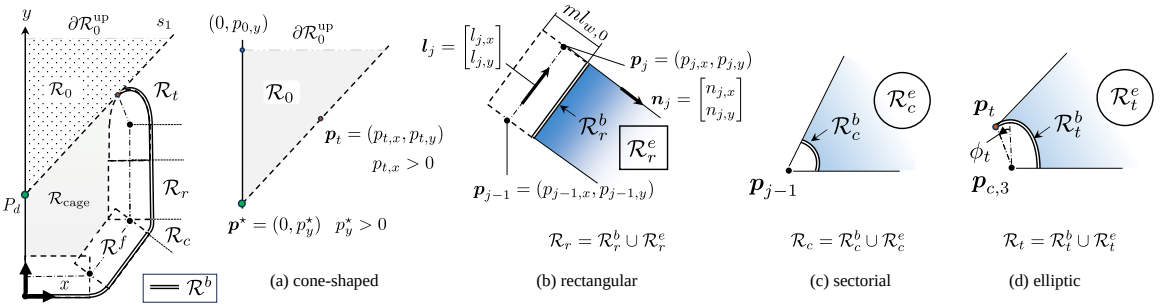


Figure B.3: Visualization of regions defined in Table B.4. (a) Cone set $\mathcal{R}_0$; (b) rectangular and curved boundaries around finger segments.

B.2 Tangent Flow

B.2.1 Closed Forms for Tangent Flow

On each rotated plane, a finger is approximated by three primitive geometric elements: rectangles (for phalanges), circular arcs (for joints), and ellipses (for fingertips). The tangent flow $\boldsymbol{e}(\boldsymbol{z})$, a unit vector field guiding motion along the hand hull boundary, is defined piecewise over the corresponding regions $\mathcal{R}_r$, $\mathcal{R}_c$, and $\mathcal{R}_t$, as illustrated in Figure B.4(b–d). The closed-form expression is given by

$$\boldsymbol{e}(\boldsymbol{z}) = \boldsymbol{R}\left(\frac{\pi}{2}\right)\boldsymbol{n}(\boldsymbol{z}), \tag{B.21}$$

$$\boldsymbol{n}(\boldsymbol{z}) = \begin{cases} \boldsymbol{n}_r & \boldsymbol{z} \in \mathcal{R}_r, \\ \boldsymbol{n}_{Q_{vc,j}} & \boldsymbol{z} \in \mathcal{R}_c, \\ \boldsymbol{n}_{Q_v} & \boldsymbol{z} \in \mathcal{R}_t, \end{cases} \tag{B.22}$$

where $\boldsymbol{R}(\pi/2)$ denotes a counterclockwise rotation by $\pi/2$, and $\boldsymbol{n}(\boldsymbol{z})$ is the outward-pointing unit normal to the hand hull at $\boldsymbol{z}$. The normal vectors for each region are defined as follows:

$$\boldsymbol{n}_r = \boldsymbol{R}\left(-\frac{\pi}{2}\right)\frac{\boldsymbol{p}_j - \boldsymbol{p}_{j-1}}{\|\boldsymbol{p}_j - \boldsymbol{p}_{j-1}\|}, \tag{B.23}$$

$$\boldsymbol{n}_{Q_{vc,j}} = \frac{\boldsymbol{Q}_{vc,j}(\boldsymbol{z} - \boldsymbol{p}_{j-1})}{\|\boldsymbol{Q}_{vc,j}(\boldsymbol{z} - \boldsymbol{p}_{j-1})\|}, \tag{B.24}$$

$$\boldsymbol{n}_{Q_v} = \frac{\boldsymbol{Q}_v(\boldsymbol{z} - \boldsymbol{p}_{c,v})}{\|\boldsymbol{Q}_v(\boldsymbol{z} - \boldsymbol{p}_{c,v})\|}, \tag{B.25}$$

where:

- $\boldsymbol{p}_j$ denotes the position of the j-th joint ($j = 1, 2, 3$),
- $\boldsymbol{p}_{c,v}$ is the center of a virtual ellipse near the fingertip,
- $\boldsymbol{Q}_{vc,j} = \boldsymbol{R}(\theta)\,\mathrm{diag}(r_{vc}^{-2}, r_{vc}^{-2})\boldsymbol{R}^\top(\theta)$, with $\theta = \sum_{i=1}^{j}\hat{q}_i$,
- $r_{vc} = \|\boldsymbol{z} - \boldsymbol{p}_{c,v}\|$ is the radial distance to the virtual center.

Near the fingertip ($\boldsymbol{z} \in \mathcal{R}_t$), the tangent flow aligns with the tangent of a virtual ellipse whose parameters are chosen to ensure smooth transition across the switching boundary s_1. Further details are provided in Appendix B.2.3.

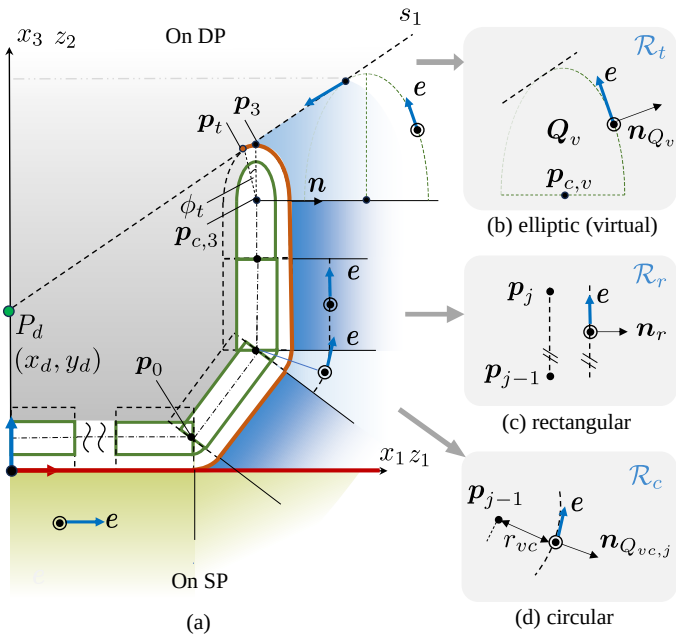


Figure B.4: Tangent flow vectors (blue) in different regions around the finger approximation.

B.2.2 Tangent Line and Tangent Point

The supporting line s_1 and its point of contact $\boldsymbol{p}_t$ with the fingertip ellipse are computed to define the boundary between $\mathcal{R}_0$ and $\mathcal{R}_1$. Consider a line of unknown slope $k > 0$ passing through the attractor $P_d = (x_d, y_d)$:

$$y = k(x - x_d) + y_d. \tag{B.26}$$

Substituting into the implicit ellipse equation (B.5) yields a quadratic in x:

$$A(k)x^2 + B(k)x + C(k) = 0, \tag{B.27}$$

with coefficients dependent on k:

$$A(k) = a_3k^2 + a_2k + a_1, \tag{B.28a}$$
$$B(k) = a_2(y_d - kx_d) + 2a_3k(y_d - kx_d), \tag{B.28b}$$
$$C(k) = a_3(y_d - kx_d)^2 + a_5(y_d - kx_d) + a_6, \tag{B.28c}$$

where a_1, a_2, a_3 are derived from the fingertip radius matrix $\boldsymbol{Q}_t$ via (B.6), (B.7) and (B.8).

Tangency requires a double root, i.e., vanishing discriminant:

$$\Delta(k) = B^2(k) - 4A(k)C(k) = 0. \tag{B.29}$$

This quartic equation in k admits two positive real solutions (see Figure B.5(a)). The steeper slope is selected to ensure the cone $\mathcal{R}_0$ remains narrow and forward-facing:

$$k = \max(k_1, k_2). \tag{B.30}$$

The tangent point and line are then:

$$p_{t,x} = -\frac{B}{2A}, \quad p_{t,y} = k(p_{t,x} - x_d) + y_d, \tag{B.31}$$
$$s_1 : \{(x, y) \mid y - kx - y_d + kx_d = 0\}. \tag{B.32}$$

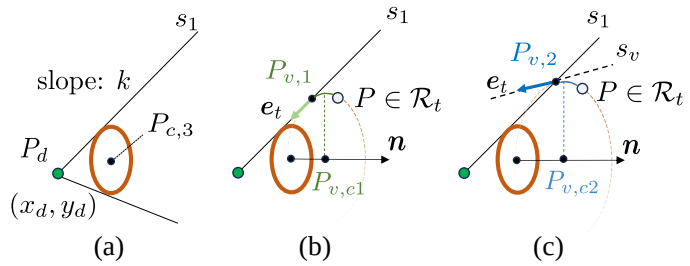


Figure B.5: (a) Two tangent lines from an external point to an ellipse. (b) When $a_1 = a_3$, the virtual ellipse is tangent to s_1. (c) When $a_1 > a_3$, tangency occurs with a modified line s_v of slope $k_v = ka_3/a_1$.

The angular parameter of the tangent point relative to the fingertip major axis is:

$$\phi_t = \arccos\left(\frac{(\boldsymbol{p}_t - \boldsymbol{p}_{c,3})^\top (\boldsymbol{p}_3 - \boldsymbol{p}_{c,3})}{\|\boldsymbol{p}_t - \boldsymbol{p}_{c,3}\| \, \|\boldsymbol{p}_3 - \boldsymbol{p}_{c,3}\|}\right), \tag{B.33}$$

where $\boldsymbol{p}_{c,3}$ is the center of the third segment.

B.2.3 Continuous Tangent Flow Across s_1 via virtual ellipse

To ensure smoothness of $\boldsymbol{e}(\boldsymbol{z})$ across s_1, a virtual ellipse is introduced in $\mathcal{R}_t$. Its parameters are constrained such that (1) The center $\boldsymbol{p}_{v,c}$ lies along the normal to the fingertip at $\boldsymbol{p}_{c,3}$. (2) The aspect ratio matches that of the physical fingertip ellipse, scaled by factor m from (B.14).

Two cases arise depending on the gain matrix $\boldsymbol{A}_{/\!/} = \mathrm{diag}(a_1, a_3)$:

(I) If $a_1 = a_3$, the virtual ellipse is tangent to s_1 at $\boldsymbol{p}_{v,1} = \boldsymbol{p}_t$ (Figure B.5(b)).

(II) If $a_1 > a_3$, the linear flow is anisotropic; the virtual ellipse is instead tangent to a modified line s_v with slope $k_v = ka_3/a_1$, intersecting s_1 at $\boldsymbol{p}_{v,2}$ (Figure B.5(c)).

In both cases, the center $\boldsymbol{p}_{v,c}$ and radius matrix $\boldsymbol{Q}_v$ are determined by solving the tangency condition (B.29), ensuring continuity of $\boldsymbol{e}(\boldsymbol{z})$ across s_1.

B.2.4 State-dependent Transition Function

The blending between linear and tangent flows is governed by a smooth transition function $\eta(\boldsymbol{z}) \in [0, 1]$. An example design is:

$$\eta(\boldsymbol{z}) = \frac{1}{2}\left[1 - \tanh\left(\sigma_1(\Gamma(\boldsymbol{z}) - \Gamma_0)\right)\right], \tag{B.34}$$

where $\sigma_1 > 0$ controls the transition sharpness and $\Gamma_0 > 0$ defines the reactivity margin.

The distance function $\Gamma(\boldsymbol{z})$ encodes proximity to the hand hull boundary $\mathcal{R}^b$:

$$\Gamma(\boldsymbol{z}) = \begin{cases} \left(\dfrac{2}{ml_{w,0}}\right)^2 \left[(\boldsymbol{z} - \boldsymbol{p}_j) \wedge \boldsymbol{l}\right]^2 & \boldsymbol{z} \in \mathcal{R}_r, \\ \left(\dfrac{2}{ml_{w,0}}\right)^2 \|\boldsymbol{z} - \boldsymbol{p}_j\|^2 & \boldsymbol{z} \in \mathcal{R}_c, \\ (\boldsymbol{z} - \boldsymbol{p}_{c,3})^\top \boldsymbol{Q}_t (\boldsymbol{z} - \boldsymbol{p}_{c,3}) & \boldsymbol{z} \in \mathcal{R}_t, \end{cases} \tag{B.35}$$

where:

- $ml_{w,0}$ is the extended finger thickness from (B.14),
- $\boldsymbol{l} = (\boldsymbol{p}_j - \boldsymbol{p}_{j-1})/\|\boldsymbol{p}_j - \boldsymbol{p}_{j-1}\|$ is the unit link direction,
- $\boldsymbol{Q}_t$ is the fingertip radius matrix from (B.16).

By construction, $\Gamma(\boldsymbol{z}) = 1$ on $\mathcal{R}^b$, and $\Gamma(\boldsymbol{z})$ increases quadratically with distance from the hull. Consequently, $\eta \to 1$ near the boundary and $\eta \to 0$ far from the attractor. The isolines of Γ are shown in Figure B.6.

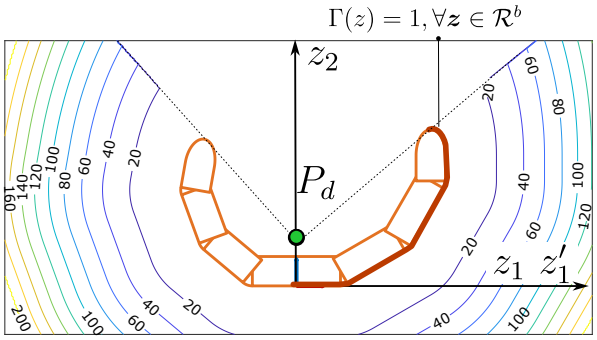


Figure B.6: Isolines of the distance function $\Gamma(\boldsymbol{z})$. The boundary $\mathcal{R}^b$ corresponds to $\Gamma = 1$.

B.2.5 Lipschitz Continuity of the Rotation Angle

Lemma 3. *For $\boldsymbol{z} \in \mathcal{R}_1$ (or $\boldsymbol{x} \in \mathcal{D}_2$), the rotation angle $\gamma(\boldsymbol{z})$ defined in* (4.6) *is locally Lipschitz continuous.*

Proof. The proof proceeds in two steps.

Step 1: Differentiability. The transition function $\eta(\boldsymbol{z})$ in (B.34) is smooth due to the analyticity of $\tanh(\cdot)$. The base angle $\gamma_0(\boldsymbol{z})$ in (4.7) is differentiable because:

1. The sign term $\operatorname{sgn}(\boldsymbol{f}_{t,w} \wedge \boldsymbol{e})$ is constant within each connected component of $\mathcal{R}_1$,
2. Both $\boldsymbol{f}_{t,w}(\boldsymbol{z})$ and $\boldsymbol{e}(\boldsymbol{z})$ are differentiable by construction,
3. $\|\boldsymbol{f}_{t,w}(\boldsymbol{z})\| > 0$ for all $\boldsymbol{z} \in \mathcal{R}_1$, avoiding singularities in (4.7).

Hence, $\gamma(\boldsymbol{z}) = \eta(\boldsymbol{z})\gamma_0(\boldsymbol{z})$ is differentiable.

Step 2: Bounded derivative. Within $\mathcal{R}_1$, the vectors $\boldsymbol{f}_{t,w}$ and $\boldsymbol{e}$ are neither parallel nor anti-parallel. Parallelism occurs only on s_1, which lies outside $\mathcal{R}_1$; anti-parallelism is precluded by hull design (see Figure 4.12). Thus, the argument of $\arccos(\cdot)$ in (4.7) remains strictly within $(-1, 1)$, ensuring the derivative of γ_0 is bounded:

$$\left\| \frac{\partial \gamma_0}{\partial \boldsymbol{z}} \right\| = \left\| \frac{-1}{\sqrt{1 - h^2(\boldsymbol{z})}} \frac{\partial h}{\partial \boldsymbol{z}} \right\| \leq L_0 < \infty,$$

where $h(\boldsymbol{z}) = \boldsymbol{f}_{t,w}^\top \boldsymbol{e}/\|\boldsymbol{f}_{t,w}\|$. Similarly, $\|\partial\eta/\partial\boldsymbol{z}\| \leq L_\eta < \infty$ due to the bounded derivative of $\tanh(\cdot)$.

Combining these bounds:

$$\left\|\frac{\partial \gamma}{\partial \boldsymbol{z}}\right\| \leq \left\|\frac{\partial \eta}{\partial \boldsymbol{z}}\right\| |\gamma_0| + |\eta| \left\|\frac{\partial \gamma_0}{\partial \boldsymbol{z}}\right\| \leq L_\gamma < \infty.$$

By the mean value theorem, $\gamma(\boldsymbol{z})$ is Lipschitz continuous on any compact subset of $\mathcal{R}_1$. □

B.3 Invariant Set

Lemma 4. *[216, Lemma 3.5] Let $P = \{\boldsymbol{z} \in \mathbb{R}^n \mid \boldsymbol{G}\boldsymbol{z} \leq \boldsymbol{b}\}$ be a polyhedral set. The set P is positively invariant under the linear dynamical system $\dot{\boldsymbol{z}} = \boldsymbol{A}\boldsymbol{z}$ if and only if, for every boundary facet $\partial P_i = \{\boldsymbol{z} \mid \boldsymbol{G}_i^\top \boldsymbol{z} = b_i\}$, the condition*

$$\boldsymbol{G}_i^\top \boldsymbol{A}\boldsymbol{z} \leq 0$$

holds for all $\boldsymbol{z} \in \partial P_i$, where $\boldsymbol{G}_i^\top$ denotes the i-th row of $\boldsymbol{G}$.

Proof. The result follows directly from Nagumo's Theorem [217, Theorem 2.7], which provides a necessary and sufficient condition for set invariance under continuous dynamics. A detailed proof is provided in [216, Lemma 3.5] and [218]. □

B.3.1 Proof of an Invariant Set

Proof. Consider the linear dynamical system defined in (4.3):

$$\dot{\boldsymbol{z}} = -\boldsymbol{A}_{/\!/}(\boldsymbol{z} - \boldsymbol{z}^\star) = -\boldsymbol{A}_{/\!/}\tilde{\boldsymbol{z}},$$

where $\tilde{\boldsymbol{z}} = [x,\, y - p_y^\star]^\top$ and $\boldsymbol{A}_{/\!/} = \operatorname{diag}(a_1, a_3)$ with $a_1 \geq a_3 > 0$. The set $\mathcal{R}_0$ is a convex polyhedron defined by $\boldsymbol{G}\boldsymbol{z} \leq \boldsymbol{b}$ as in (B.18), with three boundary facets $\partial\mathcal{R}_0^i$, $i = 1, 2, 3$.

To verify invariance, it suffices to show that the vector field points inward or is tangent to each boundary, i.e., $-\boldsymbol{G}_i^\top \boldsymbol{A}_{/\!/}\tilde{\boldsymbol{z}} \leq 0$ for all $\boldsymbol{z} \in \partial\mathcal{R}_0^i$.

(1) On $\partial\mathcal{R}_0^1$ ($x = 0$):

$$-\boldsymbol{G}_1^\top \boldsymbol{A}_{/\!/}\tilde{\boldsymbol{z}} = \begin{bmatrix} -1 & 0 \end{bmatrix} \begin{bmatrix} -a_1 x \\ -a_3(y - p_y^\star) \end{bmatrix} = 0.$$

(2) On $\partial\mathcal{R}_0^2$ ($y = p_{0,y} \geq p_y^\star$):

$$-\boldsymbol{G}_2^\top \boldsymbol{A}_{/\!/}\tilde{\boldsymbol{z}} = \begin{bmatrix} 0 & 1 \end{bmatrix} \begin{bmatrix} -a_1 x \\ -a_3(y - p_y^\star) \end{bmatrix} = -a_3(y - p_y^\star) \leq 0,$$

since $y \geq p_y^\star$.

(3) On $\partial\mathcal{R}_0^3$ (the tangent line $s_1 : y = \frac{p_{t,y} - p_y^\star}{p_{t,x}} x + p_y^\star$):

$$\begin{aligned} -\boldsymbol{G}_3^\top \boldsymbol{A}_{/\!/}\tilde{\boldsymbol{z}} &= \begin{bmatrix} p_{t,y} - p_y^\star & -p_{t,x} \end{bmatrix} \begin{bmatrix} -a_1 x \\ -a_3(y - p_y^\star) \end{bmatrix} \\ &= p_{t,x}(a_3 - a_1)(y - p_y^\star) \leq 0, \end{aligned}$$

because $p_{t,x} > 0$, $y \geq p_y^\star$, and $a_1 \geq a_3$.

Thus, the invariance condition of Lemma 4 is satisfied for all boundary facets. Therefore, $\mathcal{R}_0$ is a positively invariant set under the dynamics (4.3). □

B.4 Implementation Details in Experimental Validations

B.4.1 System Parameters

The parameters employed in all experimental evaluations of the Finger Flow framework are summarized in Table B.5. Joint configurations follow the order: metacarpal adduction, metacarpal flexion, proximal interphalangeal flexion, and distal interphalangeal flexion.

Table B.5: Parameters used in experimental validations.

Parameter	Value
Desired orientation ${}^{\mathcal{H}}\boldsymbol{R}_d$	$\boldsymbol{R}_x(\pi/2)$
Attractor position $\boldsymbol{x}^\star$	$[0,\ 0,\ 0.02]^\top$ [m]
Gain matrix $\boldsymbol{A}$ (4.10)	$3 \cdot \boldsymbol{I}_{3\times3}$
Transition sharpness σ_1 (B.34)	0.01
Reactivity margin Γ_0 (B.34)	150
Finger closure gain $\boldsymbol{Q}_f$ (4.32)	$\mathrm{diag}(80,\ 1,\ 260)$
Power-grasp configuration $\boldsymbol{q}_{f,d}$	Thumb: $[0.45,\ 0.5,\ 0.5,\ 0.5]$ rad; Little: $[0,\ 0.7,\ 0.5,\ 0.5]$ rad; Index/Middle/Ring: $[0,\ 0.5,\ 1.0,\ 1.0]$ rad
Hand-cage configuration $\boldsymbol{q}_{f,o}$	Fingers: $[0,\ 0.524,\ 0,\ 0]$ rad; Thumb: $[-0.524,\ 0.524,\ 0,\ 0]$ rad

B.4.2 Object Pouring and Placing Motion

Following grasp confirmation, a predefined joint-space trajectory executes a pouring-and-placing sequence. The arm velocity reference is generated by blending between the Finger Flow command and a target motion via a smooth time-dependent function:

$$\dot{\boldsymbol{q}}_{a,c} = k(\tau)\dot{\boldsymbol{q}}_{a,n} + (1 - k(\tau))\dot{\boldsymbol{q}}_{a,r}, \tag{B.36}$$

where:

- $\dot{\boldsymbol{q}}_{a,r}$ is the Finger Flow joint velocity from (4.22),
- $\dot{\boldsymbol{q}}_{a,n} = -\boldsymbol{A}_c(\boldsymbol{q} - \boldsymbol{q}_{a,p})$ drives the arm toward a pouring posture $\boldsymbol{q}_{a,p}$,
- $\boldsymbol{A}_c = \boldsymbol{I}_{5\times5}$ is a diagonal gain matrix,
- The blending function $k(\tau) = \frac{1}{2}[1 + \tanh(5(\tau - 1))]$ transitions smoothly from 0 to 1 over 2 seconds.

After pouring, the arm moves to a final placement configuration $\boldsymbol{q}_{a,e}$, while the fingers reopen to the hand-cage pose $\boldsymbol{q}_{f,o}$. Grasp confirmation requires at least $n_c = 6$ engaged finger joints and external torque exceeding $\tau_{i,\min} = 0.1$ Nm for more than 1 second. Parameters for this phase are listed in Table B.6.

Table B.6: Parameters for pouring and placing motion.

Parameter	Value
The gain matrix $\boldsymbol{A}_c$	$\boldsymbol{I}_{5\times5}$
Number of the engaged joints n_c	6
Torque threshold $\tau_{i,\text{min}}$	0.1 Nm
Pouring configuration $\boldsymbol{q}_{a,p}$	$[25°,\ 40°,\ -10°,\ 70°,\ -60°]^\top$
Placement configuration $\boldsymbol{q}_{a,e}$	$[25°,\ 40°,\ -10°,\ 70°,\ 40°]^\top$

Bibliography

[1] Tetsuo Fukunaga et al. “Muscle and tendon interaction during human movements”. In: *Exercise and sport sciences reviews* 30.3 (2002), pp. 106–110.

[2] Günter Wöhlke. “Automatic grasp planning for multifingered robot hands”. In: *Journal of Intelligent Manufacturing* 3 (1992), pp. 297–316.

[3] Qijin She et al. “Learning high-DOF reaching-and-grasping via dynamic representation of gripper-object interaction”. In: *ACM Trans. Graph.* 41.4 (July 2022). ISSN: 0730-0301.

[4] Seungsu Kim, Ashwini Shukla, and Aude Billard. “Catching Objects in Flight”. In: *IEEE Transactions on Robotics* 30.5 (2014), pp. 1049–1065.

[5] Iretiayo Akinola et al. “Dynamic grasping with reachability and motion awareness”. In: *2021 IEEE/RSJ International Conference on Intelligent Robots and Systems (IROS)*. IEEE. 2021, pp. 9422–9429.

[6] Oliver B Kroemer et al. “Combining active learning and reactive control for robot grasping”. In: *Robotics and Autonomous systems* 58.9 (2010), pp. 1105–1116.

[7] Giuseppe Averta. “Learning from Humans How to Grasp: A Reactive-Based Approach”. In: *Human-Aware Robotics: Modeling Human Motor Skills for the Design, Planning and Control of a New Generation of Robotic Devices*. Springer, 2022, pp. 185–202.

[8] Patrick Rosenberger et al. “Object-independent human-to-robot handovers using real time robotic vision”. In: *IEEE Robotics and Automation Letters* 6.1 (2020), pp. 17–23.

[9] José R. Medina et al. “A human-inspired controller for fluid human-robot handovers”. In: *2016 IEEE-RAS 16th International Conference on Humanoid Robots (Humanoids)*. 2016, pp. 324–331. DOI: 10.1109/HUMANOIDS.2016.7803296.

[10] Arsalan Mousavian, Clemens Eppner, and Dieter Fox. “6-dof graspnet: Variational grasp generation for object manipulation”. In: *Proceedings of the IEEE/CVF international conference on computer vision*. 2019, pp. 2901–2910.

[11] Tyler Ga Wei Lum et al. “DextrAH-G: Pixels-to-Action Dexterous Arm-Hand Grasping with Geometric Fabrics”. In: *8th Annual Conference on Robot Learning*. 2024. URL: https://openreview.net/forum?id=S2Jwb0i7HN.

[12] François Michaud and Monica Nicolescu. “Behavior-based systems”. In: *Springer handbook of robotics* (2016), pp. 307–328.

[13] Erann Gat, R Peter Bonnasso, Robin Murphy, et al. “On three-layer architectures”. In: *Artificial intelligence and mobile robots* 195 (1998), p. 210.

[14] Rodney Brooks. “A robust layered control system for a mobile robot”. In: *IEEE journal on robotics and automation* 2.1 (1986), pp. 14–23.

[15] Ryo Sakagami et al. “Robotic world models—conceptualization, review, and engineering best practices”. In: *Frontiers in Robotics and AI* 10 (2023), p. 1253049.

[16] Toki Migimatsu and Jeannette Bohg. “Object-Centric Task and Motion Planning in Dynamic Environments”. In: *IEEE Robotics and Automation Letters* 5.2 (2020), pp. 844–851.

[17] Daniel Kappler et al. “Real-time perception meets reactive motion generation”. In: *IEEE Robotics and Automation Letters* 3.3 (2018), pp. 1864–1871.

[18] Marvin Becker et al. “Motion planning using reactive circular fields: A 2D analysis of collision avoidance and goal convergence”. In: *IEEE Transactions on Automatic Control* (2023).

[19] Rodney A Brooks and Jonathan H Connell. “Asynchronous distributed control system for a mobile robot”. In: *Mobile Robots I*. Vol. 727. SPIE. 1987, pp. 77–84.

[20] Douglas Morrison, Peter Corke, and Jürgen Leitner. “Learning robust, real-time, reactive robotic grasping”. In: *The International journal of robotics research* 39.2-3 (2020), pp. 183–201.

[21] Vasileios Vasilopoulos et al. “RAMP: Hierarchical Reactive Motion Planning for Manipulation Tasks Using Implicit Signed Distance Functions”. In: *2023 IEEE/RSJ International Conference on Intelligent Robots and Systems (IROS)*. IEEE. 2023, pp. 10551–10558.

[22] Mikhail Koptev, Nadia Figueroa, and Aude Billard. “Reactive collision-free motion generation in joint space via dynamical systems and sampling-based MPC”. In: *The International Journal of Robotics Research* 43.13 (2024), pp. 2049–2069.

[23] Antonio Bicchi. “On the closure properties of robotic grasping”. In: *The International Journal of Robotics Research* 14.4 (1995), pp. 319–334.

[24] Nico Mansfeld. “Safety Awareness for Rigid and Elastic Joint Robots: An Impact Dynamics and Control Framework”. PhD thesis. Technische Universität München, 2022.

[25] Gill A Pratt and Matthew M Williamson. “Series elastic actuators”. In: *Proceedings 1995 IEEE/RSJ International Conference on Intelligent Robots and Systems. Human Robot Interaction and Cooperative Robots*. Vol. 1. IEEE. 1995, pp. 399–406.

[26] Bram Vanderborght et al. “Exploiting Natural Dynamics to Reduce Energy Consumption by Controlling the Compliance of Soft Actuators”. In: *The International Journal of Robotics Research* 25.4 (2006), pp. 343–358. DOI: 10.1177/0278364906064566.

[27] Thomas J Roberts. “Contribution of elastic tissues to the mechanics and energetics of muscle function during movement”. In: *Journal of Experimental Biology* 219.2 (2016), pp. 266–275.

[28] Thomas Lens and Oskar Von Stryk. “Investigation of safety in human-robot-interaction for a series elastic, tendon-driven robot arm”. In: *2012 IEEE/RSJ International Conference on Intelligent Robots and Systems*. IEEE. 2012, pp. 4309–4314.

[29] Pongsiri Kuresangsai, Matthew OT Cole, and Guangbo Hao. “Grasp stability and design analysis of a flexure-jointed gripper mechanism via efficient energy-based modeling”. In: *IEEE Robotics and Automation Letters* 7.4 (2022), pp. 12499–12506.

[30] F. Lotti et al. “Development of UB Hand 3: Early Results”. In: *Proceedings of the 2005 IEEE International Conference on Robotics and Automation*. 2005, pp. 4488–4493. DOI: 10.1109/ROBOT.2005.1570811.

[31] Markus Grebenstein et al. “The hand of the DLR hand arm system: Designed for interaction”. In: *The International Journal of Robotics Research* 31.13 (2012), pp. 1531–1555.

[32] Ryuta Ozawa et al. “Design and control of a three-fingered tendon-driven robotic hand with active and passive tendons”. In: *Autonomous Robots* 36 (2014), pp. 67–78. DOI: 10.1007/s10514-013-9362-z.

[33] Manuel G Catalano et al. “Adaptive synergies for the design and control of the Pisa/IIT SoftHand”. In: *The International Journal of Robotics Research* 33.5 (2014), pp. 768–782.

[34] Lael U Odhner et al. “A compliant, underactuated hand for robust manipulation”. In: *The International Journal of Robotics Research* 33.5 (2014), pp. 736–752.

[35] Digby Chappell et al. “The hydra hand: a mode-switching underactuated gripper with precision and power grasping modes”. In: *IEEE Robotics and Automation Letters* 8.11 (2023), pp. 7599–7606.

[36] Arnaud Bersier et al. “Rotograb: Combining Biomimetic Hands with Industrial Grippers using a Rotating Thumb”. In: *2024 IEEE/RSJ International Conference on Intelligent Robots and Systems (IROS)*. IEEE. 2024, pp. 5303–5310.

[37] Kai Junge and Josie Hughes. “Spatially distributed biomimetic compliance enables robust anthropomorphic robotic manipulation”. In: *Communications Engineering* 4.1 (2025), p. 76.

[38] Sebastian Wolf, Oliver Eiberger, and Gerd Hirzinger. “The DLR FSJ: Energy based design of a variable stiffness joint”. In: *2011 IEEE International Conference on Robotics and Automation*. IEEE, 2011. DOI: 10.1109/icra.2011.5980303.

[39] W. Friedl et al. “Wrist and forearm rotation of the DLR Hand Arm System: Mechanical design, shape analysis and experimental validation”. In: *2011 IEEE/RSJ International Conference on Intelligent Robots and Systems*. IEEE, 2011.

[40] Florian Petit et al. “Bidirectional antagonistic variable stiffness actuation: Analysis, design & Implementation”. In: *2010 IEEE International Conference on Robotics and Automation*. IEEE, 2010. DOI: 10.1109/robot.2010.5509267.

[41] Werner Friedl et al. “FAS A flexible antagonistic spring element for a high performance over”. In: *2011 IEEE/RSJ International Conference on Intelligent Robots and Systems*. IEEE. 2011, pp. 1366–1372.

[42] Bastian Deutschmann. “Modeling and control for a class of tendon-driven continuum mechanisms”. PhD thesis. Leibniz Universität Hannover, 2020.

[43] Jens Reinecke et al. “A robotic torso joint with adjustable linear spring mechanism for natural dynamic motions in a differential-elastic arrangement”. In: *IEEE Robotics and Automation Letters* 7.1 (2021), pp. 9–16.

[44] Sebastian Wolf et al. “neoDavid: A Humanoid Robot With Variable-Stiffness Actuation and Dexterous Manipulation Skills”. In: *IEEE Robotics & Automation Magazine* (2025).

[45] Markus Grebenstein et al. “The DLR hand arm system”. In: *2011 IEEE International Conference on Robotics and Automation*. IEEE, 2011. DOI: 10.1109/icra.2011.5980371.

[46] Koichi Koganezawa, Yoshinori Watanabe, and Nobuyuki Shimizu. “Antagonistic muscle-like actuator and its application to multi-d.o.f. forearm prosthesis”. In: *Advanced Robotics* 12.7-8 (1997), pp. 771–789. DOI: 10.1163/156855399x00135.

[47] Steven LaValle. “Rapidly-exploring random trees: A new tool for path planning”. In: *Research Report 9811* (1998).

[48] Sertac Karaman and Emilio Frazzoli. “Sampling-based algorithms for optimal motion planning”. In: *The international journal of robotics research* 30.7 (2011), pp. 846–894.

[49] Carlos E Garcia, David M Prett, and Manfred Morari. “Model predictive control: Theory and practice—A survey”. In: *Automatica* 25.3 (1989), pp. 335–348.

[50] Leena Singh, John Wen, and Harry Stephanou. “Motion planning and dynamic control of a linked manipulator using modified magnetic fields”. In: *Proceedings of the 1997 IEEE International Conference on Control Applications*. IEEE. 1997, pp. 9–15.

[51] Marvin Becker et al. “Circular Fields and Predictive Multi-Agents for Online Global Trajectory Planning”. In: *IEEE Robotics and Automation Letters* 6.2 (2021), pp. 2618–2625.

[52] Karl Van Wyk et al. “Geometric fabrics: Generalizing classical mechanics to capture the physics of behavior”. In: *IEEE Robotics and Automation Letters* 7.2 (2022), pp. 3202–3209.

[53] Seyed Mohammad Khansari-Zadeh and Aude Billard. “A dynamical system approach to realtime obstacle avoidance”. In: *Autonomous Robots* 32 (2012), pp. 433–454.

[54] Lukas Huber, Jean-Jacques Slotine, and Aude Billard. “Avoidance of concave obstacles through rotation of nonlinear dynamics”. In: *IEEE Transactions on Robotics* (2023).

[55] Oussama Khatib. “Real-time obstacle avoidance for manipulators and mobile robots”. In: *The international journal of robotics research* 5.1 (1986), pp. 90–98.

[56] Daniel E Koditschek and Elon Rimon. “Robot navigation functions on manifolds with boundary”. In: *Advances in applied mathematics* 11.4 (1990), pp. 412–442.

[57] Roland Philippsen and Roland Siegwart. “An interpolated dynamic navigation function”. In: *Proceedings of the 2005 IEEE international conference on robotics and automation*. IEEE. 2005, pp. 3782–3789.

[58] H.J.S. Feder and J.-J.E. Slotine. “Real-time path planning using harmonic potentials in dynamic environments”. In: *Proceedings of International Conference on Robotics and Automation*. Vol. 1. 1997, 874–881 vol.1.

[59] Neville Hogan. “Impedance Control: An Approach to Manipulation: Part I—Theory”. In: *Journal of Dynamic Systems, Measurement, and Control* 107.1 (1985), pp. 1–7. DOI: 10.1115/1.3140702.

[60] Liding Zhang et al. “Motion planning for robotics: A review for sampling-based planners”. In: *Biomimetic Intelligence and Robotics* (2025), p. 100207.

[61] Matei T Ciocarlie and Peter K Allen. “Hand posture subspaces for dexterous robotic grasping”. In: *The International Journal of Robotics Research* 28.7 (2009), pp. 851–867.

[62] Marek Kopicki et al. “One-shot learning and generation of dexterous grasps for novel objects”. In: *The International Journal of Robotics Research* 35.8 (2016), pp. 959–976.

[63] Jean-Philippe Saut and Daniel Sidobre. “Efficient models for grasp planning with a multi-fingered hand”. In: *Robotics and Autonomous Systems* 60.3 (2012), pp. 347–357.

[64] Andrew T Miller et al. “Automatic grasp planning using shape primitives”. In: *2003 IEEE International Conference on Robotics and Automation (Cat. No. 03CH37422)*. Vol. 2. IEEE. 2003, pp. 1824–1829.

[65] Martin Sundermeyer et al. “Contact-graspnet: Efficient 6-dof grasp generation in cluttered scenes”. In: *2021 IEEE International Conference on Robotics and Automation (ICRA)*. IEEE. 2021, pp. 13438–13444.

[66] Hao-Shu Fang et al. “Anygrasp: Robust and efficient grasp perception in spatial and temporal domains”. In: *IEEE Transactions on Robotics* (2023).

[67] Ho Jin Choi and Nadia Figueroa. “Towards Feasible Dynamic Grasping: Leveraging Gaussian Process Distance Field, SE (3) Equivariance, and Riemannian Mixture Models”. In: *2024 IEEE International Conference on Robotics and Automation (ICRA)*. IEEE. 2024, pp. 6455–6461.

[68] S. Hutchinson, G.D. Hager, and P.I. Corke. “A tutorial on visual servo control”. In: *IEEE Transactions on Robotics and Automation* 12.5 (1996), pp. 651–670.

[69] Jesse Haviland, Niko Sünderhauf, and Peter Corke. “A holistic approach to reactive mobile manipulation”. In: *IEEE Robotics and Automation Letters* 7.2 (2022), pp. 3122–3129.

[70] Ben Burgess-Limerick et al. “An architecture for reactive mobile manipulation on-the-move”. In: *2023 IEEE International Conference on Robotics and Automation (ICRA)*. IEEE. 2023, pp. 1623–1629.

[71] Wei Yang et al. “Reactive human-to-robot handovers of arbitrary objects”. In: *2021 IEEE International Conference on Robotics and Automation (ICRA)*. IEEE. 2021, pp. 3118–3124.

[72] Seyed Sina Mirrazavi Salehian, Mahdi Khoramshahi, and Aude Billard. “A dynamical system approach for catching softly a flying object: Theory and experiment”. In: *IEEE Transactions on Robotics* 32.2 (2016), pp. 462–471.

[73] Ashwini Shukla and Aude Billard. “Coupled dynamical system based arm–hand grasping model for learning fast adaptation strategies”. In: *Robotics and Autonomous Systems* 60.3 (2012), pp. 424–440.

[74] Yannick Burkhardt et al. “Multi-fingered Dynamic Grasping for Unknown Objects”. In: *2024 IEEE-RAS 23rd International Conference on Humanoid Robots (Humanoids)*. 2024, pp. 60–67.

[75] Seyed Sina Mirrazavi Salehian, Nadia Figueroa, and Aude Billard. “Coordinated multi-arm motion planning: Reaching for moving objects in the face of uncertainty.” In: *Robotics: Science and Systems*. 2016.

[76] Matteo Saveriano et al. “Dynamic movement primitives in robotics: A tutorial survey”. In: *The International Journal of Robotics Research* 42.13 (2023), pp. 1133–1184.

[77] Alexandros Paraschos et al. “Probabilistic movement primitives”. In: *Advances in neural information processing systems* 26 (2013).

[78] S. Mohammad Khansari-Zadeh and Aude Billard. “Learning Stable Nonlinear Dynamical Systems With Gaussian Mixture Models”. In: *IEEE Transactions on Robotics* 5 (2011), pp. 943–957.

[79] Nathan D Ratliff et al. “Riemannian motion policies”. In: *arXiv preprint arXiv:1801.02854* (2018).

[80] Yanlong Huang et al. “Kernelized movement primitives”. In: *The International Journal of Robotics Research* 38.7 (2019), pp. 833–852.

[81] Cheng Chi et al. “Diffusion policy: Visuomotor policy learning via action diffusion”. In: *The International Journal of Robotics Research* (2023), p. 02783649241273668.

[82] Zehang Weng et al. “Dexdiffuser: Generating dexterous grasps with diffusion models”. In: *IEEE Robotics and Automation Letters* (2024).

[83] Kilian Kleeberger et al. “A survey on learning-based robotic grasping”. In: *Current Robotics Reports* 1 (2020), pp. 239–249.

[84] Shirin Joshi, Sulabh Kumra, and Ferat Sahin. “Robotic grasping using deep reinforcement learning”. In: *2020 IEEE 16th International Conference on Automation Science and Engineering (CASE)*. IEEE. 2020, pp. 1461–1466.

[85] Dmitry Zarubin et al. “Caging complex objects with geodesic balls”. In: *2013 IEEE/RSJ International Conference on Intelligent Robots and Systems*. IEEE. 2013, pp. 2999–3006.

[86] Alberto Rodriguez, Matthew T Mason, and Steve Ferry. “From caging to grasping”. In: *The International Journal of Robotics Research* 31.7 (2012), pp. 886–900.

[87] P. Tomei. “Adaptive PD controller for robot manipulators”. In: *IEEE Transactions on Robotics and Automation* 7.4 (1991), pp. 565–570. DOI: 10.1109/70.86088.

[88] Alessandro De Luca and Fabrizio Flacco. “A PD-type regulator with exact gravity cancellation for robots with flexible joints”. In: *2011 IEEE International Conference on Robotics and Automation*. IEEE, 2011. DOI: 10.1109/icra.2011.5979615.

[89] A. de Luca and P. Lucibello. “A general algorithm for dynamic feedback linearization of robots with elastic joints”. In: *Proceedings. 1998 IEEE International Conference on Robotics and Automation (Cat. No.98CH36146)*. IEEE, 1998. DOI: 10.1109/robot.1998.677024.

[90] Gabriele Buondonno and Alessandro De Luca. “Efficient Computation of Inverse Dynamics and Feedback Linearization for VSA-Based Robots”. In: *IEEE Robotics and Automation Letters* 1.2 (2016), pp. 908–915. DOI: 10.1109/lra.2016.2526072.

[91] P.V. Kokotovic, M. Krstic, and I. Kanellakopoulos. “Backstepping to passivity: recursive design of adaptive systems”. In: *Proceedings of the 31st IEEE Conference on Decision and Control*. IEEE, 1992. DOI: 10.1109/cdc.1992.371031.

[92] Handdeut Chang, Sangjoon J Kim, and Jung Kim. “Feedforward motion control with a variable stiffness actuator inspired by muscle cross-bridge kinematics”. In: *IEEE Transactions on Robotics* 35.3 (2019), pp. 747–760.

[93] Lin Liu et al. “Impedance-Controlled Variable Stiffness Actuator for Lower Limb Robot Applications”. In: *IEEE Transactions on Automation Science and Engineering* 17.2 (2020), pp. 991–1004. DOI: 10.1109/tase.2019.2954769.

[94] C. Ott et al. “Decoupling based Cartesian impedance control of flexible joint robots”. In: *2003 IEEE International Conference on Robotics and Automation (Cat. No.03CH37422)*. IEEE, 2003. DOI: 10.1109/robot.2003.1242067.

[95] C. Ott et al. “On the Passivity-Based Impedance Control of Flexible Joint Robots”. In: *IEEE Transactions on Robotics* 24.2 (2008), pp. 416–429. DOI: 10.1109/tro.2008.915438.

[96] Thomas Wimbock et al. “Impedance control for variable stiffness mechanisms with nonlinear joint coupling”. In: *2008 IEEE/RSJ International Conference on Intelligent Robots and Systems*. IEEE. 2008, pp. 3796–3803.

[97] Maxime Chalon et al. “Impedance control of a non-linearly coupled tendon driven thumb”. In: *2011 IEEE/RSJ International Conference on Intelligent Robots and Systems*. IEEE. 2011, pp. 4215–4221.

[98] Muhammad E Abdallah, Robert Platt Jr, and Charles W Wampler. “Decoupled torque control of tendon-driven fingers with tension management”. In: *The International Journal of Robotics Research* 32.2 (2013), pp. 247–258.

[99] Cosimo Della Santina et al. “Controlling soft robots: balancing feedback and feedforward elements”. In: *IEEE Robotics & Automation Magazine* 24.3 (2017), pp. 75–83.

[100] Alessandro De Luca and Fabrizio Flacco. “Dynamic gravity cancellation in robots with flexible transmissions”. In: *49th IEEE Conference on Decision and Control (CDC)*. IEEE. 2010, pp. 288–295.

[101] Manuel Keppler et al. “Elastic structure preserving (ESP) control for compliantly actuated robots”. In: *IEEE Transactions on Robotics* 34.2 (2018), pp. 317–335.

[102] Riccardo Mengacci et al. “Elastic Structure Preserving Control for Compliant Robots Driven by Agonistic-Antagonistic Actuators (ESPaa)”. In: *IEEE Robotics and Automation Letters* 6.2 (2021), pp. 879–886.

[103] Xuming Meng, Manuel Keppler, and Christian Ott. “Elastic Structure Preserving Impedance Control of Bidirectional Antagonistic Variable Stiffness Actuation”. In: *2021 European Control Conference (ECC 2021)*. 2021, pp. 263–269. URL: https://elib.dlr.de/143334/.

[104] M.W. Spong. “On the force control problem for flexible joint manipulators”. In: *IEEE Transactions on Automatic Control* 34.1 (1989), pp. 107–111.

[105] J.K. Mills. “Stability and control of elastic-joint robotic manipulators during constrained-motion tasks”. In: *IEEE Transactions on Robotics and Automation* 8.1 (1992), pp. 119–126.

[106] F. Aghili. “A unified approach for inverse and direct dynamics of constrained multibody systems based on linear projection operator: applications to control and simulation”. In: *IEEE Trans. Robot* 21.5 (2005), pp. 834–849.

[107] Michael Mistry, Jonas Buchli, and Stefan Schaal. “Inverse dynamics control of floating base systems using orthogonal decomposition”. In: *2010 IEEE International Conference on Robotics and Automation*. 2010, pp. 3406–3412.

[108] Michael Mistry and Ludovic Righetti. “Operational Space Control of Constrained and Underactuated Systems”. In: *Robotics*. Robotics: Science and Systems. June 2011.

[109] Valerio Ortenzi et al. “An experimental study of robot control during environmental contacts based on projected operational space dynamics”. In: *2014 IEEE-RAS International Conference on Humanoid Robots*. 2014, pp. 407–412.

[110] Hsiu-Chin Lin et al. “A Projected Inverse Dynamics Approach for Multi-Arm Cartesian Impedance Control”. In: *2018 IEEE International Conference on Robotics and Automation (ICRA)*. 2018, pp. 5421–5428.

[111] Niels Dehio et al. “Enabling impedance-based physical human–multi–robot collaboration: Experiments with four torque-controlled manipulators”. In: *The International Journal of Robotics Research* 41.1 (2022), pp. 68–84.

[112] Yinzhen Xu et al. “Unidexgrasp: Universal robotic dexterous grasping via learning diverse proposal generation and goal-conditioned policy”. In: *Proceedings of the IEEE/CVF Conference on Computer Vision and Pattern Recognition*. 2023, pp. 4737–4746.

[113] Manuel Keppler, Christian Ott, and Alin Albu-Schäffer. "From underactuation to quasi-full actuation: Aiming at a unifying control framework for articulated soft robots". In: *International Journal of Robust and Nonlinear Control* 32.9 (2022), pp. 5453–5484.

[114] Marie Harder et al. "Simultaneous motion tracking and joint stiffness control of bidirectional antagonistic variable-stiffness actuators". In: *IEEE Robotics and Automation Letters* 7.3 (2022), pp. 6614–6621.

[115] Xuming Meng and Roman Weitschat. "Dynamic projection of human motion for safe and efficient human-robot collaboration". In: *2021 IEEE International Conference on Robotics and Automation (ICRA)*. IEEE. 2021, pp. 3765–3771.

[116] M. W. Spong. "Modeling and Control of Elastic Joint Robots". In: *Journal of Dynamic Systems, Measurement, and Control* 109.4 (1987), pp. 310–318.

[117] George Jose Pollayil et al. "Elastic structure preserving impedance control for nonlinearly coupled tendon-driven systems". In: *IEEE Control Systems Letters* 6 (2021), pp. 1982–1987.

[118] Sebastian Wolf et al. "Variable Stiffness Actuators: Review on Design and Components". In: *IEEE/ASME Transactions on Mechatronics* 21.5 (2016), pp. 2418–2430. DOI: 10.1109/TMECH.2015.2501019.

[119] Alin Albu-Schäffer et al. "Anthropomorphic Soft Robotics – From Torque Control to Variable Intrinsic Compliance". In: *Springer Tracts in Advanced Robotics*. Springer Berlin Heidelberg, 2011, pp. 185–207. DOI: 10.1007/978-3-642-19457-3_12.

[120] Richard M Murray, Zexiang Li, and S Shankar Sastry. *A mathematical introduction to robotic manipulation*. CRC press, 2017.

[121] Fabrizio Lotti et al. "Development of UB Hand 3: Early results". In: *Proceedings of the 2005 IEEE International Conference on Robotics and Automation*. IEEE. 2005, pp. 4488–4493.

[122] Arjan Schaft et al. *L2-gain and passivity techniques in nonlinear control*. Springer, 1996.

[123] Gerald Jay Sussman and Jack Wisdom. *Structure and interpretation of classical mechanics*. The MIT Press, 2015.

[124] Alin Albu-Schäffer et al. "Dynamic modelling and control of variable stiffness actuators". In: *2010 IEEE International Conference on Robotics and Automation*. IEEE. 2010, pp. 2155–2162.

[125] Shugen Ma, Hiroshi Yoshinada, and Shigeo Hirose. "CT ARM-I: Coupled tendon-driven manipulator model I-design and basic experiments". In: *Proceedings 1992 IEEE International Conference on Robotics and Automation*. IEEE Computer Society. 1992, pp. 2094–2095.

[126] Brian Rooks. "The harmonious robot". In: *Industrial Robot: An International Journal* (2006).

[127] Thomas Lens and Oskar von Stryk. "Design and dynamics model of a lightweight series elastic tendon-driven robot arm". In: *2013 IEEE International Conference on Robotics and Automation*. IEEE. 2013, pp. 4512–4518.

[128] N. McClamroch. "Singular systems of differential equations as dynamic models for constrained robot systems". In: *Proceedings. 1986 IEEE International Conference on Robotics and Automation*. Vol. 3. 1986, pp. 21–28.

[129] Xuming Meng, Manuel Keppler, and Christian Ott. "Passivity-based motion and force tracking control for constrained elastic joint robots". In: *IEEE Control Systems Letters* 7 (2022), pp. 217–222.

[130] Alin Albu-Schäffer, Christian Ott, and Gerd Hirzinger. "A unified passivity-based control framework for position, torque and impedance control of flexible joint robots". In: *The international journal of robotics research* 26.1 (2007), pp. 23–39.

[131] Steven M LaValle. *Planning algorithms*. Cambridge university press, 2006.

[132] Gilbert Strang. *Calculus*. Vol. 1. SIAM, 1991.

[133] Michael S Branicky, Vivek S Borkar, and Sanjoy K Mitter. "A unified framework for hybrid control: Model and optimal control theory". In: *IEEE transactions on automatic control* 43.1 (1998), pp. 31–45.

[134] Robert L Grossman et al. *Hybrid systems*. Vol. 736. Springer, 1993.

[135] Aleksei Fedorovich Filippov. "Differential equations with discontinuous right-hand side". In: *Matematicheskii sbornik* 93.1 (1960), pp. 99–128.

[136] Shankar Sastry. *Nonlinear systems: analysis, stability, and control*. Vol. 10. Springer Science & Business Media, 2013.

[137] Manuel Keppler et al. "Elastic Structure Preserving Impedance (ESPi) Control for Compliantly Actuated Robots". In: *2018 IEEE/RSJ International Conference on Intelligent Robots and Systems (IROS)*. 2018, pp. 5861–5868.

[138] Tad McGeer. "Passive Dynamic Walking". In: *The International Journal of Robotics Research* 9.2 (1990), pp. 62–82. DOI: 10.1177/027836499000900206.

[139] Weitao Xi and C. David Remy. "Optimal gaits and motions for legged robots". In: *2014 IEEE/RSJ International Conference on Intelligent Robots and Systems*. IEEE, 2014. DOI: 10.1109/iros.2014.6943015.

[140] Gerrit A. Folkertsma and Stefano Stramigioli. "Energy in Robotics". In: *Foundations and Trends in Robotics* 6.3 (2017), pp. 140–210. DOI: 10.1561/2300000038.

[141] K.F. Laurin-Kovitz, J.E. Colgate, and S.D.R. Carnes. "Design of components for programmable passive impedance". In: *Proceedings. 1991 IEEE International Conference on Robotics and Automation*. IEEE Comput. Soc. Press, 1991. DOI: 10.1109/robot.1991.131824.

[142] M. Zinn, O. Khatib, and B. Roth. "A new actuation approach for human friendly robot design". In: *IEEE International Conference on Robotics and Automation, 2004. Proceedings. ICRA '04. 2004*. IEEE, 2004. DOI: 10.1109/robot.2004.1307159.

[143] Antonio Bicchi, Michael A. Peshkin, and J. Edward Colgate. "Safety for Physical Human–Robot Interaction". In: *Springer Handbook of Robotics*. Springer Berlin Heidelberg, 2008, pp. 1335–1348. DOI: 10.1007/978-3-540-30301-5_58.

[144] G.A. Pratt and M.M. Williamson. "Series elastic actuators". In: *Proceedings 1995 IEEE/RSJ International Conference on Intelligent Robots and Systems. Human Robot Interaction and Cooperative Robots*. IEEE Comput. Soc. Press, 1995. DOI: 10.1109/iros.1995.525827.

[145] G. Tonietti, R. Schiavi, and A. Bicchi. "Design and Control of a Variable Stiffness Actuator for Safe and Fast Physical Human/Robot Interaction". In: *Proceedings of the 2005 IEEE International Conference on Robotics and Automation*. IEEE, 2005. DOI: 10.1109/robot.2005.1570172.

[146] Bianca S Homberg et al. "Robust proprioceptive grasping with a soft robot hand". In: *Autonomous Robots* 43.3 (2019), pp. 681–696.

[147] Mathieu Grossard, Javier Martin, and Gabriel Felippe da Cruz Pacheco. "Control-oriented design and robust decentralized control of the CEA dexterous robot hand". In: *IEEE/ASME Transactions on Mechatronics* 20.4 (2014), pp. 1809–1821.

[148] Ryuta Ozawa and Hiroaki Kobayashi. "A new impedance control concept for elastic joint robots". In: *2003 IEEE International Conference on Robotics and Automation (Cat. No. 03CH37422)*. Vol. 3. IEEE. 2003, pp. 3126–3131.

[149] Maxime Chalon and Brigitte d'Andréa Novel. "Backstepping experimentally applied to an antagonistically driven finger with flexible tendons". In: *IFAC Proceedings Volumes* 47.3 (2014), pp. 217–223.

[150] Jean-Jacques E Slotine, Weiping Li, et al. *Applied nonlinear control*. Vol. 199. 1. Prentice hall Englewood Cliffs, NJ, 1991.

[151] Manuel Keppler et al. "A passivity-based approach for trajectory tracking and link-side damping of compliantly actuated robots". In: *2016 IEEE International Conference on Robotics and Automation (ICRA)*. IEEE, 2016. DOI: 10.1109/icra.2016.7487239.

[152] A. De Luca and R. Mattone. "Actuator failure detection and isolation using generalized momenta". In: *2003 IEEE International Conference on Robotics and Automation (Cat. No.03CH37422)*. IEEE, 2003. DOI: 10.1109/robot.2003.1241665.

[153] Alessandro De Luca et al. "Collision Detection and Safe Reaction with the DLR-III Lightweight Manipulator Arm". In: *2006 IEEE/RSJ International Conference on Intelligent Robots and Systems*. IEEE, 2006. DOI: 10.1109/iros.2006.282053.

[154] Gianluca Garofalo, Christian Ott, and Alin Albu-Schäffer. "On the closed form computation of the dynamic matrices and their differentiations". In: *2013 IEEE/RSJ International Conference on Intelligent Robots and Systems*. 2013, pp. 2364–2359.

[155] Martin Wehr, Andreas Pott, and Karl-Heinz Wehking. "Bending Fatigue Strength and Lifetime of Fiber Ropes". In: *Cable-Driven Parallel Robots*. Ed. by Clément Gosselin et al. Cham: Springer International Publishing, 2018, pp. 73–84.

[156] Xuming Meng et al. "Finger flow: Reactive reach-while-grasp generation for robotic arms with multi-fingered hands". In: *Robotics and Autonomous Systems* (2025), p. 105222.

[157] Chao Wang et al. "Feature sensing and robotic grasping of objects with uncertain information: A review". In: *Sensors* 20.13 (2020), p. 3707.

[158] Andreas Orthey, Constantinos Chamzas, and Lydia E Kavraki. "Sampling-based motion planning: A comparative review". In: *Annual Review of Control, Robotics, and Autonomous Systems* 7 (2023).

[159] Vincent Mayer et al. "FFHNet: Generating multi-fingered robotic grasps for unknown objects in real-time". In: *2022 International Conference on Robotics and Automation (ICRA)*. IEEE. 2022, pp. 762–769.

[160] Hong Qiao et al. "The concept of "attractive region in environment" and its application in high-precision tasks with low-precision systems". In: *IEEE/ASME Transactions on Mechatronics* 20.5 (2014), pp. 2311–2327.

[161] Gaotian Wang et al. "Caging in time: A framework for robust object manipulation under uncertainties and limited robot perception". In: *The International Journal of Robotics Research* (2025), p. 02783649251343926.

[162] Thomas Feix et al. “The GRASP Taxonomy of Human Grasp Types”. In: *IEEE Transactions on Human-Machine Systems* 46.1 (2016), pp. 66–77.

[163] Marc Jeannerod. “The timing of natural prehension movements”. In: *Journal of motor behavior* 16.3 (1984), pp. 235–254.

[164] Marco Santello, Martha Flanders, and John F Soechting. “Patterns of hand motion during grasping and the influence of sensory guidance”. In: *Journal of Neuroscience* 22.4 (2002), pp. 1426–1435.

[165] Maxime Chalon. “Modeling and control of an antagonistically actuated tendon driven anthropomorphic hand”. PhD thesis. Mines ParisTech, 2013.

[166] Manuel Stoiber et al. “Fusing Visual Appearance and Geometry for Multi-modality 6DoF Object Tracking”. In: *2023 IEEE/RSJ International Conference on Intelligent Robots and Systems (IROS)*. IEEE. 2023, pp. 1170–1177.

[167] Monica Malvezzi et al. “SynGrasp: A MATLAB toolbox for grasp analysis of human and robotic hands”. In: *2013 IEEE International Conference on Robotics and Automation*. IEEE. 2013, pp. 1088–1093.

[168] Kenneth Arthur Stroud and Dexter J Booth. *Engineering mathematics*. Bloomsbury Publishing, 2020.

[169] Ernest D Fasse and Jan F Broenink. “A spatial impedance controller for robotic manipulation”. In: *IEEE Transactions on Robotics and Automation* 13.4 (1997), pp. 546–556.

[170] Ernest D Fasse and Neville Hogan. “Control of physical contact and dynamic interaction”. In: *Robotics Research: The Seventh International Symposium*. Springer. 1996, pp. 28–38.

[171] Walter Rudin et al. *Principles of mathematical analysis*. Vol. 3. McGraw-hill New York, 1964.

[172] Hans Jacob S Feder and J-JE Slotine. “Real-time path planning using harmonic potentials in dynamic environments”. In: *Proceedings of International Conference on Robotics and Automation*. Vol. 1. IEEE. 1997, pp. 874–881.

[173] Gianluca Garofalo, Christian Ott, and Alin Albu-Schäffer. “On the closed form computation of the dynamic matrices and their differentiations”. In: *2013 IEEE/RSJ International Conference on Intelligent Robots and Systems*. IEEE. 2013, pp. 2364–2359.

[174] Jörg Butterfaß et al. “DLR-Hand II: Next generation of a dextrous robot hand”. In: *Proceedings 2001 ICRA. IEEE International Conference on Robotics and Automation (Cat. No. 01CH37164)*. Vol. 1. IEEE. 2001, pp. 109–114.

[175] Ritvik Singh et al. “Dextrah-rgb: Visuomotor policies to grasp anything with dexterous hands”. In: *arXiv preprint arXiv:2412.01791* (2024).

[176] S. Ahmad. “Constrained motion (force/position) control of flexible joint robots”. In: *IEEE Transactions on Systems, Man, and Cybernetics* 23.2 (1993), pp. 374–381.

[177] Krzysztof P. Jankowski and Hoda A. ElMaraghy. “Robust hybrid position/force control of redundant robots”. In: *Robotics and Autonomous Systems* 27.3 (1999), pp. 111–127. ISSN: 0921-8890.

[178] Yan-Ru Hu and George Vukovich. “Position and force control of flexible joint robots during constrained motion tasks”. In: *Mechanism and Machine Theory* 36.7 (2001), pp. 853–871. ISSN: 0094-114X.

[179] L. Huang, S.S. Ge, and T.H. Lee. "Position/force control of uncertain constrained flexible joint robots". In: *Mechatronics* 16.2 (2006), pp. 111–120. ISSN: 0957-4158.

[180] Alessandro De Luca and Fabrizio Flacco. "Dynamic gravity cancellation in robots with flexible transmissions". In: *49th IEEE Conference on Decision and Control (CDC)*. 2010, pp. 288–295.

[181] L. Villani, C.C. De Wit, and B. Brogliato. "An exponentially stable adaptive control for force and position tracking of robot manipulators". In: *IEEE Transactions on Automatic Control* 44.4 (1999), pp. 798–802.

[182] Gianluca Antonelli. "Stability Analysis for Prioritized Closed-Loop Inverse Kinematic Algorithms for Redundant Robotic Systems". In: *IEEE Transactions on Robotics* 25.5 (2009), pp. 985–994.

[183] A. Albu-Schäffer et al. "Cartesian impedance control of redundant robots: recent results with the DLR-light-weight-arms". In: *2003 IEEE International Conference on Robotics and Automation (Cat. No.03CH37422)*. Vol. 3. 2003, 3704–3709 vol.3.

[184] M. Vidyasagar. "Decomposition techniques for large-scale systems with nonadditive interactions: Stability and stabilizability". In: *IEEE Transactions on Automatic Control* 25.4 (1980), pp. 773–779.

[185] Brad Paden and Ravi Panja. "Globally asymptotically stable 'PD+' controller for robot manipulators". In: *International Journal of Control* 47.6 (1988), pp. 1697–1712.

[186] Gianluca Garofalo, Christian Ott, and Alin Albu-Schäffer. "On the closed form computation of the dynamic matrices and their differentiations". In: *2013 IEEE/RSJ International Conference on Intelligent Robots and Systems*. 2013, pp. 2364–2359.

[187] Florian Petit. "Analysis and Control of Variable Stiffness Robots". PhD thesis. ETH-Zürich, 2014. URL: https://elib.dlr.de/113157/.

[188] Hassan K Khalil. *Nonlinear control*. Pearson Higher Ed, 2014.

[189] Werner Friedl and Máximo A Roa. "CLASH—A compliant sensorized hand for handling delicate objects". In: *Frontiers in Robotics and AI* 6 (2020), p. 138.

[190] Werner Friedl. "Evaluation of different robotic grippers for simultaneous multi-object grasping". In: *Frontiers in Robotics and AI* 11 (2024), p. 1351932.

[191] Luc Le Tien et al. "Friction observer and compensation for control of robots with joint torque measurement". In: *2008 IEEE/RSJ International Conference on Intelligent Robots and Systems*. IEEE. 2008, pp. 3789–3795.

[192] Domenico Prattichizzo and Jeffrey C Trinkle. "Grasping". In: *Springer handbook of robotics* (2016), pp. 955–988.

[193] John Schulman et al. "Motion planning with sequential convex optimization and convex collision checking". In: *The International Journal of Robotics Research* 33.9 (2014), pp. 1251–1270.

[194] Marc A Toussaint et al. "Differentiable physics and stable modes for tool-use and manipulation planning". In: (2018).

[195] Robin Verschueren et al. "acados—a modular open-source framework for fast embedded optimal control". In: *Mathematical Programming Computation* 14.1 (2022), pp. 147–183.

[196] Anusha Nagabandi et al. “Neural network dynamics for model-based deep reinforcement learning with model-free fine-tuning”. In: *2018 IEEE international conference on robotics and automation (ICRA)*. IEEE. 2018, pp. 7559–7566.

[197] Bruno Siciliano and Luigi Villani. *Robot force control*. Springer Science & Business Media, 1999.

[198] Daniel E Whitney. “Historical perspective and state of the art in robot force control”. In: *The International Journal of Robotics Research* 6.1 (1987), pp. 3–14.

[199] Siqi Zhou et al. “Bridging the model-reality gap with lipschitz network adaptation”. In: *IEEE Robotics and Automation Letters* 7.1 (2021), pp. 642–649.

[200] Andrew J Taylor et al. “Episodic learning with control lyapunov functions for uncertain robotic systems”. In: *2019 IEEE/RSJ International Conference on Intelligent Robots and Systems (IROS)*. IEEE. 2019, pp. 6878–6884.

[201] Lukas Hewing et al. “Cautious Model Predictive Control using Gaussian Process Regression”. In: *IEEE Transactions on Automatic Control*. Vol. 65. 12. IEEE, 2020, pp. 5120–5135.

[202] Maziar Raissi, Paris Perdikaris, and George E Karniadakis. “Physics-informed neural networks: A deep learning framework for solving forward and inverse problems involving nonlinear partial differential equations”. In: *Journal of Computational Physics* 378 (2019), pp. 686–707.

[203] Karl J Åström. *Introduction to stochastic control theory*. Courier Corporation, 2012.

[204] Gregory Kahn et al. “Uncertainty-aware reinforcement learning for collision avoidance”. In: *arXiv preprint arXiv:1702.01182* (2017).

[205] Zachary Hibbard et al. “Safely: Safe stochastic motion planning under constrained sensing via duality”. In: *Proceedings of Robotics: Science and Systems (RSS)*. 2022.

[206] Carlos Quintero-Peña et al. “Stochastic Implicit Neural Signed Distance Functions for Safe Motion Planning under Sensing Uncertainty”. In: *Proceedings of the IEEE International Conference on Robotics and Automation (ICRA)*. 2024.

[207] Fabio Muratore et al. “Robot learning from randomized simulations: A review”. In: *Frontiers in Robotics and AI* 9 (2022), p. 756967.

[208] Eike Matschek, Jonas Umlauft, and Sandra Hirche. “Safe machine learning-supported model predictive force and motion control in robotics”. In: *IEEE Transactions on Robotics* (2023).

[209] Yaron Lipman et al. “Flow matching for generative modeling”. In: *arXiv preprint arXiv:2210.02747* (2022).

[210] Roya Firoozi et al. “Foundation models in robotics: Applications, challenges, and the future”. In: *The International Journal of Robotics Research* 44.5 (2025), pp. 701–739.

[211] Wanxin Jin. “Complementarity-free multi-contact modeling and optimization for dexterous manipulation”. In: *arXiv preprint arXiv:2408.07855* (2024).

[212] Julius Jankowski et al. “Robust pushing: Exploiting quasi-static belief dynamics and contact-informed optimization”. In: *The International Journal of Robotics Research* (2025), p. 02783649251318046.

[213] Fabio Muratore et al. “Robot learning from randomized simulations: A review”. In: *Frontiers in Robotics and AI* 9 (2022), p. 799893.

[214] Tao Pang et al. “Global planning for contact-rich manipulation via local smoothing of quasi-dynamic contact models”. In: *IEEE Transactions on robotics* 39.6 (2023), pp. 4691–4711.

[215] W. Khalil and E. Dombre. “Modeling, Identification and Control of Robots”. In: *Applied Mechanics Reviews* 56.3 (May 2003), B37–B38. ISSN: 0003-6900.

[216] Zoltán Horváth, Yunfei Song, and Tamás Terlaky. “A novel unified approach to invariance conditions for a linear dynamical system”. In: *Applied Mathematics and Computation* 298 (2017), pp. 351–367. ISSN: 0096-3003.

[217] Mitio Nagumo. “Über die lage der integralkurven gewöhnlicher differentialgleichungen”. In: *Proceedings of the Physico-Mathematical Society of Japan. 3rd Series* 24 (1942), pp. 551–559.

[218] Franco Blanchini. “Set invariance in control”. In: *Automatica* 35.11 (1999), pp. 1747–1767.